Linear Global Nonmodal Instability Analysis of High-Speed Flows

Thesis submitted in accordance with the requirements of
the University of Liverpool for the degree of Doctor in Philosophy
by
Helio Ricardo de Aguiar Quintanilha Junior

June 2021

Abstract

Identification of all physical mechanisms responsible for the flow breakdown from laminar to turbulent remains elusive in many high-speed boundary layer flows. Predicting the onset of transition and understanding the linear mechanisms responsible for transition in supersonic and hypersonic is critical to controlling instability mechanisms and preventing a multifold increase in the thermal protection system required. In the traditional modal theory, low amplitude external disturbances are generated by receptivity mechanisms and grow exponentially, leading the flow to transition. On the other hand, for flows subjected to high external disturbance levels, a bypass of the modal amplification path can happen and a nonmodal stability analysis becomes an additional route to transition that needs to be studied.

The present thesis aims to address both modal and nonmodal stability analysis of high-speed spatially-inhomogeneous boundary-layer flows. In this effort, a massively parallel code, *Li*near *G*lobal instability for *H*ypersonic *T*ransition (*LiGHT*) has been developed to solve multi-dimensional complex non-symmetric eigenvalue problems (EVP) and Singular Value Decomposition (SVD) problems arising in the solutions of global linear fluid flow instability.

The code has been applied to four canonical flow configurations. The first flow studied has been the main motivator of the present thesis: it concerns hypersonic flow over the HiFIRE-5 elliptic cone model, which is investigated at two different flight altitudes. A new physical mechanism, unveiled by transient growth analysis, revealed that optimal conditions are associated with streamwise velocity streaks in the crossflow region. These streaks are in good qualitatively agreement with experimental results. Moreover, a quartic dependence of the maximum energy gain on the local Reynolds number was found in the highest altitude analysed, contrasting with the quadratic dependence found at the lower altitude and known from the incompressible regime. The most significant finding of the analysis on the elliptic cone concerns the role of the flight altitude: nonmodal instability becomes progressively more important as the flight altitude increases, corresponding to density and unit Reynolds number decreases. At the highest altitude examined, transient growth can be the only linear stability physical mechanism that can give rise to laminar-turbulent transition. The second and third examples are

related to understanding the importance of the shock layer in the global instability modes. In the second flow studied, instability in the region ahead of the windward face of a circular cylinder is investigated, including the bow shock in the stability analysis domain. In the third example, flow over a compression ramp is interrogated, including the separation and reattachment shocks. Results obtained in both of these cases suggest that the shocks appear to be an integral part of the modes and cannot be neglected from the analysis. The fourth and last flow investigated is the hypersonic flow over a flat plate with a base flow generated from kinetic theory. Results obtained reveal that linear stability can indeed be predicted with sufficient quality, opening a new scenario to investigate high-speed flows.

Acknowledgements

First of all, I would like to thank God, who has always been with me in the course of my PhD. I dedicate this thesis to my mother, Maria José Quintanilha, my brother, Dr. Daniel Quintanilha, my girlfriend, Julia Bukharyna and especially my father, Helio Quintanilha, who I wish could have been here. I hope I have made you all proud.

I also would like to say thank you to:

Prof. Vassilis Theofilis, my supervisor, who believed in me and gave me the opportunity to come to Liverpool. His guidance, patience and knowledge were truly appreciated during my PhD years.

Dr. Ricardo Santos, my friend, who without his help I would not have been able to finish this thesis. His help with the generalised coordinates and the parallelisation was much appreciated. He also provided me with the baseflows from the compression ramp and the circular cylinder.

All my friends and colleagues I made during my PhD in Liverpool. In special, Panagiotis Belesiotis, who I first met in Liverpool, Nicolas Cerulus who is working on the continuation of the compression ramp, Anton Burtsev who is now responsible for the circular cylinder and Angelos Klothakis who provided me with the DSMC flat plate base flow.

Rafael Quintanilha, my cousin, who gave me support to finish my PhD and is helping me with the continuation of my career.

Dr. Ardeshir Hanifi and Dr. Pedro Paredes, my co-authors in the HiFIRE-5 elliptic cone paper.

Professor Neil Sandham and Professor Olivier Cadot, my PhD examiners, for a stimulating and pleasant VIVA.

Effort sponsored by the Air Force Office of Scientific Research, Air Force Material Command, USAF, under Grant no. FA9550-15-1-0387, "Global transient growth mechanisms in high-speed flows, with application to the elliptic cone", monitored by Dr. "Pon" R. Ponnappan and Dr. Ivett Leyva. The US Government is authorized to reproduce and distribute reprints for Governmental purpose notwithstanding any copyright notation thereon. Discussions with Dr. Roger Kimmel and Dr. Ryan Gosse, who also made available the base flow analysed herein are gratefully acknowledged. Access to Copper Cray XE6m (https://www.ors. hpc.mil) was made possible by project AFVAW10102F62, with Dr. Nicholas Bisek as Principal Investigator and is gratefully acknowledged.

Contents

List of Figures

Nomenclature

x	streamwise direction
y	wall-normal direction
z	spanwise direction
ξ	transformed streamwise direction
η	self-similar variable, transformed wall-normal direction
ζ	transformed spanwise direction
t	time
ρ	density
$\mathbf{V}$	velocity vector
T	temperature
p	pressure
μ	first coefficient of viscosity
λ	second coefficient of viscosity
ν	kinematic viscosity
k	thermal conductivity
R	gas constant
L	length scale
a	speed of sound
γ	ratio of specific heats
c_v	specific heat at constant volume
Re	Reynolds number
Re'	unit Reynolds number
Ma	Mach number
Pr	Prandtl number
Ec	Eckert number
Kn	Knudsen number
$\mathbf{q}$	general vector of primitive flow quantities
$\tilde{\mathbf{q}}$	disturbance vector of primitive flow quantities
$\hat{\mathbf{q}}$	amplitude functions of primitive flow quantities
N	number of discretisation points
m	Krylov subspace

α	streamwise wave-number
β	spanwise wave-number
L_x	periodicity lenght along the streamwise direction
L_z	periodicity lenght along the spanmwise direction
i	imaginary number
ω	complex eigenvalue
ω_r	angular frequency
ω_i	growth/decay rate
$\hat{\eta}$	vorticity
Θ	phase function
J	determinant of the Jacobian
h	scale factor
$\mathcal{L}$	linear operator
$\mathcal{M}$	integral weight matrix
$\mathcal{D}$	differential operator

Subscript

E	energy
ref	reference values
∞	free-stream values
e	edge values
i	imaginary part
r	real part
stag	stagnation
opt	optimum
max	maximum
S	symmetric
A	antisymmetric
D	diameter
cBL	compressible boundary layer

Superscript

$*$	dimensional quantity
H	complex conjugate transpose

Objectives

The present thesis has two main objectives: the development of a massively parallel incompressible to hypersonic multi-dimensional linear modal and nonmodal stability analysis code (LiGHT - *Li*near *G*lobal instability for *H*ypersonic *T*ransition) and its application to high-speed canonical flows. The bulk of this thesis aims to extend the modal work of Paredes et al. (2016) on the hypersonic flow over the HiFiRE-5 elliptic cone model to understand the importance of nonmodal instabilities, where a new scenario based on transient growth has been discovered. The two following problems investigate the role in resolving the shock in both modal and nonmodal stability analysis. Finally, the compressible flat-plate boundary layer is investigated using Direct Simulation Monte Carlo (DSMC) to generate the steady base flow. This is the first step to gain confidence in performing stability analysis using kinetic theory methods.

Outline

The thesis is divided into seven chapters:

- **Chapter 1:** In the first chapter, a literature survey of linear stability theory is presented from the first observations of the instability phenomenon in fluid flows until the current broad understanding of the different paths-to-transition in high-speed flows.
- **Chapter 2:** The second chapter presents the classical modal linear stability analysis derivation, starting from the three-dimensional Navier-Stokes equations. The modern linear stability classification concepts are addressed in depth. Two different methods to solve the equations in a generalised frame of reference are detailed and compared in an example.
- **Chapter 3:** In the third chapter, attention is devoted to nonmodal stability analysis. Transient growth is explained in geometric and theoretical examples. The initial value problem is addressed along with the theoretical foundations to compute the optimal linear conditions.
- **Chapter 4:** The tools necessary to solve the one-, two- or three-dimensional complex non-symmetric eigenvalue and singular value problems are detailed. In

a matrix-forming framework, the construction of the discretised operators is addressed using the Kronecker product. The different boundary conditions available to complete the problem are presented. The (large) EVP solution based on the Krylov subspace and the subsequent singular value decomposition is shown together with a parallelisation strategy to store and invert the matrix. A brief scalability study completes the chapter.

- **Chapter 5:** In this chapter, the newly developed multi-dimensional *LiGHT* code is verified against benchmarked literature results. The code is shown to correctly obtain the linear results for the local and BiGlobal frameworks, from incompressible to compressible flows. Both modal and nonmodal stability analysis implementation is verified.

- **Chapter 6:** Chapter six contains all the new results obtained with the *LiGHT* code. Four different cases are analysed and presented in individual sections. Each of these sections is briefly described next.

  - **Section 6.1:** linear local and BiGlobal nonmodal stability analysis is presented on the hypersonic flow over an aspect ratio two elliptic cone model. Two different altitudes, namely 21 km and 33 km, are investigated.
  - **Section 6.2:** Modal and nonmodal global stability analysis was performed in the hypersonic flow ahead of the windward face of a circular cylinder.
  - **Section 6.3:** To investigate the shock boundary-layer interaction (SBLI) role in the global mode, a modal and nonmodal linear stability analysis has been carried out in the supersonic flow over a 10° compression ramp.
  - **Section 6.4:** The local linear stability analysis of the hypersonic flow over a semi-infinite flat-pate is investigated using Direct Simulation Monte Carlo (DSMC) to generate a steady base flow.

- **Chapter 7:** A summary of the thesis is presented together with ideas for future (or immediate) work.

The topics presented in this thesis, along with additional specific details, have been submitted to the following conferences/journals:

- **Paper submitted**

  - Klothakis, A., Quintanilha Jr, H., Sawant, S., Protopapadakis E., Theofilis, V., Levin, D., **Linear stability analysis of hypersonic boundary layers computed by a kinetic approach: A semi-infinite flat plate at $4.5 \leq \mathbf{M}_\infty \leq 9$**. To: *Theoretical and Computational Fluid Dynamics*

- **Papers in preparation**
  - Quintanilha Jr, H., Paredes, P., Hanifi, A. and Theofilis, V., **Global Transient-Growth Mechanisms in High-Speed Flows with Application to the Elliptic Cone Model**.
  - Santos, R., Quintanilha Jr, H., Cerulus, N., Alves, L. and Theofilis, V., **Global Modal and Nonmodal Instability Analyses of Shock Induced Separation Bubbles**.
  - Quintanilha Jr, H., Burtsev, A., Santos, R., Theofilis, V. and Alves L, **Linear Instability Mechanisms of Supersonic Flow Past Blunt Bodies**.
- **Conferences**
  - Quintanilha Jr, H., Theofilis, V., **Steady Laminar Solutions of Hypersonic Flow over Oberkampf Bodies at Cruise**. In: *AIAA SciTech*, AIAA Paper 2021-0632, 11-21 January 2021.
  - Klothakis, A., Quintanilha Jr, H., Sawant, S., Theofilis, V., Levin, D., **Slip Effects on the Stability of Supersonic Laminar Flat Plate Boundary Layer**. In: *AIAA SciTech*, AIAA Paper 2021-1659, 11-21 January 2021.
  - Cerulus, N., Quintanilha Jr, H., Theofilis, V., **Global Linear Stability Analysis of the Supersonic Flows Over a Hollow Cylinder Flare Model**. In: *AIAA SciTech*, AIAA Paper 2021-0052, 11-21 January 2021.
  - Burtsev, A., Quintanilha Jr, H., Santos, R., Alves, L., Theofilis, V., **Linear Instability Mechanisms of Supersonic Flow Past Blunt Bodies**. In: *AIAA SciTech*, AIAA Paper 2021-0050, 11-21 January 2021.
  - Quintanilha Jr, H., Cerulus, N., Theofilis, V., **Linear Instability Mechanisms of Supersonic Flow Over a Hollow Cylinder Flare Model**. In: *APS Fluid Dynamics*, 22-24 November 2020.
  - Cerulus, N., Quintanilha Jr, H., Theofilis, V., Santos, R., Alves, L., **Stability of laminar supersonic flow on compression ramps**. In: *APS Fluid Dynamics*, 22-24 November 2020.
  - Klothakis, A., Quintanilha Jr, H., Sawant, S., Theofilis, V., Levin, D., **On the Effect of Velocity Slip and Temperature Jump on the Flat Plate Boundary-Layer Stability at Mach 4.5**. In: *APS Fluid Dynamics*, 22-24 November 2020.
  - Quintanilha Jr, H., Theofilis, V., Hanifi, A., **Global Transient-Growth Analysis of Hypersonic Flow on the HIFiRE-5 Elliptic Cone Model**. In: *AIAA SciTech*, AIAA Paper 2019-2148, 07-11 January 2019.

- Quintanilha Jr, H., Belesiotis, P., Theofilis, V., Hanifi, A., **Non-modal Stability Analysis of the HIFiRE-5 Elliptic Cone Model Flow in Different Flight Altitudes**. In: *IACAS*, Paper 1543-1555, 14-15 March 2018.
- Quintanilha Jr, H., Santos, R., Alves, L., Theofilis, V., **Distributed Solution of Global Eigenvalue Problems on Large Clusters**. In: *AIAA Aviation*, AIAA Paper 2017-4510, 05-09 June 2017.

- **Posters**
  - Quintanilha Jr, H., Santos, R., Alves, L., Theofilis, V., **Linear Instability Mechanisms of Supersonic Flow Past Blunt Bodies**. In: *IX IUTAM Symposium on Laminar-Turbulent Transition*, London UK, 02-06 September 2019.
  - Quintanilha Jr, H., Santos, R., Cerulus, N., Alves, L. and Theofilis, V., **Linear Instability in a Supersonic Compression Ramp**. In: *IX IUTAM Symposium on Laminar-Turbulent Transition*, London UK, 02-06 September 2019.

Chapter 1

Introduction

Primary linear instability

A system is considered stable when it is immune to small disturbances such that, when perturbed, it returns to its original state. In other words, when a system is perturbed away from, but still remains close to its state of equilibrium, it eventually returns to the equilibrium state after enough time has passed. If the disturbance tends to zero, the system is called asymptotically stable. If the disturbance grows, the system is unstable. Finally, if the disturbance neither increases or decreases, the system is defined as neutrally stable. The first concepts and observations of the instability phenomenon in fluid flows were reported by Helmholtz (1868), Thomson (1871) , Kelvin (1871) and concerned inviscid disturbances in incompressible shear flows. When two viscous layers are in relative motion to each other, they will generate shear between them. The associated vorticity causes the fluid in each layer to mix, and the flow becomes highly unstable. Disturbances often grow large enough to generate vortical structures in a process known as Kelvin-Helmholtz instability. Lord Rayleigh (1878, 1880) considered the role of inviscid disturbances in two-dimensional flows. One of the most important results of this period was Rayleigh's theorem on the role of inflexion points as a necessary condition for the onset of inviscid instabilities. A review of the early inviscid and viscous instability theory can be found in Drazin and Reid (1981).
One of the most famous experiments in fluid mechanics was also performed in the 19^{th} century by Reynolds (1883). It was the first laminar-turbulent transition experiment reported and marks the beginning of a methodical and now abundant study of stability of viscous shear flows. Lord Rayleigh (1878, 1880) first suggested the existence of sinusoidal disturbances prior to the transition in a boundary layer flow. Reynolds' experiment motivated the independent theoretical investigations of Orr (1907) and Sommerfeld (1908), who studied the evolution of infinitesimal disturbances upon a steady, parallel flow. Contrary to the understanding at the time, Tollmien (1929) and Schlichting (1932) independently showed that viscosity could have destabilising effects. They computed viscous instabilities in the two-dimensional incompressible flat

plate boundary layer by solving the Orr-Sommerfeld equation and found that these instabilities take the form of travelling waves. These waves are now known as Tollmien-Schlichting (TS) waves. Squire (1933) introduced a transformation showing that for incompressible two-dimensional shear flows, there exists a two-dimensional disturbances more dangerous than the three-dimensional. Squire's theorem can be used to limit the analysis to two-dimensional disturbances. Schubauer and Skramstad (1947) in their famous experiment during the Second World War confirmed the sinusoidal disturbances in the flat-plate boundary layer. They quantified characteristics of the TS waves and found that these disturbances break down into turbulent spots leading to turbulence. Figure 1.1 compares the experimental results of Schubauer and Skramstad (1947) with the analytic solutions obtained by Tollmien (1929) and Schlichting (1932) in a neutral stability curve, splitting the regions of stable and unstable flow.

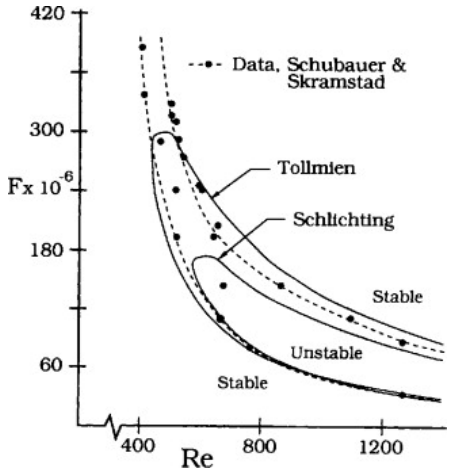

Figure 1.1: Comparison between analytic solutions of the Orr-Sommerfeld equations calculated by Tollmien (1929) and Schlichting (1932) with the measured experimental results of Schubauer and Skramstad (1947).

In the initial stage of transition, exponential growth of TS waves can be predicted by linear stability theory. After that, a secondary instability (more details shortly) develops and is responsible for the appearance of vortical structures that will eventually form the turbulent spots. However, since the distance between the region where the linear theory holds and the actual breakdown to turbulence happens can be short, most practical transition prediction methods are based on linear stability theory. The amplitude of the most unstable perturbation propagating downstream is amplified, and a total growth rate can be determined. The envelope of all unstable modes at different frequencies is the basis of the so-called N-factor, transition prediction method still largely in use in industry. This envelope was used by Van Ingen (1956) and Smith and Gamberoni (1956) to define the onset of the transition and is known as the e^N method. In incompressible flows, N-factors between 9 to 10 are typical values for TS waves and 4 to 5 for crossflow modes.

Lees and Lin (1946) and Lees (1947) considered the effects of compressibility and derived a generalisation of Rayleigh's theorem of inflexion point. The so-called generalised inflexion point shows that inviscid instability increases with Mach number as the generalised inflexion point moves away from the wall. On the other hand, viscosity has a stabilising effect on two-dimensional waves. Furthermore, they first reported that wall cooling has a stabilising effect on the two-dimensional compressible boundary layer flow. Laufer and Vrebalovich (1960) experimentally showed instability modes in a supersonic laminar boundary layer. These authors showed that the adiabatic compressible boundary layer at $Ma < 2.2$ is more stable than its incompressible counterpart. Kendall (1975) and later Kosinov et al. (1990) experimentally found evidence of the possible existence of high-frequency modes in high-speed boundary layers. Mack (1965, 1969, 1976, 1984, 1987) confirmed Lees (1947) theorem of generalised inflexion point that inviscid instability increases with Mach number and that viscous instability eventually disappears for $Ma > 3$. He found different instability scenarios as the Mach number increases. First, for subsonic flows, two-dimensional waves are the most unstable, in line with Squire's theorem (Squire 1933). In the lower supersonic regime, however, oblique waves (three-dimensional TS waves) are more unstable. Finally, probably the most important result obtained by Mack was to numerically unravel the existence of a dominant unstable high-frequency mode at $Ma > 4$. This mode is a two-dimensional wave, commonly referred to in the literature as Mack mode and is more unstable than the first TS mode; see Fedorov (2011) for a further discussion. Furthermore, Mack numerically confirmed that cooling the wall stabilises the first mode, in agreement with Lees (1947), but destabilises the second Mack mode. In other words, cooling the wall will destabilise the boundary layer at high-speed flows. These findings were experimentally confirmed by Lysenko and Maslov (1984) and validated through direct numerical simulation (DNS), e.g. by Erlebacher and Hussaini (1990).

Most of the high-speed boundary layer problems considered in the literature at this time neglected the presence of a shock in the stability calculations (Mack 1984, 1987, Gasperas 1987, Macaraeg and Streett 1988, Malik 1989, Balakumar and Reed 1991, Balakumar and Malik 1992). The first theoretical investigation of the interaction of a shock with linear perturbations was published by Ribner (1954) and McKenzie and Westphal (1968) and later applied by Anyiwo and Bushnell (1982) in the context of amplifying turbulence. They confirmed Kovasznay (1953) findings that free-stream disturbances can interact with the shock and generate acoustic, entropy or vorticity modes. This interaction was later confirmed in a multitude of DNS simulations including Zang et al. (1984). Kumar et al. (1989) found that the shock can be unstable to perturbations travelling normal to the shock when the tangential flow is subsonic. The first study of the interaction between the shock with the boundary layer was performed by Petrov (1985). He employed linearised Rankine-Hugoniot conditions as boundary

conditions at the shock. This procedure was applied to wedges and cones in the work of Chang et al. (1990). They found that when the shock is located close to the boundary layer edge, it can stabilise the first and second modes. Moreover, they did not find a relationship between the shock and the Mack mode, seen as the dominant mode at hypersonic speeds in experiments (Fischer and Weinstein 1972, Schneider 2004). Their analysis, however, did not resolve the shock but modelled it as a boundary condition. Malik and Anderson (1991) investigated real gas effects, adding chemical reaction to the base flow and gas property variations. They found that real gas effects stabilise the TS waves and destabilise the second Mack mode at high Mach numbers ($Ma > 10$) and showed that the frequency of the unstable Mack mode decreases. Stuckert and Reed (1994) analysed the stability of a 10 degrees half-angle cone considering equilibrium, non-equilibrium and ideal gas flows. They used shock fitting methods for the base flow calculation and linearised Rankine-Hugoniot boundary conditions for the stability analysis. They also found that, contrary to ideal gas flows, the second Mack mode is shifted to lower frequencies if either equilibrium or non-equilibrium is considered. They explained this shift due to "the increase in the size of the region of relative supersonic flow due to the lower speeds of sound in the relatively cooler boundary layers". More recently, Miró Miró et al. (2019) and Miró Miró and Pinna (2020) considered the effects of high-enthalpy models, ionisation and dissociation in the second Mack mode. They found that ionisation has a stabilising impact, whereas dissociation destabilises the Mack mode. Moreover, they attribute the appearance of an unstable supersonic mode to the effects of high-enthalpy, opposite to wall cooling. They also used Rankine-Hugoniot boundary conditions but claimed that little effect was noticed in the ultimate N-Factor.

All the aforementioned results for high Mach number flows considered the continuum approach. However, the internal shock layer structure (which is inaccessible to the Navier-Stokes equations) and its potential effect on boundary layer stability were either neglected or modelled through the boundary conditions. It would thus appear natural to apply kinetic theory methods to address linear flow instability. The use of particle-method based linear stability analysis was pioneered by Pérez et al. (2017). They applied the Lattice Boltzmann Method (LBM) to analyse incompressible flows and showed excellent agreement with known results in a multitude of flow configurations. However, they found that certain LBM discretization approaches can introduce spurious modes in the eigenspectrum. Very recently, Klothakis et al. (2021) performed a linear stability analysis in a compressible boundary layer using Direct Simulation Monte Carlo (DSMC) method to compute the compressible boundary layer base flow. These authors also disturbed the flow imposing a transversal pulsating jet on the wall and showed that the perturbations in the shock have similar wavelengths as the ones in the boundary layer. This topic will be further discussed in section 5.1 of this thesis.

Secondary instability

In a boundary layer flow, only the initial stage of transition is governed by primary linear stability theory. The precursor of transition to turbulence is given by secondary instability. Figure 1.2 shows the path to turbulence on a flat plate, from the excitation of primary and secondary instabilities to the ultimate breakdown to turbulence. This new scenario was investigated almost simultaneously in the theoretical work of Herbert (1984a,b, 1988), the experimental work of Kachanov and Levchenko (1984), Kachanov (1994), Saric and Thomas (1984) and DNS (Kleiser and Schumann 1984, Gottlieb et al. 1984, Henningson et al. 1993). When the most unstable mode of primary instability grows in amplitude (when the TS waves reach an amplitude of approximately 1% of the free-stream velocity (Klebanoff et al. 1962), it may modify the base flow to a new steady state. This new baseflow can be unstable to exponentially small disturbances, particularly three-dimensional waves in the boundary layer (Herbert 1988). Since the new formulation will involve equations with periodic coefficients, Floquet theory analyses this newly modified state. Physically, secondary instabilities represent lambda-shaped vortices formed during the late stages of transition near the boundary layer edge. In this matter, three classes of linear secondary instabilities have been identified experimentally by Kachanov and Levchenko (1984) and Saric and Thomas (1984).

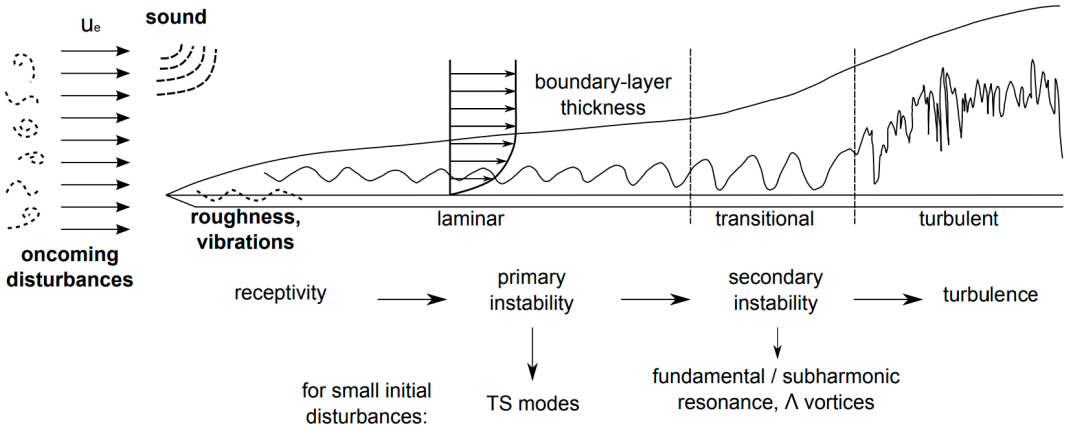

Figure 1.2: Boundary-layer transition on a flat plate (Kloker 2008).

The first one is fundamental instability/resonance, also referred to as K-type instability, due to the experimental work of Klebanoff et al. (1962). In this case, the secondary waves have the exact streamwise wavenumber as the primary waves and are aligned with each other. The second one is subharmonic resonance also known as H-type instability (H- for Herbert (1988)). In this case, the streamwise wavenumber of the secondary instability is twice the primary and forms a staggered vortices pattern. DNS simulations performed by Spalart and Yang (1987) showed that the H-type instability is the most unstable secondary instability in an incompressible boundary layer. However,

in experiments, K-type is often seen in many cases where theoretically, H-type should prevail. This is explained due to low amplitudes streamwise vorticity in the background flow (Schmid and Henningson 2001). The third class is referred to as O-type instability (O- from oblique breakdown) and was discovered by Thumm (1991), Fasel et al. (1993). This breakdown starts from the nonlinear interaction of two oblique instability waves with equal wave angles but in opposite directions.

At higher speeds, Erlebacher and Hussaini (1990) numerically investigated the compressible boundary layer at $Ma = 4.5$ using DNS. They found that an interaction between a two-dimensional and an oblique wave triggers secondary instability. This instability was found to have similarities with the K-type breakdown seen in the incompressible counterpart. However, they found that even when high amplitude disturbances are applied to the compressible flow, the incompressible boundary layer is still more unstable. Ng and Erlebacher (1992) studied secondary instability of low-speed and high-speed flows up to $Ma = 4.5$. At the supersonic Mach number, they found that secondary instability is stronger for the primary Mack mode than the primary TS mode. Moreover, the dominant instabilities are associated with the subharmonic and the combination resonance modes. Overall, increasing the Mach number minimises the subharmonic growth rate (Masad and Nayfeh 1990, 1991, Ng and Erlebacher 1992). In the compressible boundary layer, at lower supersonic speeds, Kosinov et al. (1990), Fasel et al. (1993), Sandham and Adams (1993) found that primary instabilities can be responsible for the laminar-turbulent transition. If nonlinear interactions of oblique waves are strong enough, they can directly break down into turbulence. In this case, no secondary instability is necessary. Sandham et al. (1995) found that the reason for this behaviour was nonlinear interactions of primary three-dimensional disturbances generate vortices in the streamwise direction with high shear layer. This layer will roll up and produce more vortices, eventually breaking down into turbulence. The onset of turbulence in a compressible boundary layer at $Ma = 4.5$ was studied by Adams and Kleiser (1996) using DNS. A subharmonic secondary instability appeared by superimposing a Mack mode with some white noise on the laminar base flow, as predicted by the secondary stability theory. The transition process starts from the formation of lambda-vortices near the critical layer generated from oblique subharmonic instabilities. Two different transition scenarios were documented. In the first case, a Y-shaped shear layer breaks up to create new vortices located above the sonic layer. The second phase is located above the boundary layer edge and is similar to the incompressible case, where the lambda-vortices peaks mainly at peak planes. This transition pattern is not observed in the low Mach number flows.

Non-local instability

Early linear stability studies of a boundary layer over concave surfaces (Görtler 1955) were investigated under the parallel flow approximation. Local primary stability theory, using this assumption does not account for the growth of the boundary layer in the streamwise direction. In order to consider non-parallel effects, Hall (1983) first introduced the idea to solve parabolic evolution equations for steady Görtler vortices. He argued that marching techniques are the only mathematically consistant approach since parallel approximations are only valid for the limit when the spanwise wave number is larger than unity. When a boundary layer is formed over a curved wall, the flow is subject to a centrifugal type of instability, resulting in streamwise align periodic counter-rotating vortices, known as Görtler vortices (Görtler 1941). These instabilities are inviscid in nature and arise from the disequilibrium between the normal pressure gradient and the centrifugal force (Rayleigh 1917). They can be active in either two- or three-dimensional boundary layers (Saric 1994). Herbert and Bertolotti (1987), Bertolotti et al. (1992), Simen (1992) independently developed the idea of Hall for the flat plate boundary layer and general non-parallel flows, and named the approach Parabolised Stability Equations (PSE). In the PSE, the flow is assumed to slowly vary in the streamwise direction and the base flow wall-normal velocity component is included in the analysis, accounting for the boundary layer growth. By initialising the initial value problem (IVP) with an initial condition given by the dominant local mode, the solution will converge to the respective nonlocal solution. This is accomplished by an auxiliary condition which forces the solution to converge to the least stable or most unstable mode. Further details of this method can be found in Bertolotti (1991), Herbert (1994, 1997). Due to a pressure gradient in the streamwise direction, the PSE equations are still elliptic. Therefore, when the marching step is too small, the solution will diverge. Lin and Malik (1995) showed that this issue could be addressed without loss in the solution for moderate values of wave-number by dropping out the streamwise pressure gradient term. Nevertheless, a still important aspect of the PSE is choosing an appropriate initial amplitude of the disturbances. Airiau and Casalis (1994) studied different possibilities in their review paper. Direct numerical simulations have been used to understand flow instabilities, including non-parallel / non-linear effects and to confirm and validate linear stability tools. Fasel (1976) and Kleiser and Zang (1991) investigated the incompressible boundary layer and successfully recovered linear stability results using DNS. Bertolotti et al. (1992) investigated the linear and non-linear evolution of TS waves. The results obtained from PSE and DNS were in excellent agreement. Berlin (1998) compared non-local PSE and DNS results by recovering neutral stability curves. Figure 1.3 presents the excellent agreement found between both curves. Moreover, both curves agree well with the experimental results of Kligmann et al. (1993).

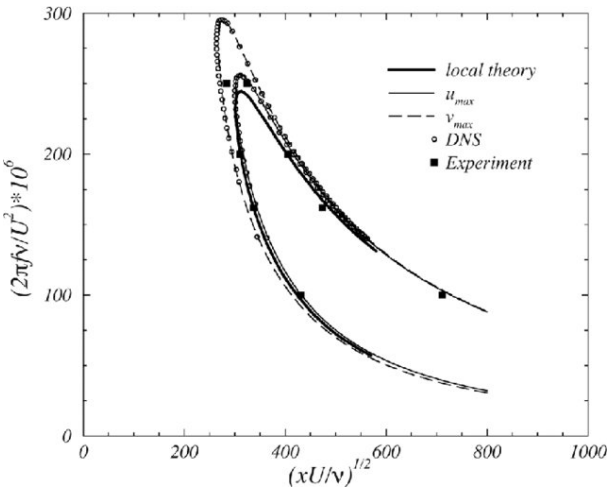

Figure 1.3: Neutral stability curves (Juniper et al. 2014) comparing non-local results with DNS calculations (Berlin 1998) and experimental data (Kligmann et al. 1993).

The discussion so far has been focused on two-dimensional boundary layers. When a three-dimensional boundary layer exists, the mean profile can be decomposed into the Cartesian frame of reference. In the direction of the external streamline, x, and in the direction normal to the streamline, z. The latter is called crossflow velocity profile and it is depicted in figure 1.4. Since this profile has an inflexion point, inviscid instabilities can exist. They are known as crossflow vortices (Gregory et al. 1955). Reed and Saric (1989) and Saric et al. (2003) present an extensive review on this topic.

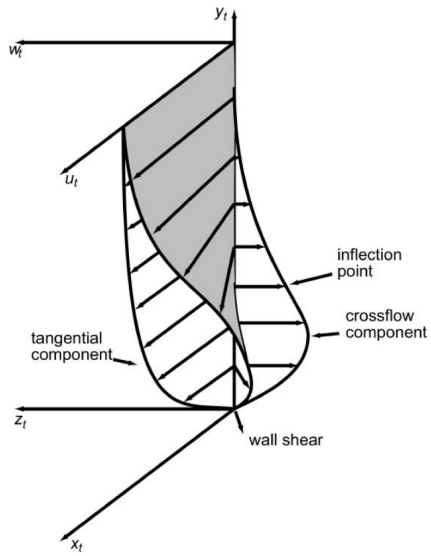

Figure 1.4: Three-dimensional boundary layer profile. The crossflow component has an inflexion point (Saric et al. 2003).

Bippes (1990), Bippes and Nitschke-Kowsky (1990) experimentally studied two different types of crossflow vortices, travelling and stationary; whereas the former is ex-

cited by high external turbulent levels, the latter is caused by micron-sized roughness. The stationary crossflow vortices usually are weak; however, the normal and spanwise velocity disturbances can modify the streamwise velocity profile. Furthermore, a favourable pressure gradient is known to destabilise crossflow vortices (and stabilises the TS waves). Haynes and Reed (2000) studied a crossflow dominated case employing Non-linear Parabolised Stability Equations (NPSE). They showed that the linear stability theory does not correctly predict what is seen from experiments (Reibert et al. 1996) in the case of a strongly favourable pressure gradient and NPSE needs to be employed. On the other hand, if the favourable pressure gradient is weak, the linear theory predicts well, and it is not necessary to include the complicated effects of nonlinearity in the analysis.

Global stability theory

The assumption of independence/weak dependence of the base flow on two or three spatial coordinates may be relaxed and global instability analysis can be performed. Before addressing the multidimensional stability analysis, it is essential to clarify the terminology related to the word "global". In the local primary and secondary stability theory, two different types of instabilities have been documented: convective and absolute. The concepts of both instabilities have been explained by Huerre and Monkewitz (1985) and Huerre and Monkewitz (1990). This type of instabilities can be mathematically distinguished by the Briggs-Bers criterion (Briggs 1964) and will be mathematically explained in detail in the next chapter. From a physical point of view, one must analyse the flow response to an impulse. Figure 1.5 presents the three possible response; if the impulse decays in every direction in space and time, the flow is stable (fig. 1.5a). If this impulse grows as it is convected downstream but disappears from a fixed position in space as time evolves, the flow is classified as convectively unstable (fig. 1.5b). Finally, if the impulse grows in both upstream and downstream directions, contaminating the whole flow at every point in time and space, the flow is classified as absolute unstable (fig. 1.5c).

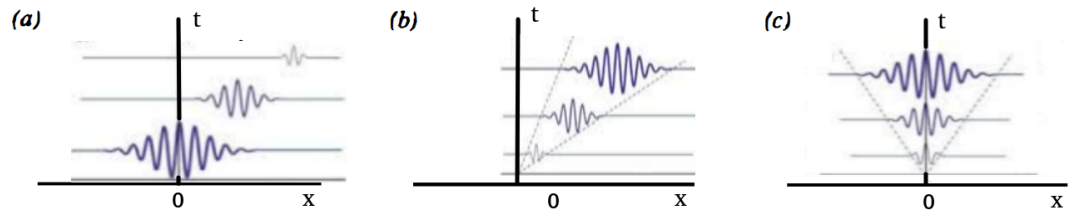

Figure 1.5: Schematic of the three types of instability adapted from Huerre and Monkewitz (1990): (a) stable flow. (b) convectively unstable flow. (c) absolute unstable unstable flow.

In the work of Chomaz et al. (1988), the definition of the word "global" comes from the analysis of absolute instabilities in weakly non parallel flows (Chomaz 2005). On the other hand, Theofilis (2003) proposed the terms BiGlobal and TriGlobal analysis to describe linear instabilities in two- and three-dimensional inhomogeneous flow directions. In what follows, the terminology proposed by Theofilis (2003) is used.

Global stability results

In the last two decades, global instability results have been obtained in a series of configurations that were previously inaccessible to either local or PSE analysis. In the global analysis of separated laminar boundary layer flow (Theofilis et al. 2000, Theofilis 2003, Rodríguez and Theofilis 2010, 2011), new physics were also discovered when considering the separated flow region as an essentially nonparallel, three-dimensional spanwise homogeneous flowfield. It was demonstrated that, beyond a certain level of flow recirculation in the bubble, the laminar separation zone could become self-excited and amplify stationary, spanwise periodic three-dimensional perturbations, a behaviour of the separation zone known as an oscillator. Furthermore, corner and backsteps geometries (Barkley et al, 2002), lid-driven (Theofilis 2000a, Albensoeder et al. 2001, Theofilis, Duck and Owen 2004, González et al. 2007a) and open cavities (Sipp and Lebedev 2007, De Vicente et al. 2014, Meseguer-Garrido et al. 2014), Attachment-line flows (Lin and Malik 1995, 1996, Theofilis et al. 2003), the flowfield around entire airfoils and low-pressure turbine cascades (Kitsios et al. 2009, Abdessemed, Sherwin and Theofilis 2009) are some examples within a spanwise homogeneous flow approximation and a BiGlobal linear modal analysis framework.

In compressible flows, some examples of the application of modal BiGlobal stability analysis in the literature are in the flow over a swept leading edge (Theofilis, Fedorov and Collis 2004, Li and Choudhari 2008, Mack and Schmid 2010, Li and Choudhari 2011, Gennaro et al. 2011, 2013), open cavities Theofilis and Colonius (2004), Bres and Colonius (2008), turbulent separation bubble (Touber and Sandham 2009) or in the more recent work of Choudhari, Chang, Jentink, Li, Berger, Candler and Kimmel (2009), Paredes and Theofilis (2015), Paredes et al. (2016) on the hypersonic flow over the HiFIRE-5 elliptic cone model, Nichols et al. (2017) in the shock/boundary layer interaction and Timme (2020) on the onset of shock-buffet on wings. The first modal global linear instability analysis of interest to shock-induced separation has been the two-dimensional global mode analyses of Crouch et al. (2007, 2009). They monitored the separated flow over an airfoil at transonic conditions. These authors' results could successfully associate the buffeting phenomenon observed on airfoils with the frequency of the most-amplified two-dimensional global mode of the underlying turbulent mean flow. The latter obtained by solution of the Reynolds Averaged Navier Stokes equations. On the other hand, the work of Robinet (2007) has been the first documented global

linear instability analysis of a separation bubble generated by shock wave / laminar boundary layer interaction. It was asserted that the analogue of the stationary three-dimensional global mode discovered by Theofilis et al. (2000) in incompressible flow is also the most amplified instability at the supersonic conditions examined. An analogous result regarding the existence of self-excited stationary three-dimensional eigenmodes has been obtained in the recent work of Nichols et al. (2017), who analysed a mean turbulent bubble instead of a steady laminar separation bubble.

The PSE-3D approach extends the classic PSE to deal with global instability analysis of flows that depend strongly on two and weakly on the third spatial direction. It can be seen as the step to take between the two classes of spanwise homogeneous and fully inhomogeneous three-dimensional flows. The boundary layer flow in the wake behind an elliptic wing (He et al. 2017) and in the wake of an isolated roughness element (De Tullio et al. 2013) and (Paredes et al. 2016) are examples of incompressible, supersonic and hypersonic applications of the capacity of the PSE-3D. The methodology can recover results otherwise only accessible to spatial direct numerical simulation at orders of magnitude higher level of computational effort. More details about instability and receptivity analysis behind roughness-induced wakes can be found in Choudhari, Li and Edwards (2009), Choudhari et al. (2010, 2013), Duan and Choudhari (2012), De Tullio (2013), De Tullio et al. (2013), Iyer and Mahesh (2013), De Tullio and Sandham (2015), Paredes et al. (2015), Montero and Pinna (2020).

Flows that are fully inhomogeneous in all three spatial dimensions have also been analysed by TriGobal linear analysis with respect to their potential to amplify small-amplitude three-dimensional perturbations: an ellipsoid at an angle of attack (Tezuka and Suzuki 2006), jet flow through an orifice into a crossflow (Bagheri et al. 2009), the classic three-dimensional lid-driven cavity Leriche and Labrosse (2007), Giannetti et al. (2009), Feldman and Gelfgat (2010), flow around a sphere (Morzyński and Thiele 2008) or, more recently, in the shock-buffet on a finite wing (Timme 2020) are some examples of the application of the so-called TriGlobal linear modal instability analysis. However, performing TriGlobal stability analysis in complex geometries, even with the hardware capabilities to date, is still a challenge. In this case, the use of reduced or low order models based on data analysis is still necessary. The review of Taira et al. (2017) and references therein outlines the different data-driven methods available in the literature. Global linear stability analysis of turbulent mean flows will not be discussed in this thesis but it is important to highlight the work of Barkley (2006), who performed a primary linear instability analysis of mean flow around the wake of a cylinder. Sipp and Lebedev (2007) studied the primary instability over mean flows with application to cylinder and open cavity and Beneddine et al. (2016) provided theoretical conditions in order to validate the use of mean flows for instability analysis.

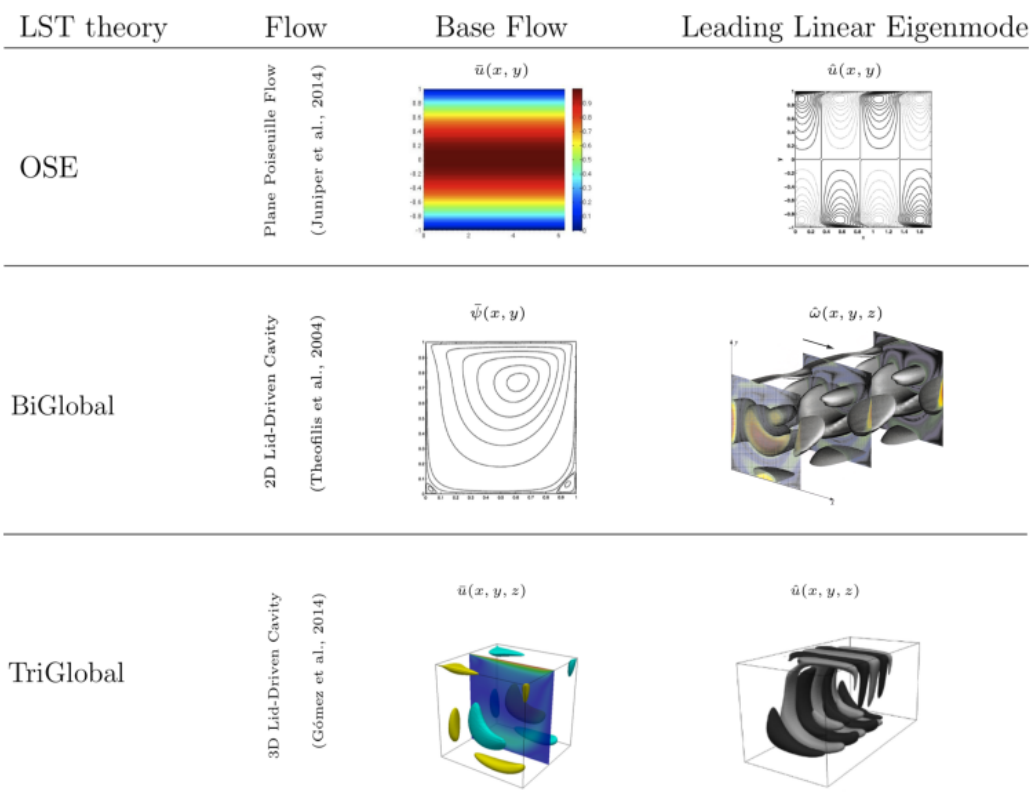

Figure 1.6: Examples of local, BiGlobal and TriGlobal instability theories (Theofilis 2018).

Numerical implementation

Riding on the crest of ever-increasing computing power and a wider availability of open-source libraries for large-scale linear algebra computations, the scope of global instability research has broadened substantially in the past two decades. The global instability solutions can be obtained into two steps: discretisation of the linear operator and the solution of the subsequent eigenvalue or singular value problem. Starting with the former, the global stability operator needs first to be discretised, and the inhomogeneous directions can be treated independently and the same spatial discretization can be used from the local analysis. Usually, a spectral collocation method based on Chebyshev Gauss-Lobatto (Orszag and Gottlieb 1980, Gottlieb et al. 1984, Zebib 1984, Canuto et al. 1988, 2006, 2012) is used due to its high order accuracy. However, different finite difference methods are also employed, based on Pade (Lele 1992), Dispersion-Relation-Preserving (Tam and Webb 1993) and the high order finite difference method FD-q (Hermanns and Hernández 2008, Paredes et al. 2013). Finite volume and finite elements methods are also employed (Jackson 1987, Dijkstra 1992, Morzynski and Thiele 1991, Morzyński and Thiele 2008, Albensoeder et al. 2001, González et al. 2007b). In these cases, since a high number of points are necessary to converge sharp gradients,

there is a trade-off between the efficiency of a high-order method and the flexibility of using unstructured meshes. In order to relax this trade-off, spectral/hp-element method (Karniadakis and Sherwin 2005) can be used (Barkley and Henderson 1996, Theofilis et al. 2002). Numerical methods to the solution of the discretised global instability operator have matured in both of this analysis's two major flavours: matrix-forming and time-stepping, to be discussed next. In the matrix-forming approach, the discretised eigenvalue problem can be solved using the well-known QZ algorithm (Golub and van Loan 1996) available in the open-source linear algebra library LAPACK. However, the "full" computation of the eigenspectrum scales with $O(N^2)$, $O(N^4)$ and $O(N^6)$ in terms of memory required for one-,two- and three-dimensional EVP, respectively (N being the leading dimension of the problem). This "full" computation is also referenced as "global eigenvalue problem solution" in the local primary stability work of Malik and Orszag (1987). Although this can be feasible for local stability problems, this is not appropriate for multi-dimensional calculations. In this context, iterative algorithms can be used to retrieve the leading eigenvalues, drastically reducing hardware requirements. The Arnoldi algorithm (Arnoldi 1951, Saad 1980) based on Krylov subspace is widely used (see Theofilis (2003, 2011)) in the global stability calculations, and it will be mathematically described in section 3. Massively parallel solutions have been employed to enable the usage of high-order spectral collocation methods (Rodríguez and Theofilis 2009, Quintanilha Jr et al. 2017) in the discretisation of multidimensional EVP. A different approach was presented by Crouch et al. (2007) using sparse direct solvers, exploiting the spasticity patterns when using finite difference methods. This concept was expanded by Paredes et al. (2013), who employed a high order finite difference method based on FD-q and showed that sparse linear algebra could be used without significant loss in accuracy. The matrix-forming approach has many advantages, like simplicity and flexibility. The operator can be formed and extended to include new regimes (incompressible to hypersonic) or even new physics (non-Newtonian flows) with relative simplicity and no change in the algorithm. The trade-off is the need to store and operate large matrices, which can increase with dimensionality, grid refinement and additional equations (as in including real gas effects).

When this storing the matrix is not a viable option, the time-stepping approach can be employed (Eriksson and Rizzi 1985, Edwards et al. 1994, Chiba 1998, Tezuka and Suzuki 2006, Barkley et al. 2008, Mack et al. 2008, Gomez et al. 2014). The key idea is to emulate the inverse operator without forming or inverting the matrix. No memory restrictions are present since the method is based on the DNS code used to generate steady states. The downside of time-stepping is requirement of a validates solver appropriated for the (incompressible, compressible, hypersonic) flow change studied. The flexibility given by the matrix-forming approach is wholly lost. Moreover, the time integration length is unknown. Implementation details the time-stepping method can

be found in the work of Gómez et al. (2012).

Nonmodal linear stability analysis

Transient growth

Laminar-turbulent transition research has traditionally sought to identify exponentially amplifying in the limit of asymptotically large time small-amplitude perturbations, that potentially lead a laminar flow to break down to turbulence through linear instability mechanisms. This so-called modal linear instability scenario (Lin 1955) can explain classic laminar flow instability mechanisms, such as TS waves and crossflow vortices in the boundary layers. In this context, the objective is the identification of a minimum critical parameter, such as the flow Reynolds number in a boundary layer, rotation rate in Taylor-Couette flow, or Rayleigh number in the classic Rayleigh-Bernard convection, beyond which a specific initial small-amplitude perturbation grows exponentially in time and/or space. This minimum value of the critical parameter is calculated via an eigenvalue decomposition of the linearised operator, which describes the time- or space-evolution of small amplitude perturbations superposed upon a given flow. The associated eigenvalues dictate the perturbation behaviour, namely exponentially growing or decaying flow instabilities at asymptotically large time. The linear modal theory is shown to deliver accurate predictions in several flow paradigms, such as the Rayleigh-Bernard convection, where a critical Rayleigh number of $Ra = 1708$ is predicted. Consistently, experiments show $Ra = 1710$, confirming the modal analysis's ability to predict flow instability physics correctly. However, the linear modal theory has also produced glaring failures, starting with the Reynolds (1883) experiment. The theoretically predicted flow stability for all Reynolds numbers starkly contrasts with experimental reality, which shows a transition to turbulent flow at Reynolds numbers $Re = O(2000)$. Incomplete predictions are also delivered by the solution of the famous Orr-Sommerfeld equation for plane channel flow, where again experimental evidence of transition at Reynolds number $Re = O(1500)$ cannot be matched by the theoretical prediction of modal analysis, $Re = 5772$ or in one of the first applications of global linear theory to the rectangular duct (Tatsumi and Yoshimura 1990). These discrepancies have been attributed to the linearisation of the governing equations within a modal context. Hence, in flows where the primary and secondary stability theories do not hold, the transition was understood to be triggered directly from nonlinearities.

However, the possibility of transient perturbations achieving substantial growth of energy before decaying was already suggested by Orr (1907). The so-called Orr mechanism (fig. 1.7a), also called Reynolds stress mechanism by Butler and Farrell (1992), is one of the mechanisms responsible for bypassing modal transition. The structures tilted against the shear by the disturbances will rise to an upright position due to the

Reynolds stress, extracting energy from the mean shear. The disturbances then begin to lose energy to the mean shear until they are aligned with the base flow. More details can be found in Lucas (2014).

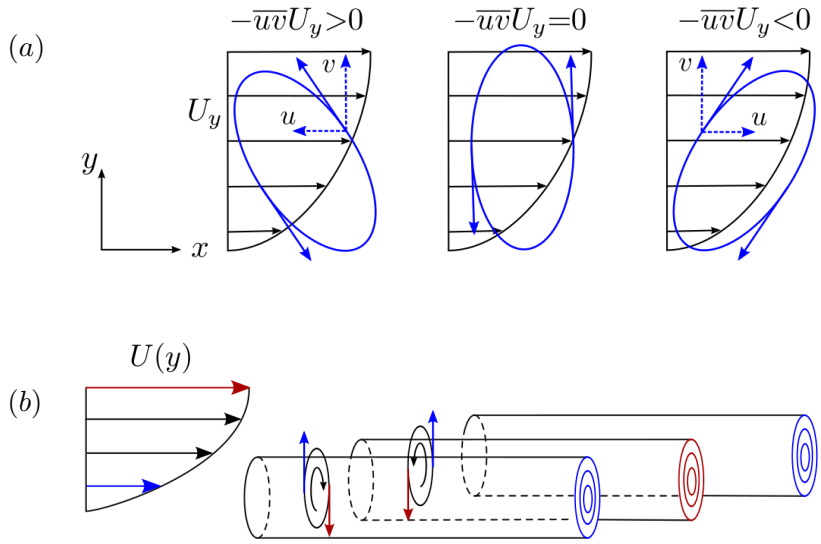

Figure 1.7: Sketch of (a) the Orr (Reynolds stress) mechanism, (b) the lift-up effect (Lucas 2014).

Another mechanism is the so-called lift-up effect (fig. 1.7b), first discovered by Landahl (1975, 1980) in the context of inviscid and incompressible flows without an inflexion point. Ellingsen and Palm (1975) showed that by introducing a small amplitude longitudinal vortex in a shear flow, alternating low and high speed streamwise align structures, also known as streaks, can grow algebraically at short time. The shear layer will lift-up low momentum flow from the plate due to the interaction with the longitudinal vortices. The streaks generated from this effect have been seen in experimental investigations when free-stream disturbance level is enhanced (Klebanoff et al. 1962, Klebanoff and Tidstrom 1972, Gulyaev et al. 1989, Matsubara and Alfredsson 2001).
The mathematical explanation of the existence of transient growth and the erroneous predictions of modal analysis lies in the fact that the operator describing the linearised Navier-Stokes equations is non-normal. Several of its eigenvectors are nearly parallel, and the condition number of the matrix that discretises this operator is (extremely) large. Amplification of infinitesimal disturbances is possible even if the eigenvalues of a linear system are found to be stable, the reason being that, when the eigenvectors of the system are not orthogonal to each other, growth of their resultant magnitude can occur over short time horizons, even though the eigenvalues are stable and the eigenvectors are decaying in time. This procedure can be better understood in the example shown in figure 1.8. Operators exhibiting a set of non-orthogonal eigenvectors are referred to as non-normal operators (Trefethen et al. 1993, Trefethen 1997, Schmid and Henningson

2001), and the associated short-time horizon algebraic growth is referred to as nonmodal or transient growth.

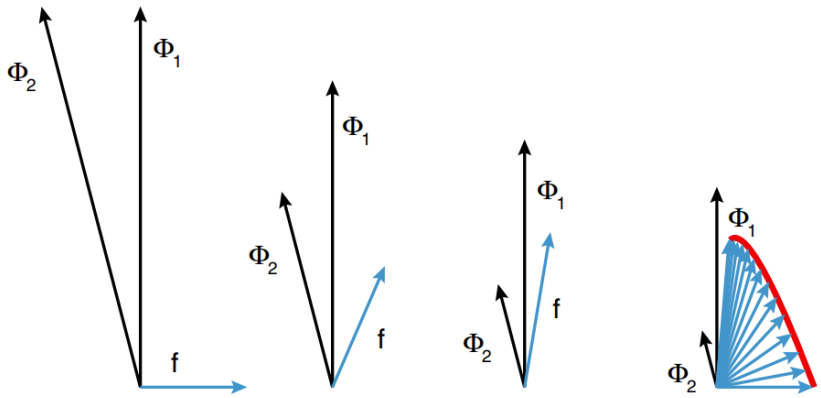

Figure 1.8: Example of two non-normal vectors (ϕ_1 and ϕ_2) and its difference (vector f). The superposition of non-orthogonal eigenvectors can generate a initial growth in the norm of the disturbance (Schmid 2007).

In a local analysis framework, the incompressible boundary layer has been widely investigated (Hultgren and Gustavsson 1981, Boberg and Brosa 1988, Butler and Farrell 1992, Schmid and Henningson 1994, Reddy and Henningson 1993, Henningson et al. 1993). Butler and Farrell (1992) and Reddy and Henningson (1993) discovered a scaling of the transient growth for small wavenumbers as a function of Re. While the time of the maximum transient growth scales with Re, the maximum value of the energy gain scales with Re^2. They theoretically confirmed that the optimal transient growth appears for streamwise aligned structures. Corbett and Bottaro (2001), Andersson et al. (1999, 2001), Luchini (2000) introduced the calculation of transient growth using temporal and spatial optimisation techniques to solve the direct-adjoint equations iteratively. This optimisation approach is detailed in the review of Luchini and Bottaro (2014). Cossu et al. (2000) studied spatial transient growth for concave walls. Overall, the effect of curvature is to increase the perturbation spatially downstream. Tumin and Reshotko (2001) calculated spatial transient growth and showed that optimal transient growth is associated with steady streamwise aligned vortices. Corbett and Bottaro (2001) first pointed out the intimate relationship between the structures at short and long time in a three-dimensional boundary layer. They found that nonmodal stability is responsible for the initial amplification of modal perturbations. Cossu and Brandt (2002) found that finite amplitude optimal streaks can be used to stabilise TS waves, motivating the work of Fransson et al. (2005), Carpenter et al. (2008). Pralits et al. (2007) developed two different methods to calculate optimal conditions in a spatial framework based on tracking a single-mode and in the PSE. In the latter, an advantage is taken in the fact that in three-dimensional boundary layers, the perturbations usually are pointing in the same direction as the external streamline. However, since this is not

entirely true, errors in the energy gain can be computed when marching the equations over long distances. Byström et al. (2007) also pointed out that optimal conditions can initialise modal instabilities, showing the close relation between modal and nonmodal in three-dimensional flows. Transient growth analysis has also been used in turbulent boundary layer (Cossu et al. 2009), where the optimal conditions are associated with streamwise aligned vortices. Tempelmann et al. (2010) investigated the spatial transient growth in a Falkner-Skan-Cooke (FSC) boundary layer subject to adverse and favourable pressure gradients. They found that, contrary to the two-dimensional case, the optimal condition in the three-dimensional boundary layer is associated with both Orr mechanisms and the lift-up effect. Overall, adverse pressure gradient has a destabilising impact on transient growth, as already pointed out by Corbett and Bottaro (2001). They also confirmed that transient growth is converted to modal instabilities in the form of crossflow vortices in a three-dimensional boundary layer.

Comparatively, fewer nonmodal instability analyses have been performed in compressible flow. Following work in the incompressible flat plate boundary layer, temporal transient growth analyses of the compressible boundary layer were performed by Hanifi et al. (1996). They observed this flow's potential to sustain the algebraic growth of streamwise aligned perturbations at conditions subcritical to the exponential amplification of Tollmien-Schlichting or crossflow disturbances. Moreover, they found the same Re^2 scaling for the maximum transient growth as in the incompressible counterpart. Compressibility was found to be responsible to enhance transient growth (Farrell and Ioannou 2000). Zuccher et al. (2006) found that, for the high-speed flow over a sphere, wall cooling has a destabilising effect on the energy growth at short time. Tempelmann et al. (2012) considered the effects of compressibility and wall curvature in the FSC boundary layer. They found that they both have a destabilising effect on transient growth.

The formation of turbulent spots generated by nonmodal mechanisms and preceding the ultimate breakdown to turbulence was detailed in DNS work of Krishnan and Sandham (2006a,b). These authors found that the structures of the turbulent spots are characterised by both hairpins as well as streamwise vortices. Moreover, they concluded that the turbulent spots' lateral spreading decreases substantially when the Mach number increases. Wang and Zhong (2008) calculated the influence of transient growth in a boundary layer with surface roughness. They found only a weak relationship between them. Roughness induced elements can be responsible for an early transition that can be associated with transient growth. Recently, the Space Shuttle Endeavour experienced asymmetric transition during reentry caused by isolated roughness near the nose (Horvath et al. 2012). This early transition agreed with the experimental results performed at high speeds (Corke et al. 1986, Fujii 2006, Schneider 2008a,b, Borg and Schneider 2008). Reshotko (2001) linked the transition induced by roughness elements

to transient growth in incompressible boundary layers. However, experimental results showed that the transient growth does not match the theoretical calculations (White 2002, White et al. 2005, Downs et al. 2008).

The majority of transient growth work has been performed in a local analysis framework, considering flows with two homogeneous spatial directions. However, global linear theory also permits the monitoring of nonmodal disturbances. This was performed in the flow inside an S-shaped rounded-corner duct (Marquet et al. 2008), on an induced separation on a flare plate Ehrenstein and Gallaire (2008), a rounded-corner open-cavity (Arkevik et al. 2007), the flow over a two-dimensional rectangular backwards-facing-step (Blackburn, Barkley and Sherwin 2008) and in pulsatile stenotic flows (Blackburn, Sherwin and Barkley 2008), where $G_{\max} = \mathrm{O}(10)$ when laminar separation is present. In the latter, transient growth was expected to be the physical mechanism responsible for the transition since the three-dimensional global modes recovered by the DNS of Barkley et al. (2002) could only be seen intrinsically in experiments through careful observation (Beaudoin et al. 2004). They found evidence that strong transient growth exists under subcritical modal conditions. Abdessemed, Sharma, Sherwin and Theofilis (2009) found the same evidence in the incompressible flow around a circular cylinder. Moreover, they relate the initial optimal condition to saturate into the von-Karman street vortex. Strong transient growth was also observed in the analysis of the flow through a sudden expansion in a circular pipe (Cantwell et al. 2010) and in the modally stable flow past a Low-Pressure Turbine (LPT) cascade (Sharma et al. 2011). Their investigation pointed out that nonmodal instabilities can be the responsible mechanism leading to transition. About the same time, global nonmodal stability has also been applied on a duct of square cross-section where the flow is linearly stable for all ranges of Reynolds number (Biau et al. 2008, Biau and Bottaro 2009, Boiko et al. 2010). Recent work has considered the stability of flow over stalled airfoils and has also demonstrated this flow's potential to sustain strong nonmodal instability, besides the previously known travelling Kelvin-Helmholtz and stationary global mode paths to transition (He et al. 2017). Finally, Paredes et al. (2017, 2018) studied the blunt-body paradox. This phenomenon is observed on high-speed spherical forebodies that are asymptotically stable due to the strongly favourable pressure gradient and its convex curvature. However, transition has been observed in many different experiments (Murphy and Rubesin 1966, Hollis 2010, Reshotko et al. 2016). A linear PSE procedure was used (Pralits et al. 2000, Tempelmann et al. 2010, 2012, Paredes et al. 2017) to investigate transient growth as the possible transitional mechanism. They showed the importance of choosing an appropriate energy norm that needs to be changed depending on physics. Therefore, they highlighted the need to investigate further the optimal-growth criterion underlying the Reshotko-Tumin correlation (Reshotko and Tumin 2004). They concluded that roughness-induced transition

(De Tullio 2013) can occur upstream of the sonic line and may explain the transition observed in experiments.

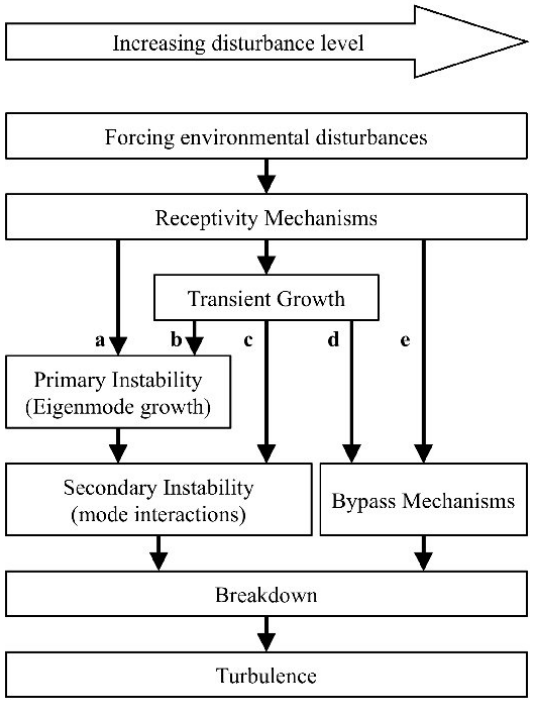

Figure 1.9: Updated roadmap to transition, adapted from Morkovin (1994) (Meersman et al. 2018).

In summary, in boundary layer flows, the laminar-turbulent transition scenario based on short-time (transient) algebraic growth of nonmodal perturbations, typically streamwise aligned streaks, is a second possible path to transition at subcritical Reynolds number, alternative to the modal scenario based on exponential amplification of Tollmien-Schlichting waves and crossflow eigenmodes. Under certain subcritical flow conditions, the transient growth scenario can bypass that based on modal exponential amplification, rendering the modal decay irrelevant. In other situations, optimal perturbations usually associated with relatively large environmental disturbances growing algebraically at early times transform into modal perturbations that eventually grow exponentially. Nonmodal perturbations growing algebraically are known to modify the underlying base state, which can then undergo laminar-turbulent flow transition on account of exponentially amplifying secondary disturbances. The currently accepted "updated roadmap to transition", due to Morkovin (1994) summarises these possible paths leading laminar flow to turbulence and is shown in figure 1.9. With an increased forcing level of environmental disturbances, the path changes from left to right, i.e. from path **a** to path **e**, accordingly. The path **a** corresponds to transition due to amplification of primary instabilities, and therefore an eigenmode growth is responsible for the onset of the laminar-turbulent transition. The disturbances are normally Tollmien-Schlichting

(TS) waves and/or crossflow eigenmodes in three-dimensional flows. The primary instabilities can interact with each other (secondary instabilities), ultimately leading to turbulence. When the disturbance level increases, algebraic growth (transient growth) plays a role in the transition path. Depending on the external level, modal and non-modal can co-exist (path **b**) or, when high enough, transient growth will directly trigger mode interaction, as seen in path **c**. In this case, the boundary layer can exhibit large transient growth associated with streamwise aligned structures (streaks). In path **d**, transient growth is high enough to bypass both primary and secondary instabilities leading to a breakdown. Finally, in patch **e**, a considerable disturbance level bypasses the whole *linear* regime, and the flow does not pass through a transitional process.

Chapter 2

Linear global instability analysis

2.1 The equations of motion

The Navier-Stokes and continuity equations are the governing equations of fluid motion of viscous and Newtonian fluid. Admitting a perfect gas and using an asterisk to represent dimensional quantities, the equations can be written as

$$\frac{\partial \rho^*}{\partial t^*} + \nabla^*.(\rho^* \mathbf{V}^*) = 0, \tag{2.1}$$

$$\begin{gathered} \rho^* \left[\frac{\partial \mathbf{V}^*}{\partial t^*} + (\mathbf{V}^*.\nabla^*)\mathbf{V}^* \right] = \\ -\nabla^* p^* + \nabla^* \left[\lambda^* (\nabla^*.\mathbf{V}^*) \right] + \nabla^*.\left[\mu^* \left((\nabla^* \mathbf{V}^*) + (\nabla^* \mathbf{V}^*)^T \right) \right], \end{gathered} \tag{2.2}$$

$$\begin{gathered} \rho^* c_p^* \left[\frac{\partial T^*}{\partial t^*} + (\mathbf{V}^*.\nabla^*)T^* \right] - \frac{\partial p^*}{\partial t^*} - (\mathbf{V}^*.\nabla^*)p^* = \\ \nabla^*.(k^* \nabla T^*) + \lambda^* (\nabla^*.\mathbf{V}^*)^2 + \frac{\mu^*}{2} \left[(\nabla^* \mathbf{V}^*) + (\nabla^* \mathbf{V}^*)^T \right]^2, \end{gathered} \tag{2.3}$$

$$p^* = \rho^* \mathcal{R} T^*, \tag{2.4}$$

where ρ^* is the density, $\mathbf{V}^*$ is the velocity vector $(u, v, w)^T$, T^* is the temperature, p^* is the pressure, μ^* and λ^* are the first and second coefficient of viscosity, respectively, c_p^* is the specific heat at constant pressure, k^* is the thermal conductivity and R is the gas constant.

In order to non-dimensionalise the equations, the following reference values are used

- Lengths are scaled by a reference length L^*_{ref};
- Velocities are scaled by a reference velocity U^*_{ref};
- Temperature is scaled by a reference temperature T^*_{ref};

- Pressure is scaled by $p^*_{\text{ref}} = \rho^*_{\text{ref}}(U^*_{\text{ref}})^2$;
- Free-stream speed of sound is $a^*_{\text{ref}} = \sqrt{(\gamma^* \mathcal{R} T^*)}$;

where $\gamma = \frac{c^*_{p,\text{ref}}}{c^*_{v,\text{ref}}}$ and c_v is the specific heat at constant volume. The corresponding dimensionless parameters are

$$Re = \frac{\rho^*_{\text{ref}} U^*_{\text{ref}} L^*_{\text{ref}}}{\mu^*_{\text{ref}}}, \qquad Ma = \frac{U^*_{\text{ref}}}{a^*_{\text{ref}}}, \qquad Pr = \frac{c^*_{p,\text{ref}} \mu^*_{\text{ref}}}{k^*_{\text{ref}}}, \qquad Ec = (\gamma - 1) Ma^2, \quad (2.5)$$

where Re is the Reynolds number, Ma is the Mach number, Pr is the Prandtl number and Ec is the Eckert number.

After substituting the reference values into the equations (2.1) to (2.4) and introducing the dimensionless parameters from equation (2.5), the non-dimensional Navier-Stokes and continuity equations can be written as

$$\frac{\partial \rho}{\partial t} + \nabla.(\rho \mathbf{V}) = 0, \quad (2.6)$$

$$\frac{\partial (\rho \mathbf{V})}{\partial t} + \nabla.(\rho \mathbf{V}\mathbf{V}) = -\nabla p + \frac{1}{Re} \nabla.\sigma, \quad (2.7)$$

$$\rho \left[\frac{\partial T}{\partial t} + (\mathbf{V}.\nabla) T \right] - Ec \left[\frac{\partial p}{\partial t} + (\mathbf{V}.\nabla) p \right] = \frac{1}{RePr} \nabla.(k \nabla T) + \frac{Ec}{Re} \left[\frac{1}{2} (\nabla \mathbf{V} + \nabla \mathbf{V}) : \sigma \right], \quad (2.8)$$

$$p = \frac{\rho T}{\gamma Ma^2}, \quad (2.9)$$

where

$$\sigma = [\mu(\nabla \mathbf{V} + (\nabla \mathbf{V})^T)] + \nabla[\lambda(\nabla.\mathbf{V})]$$

is the viscous stress tensor. The asterisks are dropped to represent dimensionless quantities. The equation of state for a perfect gas with constant $\gamma = 1.4$ is also presented. The Prandtl number Pr is chosen as constant and equals 0.72, and Stokes' hypothesis can be applied to calculate λ. For the viscosity, Sutherland's law is used, where

$$\mu = T^{\frac{3}{2}} \frac{1 + C}{T + C}. \quad (2.10)$$

For standard air conditions, $C = 110.4 \text{ K}/T^*_{\text{ref}}$ and $\mu_0 = 1.458 \times 10^{-6}$ N s/m^2. In what follows, the thermal conductivity is calculated based on the viscosity $k = \mu$.

2.2 The linearised Navier-Stokes equations (LNSE)

The linearised Navier-Stokes equations (LNSE) result from the substitution of a linear decomposition of all flow quantities, $\mathbf{q} = (\rho, u, v, w, T)^T$ into a steady laminar base or mean flow $\bar{\mathbf{q}}$ and a small amplitude disturbance $\tilde{\mathbf{q}}$, according to

$$\mathbf{q}(\mathbf{x}, t) = \bar{\mathbf{q}}(\mathbf{x}) + \epsilon\tilde{\mathbf{q}}(\mathbf{x}, t), \qquad with \quad \epsilon \ll 1. \tag{2.11}$$

The $O(1)$ resulting equations are those governing the base state and are satisfied by construction. The $O(\epsilon^2)$ equations are neglected on account of smallness of the perturbation amplitudes. The $O(\epsilon)$ equations are the LNSE, that need to be solved, either as an eigenvalue problem (modal analysis) or as an initial value problem (nonmodal analysis).

2.3 Local and global linear stability analysis

The decomposition (2.11) is valid irrespectively of the spatial dimensionality of the base flow and small perturbations. The classification of Table 2.1 shows the modern linear stability analysis concepts into Local, NonLocal and Global theories where the local, BiGlobal and TriGlobal theories are explained in depth in what follows.

2.3.1 Local eigenvalue problem

In local analysis, as defined in Table 2.1, only one spatial direction is inhomogeneous in both the base flow and the amplitude functions. Parallel shear flows (Schmid and Henningson 2001, Schmidt and Rist 2011) can be analysed using this concept, in which the velocity field comprises a streamwise and a spanwise component, both of which are functions of the transverse spatial direction only, while the transverse/wall-normal base flow velocity component is neglected. In axisymmetric geometries, the base flow and amplitude functions depend only on the radial coordinate. Applying separation of variables, the two homogeneous directions can be decomposed into the Fourier space. The linearized equations of motion may be re-written as a system of linear ordinary differential equations, as discussed by Mack (1984), one of which is the celebrated Orr-Sommerfeld equation (OSE).
Mathematically, assuming x and z as the homogeneous spatial directions, such that the base flow is only dependent on the y spatial coordinate, modal perturbations are written as normal modes

$$\tilde{\mathbf{q}}(x, y, z, t) = \hat{\mathbf{q}}(y)\ e^{[i\ (\alpha x + \beta z - \omega t)]}, \tag{2.12}$$

where $\alpha = 2\pi/L_x$ and $\beta = 2\pi/L_z$ are the wave-numbers with L_x and L_z as periodicity lengths along the homogeneous spatial directions x and z, respectively and ω is the angular frequency.

Table 2.1: Classification of linear stability theories Juniper et al. (2014).

	Denomination	Base Flow assumptions		Amplitude function	Phase function
	TriGlobal	—	$\overline{\mathbf{q}}(x,y,z)$	$\hat{\mathbf{q}}(x,y,z)$	ωt
Global	PSE-3D	$\partial_x\overline{\mathbf{q}} \ll \partial_y\overline{\mathbf{q}}$	$\overline{\mathbf{q}}(X,y,z)$	$\hat{\mathbf{q}}(X,y,z)$	$\int_0^X \alpha(\xi)d\xi - \omega$t
	BiGlobal	$\partial_x\overline{\mathbf{q}} = 0$	$\overline{\mathbf{q}}(y,z)$	$\hat{\mathbf{q}}(y,z)$	$\alpha x - \omega$t
Nonlocal	PSE	$\partial_x\overline{\mathbf{q}} \ll \partial_y\overline{\mathbf{q}}; \partial_z\overline{\mathbf{q}} = 0$	$\overline{\mathbf{q}}(X,y)$	$\hat{\mathbf{q}}(X,y)$	$\int_0^X \alpha(\xi)d\xi + \beta z - \omega$t
Local	OSE	$\partial_x\overline{\mathbf{q}} = \partial_z\overline{\mathbf{q}} = 0$	$\overline{\mathbf{q}}(y)$	$\hat{\mathbf{q}}(y)$	$\alpha x + \beta z - \omega$t

In the incompressible limit, the resulting system, after the Ansatz substitution (2.12) into equations (2.6) to (2.8), can be reduced into two coupled ordinary differential equations by eliminating the pressure variable and using the definition of normal vorticity,

$$[(-i\omega + i\alpha\bar{u})(D_{yy}^2 - k^2) - i\alpha\bar{u}_{yy} - \frac{1}{Re}(D_{yy}^2 - k^2)]\hat{v} = 0, \tag{2.13}$$

$$[(-i\omega + i\alpha\bar{u}) - \frac{1}{Re}(D_{yy}^2 - k^2)]\hat{\eta} = -i\beta\bar{u}_y\bar{v}, \tag{2.14}$$

where $\hat{v}$ and $\hat{\eta}$ stand for the wall-normal velocity and vorticity, $k^2 = \alpha^2 + \beta^2$ and D represents the derivative matrix. Equation (2.13) is the Orr-Sommerfeld equation and equation (2.14) is the Squire equation. Despite the simplicity of these equations, they provide the exact eigenmodes of strictly parallel flows. They are reasonable approximations for quasi-parallel, slowly diverging flows, such as the boundary layer or a free shear layer. The $Re \to \infty$ limit of the Orr-Sommerfeld was derived by Lord Rayleigh and describes the inviscid instability of flows with inflectional base flow profiles.
The complete system of equations representing the linearized incompressible Navier-stokes equations can be written as

$$\begin{aligned} i\alpha\hat{u} + \hat{v}' + i\beta\hat{w} &= 0, \\ \mathcal{L}\hat{u} + \bar{u}'\hat{v} + i\alpha\hat{p} &= 0, \\ \mathcal{L}\hat{v} + \hat{p}' &= 0, \\ \mathcal{L}\hat{w} + \bar{w}'\hat{v} - i\beta\hat{p} &= 0, \end{aligned} \tag{2.15}$$

where $\mathcal{L} = i\alpha\bar{u} + i\beta\bar{w} - \frac{1}{Re}[D'' - \beta^2 - \alpha^2] - i\omega$ and primes denote derivatives in respect to the spatial direction y.
The linear perturbations may grow in time or space; depending on this choice, a temporal or spatial analysis is investigated, respectively. In the temporal framework, the wave-number is assumed to be a real parameter, and the problem is solved for a complex eigenvalue ω. In this case, the real part of ω is the frequency and the imaginary part is the growth or decay rate. Both approaches are equivalents close to neutral stability and related using Gaster's transformation (Gaster 1962). In these neutral limits, where the growth rate is zero ($d\omega_i/d\alpha_i = 0$ for both approaches, respectively), the curve for different Reynolds numbers is called the neutral curve. This curve delimits stable flow (outside the curve) as well as unstable flow (inside the curve) regions.
The temporal *linear* eigenvalue problem (EVP) can be written in matrix form as

$$\mathcal{A}\hat{\mathbf{q}} = \omega\mathcal{B}\hat{\mathbf{q}}, \tag{2.16}$$

while the spatial EVP assumes a real perturbation frequency ω and solves the *nonlinear* eigenvalue problem

$$\mathcal{A}\hat{\mathbf{q}} = \sum_{k=1}^{2}\alpha^k\mathcal{B}_k\hat{\mathbf{q}}, \tag{2.17}$$

for a complex eigenvalue α. The nonlinear EVP (2.17) can be converted into a linear EVP using a companion matrix method (Bridges and Morris 1984, Theofilis 1995, Heeg and Geurts 1997). The entries of the operators $\mathcal{A}$ and $\mathcal{B}$ in the compressible regime can be found in Appendix A for the perturbation variables $\mathbf{q} = (u, v, w, T, p)$.

2.3.2 Phase and group velocities

The phase function Θ in table 2.1 from the local stability analysis can also be written as

$$\Theta = \alpha(x - ct), \tag{2.18}$$

where $\beta = 0$ is assumed for convenience. The velocity of the wave crest, also denominated phase velocity is $c = \omega/\alpha$. In other words, for a given α, the value of the amplitude function $\hat{\mathbf{q}}$ is constant along a particular ray with $(x - ct) =$ constant. According to Kundu et al. (1990), if, and only if, ω is directly proportional to α, every wave-number has the same phase velocity and the unstable waves are known as non-dispersive. Otherwise, they are known as dispersive, i.e. each wave-number has a different phase velocity. According to Rayleigh (1896), a perturbation usually consists of a superposition of many waves, also called wave packet. These waves can interfere with each other either constructively or destructively. The nature of the interference pattern causes the perturbation to have an identifiable envelope. Although the wave crests of each wave-number travel at their respective phase velocities, the envelope travels at the so-called group velocity and it is defined as $d\omega/d\alpha$. In a non-dispersive wave packet, the group velocity is identical to the phase velocity, and the envelope remains with its shape in time. However, for dispersive wave packets, since the phase velocity is different from the group velocity, the envelope changes shape over time.

2.3.3 Convective and absolute instabilities

Within the local stability framework, it is necessary to differentiate between two types of instabilities: convective and absolute instabilities (Huerre and Monkewitz 1985, 1990). They are dependent on the response of the base flow to a determinate impulse. First, if the impulse always decays in every direction, the base flow is defined as *stable*. If the impulse grows while it is convected downstream with the flow, in a way that does not stay in the position in space where the impulse was inserted, the base flow is called *convectively unstable*. In other words, if perturbations were added at the initial condition only, their amplitude would initially grow but eventually decay in time at a fixed point in space. Alternatively, if a continuous source of perturbations exists, either periodic or stationary signal would be observed. Finally, if the impulse grows both downstream and upstream of the flow direction, the base flow is called *absolutely unstable*. Hence, perturbation amplitudes will eventually grow in time at any fixed

point in space, contaminating the whole flow. Additional details can be found in the review of Huerre and Monkewitz (1985). In general, convectively unstable flows behave as noise amplifiers, i.e. they are susceptible to small amplitude inlet perturbations. On the other hand, absolutely unstable flows behave as oscillators.

2.3.4 BiGlobal eigenvalue problem

If the base flow is now assumed to be dependent on two spatial directions, say z and y and homogeneous on the third x, BiGlobal linear instability theory can be applied Theofilis (2003). A harmonic dependence of the small-amplitude perturbations is assumed along the homogeneous spatial direction, x, with periodicity length $L_x = 2\pi/\alpha$, permitting further expansion of (2.11) using

$$\tilde{\mathbf{q}}(x, y, z, t) = \hat{\mathbf{q}}(y, z)e^{[i(\alpha x - \omega t)]}. \tag{2.19}$$

In the incompressible regime, substituting the above Ansatz in the LNSE, the resulting system of equations can be written in Cartesian coordinates

$$\begin{aligned}
\mathcal{L}\hat{u} + \frac{\partial \bar{u}}{\partial y}\hat{v} + \frac{\partial \bar{u}}{\partial z}\hat{w} + i\alpha\hat{p} = 0,\\
(\mathcal{L} + \frac{\partial \bar{v}}{\partial y})\hat{v} + \frac{\partial \bar{v}}{\partial z}\hat{w} + \frac{\partial \hat{p}}{\partial y} = 0,\\
(\mathcal{L} + \frac{\partial \bar{w}}{\partial z})\hat{w} + \frac{\partial \bar{w}}{\partial y}\hat{v} + \frac{\partial \hat{p}}{\partial z} = 0,\\
i\alpha\hat{u} + \frac{\partial \hat{v}}{\partial y} + \frac{\partial \hat{w}}{\partial z} = 0,
\end{aligned} \tag{2.20}$$

where $\mathcal{L} = i\alpha\bar{u} + \bar{v}\frac{\partial}{\partial y} + \bar{w}\frac{\partial}{\partial z} - \frac{1}{Re}\left[\frac{\partial^2}{\partial y2} + \frac{\partial^2}{\partial y2} - \alpha^2\right] - i\omega$.
In the compressible regime, the temporal operators ($\mathcal{A}$ and $\mathcal{B}$) can be written in matrix notation as

$$\begin{pmatrix} \mathcal{A}_{11} & \mathcal{A}_{12} & \mathcal{A}_{13} & \mathcal{A}_{14} & \mathcal{A}_{15} \\ \mathcal{A}_{21} & \mathcal{A}_{22} & \mathcal{A}_{23} & \mathcal{A}_{24} & \mathcal{A}_{25} \\ \mathcal{A}_{31} & \mathcal{A}_{32} & \mathcal{A}_{33} & \mathcal{A}_{34} & \mathcal{A}_{35} \\ \mathcal{A}_{41} & \mathcal{A}_{42} & \mathcal{A}_{43} & \mathcal{A}_{44} & \mathcal{A}_{45} \\ \mathcal{A}_{51} & \mathcal{A}_{52} & \mathcal{A}_{53} & \mathcal{A}_{54} & \mathcal{A}_{55} \end{pmatrix} \begin{pmatrix} \hat{u} \\ \hat{v} \\ \hat{w} \\ \hat{T} \\ \hat{p} \end{pmatrix} = \omega \begin{pmatrix} \mathcal{B}_{11} & 0 & 0 & 0 & 0 \\ 0 & \mathcal{B}_{22} & 0 & 0 & 0 \\ 0 & 0 & \mathcal{B}_{33} & 0 & 0 \\ 0 & 0 & 0 & 0 & \mathcal{B}_{45} \\ 0 & 0 & 0 & \mathcal{B}_{54} & \mathcal{B}_{55} \end{pmatrix} \begin{pmatrix} \hat{u} \\ \hat{v} \\ \hat{w} \\ \hat{T} \\ \hat{p} \end{pmatrix} \tag{2.21}$$

The explicit form of these operators in a Cartesian reference system can be found in Appendix B. Paredes et al. (2016) presents the coefficients for the variables $\mathbf{q} = (\rho, u, v, w, T)$.
In this approach, α is the disturbance wave-number and can be related to the periodicity length along the homogeneous spatial direction x as $\alpha = 2\pi/L_x$. The complex eigenvalue is $\omega = (\omega_r + i\omega_i)$, where the real part is related to the angular frequency

and the imaginary part is responsible for the temporal exponentially growth or decay rate of the perturbations.

2.3.5 TriGlobal eigenvalue problem

In the most general scenario, no assumptions are made regarding the homogeneity of the baseflow in all three spatial directions and the Ansatz is written as

$$\tilde{\mathbf{q}}(x, y, z, t) = \hat{\mathbf{q}}(x, y, z)e^{[-\omega t]}. \tag{2.22}$$

In the TriGlobal analysis, the substitution $\omega \rightarrow i\omega$ is possible to generate a real arithmetic eigenvalue problem (Theofilis 2003, 2011). Hence, in this case, ω_r is the decay or growth rate and ω_i is the angular frequency of the perturbation. Even though no TriGlobal example is investigated, the equations are used to solve complex geometries applying the chain rule method (to be defined next) in a generalised framework of reference. The entries of the matrices $\mathcal{A}$ and $\mathcal{B}$ can be found in Appendix C for the variables $\mathbf{q} = (u, v, w, T, p)$ while Paredes et al. (2016) demonstrates the entries for the variables $\mathbf{q} = (\rho, u, v, w, T)$.

2.4 Instability analysis in generalised coordinates

In order to extend the classical Cartesian coordinates analysis to account for complex curvilinear geometries, the governing stability equations need to be transformed. To achieve it, two different methods can be employed, depending on the space required to work on and the type of transformation wanted. The first method, called *chain rule*, can be used for both orthogonal and non-orthogonal grids. In contrast, the second method, *metric factor*, can only be used where an orthogonal transformation is provided. Both methods will be described next and the output in an orthogonal frame of reference will be compared in an example.

2.4.1 Chain rule

The first method used to transform the system of equations is the *chain rule* method that can be used for both orthogonal or non-orthogonal transformations. A random position in the physical space (x, y, z) can be defined by the vector (Paredes 2014)

$$\mathbf{s} = x(\xi, \eta, \zeta)\mathbf{i} + y(\xi, \eta, \zeta)\mathbf{j} + z(\xi, \eta, \zeta)\mathbf{k}, \tag{2.23}$$

where (ξ, η, ζ) are the independent curvilinear coordinates and $\mathbf{i}, \mathbf{j}, \mathbf{k}$ are orthogonal unit vectors in the physical space.

The generalised three-dimensional coordinate system can be obtained by relating the computational domain (ξ, η, ζ) to the physical domain (x, y, z). The following general

transformation can be used

$$\xi = \xi(x, y, z), \qquad \eta = \eta(x, y, z), \qquad \zeta = \zeta(x, y, z). \tag{2.24}$$

To express the first order partial derivatives, the chain rule can be used

$$\begin{aligned}
\frac{\partial}{\partial x} &= \xi_x \frac{\partial}{\partial \xi} + \eta_x \frac{\partial}{\partial \eta} + \zeta_x \frac{\partial}{\partial \zeta}, \\
\frac{\partial}{\partial y} &= \xi_y \frac{\partial}{\partial \xi} + \eta_y \frac{\partial}{\partial \eta} + \zeta_y \frac{\partial}{\partial \zeta}, \\
\frac{\partial}{\partial z} &= \xi_z \frac{\partial}{\partial \xi} + \eta_z \frac{\partial}{\partial \eta} + \zeta_z \frac{\partial}{\partial \zeta}.
\end{aligned} \tag{2.25}$$

The metrics appearing in these equations $(\xi_x, \xi_y, \xi_z, \eta_x, \eta_y, \eta_z, \zeta_x, \zeta_y, \zeta_z)$ can be obtained directly if an explicit expression for ξ, η and ζ is provided. Otherwise, they are determined solving the system

$$\begin{aligned}
\begin{pmatrix} \xi_x & \xi_y & \xi_z \\ \eta_x & \eta_y & \eta_z \\ \zeta_x & \zeta_y & \zeta_z \end{pmatrix} &= \begin{pmatrix} x_\xi & x_\eta & x_\zeta \\ y_\xi & y_\eta & y_\zeta \\ z_\xi & z_\eta & z_\zeta \end{pmatrix}^{-1} = \\
= J \begin{pmatrix} y_\eta z_\zeta - y_\zeta z_\eta & -(x_\eta z_\zeta - x_\zeta z_\eta) & x_\eta y_\zeta - x_\zeta y_\eta \\ -(y_\xi z_\zeta - y_\zeta z_\xi) & x_\xi z_\zeta - x_\zeta z_\xi & -(x_\xi y_\zeta - x_\zeta y_\xi) \\ y_\xi z_\eta - y_\eta z_\xi & -(x_\xi z_\eta - x_\eta z_\xi) & x_\xi y_\eta - x_\eta y_\xi \end{pmatrix},
\end{aligned} \tag{2.26}$$

where J is the determinant of the Jacobian of the transformation and can be obtained as

$$J = \frac{\partial(\xi, \eta, \zeta)}{\partial(x, y, z)} = \frac{1}{\frac{\partial(x,y,z)}{\partial(\xi,\eta,\zeta)}} = \frac{1}{x_\xi(y_\eta z_\zeta - y_\zeta z_\eta) - x_\eta(y_\xi z_\zeta - y_\zeta z_\xi) + x_\zeta(y_\xi z_\eta - y_\eta z_\xi)}. \tag{2.27}$$

For cases where the transformation is the direct result of the grid generation scheme, the metrics can be computed numerically. In the case of second-order derivatives in terms of computational coordinate, the result from the system 2.26 can be derived with respect to the appropriated variable leading to the second derivative metric. Particularly, the derivative of ξ_x with respect to x is

$$\begin{aligned}
\frac{\partial^2 \xi}{\partial x^2} \;=\; J\Bigg[& -\frac{\partial z}{\partial \eta}\left(\frac{\partial \eta}{\partial x}\frac{\partial^2 y}{\partial \eta \partial \zeta} + \frac{\partial \xi}{\partial x}\frac{\partial^2 y}{\partial \xi\, \partial \zeta} + \frac{\partial \zeta}{\partial x}\frac{\partial^2 y}{\partial \zeta^2}\right) \\
& + \frac{\partial y}{\partial \eta}\left(\frac{\partial \eta}{\partial x}\frac{\partial^2 z}{\partial \eta \partial \zeta} + \frac{\partial \xi}{\partial x}\frac{\partial^2 z}{\partial \xi\, \partial \zeta} + \frac{\partial \zeta}{\partial x}\frac{\partial^2 z}{\partial \zeta^2}\right) \\
& + \frac{\partial z}{\partial \zeta}\left(\frac{\partial \zeta}{\partial x}\frac{\partial^2 y}{\partial \eta \partial \zeta} + \frac{\partial \xi}{\partial x}\frac{\partial^2 y}{\partial \xi \partial \eta} + \frac{\partial \eta}{\partial x}\frac{\partial^2 y}{\partial \eta^2}\right) \\
& - \frac{\partial y}{\partial \zeta}\left(\frac{\partial \zeta}{\partial x}\frac{\partial^2 z}{\partial \eta \partial \zeta} + \frac{\partial \xi}{\partial x}\frac{\partial^2 z}{\partial \xi \partial \eta} + \frac{\partial \eta}{\partial x}\frac{\partial^2 z}{\partial \eta^2}\right)\Bigg] \\
& + \left(\frac{\partial y}{\partial \eta}\frac{\partial z}{\partial \zeta} - \frac{\partial y}{\partial \zeta}\frac{\partial z}{\partial \eta}\right)\left(\frac{\partial J}{\partial \zeta}\frac{\partial \zeta}{\partial x} + \frac{\partial J}{\partial \eta}\frac{\partial \eta}{\partial x} + \frac{\partial J}{\partial \xi}\frac{\partial \xi}{\partial x}\right).
\end{aligned} \tag{2.28}$$

Second-order derivatives can be expressed in terms of the computational coordinate system as

$$\frac{\partial f}{\partial c_i} = \chi^j_{c_i}\frac{\partial f}{\partial \chi^j} = J\frac{\partial}{\partial \chi^j}\left(\frac{\chi^j_{c_i} f}{J}\right) - Jf\left[\frac{\partial}{\partial \chi^j}\frac{\chi^j_{c_i}}{J}\right], \qquad i = 1, 2, 3. \tag{2.29}$$

In this case, f is an arbitrary function, $(c_1, c_2, c_3) = (\mathrm{x,y,z})$ and $(\chi_1, \chi_2, \chi_3) = (\xi, \eta, \zeta)$. Substituting the metrics (2.26) into the term with square brackets of equation (2.29), it can be showed that this term is zero. The mix derivatives of the Navier-Stokes equations can be expressed as

$$\frac{\partial^2 f}{\partial c_i c_j} = \chi^k_{c_i}\chi^l_{c_j}\frac{\partial^2 f}{\partial \chi^k \chi^l} + J\frac{\partial}{\partial \chi^k}\left(\frac{\chi^k_{c_i}\chi^l_{c_j}}{J}\right)\frac{\partial f}{\partial \chi^l}. \tag{2.30}$$

If the flow is fully resolved in the wall-normal direction y and the spanwise direction x, the second-order derivatives can be expressed as

$$\begin{aligned}
\frac{\partial^2}{\partial y^2} &= \xi_y^2\frac{\partial^2}{\partial \xi^2} + \eta_y^2\frac{\partial^2}{\partial \eta^2} + \zeta_y^2\frac{\partial^2}{\partial \zeta^2} \\
&+ 2\xi_y\eta_y\frac{\partial^2}{\partial \xi \partial \eta} + 2\xi_y\zeta_y\frac{\partial^2}{\partial \xi \partial \zeta} + 2\eta_y\zeta_y\frac{\partial^2}{\partial \eta \partial \zeta} \\
&+ J\left[\frac{\partial}{\partial \xi}\left(\frac{\xi_y^2}{J}\right) + \frac{\partial}{\partial \eta}\left(\frac{\xi_y\eta_y}{J}\right) + \frac{\partial}{\partial \zeta}\left(\frac{\xi_y\zeta_y}{J}\right)\right]\frac{\partial}{\partial \xi} \\
&+ J\left[\frac{\partial}{\partial \xi}\left(\frac{\xi_y\eta_y}{J}\right) + \frac{\partial}{\partial \eta}\left(\frac{\eta_y^2}{J}\right) + \frac{\partial}{\partial \zeta}\left(\frac{\eta_y\zeta_y}{J}\right)\right]\frac{\partial}{\partial \eta} \\
&+ J\left[\frac{\partial}{\partial \xi}\left(\frac{\xi_y\zeta_y}{J}\right) + \frac{\partial}{\partial \eta}\left(\frac{\eta_y\zeta_y}{J}\right) + \frac{\partial}{\partial \zeta}\left(\frac{\zeta_y^2}{J}\right)\right]\frac{\partial}{\partial \zeta}
\end{aligned} \tag{2.31}$$

and

$$\begin{aligned}
\frac{\partial^2}{\partial x^2} &= \xi_x^2\frac{\partial^2}{\partial \xi^2} + \eta_x^2\frac{\partial^2}{\partial \eta^2} + \zeta_x^2\frac{\partial^2}{\partial \zeta^2} \\
&+ 2\xi_x\eta_x\frac{\partial^2}{\partial \xi \partial \eta} + 2\xi_x\zeta_x\frac{\partial^2}{\partial \xi \partial \zeta} + 2\eta_x\zeta_x\frac{\partial^2}{\partial \eta \partial \zeta} \\
&+ J\left[\frac{\partial}{\partial \xi}\left(\frac{\xi_x^2}{J}\right) + \frac{\partial}{\partial \eta}\left(\frac{\xi_x\eta_x}{J}\right) + \frac{\partial}{\partial \zeta}\left(\frac{\xi_x\zeta_x}{J}\right)\right]\frac{\partial}{\partial \xi} \\
&+ J\left[\frac{\partial}{\partial \xi}\left(\frac{\xi_x\eta_x}{J}\right) + \frac{\partial}{\partial \eta}\left(\frac{\eta_x^2}{J}\right) + \frac{\partial}{\partial \zeta}\left(\frac{\eta_x\zeta_x}{J}\right)\right]\frac{\partial}{\partial \eta} \\
&+ J\left[\frac{\partial}{\partial \xi}\left(\frac{\xi_x\zeta_x}{J}\right) + \frac{\partial}{\partial \eta}\left(\frac{\eta_x\zeta_x}{J}\right) + \frac{\partial}{\partial \zeta}\left(\frac{\zeta_x^2}{J}\right)\right]\frac{\partial}{\partial \zeta}.
\end{aligned} \tag{2.32}$$

The mixed derivatives are expressed as

$$
\begin{aligned}
\frac{\partial^2}{\partial x \partial y} = \frac{\partial^2}{\partial y \partial x} \;=\; & \xi_x \xi_y \frac{\partial^2}{\partial \xi^2} + \eta_x \eta_y \frac{\partial^2}{\partial \eta^2} + \zeta_x \zeta_y \frac{\partial^2}{\partial \zeta^2} \\
& + \; (\xi_x \eta_y + \xi_y \eta_x) \frac{\partial^2}{\partial \xi \partial \eta} + (\xi_x \zeta_y + \xi_y \zeta_x) \frac{\partial^2}{\partial \xi \partial \zeta} + (\eta_x \zeta_y + \eta_y \zeta_x) \frac{\partial^2}{\partial \eta \partial \zeta} \\
& + \; J \left[\frac{\partial}{\partial \xi} \left(\frac{\xi_x \xi_y}{J} \right) + \frac{\partial}{\partial \eta} \left(\frac{\xi_x \eta_y}{J} \right) + \frac{\partial}{\partial \zeta} \left(\frac{\xi_x \zeta_y}{J} \right) \right] \frac{\partial}{\partial \xi} \\
& + \; J \left[\frac{\partial}{\partial \xi} \left(\frac{\xi_y \eta_x}{J} \right) + \frac{\partial}{\partial \eta} \left(\frac{\eta_x \eta_y}{J} \right) + \frac{\partial}{\partial \zeta} \left(\frac{\eta_x \zeta_y}{J} \right) \right] \frac{\partial}{\partial \eta} \\
& + \; J \left[\frac{\partial}{\partial \xi} \left(\frac{\xi_y \zeta_x}{J} \right) + \frac{\partial}{\partial \eta} \left(\frac{\eta_y \zeta_x}{J} \right) + \frac{\partial}{\partial \zeta} \left(\frac{\zeta_x \zeta_y}{J} \right) \right] \frac{\partial}{\partial \zeta}.
\end{aligned}
\tag{2.33}
$$

Applying the transformation (2.25) and (2.29) to the compressible Navier-Stokes equations leads to the compressible generalised Navier-Stokes equations in the chain rule formulation. Once the Jacobian is provided (analytically or numerically), the linear stability of flows around or through any complex geometry can be analysed.

2.4.2 Metric factor

The second method followed is the *metric factor*. In this formulation, an orthogonal coordinate system is assumed. In this case, conformal mapping is applied, and the orthogonality of the curved space is retained. For orthogonal curvilinear coordinates (ξ, η, ζ), the metric tensor does not contain elements outside the diagonal. Therefore, line elements can always be defined as

$$
d\mathbf{s}^2 = \sum_{n=1}^{3} h_n^2 (d\chi_n)^2, \tag{2.34}
$$

where $(\chi_1, \chi_2, \chi_3) = (\xi, \eta, \zeta)$. The so-called scale factors h_n can be defined as

$$
h_i = \sqrt{g_{ii}} = \sqrt{\left(\frac{\partial x}{\partial \chi_i} \right)^2 + \left(\frac{\partial y}{\partial \chi_i} \right)^2 + \left(\frac{\partial z}{\partial \chi_i} \right)^2}, \qquad i = (1, 2, 3). \tag{2.35}
$$

In this formulation, the differential operators appearing in the Navier-Stokes equations become

$$
\begin{aligned}
\text{grad} = \nabla &= \frac{1}{h_1} \frac{\partial}{\partial \xi} + \frac{1}{h_2} \frac{\partial}{\partial \eta} + \frac{1}{h_3} \frac{\partial}{\partial \zeta}, \\
\text{div} = \nabla. &= \frac{1}{h_1 h_2 h_3} \left[\frac{\partial}{\partial \xi}(h_2 h_3) + \frac{\partial}{\partial \eta}(h_3 h_1) + \frac{\partial}{\partial \zeta}(h_1 h_2) \right], \\
\text{curl} = \nabla\times &= \frac{1}{h_1 h_2 h_3} \sum_{l,m,n} h_l \left[\frac{\partial}{\partial \chi_m}(h_n) - \frac{\partial}{\partial \chi_n}(h_m) \right], \\
\text{div grad} = \nabla^2 &= \frac{1}{h_1 h_2 h_3} \left[\frac{\partial}{\partial \xi} \left(\frac{h_2 h_3}{h_1} \right) + \frac{\partial}{\partial \eta} \left(\frac{h_3 h_1}{h_2} \right) + \frac{\partial}{\partial \zeta} \left(\frac{h_1 h_2}{h_3} \right) \right],
\end{aligned}
\tag{2.36}
$$

where $l, m, n = 1, 2, 3$ or $2, 3, 1$ or $3, 1, 2$.

Christoffel symbols

In order to express the divergence of a second-order tensor field (as $\nabla.\tau$ appearing in the Navier-Stokes equations) in curvilinear coordinates, it is necessary to define the Christoffel symbols (Aris 1962, Bishop and Goldberg 2012). They are nothing more than an array of numbers describing a metric connection. In general, an infinite number of metric connections may exist but only one is free of torsion: the Levi-Civita connection. In Euclidean spaces, the change in the local coordinates bases from point to point is described by the Christoffel symbols. In this case

$$\nabla.\tau = \left[\frac{\partial \tau_{ij}}{\partial \chi^k} - \Gamma^l_{ki}\tau_{lj} - \Gamma^l_{kj}\tau_{il}\right] g^{ik}, \tag{2.37}$$

where Γ^l_{ki} and Γ^l_{kj} are the Christoffel symbols of the second kind. Since the symbols are symmetric in the lower two indices, the Christoffel symbols can be obtained as a function of the metric tensor by permuting the indices and re-summing (Bishop and Goldberg 2012)

$$\Gamma^l_{ki} = \frac{1}{2}\left(\frac{\partial g_{mk}}{\partial \chi^i} + \frac{\partial g_{mi}}{\partial \chi^k} - \frac{\partial g_{ki}}{\partial \chi^m}\right) g^{lm}, \tag{2.38}$$

where the metric tensor g in the different basis can be related as

$$g^{ij} = (g^{-1})_{ij}. \tag{2.39}$$

With these transformations calculated, the linearized Navier-Stokes equations written in Cartesian coordinates can be transformed into an orthogonal curvilinear coordinate system. If the calculations are to be performed using this method, the resulting eigenfunctions from the stability analysis need to be transformed into physical space for visualization. The compressible BiGlobal equations written using the *metric factor* can be found in Appendix D.

2.4.3 Example of the methods in cylindrical polar coordinates

To better illustrate the difference in applying both methods previously discussed, a simple example in calculating the divergence of a vector is presented in the cylindrical polar coordinates system. The relation between physical and curvilinear space can be obtained in cylindrical polar coordinates as

$$\begin{aligned} x &= \xi \ \cos(\eta), \\ y &= \xi \ \sin(\eta). \end{aligned} \tag{2.40}$$

The metrics can be directly obtained from the above transformation and are defined as

$$\begin{aligned} \frac{\partial x}{\partial \xi} &= \cos(\eta), \quad & \frac{\partial x}{\partial \eta} &= -\xi \ \sin(\eta), \\ \frac{\partial y}{\partial \xi} &= \sin(\eta), \quad & \frac{\partial y}{\partial \eta} &= \ \ \xi \ \cos(\eta), \end{aligned} \tag{2.41}$$

$$\begin{aligned} \frac{\partial \xi}{\partial x} &= \ \ J \ \frac{\partial y}{\partial \eta} = \ \ \cos(\eta), & \frac{\partial \xi}{\partial y} &= -J \ \frac{\partial x}{\partial \eta} = \sin(\eta), \\ \frac{\partial \eta}{\partial x} &= -J \ \frac{\partial y}{\partial \xi} = -\frac{\sin(\eta)}{\xi}, & \frac{\partial \eta}{\partial y} &= \ \ J \ \frac{\partial x}{\partial \xi} = \frac{\cos(\eta)}{\xi}, \end{aligned} \tag{2.42}$$

where the Jacobian J can be calculated as

$$J = \left(\frac{\partial x}{\partial \xi} \ \frac{\partial y}{\partial \eta} - \frac{\partial x}{\partial \eta} \ \frac{\partial y}{\partial \xi} \right)^{-1} = \frac{1}{\xi}. \tag{2.43}$$

The shape factors necessary for the metric factor method can be obtained as

$$\begin{aligned} h_1 &= \sqrt{\left(\frac{\partial x}{\partial \xi} \right)^2 + \left(\frac{\partial y}{\partial \xi} \right)^2} = 1, \\ h_2 &= \sqrt{\left(\frac{\partial x}{\partial \eta} \right)^2 + \left(\frac{\partial y}{\partial \eta} \right)^2} = \xi. \end{aligned} \tag{2.44}$$

In this case, the vector transformation from (ξ, η)-domain to (x,y)-domain is

$$\begin{aligned} u_\xi &= u_x \ \frac{1}{h_1} \frac{\partial x}{\partial \xi} + u_y \ \frac{1}{h_1} \frac{\partial y}{\partial \xi} = \ \ \ u_x \cos(\eta) + u_y \sin(\eta), \\ u_\eta &= u_x \ \frac{1}{h_2} \frac{\partial x}{\partial \eta} + u_y \ \frac{1}{h_2} \frac{\partial y}{\partial \eta} = -u_x \sin(\eta) + u_y \cos(\eta), \end{aligned} \tag{2.45}$$

whereas the inverse transformation from (x,y)-domain to (ξ, η)-domain is defined as

$$\begin{aligned} u_x &= \frac{h_1 u_\xi \frac{\partial y}{\partial \eta} - h_2 u_\eta \frac{\partial y}{\partial \xi}}{\left(\frac{\partial y}{\partial \eta} \frac{\partial x}{\partial \xi} - \frac{\partial x}{\partial \eta} \frac{\partial y}{\partial \xi} \right)} = u_\xi \cos(\eta) - u_\eta \sin(\eta), \\ u_y &= \frac{h_1 u_\xi \frac{\partial x}{\partial \eta} - h_2 u_\eta \frac{\partial x}{\partial \xi}}{\left(\frac{\partial y}{\partial \xi} \frac{\partial x}{\partial \eta} - \frac{\partial x}{\partial \xi} \frac{\partial y}{\partial \eta} \right)} = u_\xi \sin(\eta) + u_\eta \cos(\eta). \end{aligned} \tag{2.46}$$

A geometrical interpretation is used to better visualise the vector transformation between both coordinate system (Fig. 2.1). The velocity components u_ξ and u_η can be decomposed in u_x and u_y and vice-versa using the angle η.
With all metrics and transformations calculated, the two different methods can be explained in what follows.

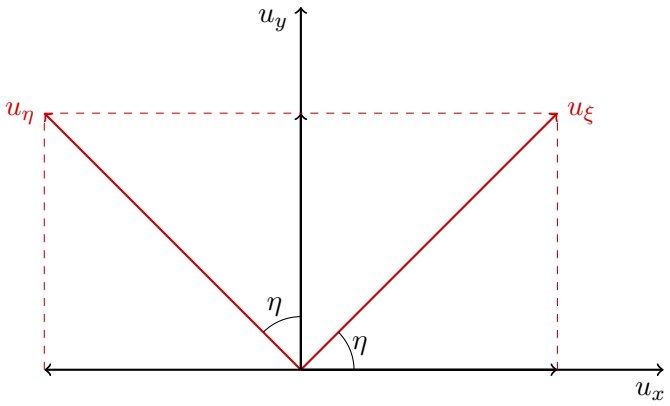

Figure 2.1: Geometric interpretation of the vector transformation between the coordinates (ξ, η) and (x, y).

Method 1: The Chain Rule

For the first method, the divergent of the velocity vector $\nabla.u$ is written in physical components as

$$\frac{\partial u_x}{\partial x} + \frac{\partial u_y}{\partial y} = 0 \tag{2.47}$$

but from equation (2.25) in two-dimensions

$$\begin{aligned} \frac{\partial}{\partial x} &= \xi_x \frac{\partial}{\partial \xi} + \eta_x \frac{\partial}{\partial \eta}, \\ \frac{\partial}{\partial y} &= \xi_y \frac{\partial}{\partial \xi} + \eta_y \frac{\partial}{\partial \eta}. \end{aligned} \tag{2.48}$$

Substituting the chain rule in the divergence operator

$$\xi_x \frac{\partial u_x}{\partial \xi} + \eta_x \frac{\partial u_x}{\partial \eta} + \xi_y \frac{\partial u_y}{\partial \xi} + \eta_y \frac{\partial u_y}{\partial \eta} = 0. \tag{2.49}$$

In cylindrical polar coordinates

$$\cos(\eta) \frac{\partial u_x}{\partial \xi} - \frac{\sin(\eta)}{\xi} \frac{\partial u_x}{\partial \eta} + \sin(\eta) \frac{\partial u_y}{\partial \xi} + \frac{\cos(\eta)}{\xi} \frac{\partial u_y}{\partial \eta} = 0. \tag{2.50}$$

Equation (2.49) is how the first method is programmed. The velocity variables are in physical space; therefore, no transformation needs to be done with the base flow or eigenfunctions resulting from the stability analysis. In other words, the derivatives are transformed through the metrics to physical space. However, in comparing equation (2.50) with the literature, the divergence of a vector in cylindrical polar coordinates is written in the computational domain (ξ, η). Using the vector transformation from physical to computational (2.46)

$$\cos(\eta)\frac{\partial}{\partial\xi}\Big[u_\xi\cos(\eta)-u_\eta\sin(\eta)\Big]-\frac{\sin(\eta)}{\xi}\frac{\partial}{\partial\eta}\Big[u_\xi\cos(\eta)-u_\eta\sin(\eta)\Big]+$$
$$\sin(\eta)\frac{\partial}{\partial\xi}\Big[u_\xi\sin(\eta)+u_\eta\cos(\eta)\Big]+\frac{\cos(\eta)}{\xi}\frac{\partial}{\partial\eta}\Big[u_\xi\sin(\eta+u_\eta\cos(\eta))\Big]=0. \tag{2.51}$$

applying the derivatives and using trigonometric identities

$$\frac{\partial u_\xi}{\partial\xi}+\frac{u_\xi}{\xi}+\frac{1}{\xi}\frac{\partial u_\eta}{\partial\eta}=0, \tag{2.52}$$

which is the divergence of a vector in cylindrical coordinates found everywhere in the literature. This transformation is made here only to compare and prove that the equations are indeed correct. It is important to consider that in the *chain rule* method, equation (2.49) is programmed.

Method 2: Tensor Form

In the second method, the divergence is written directly in a general form in curvilinear space as

$$\nabla.\mathbf{u}=\frac{1}{h_1h_2}\frac{\partial}{\partial\xi}\left[h_1h_2\frac{u_\xi}{h_1}\right]+\frac{\partial}{\partial\eta}\left[h_1h_2\frac{u_\eta}{h_2}\right]. \tag{2.53}$$

Using the shape factor (2.44) and applying the derivatives we obtain

$$\frac{\partial u_\xi}{\partial\xi}+\frac{u_\xi}{\xi}+\frac{1}{\xi}\frac{\partial u_\eta}{\partial\eta}=0, \tag{2.54}$$

which is the same as the chain rule method described before after the velocity vector transformation. For this method, since all variables are required to be in the computational domain, the transformations (2.45) and (2.46) need to be used in the base flow components to convert them to the computational domain. This procedure is also applied in the resulting eigenfunctions to back transform them to physical space. Although this method appears more straightforward, it is only valid on orthogonal transformation systems, such as cylindrical polar or elliptical transformations. In the case of the *HiFIRE-5* elliptic cone mode that will be investigated later, the transformation is not orthogonal in the streamwise direction. In this case, the *chain rule* method is used.

Chapter 3

Global transient growth in compressible 3D flows

The objective of the present effort is the development of global linear modal and non-modal/transient growth (TG) instability analysis tools for hypersonic spatially inhomogeneous flows. Subsequently, the code developed herein will be applied to determine the relative importance of modal and nonmodal scenarios on a compression ramp, a supersonic cylinder and an elliptic cone. The approach followed first computes the pseudospectrum of the discretized Jacobian and subsequently computes optimal initial perturbations and their time-evolution. The level of transient energy growth, $G(t)$, may be used to identify the potential of high-speed flows to sustain linear algebraically growing perturbations in low-disturbance (flight) and high-disturbance (wind-tunnel) environments.

3.1 Geometric interpretation of transient growth

Before addressing specific forms of the equations, the above ideas are described by a generic Initial Value Problem (IVP) of the form

$$\partial_t \hat{\mathbf{q}} = \mathcal{L}(\bar{\mathbf{q}})\hat{\mathbf{q}}, \tag{3.1}$$

where $\bar{\mathbf{q}}$ is the state whose linear perturbations $\hat{\mathbf{q}}$ are sought. In a fluid context the operator $\mathcal{L}$ would contain the base flow and its spatial derivatives from the Linearized Navier-Stokes Equations (LNSE) in which the Reynolds, Re, and Mach, Ma, numbers would appear as parameters. However, the discussion at this point is broader and as IVP can arise in a number of fields in physics (Trefethen 1992). The exact solution of the IVP is written with the aid of the matrix exponential (Moller and van Loan 1978, 2003),

$$\hat{\mathbf{q}}(t) = \hat{\mathbf{q}}(0)e^{\mathcal{A}t}, \tag{3.2}$$

where matrix $\mathcal{A}$ represents the numerical discretisation of the linear operator $\mathcal{L}$. In the case of a normal matrix, the eigenvalue spectrum can be used to simplify this expression. However, the high non-normality of the LNSE discretised linear operator $\mathcal{A}$ leads to a non-trivial behavior at early (short) time, which arises as a result of the near-parallel nature of certain eigenvectors (Schmid and Henningson 2001) in the eigenspectrum.

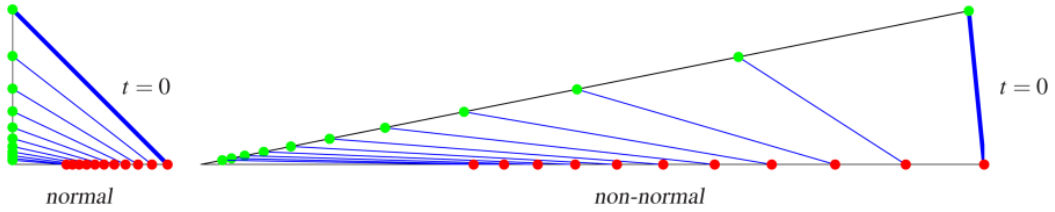

Figure 3.1: Geometric interpretation of transient growth (Schmid and Brandt 2014)

Figure 3.1 (Schmid and Brandt 2014) illustrates the transient growth phenomenon graphically for a simple example. On the left hand side of the figure, the eigenvectors are normal to each other. As a result, when the eigenvalues are decaying, the eigenvectors are also decaying in size. On the other side, the eigenvectors are non-normal to each other. Therefore, although the eigenvalues are damped, it can be noticed that the eigenvectors transiently grow in size before their ultimate start to decay. This geometric interpretation helps clarify a central idea in transient growth analysis, namely that *in a short time-horizon (time is a parameter in the analysis) linear superposition of decaying non-orthogonal eigenvectors can indeed produce growth in the size (norm) of a disturbance*. The decaying nature of the individual eigenvectors will only manifest itself at asymptotically large time.

3.2 A quantitative example of transient growth

The next example adapted from Trefethen (1992) demonstrates the idea of transient growth quantitatively. Take the following matrices

$$A = \begin{bmatrix} -1 & 1 \\ 1 & -10 \end{bmatrix}, \quad A = \begin{bmatrix} -1 & 10 \\ 0 & -2 \end{bmatrix}, \quad \text{and} \quad A = \begin{bmatrix} 0.2 & 0.1 \\ 0 & -0.2 \end{bmatrix}$$

and solve the Initial Value Problems (IVP)

$$\partial_t \hat{\mathbf{q}} = \mathrm{A}\hat{\mathbf{q}} \quad \text{with A normal, 2 negative EVs,} \tag{3.3}$$

$$\partial_t \hat{\mathbf{q}} = \mathrm{A}\hat{\mathbf{q}} \quad \text{with A non-normal, 2 negative EVs,} \tag{3.4}$$

$$\partial_t \hat{\mathbf{q}} = \mathrm{A}\hat{\mathbf{q}} \quad \text{with A non-normal, 1 positive / 1 negative EV.} \tag{3.5}$$

The respective eigenvalues are $\Lambda\{A\} = \{-1, -1\}$, $\Lambda\{A\} = \{-2, -1\}$ and $\Lambda\{A\} = \{-0.2, 0.2\}$.

The solutions of (3.3-3.5) with the initial condition $\hat{q}(0) = 1$ are shown in Figure 3.2. One notes the expected behavior of A and A. The negative eigenvalues of A are reflected in the monotonic decay of the signal (left figure) and in the constant slope of the decaying straight line (right figure). Analogously for A, the positive eigenvalue determines the monotonic growth of the respective signal, as seen in both linear and semi-logarithmic scales. By contrast, the signal corresponding to A, which only has negative eigenvalues and should also display monotonic decay in time, can clearly be seen to grow at early time, before ultimately decaying as the eigenvalues would predict. This *transient* growth at early times is due to the non-normality of A, which contrasts with the normal behavior of the matrices A and A.

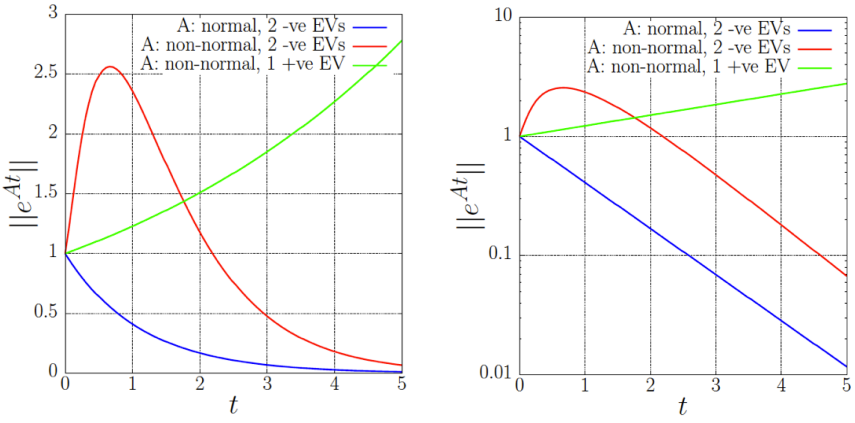

Figure 3.2: Solutions of (3.3-3.5) in linear (left) and semi-logarithmic (right) scales (adapted from Trefethen and Embree (2005))

The behavior exhibited by A is common to non-normal matrices, such as those resulting from spatial discretization of the linearized Navier-Stokes equations (LNSE). Consequently, rather than focusing on the eigenvalue problem (EVP) alone, one needs to solve both of the EVP and the initial value problem (IVP) in order for accurate predictions on the *linear* instability behavior to be obtained. The (matrix exponential) solution may exhibit transient growth (at short time), even if the eigenvalue predicts decay in (asymptotically large) time. Of course, the EVP predictions are identical with those yielded by the asymptotically large time, $t \to \infty$ in the solution of the IVP (and will always be used for verification purposes). This behavior is absent in normal matrices (here the "blue" and "green" example matrices) in which the eigenvalues completely determine the dynamic behavior of the system. From a numerical analysis point of view, the growth observed transiently is intimately linked with, and is actually proportional to, the condition number of the discretized matrix in question.

A new concept, that of $\epsilon-$*pseudospectrum* (Trefethen et al. 1993), which extends the well-known eigenspectrum, is necessary to quantify the transient behavior of non-normal matrices. In order for quantitative predictions to be made, first the *resolvent*

of $\mathcal{A}$ is defined as

$$(zI - \mathcal{A})^{-1}, \quad z \in \mathbb{C}. \tag{3.6}$$

The resolvent becomes infinite when z is an eigenvalue of $\mathcal{A}$. With the help of the resolvent, the $\epsilon-$*pseudospectrum* of $\mathcal{A}$, is defined as

$$\begin{aligned}
\Lambda_\epsilon(\mathcal{A}) &\equiv \left\{z \in \mathbb{C} : ||(zI - \mathcal{A})^{-1}|| \geq \epsilon^{-1}\right\} && (3.7)\\
&\equiv \left\{z \in \mathbb{C} : \sigma_{\min}(zI - \mathcal{A})^{-1} \leq \epsilon\right\} && (3.8)\\
&\equiv \{z \in \mathbb{C} : z \text{ is an eigenvalue of } \mathcal{A} + \mathcal{E}, \text{ for some } \mathcal{E} \text{ with } ||\mathcal{E}|| \leq \epsilon\} && (3.9)
\end{aligned}$$

Here $||.||$ is the L2-norm of a vector and σ is a singular value of a matrix. Any of the three definitions,

- resolvent norm,
- minimum singular value of the resolvent, or
- eigenspectrum of the randomly perturbed matrix

may be used to compute the ϵ-pseudospectrum. When the latter is employed (matrix-perturbations approach), transient growth is expected to occur in the non-sharply defined parts of the eigenspectrum, as a consequence of the superposition of the corresponding non-orthogonal eigenvectors. When solving the matrix exponential, time becomes a parameter; such transient growth theory permits analysis of time-dependent flows. However, a reasonably large time-window needs to be examined, in order to cover both the early-time and the asymptotic-time perturbation behavior. Again, it should also be noted that the asymptotically long time result of transient growth theory is identical with that predicted by modal analysis via solution of the EVP.
Finally, The *gain function*, $G(t)$, is defined (Schmid and Henningson 2001) at an arbitrary time, t, as the ratio of perturbation energy at any time to initial perturbation energy of an eigenvector $\hat{\mathbf{q}}$, itself a function of the streamwise and spanwise wavenumbers, α and β respectively, as

$$G(t) = G(\alpha, \beta, Re, t) = \max_{\hat{\mathbf{q}}(0)} \frac{||\hat{\mathbf{q}}(t)||_E^2}{||\hat{\mathbf{q}}(0)||_E^2} = ||e^{-it\mathcal{L}}||_E^2 = ||\mathbf{F}\Lambda\mathbf{F}^{-1}||_2^2 \tag{3.10}$$

Since transient growth analysis is linear, it is necessary to refer predictions at any given time, t, to an initial level of the monitored quantity. From a physical point of view it is meaningful to define the gain in terms of an initial perturbation energy and monitor its evolution in time. The level of TG is then quantified by $G_{\max}(t)$, the maximum value of the gain function attained over time, and referred to its initial value that is commonly scaled to unity in this linear context. As can be seen in equation

(3.10) the base flow may be time-dependent, since time is treated in as a parameter of transient growth analysis. The objective of linear TG analysis is the identification of conditions that yield large energy gains and can give rise to flow nonlinearities. The analysis can also identify the (optimal) initial conditions that give rise to transiently most amplified perturbations. From a technical point of view, one solves the direct and adjoint eigenvalue problems, and by using the bi-orthogonality conditions, the mode amplitudes as well as the solution of the IVP are reconstructed using the small numbers of vectors that have been retained. (Theofilis et al. 2003, Rodríguez et al. 2011).

3.3 The initial value problem

The decomposition of any flow quantity ($\mathbf{q}$) into a steady laminar base or mean flow plus a small amplitude disturbance

$$\mathbf{q}(\mathbf{x},t) = \bar{\mathbf{q}}(\mathbf{x}) + \epsilon\tilde{\mathbf{q}}(\mathbf{x},t), \qquad with \quad \epsilon \ll 1, \tag{3.11}$$

that is substituted into the compressible Navier-Stokes equations, presented in the earlier section, yields the well-known compressible linearized Navier-Stokes equations (LNSE). They can be written as an initial-value-problem (IVP) in the form of

$$\mathcal{B}\frac{\partial\tilde{\mathbf{q}}}{\partial t} = \mathcal{A}\tilde{\mathbf{q}} \tag{3.12}$$

where the matrices $\mathcal{A}$ and $\mathcal{B}$ contain the spatial discretization, the base flow and its derivatives.
Multiplying both sides of the system by $\mathcal{B}^{-1}$ gives

$$\frac{\partial\tilde{\mathbf{q}}}{\partial t} = \mathcal{L}\tilde{\mathbf{q}} \tag{3.13}$$

where $\tilde{\mathbf{q}}(x,y,z,t) = (\tilde{u},\tilde{v},\tilde{w},\tilde{T},\tilde{P})^T$ is the vector containing the disturbance functions of velocity, temperature and pressure (Theofilis 2011) and $\mathcal{L} = \mathcal{B}^{-1}\mathcal{A}$ is a linear operator mapping the flow field to its time derivative and contain the appropriated boundary conditions. Note that the matrix $\mathcal{B}$ is non-singular in the compressible regime, so it is possible to compute its inverse.
The solution of the IVP is given in general form by

$$\tilde{\mathbf{q}} = \exp(t\mathcal{L})\tilde{\mathbf{q}}_{\mathbf{0}}, \tag{3.14}$$

where $\tilde{q}_0$ is the initial condition. It is important to notice that, so far, no approximations regarding the shape of the disturbances or their temporal behavior have been introduced. The matrix exponential $\mathcal{L}$ can also been seen as the stability operator after the linearization step described before.

3.3.1 Quantitative description of energy growth - the Gain function

Defining stability as the amplification of initial disturbance energy over a prescribed time interval (Schmid and Henningson 2001, Schmid 2007) and optimizing it over all permissible initial conditions, the *gain function* $G(t)$ may be defined as the maximum optimal energy amplification

$$G(t) = \underset{\tilde{\mathbf{q}}_0}{max} \frac{E(\tilde{\mathbf{q}}(t))}{E(\tilde{\mathbf{q}}_0)}, \tag{3.15}$$

with $(E\tilde{\mathbf{q}})$ being the energy of the disturbance. Substituting (3.14) into the above definition of energy amplification yields

$$G(t) = \underset{\tilde{\mathbf{q}}_0}{max} \frac{||\tilde{\mathbf{q}}(t)||_E^2}{||\tilde{\mathbf{q}}_0||_E^2} = \underset{\tilde{\mathbf{q}}_0}{max} \frac{||\exp(t\mathcal{L}\tilde{\mathbf{q}}_0)||_E^2}{||\tilde{\mathbf{q}}_0||_E^2} = ||\exp(t\mathcal{L})||_E^2 \tag{3.16}$$

The norm of the disturbance will be defined shortly. This energy norm of the matrix exponential represents the largest amplification of energy that any infinitesimal initial disturbance can experience given a time interval. As discussed by Moller and van Loan (1978), the large conditions number of the matrix discretising the linear operator makes the exact computation of the matrix exponential challenging. Here, an eigenvalue decomposition of the numerical linear operator $\mathcal{L}$ is used to approximate the matrix exponential by

$$||\exp(t\mathcal{L})||_E^2 = ||\exp(t\mathcal{V}\Lambda\mathcal{V}^{-1})||_E^2 = ||\mathcal{V}\exp(t\Lambda)\mathcal{V}^{-1}||_E^2 \tag{3.17}$$

where $\mathcal{V}$ is the matrix containing the normalized eigenvectors and Λ is a matrix containing the eigenvalues in its diagonal. The above expression is very important to understand the difference between the present analysis and a classical stability analysis. The eigenvalues of Λ represent only part of G(t), and this will predict indeed the behavior of the disturbances only if the similarity transformation give by the eigenvectors does not change the value of the norm. This is true only when the eigenvectors are orthogonal to each other. System matrices resulting in non orthogonal eigenvectors are called non-normal matrices, whereas matrices with orthogonal eigenvectors are called normal. Schmid and Henningson (2001) summarized this by presenting upper and lower bounds (estimates) of the operator exponential norm. They showed that since the energy cannot decay at a faster rate than that given by the least stable eigenvalue the lower bound is given by this mode. For the upper bond, the eigenvalue decomposition 3.17 is used evoking the triangle inequality to split the norm

$$\exp(2t\lambda_{max}) \quad \leq \quad ||\exp(t\mathcal{L})||_E^2 \quad \leq \quad ||\mathcal{V}||_E^2||\mathcal{V}^{-1}||_E^2 \ \exp(2t\lambda_{max}). \tag{3.18}$$

From these bounds, two cases can be distinguished. If $||\mathcal{V}||_E^2||\mathcal{V}^{-1}||_E^2 = 1$ then the upper and lower bound are the same. In this case, the energy amplification is indeed

governed by the least stable eigenvalue λ_{max}. However, if this value is much larger then 1, the upper and lower bound differ significantly and the energy amplification is governed by the least stable eigenvalue only for asymptotic period of time.

To capture the short time dynamics, the energy growth rate is expanded around $t = 0^+$ using a Taylor-series. The initial growth rate is given by

$$\left.\frac{dG}{dt}\right|_{t=0^+} = \frac{\langle \tilde{\mathbf{q}}_\mathbf{0}, (\mathcal{L} + \mathcal{L}^H)\tilde{\mathbf{q}}_\mathbf{0}\rangle}{\tilde{\mathbf{q}}_\mathbf{0}, \tilde{\mathbf{q}}_\mathbf{0}} = \lambda_{max}(\mathcal{L} + \mathcal{L}^H) \tag{3.19}$$

where $(\mathcal{L} + \mathcal{L}^H)$ is hermitian. The full calculation is showed by Farrell and Ioannou (1996), Schmid and Henningson (2001) and Trefethen and Embree (2005). The slope of G(t) at $t = 0^+$ is given by the largest eigenvalue of $(\mathcal{L}+\mathcal{L}^H)$ as addressed in (3.19). This quantity is known as the numerical abscissa. This expression can be further generalized using the concept of numerical range or field of values. Following a similar procedure:

$$\frac{d}{dt}||\tilde{\mathbf{q}}||_E^2 = \left\langle \frac{d}{dt}\tilde{\mathbf{q}}, \tilde{\mathbf{q}} \right\rangle_E + \left\langle \tilde{\mathbf{q}}, \frac{d}{dt}\tilde{\mathbf{q}} \right\rangle_E = 2\Re\{\langle \mathcal{L}\tilde{\mathbf{q}}, \tilde{\mathbf{q}}\rangle_E\}. \tag{3.20}$$

This establishes the set of all Rayleigh quotients of $\mathcal{L}$ in the complex plane. The maximum real part of the numerical range is equivalent to the numerical abscissa. Thus, the slope of G(t) at $t = 0^+$ corresponds to the maximum protrusion of the numerical range into the unstable half-plane. Two important properties of the numerical range can be addressed. The numerical range is convex and, for normal $\mathcal{L}$, it is simply the convex hull of the spectrum. To summarize, for non-normal stability problems, the numerical range (abscissa) governs the very short time behavior whereas the least stable eigenvalue governs the long time behavior.

For intermediate time, the amount of maximum transient growth can be approximated by the ϵ-pseudospectrum. The ϵ-pseudospectra can be defined as the set in the complex plane, parameterized by ϵ, where the resolvent norm is larger than the inverse of ϵ. Measuring how far the contours of this norm extend into the unstable half-plane, indicates a lower bound for the maximum achievable transient growth in time. Trefethen and Embree (2005) defined a constant $\mathcal{K}$, known as the Kreiss constant, used to determine this lower band as $max_{t>0}\ G(t) \geq \mathcal{K}^2$.

The concepts explained here are better understood by calculating the spectrum, numerical range and the ϵ-pseudospectrum for the two-dimensional plane Poiseuille flow and the results can be seen in Fig. 3.3. The eigenvalues are displayed as blued dots, and for the parameters chosen, they are all asymptotically stable (driven by the least stable eigenvalue). The boundary of numerical range is indicated in red and it extends into the unstable half-plane, showing that transient growth is expect for small times. The red dot represents the numerical abscissa, which measures the maximum protrusion of the numerical range into the unstable half-plane. The numerical abscissa gives the slope of the initial maximum energy growth G(t) as presented in (3.19). Finally,

the square of the Kreiss constant ($\mathcal{K}^2$), indicated by a black dot, gives a lower estimate for the peak of energy amplification.

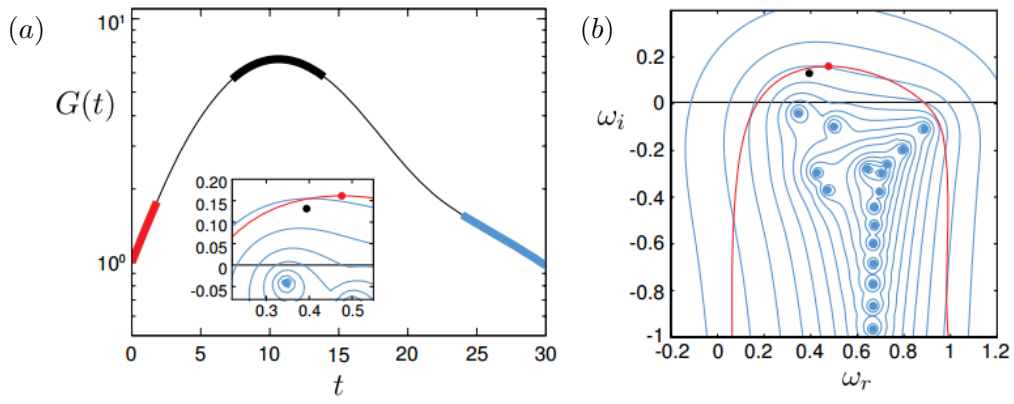

Figure 3.3: Transient growth of disturbance energy for the two-dimensional plane Poiseuille flow at $Re = 10^3$ and $\alpha = 1$. (a) Energy growth as functions of time. (b) Contour plot (blue lines) of the resolvent norm in the complex plane (Schmid 2007).

Another interpretation of the resolvent norm comes in the form of eigenvalue sensitivity. For a well-posed system, it is expected that small disturbances have a minimum effect. Disturbing the matrix exponential $\mathcal{L}$ by random matrices of small norm and estimating the effect on the eigenvalues show that resolvent contours contain eigenvalues of the disturbed matrix. Therefore, highly sensitive eigenvalues are often the first sign of non-normality.

3.3.2 Definition of the energy norm

Recapitulating the start of the analysis, (3.15) requires the definition of an inner product and its associated norm. These quantities constitute the fundamental measure and orthogonality describing the transient behavior. As pointed out by Hanifi et al. (1996), the energy density of a disturbance is a natural and physically meaningful measure of its size in the context of an incompressible flow. However, no obvious choice exists when dealing with compressible flows. For this reason, they re-derived the norm proposed by Mack (1969) in the context of modal instability, requiring pressure work to be conservative. Chu (1965) also described this energy norm, and the possibility to use different disturbance vectors $\tilde{\mathbf{q}}$ in primitive variables. Mathematically, the inner product can be written in a two-dimensional generalized framework of reference as

$$(\tilde{\mathbf{q}}_\mathbf{i}, \tilde{\mathbf{q}}_\mathbf{j}) = \int_0^\infty \int_0^\infty \tilde{\mathbf{q}}_\mathbf{i}^H \mathcal{M} \tilde{\mathbf{q}}_\mathbf{j} \; J \; dy \; dz \tag{3.21}$$

where J is the Jacobian of the coordinate transformation. The associated norm is

$$2E = (\tilde{\mathbf{q}}, \tilde{\mathbf{q}}) = ||\tilde{\mathbf{q}}||_E^2 \tag{3.22}$$

with

$$\mathcal{M} = \text{diag}\left(\bar{\rho}, \bar{\rho}, \bar{\rho}, \frac{\bar{T}}{\bar{\rho}\gamma M^2}, \frac{\bar{\rho}}{\gamma(\gamma-1)\bar{T}M^2}\right). \tag{3.23}$$

with the overbar indicating base flow quantities. The relation between the above energy norm and the standard Euclidean L_2 norm can be established by the following transformation (Reddy and Henningson 1993, Schmid and Henningson 2001, Trefethen and Embree 2005):

$$E(\tilde{\mathbf{q}}) = ||\tilde{\mathbf{q}}||_E^2 = \langle \tilde{\mathbf{q}}, \tilde{\mathbf{q}} \rangle_E = \tilde{\mathbf{q}}^H \mathcal{M} \tilde{\mathbf{q}} = \tilde{\mathbf{q}}^H F^H F \tilde{\mathbf{q}} = \langle F\tilde{\mathbf{q}}, F\tilde{\mathbf{q}} \rangle_2 = ||F\tilde{\mathbf{q}}||_2^2. \tag{3.24}$$

The energy weight matrix $\mathcal{M}$ is defined in (3.23). This matrix is positive definite since it contains positive quantities (energy norm). Thus, it can be decomposed via a Cholesky decomposition, generating F and F^H. The energy norm of the disturbance is then equivalent to taking the Euclidean L_2 norm of the vector $F\tilde{\mathbf{q}}$. For matrices, using the definition of a vector-induced norm

$$||\mathcal{L}||_E = \underset{\tilde{\mathbf{q}}}{max} \frac{||\mathcal{L}\tilde{\mathbf{q}}||_E}{||\tilde{\mathbf{q}}||_E} = \underset{\tilde{\mathbf{q}}}{max} \frac{||F\mathcal{L}F^{-1}F\tilde{\mathbf{q}}||_2}{||F\tilde{\mathbf{q}}||_2} = ||F\mathcal{L}F^{-1}||_2. \tag{3.25}$$

Therefore, for matrices, a simple similarity transformation using the Cholesky decomposition relates the energy norm to the Euclidean L_2 norm.

3.4 Computation of transient energy growth

In order to address nonmodal linear local and two-dimensional instability, the linearized governing equations (3.13) are written for an expansion of the vector quantities $\tilde{\mathbf{q}}$ which is inhomogeneous in the spatial directions z, and y, while it is treated as homogeneous along the third spatial direction x. Explicitly, the Ansatz employed is

$$\tilde{\mathbf{q}}(x, y, z, t) = \hat{\mathbf{q}}(z, y)\ e^{i(\alpha x - \omega t)}, \tag{3.26}$$

where α is a real wavenumber along the x direction, associated with a streamwise periodicity length, $L_x = 2\pi/\alpha$ and ω is a complex eigenvalue, obtained from solution of the complex non-symmetric generalised eigenvalue problem

$$\mathcal{A}\hat{\mathbf{q}} = \omega\mathcal{B}\hat{\mathbf{q}}, \tag{3.27}$$

shown in eq. (2.19) with coefficients presented in appendix B.
It is also noted that the linear operator $\mathcal{L}$ defined in (3.13) is a shorthand notation for

$$\mathcal{L} = \mathcal{B}^{-1}\mathcal{A}. \tag{3.28}$$

The BiGlobal linear stability equations can be reduced to the well-known linear Parabolized Stability Equations (PSE) that govern the instabilities of the boundary layer, derived and solved by Pralits et al. (2000), when the assumption of weak dependence of the underlying base flow on one of the two resolved spatial coordinates is made. As shown in a number of studies in the incompressible limit (e.g. Alizard and Robinet 2007, Theofilis 2017) the BiGlobal linear stability equations and the linear PSE lead to identical results when initialised with consistent inflow boundary conditions for the flow perturbations.

In this thesis, a temporal analysis is chosen and the flow is classified as linearly unstable if the imaginary part of the eigenvalue ω is positive. Since a decision about the scalar product and norm has already been made, the transient growth analysis can be further investigated. Restricting the analysis to the space spanned by the first N eigenfunctions of (3.27)

$$span\{\hat{\mathbf{q}}_1, \hat{\mathbf{q}}_2, \hat{\mathbf{q}}_3, ..., \hat{\mathbf{q}}_N\} \tag{3.29}$$

the state vector $\tilde{\mathbf{q}}$ can be expressed in terms of this basis:

$$\tilde{\mathbf{q}} = \sum_{k=1}^{N} \mathcal{K}_k(\tau)\hat{\mathbf{q}}_k, \tag{3.30}$$

where

$$\mathcal{K}_k(\tau) = \mathcal{K}_k(0)\ \exp(-i\omega_k\tau) \tag{3.31}$$

and $\mathcal{K}_k$ are time-dependent expansion coefficients. Thus, the eigenvalues represent the linear evolution operator projected onto the space spanned by the first N eigenvectors. Restricting the transient growth analysis to this space and applying the scalar product and the energy norm defined previously leads to

$$G(\tau) = G(\alpha, Re, M, \tau) = \underset{\tilde{\mathbf{q}}_0}{max}\frac{||\tilde{\mathbf{q}}(\tau)||_E^2}{||\tilde{\mathbf{q}}(0)||_E^2} = ||\exp(-i\tau\mathcal{B}^{-1}\mathcal{A})||_E^2 = ||F\Lambda F^{-1}||_2^2, \tag{3.32}$$

where

$$\Lambda = \mathrm{diag}(\exp(-i\tau\omega_1), \exp(-i\tau\omega_2), ..., \exp(-i\tau\omega_N)), \qquad \mathcal{F} = F^H F, \tag{3.33}$$

and $\mathcal{F}$ is defined as the scalar product presented in (3.21). The maximum gain is thus obtained as the square of the largest singular value (e.g Taira et al. 2017).

3.5 Computation of linear optimal disturbances

In non-normal systems exhibiting algebraic energy growth, it is interesting to compute the initial condition that maximizes energy amplification at early times, $G_{opt} \equiv G(\tau_{\mathrm{opt}})$.

This initial condition can be different for different time and the resulting curve $G(t)$ can be seen as the envelope of the energy evolution over all individual initial conditions. In order to determine the initial condition that leads to maximum amplification at a given time, τ_{opt}, a singular value decomposition (SVD) of the expression in (3.32) can be performed,

$$\mathcal{C}V = U\Sigma, \tag{3.34}$$

where $\mathcal{C} = F\Lambda F^{-1}$ and V and U are unitary matrices with ortho-normalized columns and Σ is a diagonal matrix consisting of the singular values, ordered in size, i.e. $\sigma_1 \geq \sigma_2 \geq ...\sigma_N$. The dominant singular value is equivalent to the energy norm of $\exp(-\tau\omega_k)$. Thus, extracting the principal column vectors of V and U leads to

$$\mathcal{C}v_1 = \sigma_1 u_1. \tag{3.35}$$

As pointed out by Schmid and Henningson (1994), this equation can be interpreted as a mapping $\mathcal{C}$ of an input vector v_1 onto an output vector u_1 stretched by a factor of the largest singular value; see also the related discussion by Taira et al. (2017). Therefore, the optimal initial condition can be obtained from the principal right singular value vector. Finally, to recover the initial expansion coefficients of equation (3.30), which give the optimal disturbances associated with a particular amplification, it is necessary to write v_1 in the basis $\{\hat{\mathbf{q}}_1, ..., \hat{\mathbf{q}}_N\}$ as:

$$v_1 = F\mathcal{K}_0. \tag{3.36}$$

In summary, the computational steps required to recover the optimal initial condition starts with a Singular Value Decomposition of the matrix exponential evaluated at different times τ. The matrix exponential is calculated using an eigenvalue decomposition. Following this, the energy growth $G(\tau)$ can be computed after transforming the energy norm to a standard euclidean norm. In what follows, τ_{opt} can be identified as the time where $G_{\text{opt}} = G(\tau = \tau_{\text{opt}})$ acquires its largest value at short times and $G_\infty = G(\tau \to \infty)$ for the maximum value at asymptotically large times.

Chapter 4

Numerical implementation

In order to investigate the modal and nonmodal behaviour of linear fluid flow instabilities, a new code was developed by the author. The *Li*near *G*lobal instability for *H*ypersonic *T*ransition (*LiGHT*) code was developed in Fortran and it is suite of subroutines for the massively parallel solution of multi-dimensional complex non-symmetric eigenvalue problems (EVP) and Singular Value Decomposition (SVD) problems arising in global linear fluid flow instability. In the high supersonic and hypersonic regimes of interest, and in using high-order spatial discretisation, these eigenvalue problems result in dense matrices. Therefore, the ScaLAPACK library (Blackford et al. 1997), available as part of vendor-optimized libraries on most modern supercomputers, including the UK open research supercomputer Archer[1]. is used to perform a full distributed LU-decomposition, as required by the shift-and-invert strategy implemented in equation (4.28) which promote physically-interesting and suppress spurious eigenmodes. The distribution of the matrices, the iterative generation of Krylov subspaces, the computation of the Ritz vectors and the Singular Value Decomposition can all be performed by linear algebra operations distributed over the available processors, in either real or complex arithmetic. Full numerical implementation is detailed next.

4.1 Spatial discretisation using spectral collocation

4.1.1 Non-Periodic discretisation

Spatial discretisation of the linearized Navier-Stokes operators have been demonstrated in the literature using low- or high-order finite-difference, finite-volume, finite element, spectral collocation or spectral element methods. Invariably, low-order methods require high-resolution grids to obtain reliable results. A high-order method is preferable in a matrix-forming context, such as that used presently, unless sparse matrix storage is used. On the other hand, sparse storage is not exploited presently since the matrix multiplication (4.33) on which the formation of the SVD matrix is based would destroy

[1] https://www.archer.ac.uk

any sparsity pattern that matrix $\mathbf{C}$ or its adjoint $\mathbf{C}^*$ may have. On account of these considerations, spatial discretisation is performed by spectral collocation methods based on the standard Chebyshev Gauss-Lobatto (CGL) points (Canuto et al. 1988, Boyd 1989)

$$y_j = \cos\left(\frac{\pi j}{N}\right), \qquad j = 0, .., N, \tag{4.1}$$

defined in the standard interval [-1,1]. This numerical discretisation method is known to offer the highest resolution power on the lowest number of discretisation nodes compared with any alternative (e.g. Paredes et al. 2013).

A variety of mappings are used to transfer data from the standard CGL domain to the physical domain of interest. Examples include a simple linear mapping or boundary-layer types of mappings that cluster points near a wall, such as the well-tested analytical transformation

$$\eta_j = a\frac{1+y_j}{b-y_j}, \tag{4.2}$$

where

$$a = \frac{\eta_j \eta_{max}}{\eta_{max} - 2\eta_j} \qquad \text{and} \qquad b = 1 + \frac{2a}{\eta_{max}}.$$

An arbitrary function defined in the CGL grid can be approximated by its Chebyshev expansion:

$$f(y) = \sum_{n=0}^{N} a_n \mathcal{T}_n(y) \tag{4.3}$$

with $\mathcal{T}_n(y) = \cos(n\ \cos^{-1}(y))$.

Differentiation on the CGL grid can be performed by application of the collocation differentiation matrix, $\mathcal{D}$

$$\left(\frac{df}{dy}\right)_i = \sum_{j=0}^{N} \mathcal{D}_{ij} f_j, \tag{4.4}$$

where

$$\mathcal{D}_{i,j} = \begin{cases} \frac{2N^2+1}{6}, & i = j = 0, \\ -\frac{y_j}{2(1-y_j^2)}, & i = j \neq 0, N \\ \frac{\overline{c}_i}{\overline{c}_j}\frac{(-1)^{i+j}}{y_i - y_j}, & i \neq j \\ -\frac{2N^2+1}{6}, & i = j = N \end{cases} \tag{4.5}$$

where

$$\overline{c}_j = \begin{cases} 2, & j = 0 \text{ or } j = N, \\ 1, & 1 \leq j \leq N-1 \end{cases} \tag{4.6}$$

Introducing the inner product

$$(f,g) = \sum_{i=0}^{N} b_i f(y_i)\ g(y_i), \tag{4.7}$$

with b_0=b_N=1/2, b_i=1 for the interval $0 < i < N$ and with y_i as the location of the extrema of the N^{th} Chebyshev polynomial

$$y_i = \cos\left(\frac{i\pi}{N}\right), \qquad i = 0, 1, ...N, \tag{4.8}$$

it can be shown that

$$(T_m(y), T_n(y)) = \begin{cases} 0, & \text{if } m \neq n, \\ N, & \text{if } m = n = 0 \text{ and } N, \\ \frac{N}{2}, & \text{if } m = n \neq 0 \text{ and } N. \end{cases} \tag{4.9}$$

Thereby, the coefficients a_n are defined as

$$a_n = \frac{c_n}{N} \sum_{i=0}^{N} b_i f(y_i) T_n(y_i) \tag{4.10}$$

where c_0=c_N=1 and c_n=2 for the interval $0 < n < N$. The function can thus be integrated with spectral accuracy using the relation

$$\int_{-1}^{1} f(y)dy = \sum_{i=0}^{N} f(y_i)\mathcal{W}(y_i), \tag{4.11}$$

where $\mathcal{W}$ is the Chebyshev integral weight function and it can be found as

$$f(y) = \sum_{n=0}^{N} a_n T_n(y) = \sum_{n=0}^{N} c_n T_n(y) \sum_{i=0}^{N} \frac{b_i}{N}\ f(y_i) T_n(y_i). \tag{4.12}$$

Integrating the above expression over y leads to

$$\int_{-1}^{1} f(y)dy = \frac{1}{N}\ \sum_{i=0}^{N} b_i f(y_i) \sum_{n=0}^{N} c_n T_n(y_i) \int_{-1}^{1} T_n(y)dy. \tag{4.13}$$

Finally, one can write

$$\int_{-1}^{1} T_n(y)dy = \begin{cases} 0, & \text{if } n \text{ is odd}, \\ \frac{2}{(1-n^2)}, & \text{if } n \text{ is even}\ . \end{cases} \tag{4.14}$$

with

$$\mathcal{W}(y_i) = \frac{b_i}{N}\ \left\{2 + \sum_{n=2}^{N} c_n \frac{(1+(-1)^n)}{(1-n^2)} \cos\left(\frac{ni\pi}{N}\right)\right\}. \tag{4.15}$$

This leads to an expression $\mathcal{W}$ containing the integration weights to compute the integral on the interval [-1,1]. However, since mapping is used to map the physical domain onto the CGL interval, equation (4.15) is replaced by

$$\mathcal{W}(y_i) = \frac{b_i}{N}\sum_{n=0}^{N} c_n \cos\left(\frac{ni\pi}{N}\right)\int_{-1}^{1} T_n(y)\frac{d\eta}{dy}dy. \tag{4.16}$$

4.1.2 Periodic discretisation

In some flows, the use of periodic spatial discretisation can be addressed by Fourier spectral collocation method. Canuto et al. (1988) present the derivative matrix coefficients for both even or odd grid points. In this work, an even number of points is considered with a spacing of $h = \frac{2\pi}{N}$. Differentiation on the periodic grid can then be performed by applying the Fourier collocation differentiation matrix

$$\mathcal{D}_{i,j} = \begin{cases} 0, & i = j \\ \\ \frac{1}{2}(-1)^{(i+j)}\cot\left[(i-j)\frac{\pi}{(N+1)}\right], & i \neq j \end{cases} \tag{4.17}$$

with i and j from $[0, 1, ...N]$.

4.2 Formation of the discretised LNSE using the Kronecker product

The Kronecker product plays a key role in forming the matrix eigenvalue problem in multiple spatial dimensions. Its associative multiplication property makes the extension of the Kronecker product to higher dimensions straightforward. It also permits a simple construction of the linearised Navier-Stokes operator, or the spatial discretisation of any linear system, including introduction of the base flow and its derivatives, as will be discussed shortly.

Formation of the linearised operator is also transparent to the details of the differentiation matrix used, making a Kronecker-product based strategy both flexible and general: distinct spatial differentiation schemes and the corresponding differentiation matrices may be defined independently along each direction, using the Kronecker product to construct tensor product grids in two or three spatial dimensions. In case a spatial direction is inhomogeneous, it may be discretised by typical (Chebyshev or Legendre) spectral collocation differentiation matrices based on Jacobi polynomials. However, any differentiation operator that can be written in matrix-forming, such as low- or high order standard or compact finite-differences, may be used. If the spatial direction in question is homogeneous, Fourier collocation derivative matrices may be used to discretise it, although a flow instability problem in which homogeneous spatial directions exist can be reduced to one described by differential equations of lower order.

In general, if $\mathbf{A} \in \mathbb{C}^{P\times Q}, \quad \mathbf{B} \in \mathbb{C}^{R\times S}$, the Kronecker product $\mathbf{A} \otimes \mathbf{B}$ is defined as the rectangular matrix $\mathbf{C} \in \mathbb{C}^{PR\times QS}$ (Theofilis 2020)

$$\mathbf{C} \equiv \mathbf{A} \otimes \mathbf{B} = \begin{pmatrix} a_{11}\mathbf{B} & a_{12}\mathbf{B} & \cdots & a_{1q}\mathbf{B} \\ a_{21}\mathbf{B} & a_{22}\mathbf{B} & \cdots & a_{2q}\mathbf{B} \\ \vdots & \vdots & \ddots & \vdots \\ a_{p1}\mathbf{B} & a_{p2}\mathbf{B} & \cdots & a_{pq}\mathbf{B} \end{pmatrix}.$$

In compact form, the elements $a_{p,q}$, $b_{r,s}$ and $c_{\mu,\nu}$ of matrices $\mathbf{A}, \mathbf{B}$ and $\mathbf{C}$ are related by the identity

$$c_{\mu,\nu} = c_{\{(p,q);(r,s)\}} = c_{R(p-1)+r,S(q-1)+s} = a_{p,q}b_{r,s}. \tag{4.18}$$

indicating that element (μ, ν) is found at position (r, s) of block (p, q). The following properties are of interest, where $+$ is the common addition:

$$\mathbf{A} \otimes (\mathbf{B} + \mathbf{C}) = \mathbf{A} \otimes \mathbf{B} + \mathbf{A} \otimes \mathbf{C}, \tag{4.19}$$

$$(\mathbf{A} + \mathbf{B}) \otimes \mathbf{C} = \mathbf{A} \otimes \mathbf{C} + \mathbf{B} \otimes \mathbf{C}, \tag{4.20}$$

$$(k\mathbf{A}) \otimes \mathbf{B} = \mathbf{A} \otimes (k\mathbf{B}) = k(\mathbf{A} \otimes \mathbf{B}), \tag{4.21}$$

$$(\mathbf{A} \otimes \mathbf{B}) \otimes \mathbf{C} = \mathbf{A} \otimes (\mathbf{B} \otimes \mathbf{C}) \tag{4.22}$$

In the particular case of square matrices $\mathbf{A}$ and $\mathbf{B}$ with leading dimensions P and R respectively, Kronecker addition, $\oplus$, is defined as

$$\mathbf{A} \oplus \mathbf{B} = \mathbf{A} \otimes \mathbf{I}_R + \mathbf{I}_P \otimes \mathbf{B}. \tag{4.23}$$

4.2.1 Matrix-forming construction

Spectral collocation can be used to discretise the multi-dimensional EVP or SVD from the modal and nonmodal analysis, respectively. A key element in a matrix forming framework is the use of the Kronecker product. If (N_x, N_y, N_z) nodes discretise the (x, y, z) spatial directions and differentiation along these directions is performed by matrices $D_x \in C^{N_x\times N_x}$, $D_y \in C^{N_y\times N_y}$ and $D_z \in C^{N_z\times N_z}$, then coupled discretisation of $\mathcal{L}_{1d}, \mathcal{L}_{2d}$ and $\mathcal{L}_{3d}$ may be represented by a matrix $\mathbf{A} \in C^{N_y\times N_y}$, $C^{(N_x\times N_y)\times(N_x\times N_y)}$, and $C^{(N_x\times N_y\times N_z)\times(N_x\times N_y\times N_z)}$, respectively. The building block for $\mathcal{L}_{1d}$ is D_y itself, while those for $\mathcal{L}_{2d}$ and $\mathcal{L}_{3D}$ are the Kronecker products $D_x \otimes D_y$ and $D_x \otimes D_y \otimes D_z$, respectively. In other words, the size of $\mathbf{A}$ pertinent to one-dimensional eigenvalue problem is $16 \times (N_y)^2$, while that of two- and three-dimensional are $16(N_x \times N_y)^2$ and $16(N_x \times N_y \times N_z)^2$, respectively. The pre-multiplying factor 4^2 arises from the number of equations solved in incompressible flow and becomes 5^2 if instability of compressible flow is addressed and $(5 + m)^2$ in hypersonic flow in which m equations are used to describe chemistry.

4.3 Boundary conditions

The eigenvalue problem (EVP) solution must be complemented with the appropriate choice of the boundary conditions for all the flow disturbance variables. In the *LiGHT* code, the boundary conditions are programmed in the computational domain (ξ, η, ζ). The standard homogeneous Dirichlet boundary condition is programmed to account for disturbances that decay far away from the region of interest and for no-slip/no-penetration conditions. Moreover, in flows where the presence of the shock defines a boundary, all perturbations are forced to decay through the imposition of a sponge region within which a smooth function artificially decreases the local Reynolds number (Meliga et al. 2012, Paredes et al. 2016) such that homogeneous Dirichlet boundary conditions can be imposed at this boundary. Neumann boundary conditions ($\frac{\partial}{\partial \chi} = 0$, where $\chi = (\xi, \eta, \zeta)$) are also programmed as well as Laplace boundary conditions ($\frac{\partial^2}{\partial \chi^2} = 0$). With these conditions programmed, symmetries of the flow can be exploited (if any), and symmetric or antisymmetric boundary conditions can be applied to reduce computational coast. In order to account for disturbances exiting the domain, linear extrapolation of the points inside the computational domain is programmed.

4.3.1 The linearized pressure Poisson equation

In a matrix-forming approach using primitive variables on which the *LiGHT* code is based, the appropriated choice of the pressure boundary condition is necessary when dealing with incompressible flows. Theofilis (2017) derived a set of independent of the field equations provided by the pressure Poisson equation.

$$\Delta p + \nabla.((\mathbf{V}.\nabla)\mathbf{V}) = 0. \tag{4.24}$$

After linearization and substitution of the Ansatz (2.19) the two-dimensional linearized pressure Poisson equation (LPPE) can be obtained in Cartesian form as:

$$\begin{aligned}\left(-\alpha^2 + \frac{\partial^2}{\partial y^2} + \frac{\partial^2}{\partial z^2}\right)\hat{p} + 2\left(\frac{\partial \bar{u}}{\partial y} i\alpha + \frac{\partial \bar{v}}{\partial y}\frac{\partial}{\partial y} + \frac{\partial \bar{w}}{\partial y}\frac{\partial}{\partial z}\right)\hat{v} + \\ 2\left(\frac{\partial \bar{u}}{\partial z} i\alpha + \frac{\partial \bar{v}}{\partial z}\frac{\partial}{\partial y} + \frac{\partial \bar{w}}{\partial z}\frac{\partial}{\partial z}\right)\hat{w} = 0.\end{aligned} \tag{4.25}$$

Since first- and second-order derivatives appears in the LPPE (4.25), both equations (2.25) and (2.29) are used to transform the LPPE to computational domain. The resulting equation reads:

$$\begin{aligned}\Bigg(-i\alpha + (\eta_y^2+\eta_z^2)\frac{\partial^2}{\partial\eta^2} + (\zeta_y^2+\zeta_z^2)\frac{\partial^2}{\partial\zeta^2} + 2(\eta_y\zeta_y+\eta_z\zeta_z)\frac{\partial^2}{\partial\eta\partial\zeta} + \\ (y2+z2)\frac{\partial}{\partial\eta} + (y3+z3)\frac{\partial}{\partial\zeta}\Bigg)\hat{p} + \\ 2\Bigg(\frac{\partial\bar{u}}{\partial y}i\alpha + (\frac{\partial\bar{v}}{\partial y}\eta_y + \frac{\partial\bar{w}}{\partial y}\eta_z) + (\frac{\partial\bar{v}}{\partial y}\zeta_y + \frac{\partial\bar{w}}{\partial y}\zeta_z)\Bigg)\hat{v} + \\ 2\Bigg(\frac{\partial\bar{u}}{\partial z}i\alpha + (\frac{\partial\bar{v}}{\partial z}\eta_y + \frac{\partial\bar{w}}{\partial z}\eta_z) + (\frac{\partial\bar{v}}{\partial z}\zeta_y + \frac{\partial\bar{w}}{\partial z}\zeta_z)\Bigg)\hat{w} = 0,\end{aligned} \tag{4.26}$$

where

$$\begin{aligned} y2 &= J\left[\frac{\partial}{\partial\eta}\left(\frac{\eta_y^2}{J}\right) + \frac{\partial}{\partial\zeta}\left(\frac{\eta_y\zeta_y}{J}\right)\right]\frac{\partial}{\partial\eta} \\ z2 &= J\left[\frac{\partial}{\partial\eta}\left(\frac{\eta_y\zeta_y}{J}\right) + \frac{\partial}{\partial\zeta}\left(\frac{\zeta_y^2}{J}\right)\right]\frac{\partial}{\partial\zeta} \\ y3 &= J\left[\frac{\partial}{\partial\eta}\left(\frac{\eta_z^2}{J}\right) + \frac{\partial}{\partial\zeta}\left(\frac{\eta_z\zeta_z}{J}\right)\right]\frac{\partial}{\partial\eta} \\ z3 &= J\left[\frac{\partial}{\partial\eta}\left(\frac{\eta_z\zeta_z}{J}\right) + \frac{\partial}{\partial\zeta}\left(\frac{\zeta_z^2}{J}\right)\right]\frac{\partial}{\partial\zeta}. \end{aligned} \tag{4.27}$$

It is important to notice that these conditions are independent of the Reynolds number compared to the usual pressure compatibility (PC) boundary conditions.

4.4 Iterative eigenvalue problem computation

The iterative numerical solution of the large-scale eigenvalue problems encountered in this analysis implements Krylov subspace iteration based on serial and parallel (to be discussed shortly) versions of the Arnoldi algorithm. This approach delivers several eigenvalues in the vicinity of a specific target eigenvalue and is substantially less expensive than the classic QZ method (Arnoldi 1951, Saad 1980). The number of eigenvalues delivered is determined by the Krylov subspace dimension, a free parameter in the analysis, whose limit is the leading dimension of matrices **A** and **B**. In this eigenvalue problem, a so-called shift-and-invert strategy is also implemented, in which the problem solved is (Theofilis 2003)

$$\mathbf{CX} = \mu\mathbf{X}, \qquad C = (\mathbf{A}-\sigma\mathbf{B})^{-1}\mathbf{B}, \qquad \mu = \frac{1}{\omega-\sigma} \tag{4.28}$$

where μ is the new eigenvalue searched, ω is the shift parameter, and the Krylov subspace is constructed by

$$K_m = span(\mathbf{v}, C.\mathbf{v}, C^2.\mathbf{v}, ..., C^{m-1}.\mathbf{v}) \tag{4.29}$$

where m is the Krylov subspace dimension.

The vectors $\mathbf{v}$ forming the basis are ordered by columns into the matrix $\mathbf{V}_m$. The projection of the linear operator on that basis yields the relation

$$\mathbf{V}_m^H C \mathbf{V}_m = \mathbf{H}_m \tag{4.30}$$

where $\mathbf{H}_m$ is an upper triangular Hessenberg matrix. The restrictions of the eigenvalue problem to the Krylov subspace K_m is

$$\mathbf{H}_m \mathbf{V}_m^H . \hat{\mathbf{q}} = \mu \mathbf{V}_m^H . \hat{\mathbf{q}} \tag{4.31}$$

The eigenvalues of the Hessenberg matrix $\mathbf{H}_m$ are approximations to the m largest eigenvalues of the original problem.
Concerning the eigenvectors, if $y_i^{(m)}$ is the eigenvector corresponding to the i-th eigenvalue of the $\mathbf{H}_m$ the corresponding approximation to the eigenvector of the original problem, known as Ritz vector, is

$$\hat{\mathbf{q}}_i = \mathbf{V}_m . \mathbf{y}^{(m)} \tag{4.32}$$

4.5 Singular Value Decomposition

The singular-value decomposition (SVD) is a generalization of the eigenvalue decomposition for positive semi-definite normal rectangular matrices. Its relevance to the problem at hand is that for any complex matrix $\mathbf{C}$, as defined in (4.28) a matrix $\mathbf{M}$ can be constructed using the adjoint (complex conjugate, transposed) matrix $\mathbf{C}^*$ as

$$\mathbf{M} = \mathbf{C}^* \mathbf{C}. \tag{4.33}$$

The SVD of a general $m \times n$ matrix $\mathbf{M}$ takes the form (Taira et al. 2017)

$$\mathbf{M} = \mathbf{U} \Sigma \mathbf{V}^*, \tag{4.34}$$

where U is an $m \times m$ unitary matrix, Σ is a diagonal $m \times n$ matrix with non-negative real numbers on the diagonal, V is an $n \times n$ unitary matrix and V^* is the conjugate transpose of V. The diagonal entries σ_i of Σ are known as the singular values of M and they are ordered in size, i.e. $\sigma_1 \geq \sigma_2 \geq ... \geq \sigma_n$. Also, it is important to notice that singular value decomposition is defined for all matrices (rectangular or square), unlike the more commonly used spectral decomposition in Linear Algebra. In contrast to the eigenvalue decomposition, the columns of V in the singular value decomposition, called the right singular vectors, always form an orthogonal set with no assumptions on the matrix $\mathbf{M}$. The columns of U are called the left singular vectors, and they also form an orthogonal set.
The Singular Value Decomposition can be understood in a simple geometrical two-dimensional example. If $\mathbf{M} = \mathbf{U} \Sigma \mathbf{V}^*$, then:

$$\begin{aligned} \mathbf{MV} &= (\mathbf{U}\Sigma\mathbf{V}^*)\mathbf{V} \\ \mathbf{MV} &= \mathbf{U}\Sigma I \\ \mathbf{MV} &= \mathbf{U}\Sigma \end{aligned} \tag{4.35}$$

where I is the identity matrix. Figure 4.1 shows an example of a unit circle linearly transformed by the matrix **M** to an ellipse. The entries of the pre-factor **U** correspond to the minor and major axis of the ellipse. On the other hand, $\mathbf{V}^*$ are the radius that gets mapped by the transformation to the ellipse axis.

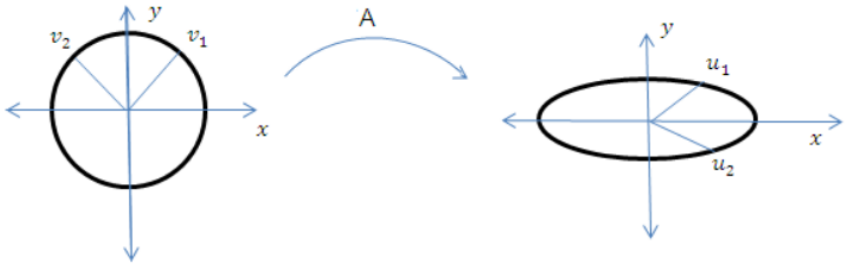

Figure 4.1: Geometric interpretation of the Singular Value Decomposition (Taira et al. 2017, Raghavendar and Dharmaiah 2017).

4.6 Parallelization strategy

The preceding discussion highlights the need for a distributed solution to large-scale global eigenvalue problems. The matrix-forming approach adopted in the present study alongside the use of high-order spectral collocation methods in the spatial discretisation of the inhomogeneous flow directions suggests that *off-the-shelf* parallelisation of the formed matrix using OpenMP libraries and multithreading (Paredes et al. 2013, 2016) may not be a viable approach, depending on the size of the matrices involved. Figure 4.2 shows two different sparsity patterns of the BiGlobal stability matrix A for (a) the case of a simple two-dimensional Cartesian metric, as seen in problems such as the flow over an attachment-line and (b) a two-dimensional generalised coordinates as seen in the solution of the HIFiRE-5 elliptic cone model.

In the *LiGHT* code, the stability matrix A is treated as dense to switch between metrics easily. To do so, the matrix A can be distributed over a large number of processors, using the well-tested ScaLAPACK library (Blackford et al. 1997), which is optimized on native libraries available on supercomputers such as the UK National Supercomputing Service Archer[1]. Schematically, the process of distributing the matrix over n available processors and the implemented solution of the EVP is shown in figure

[1] https://www.archer.ac.uk

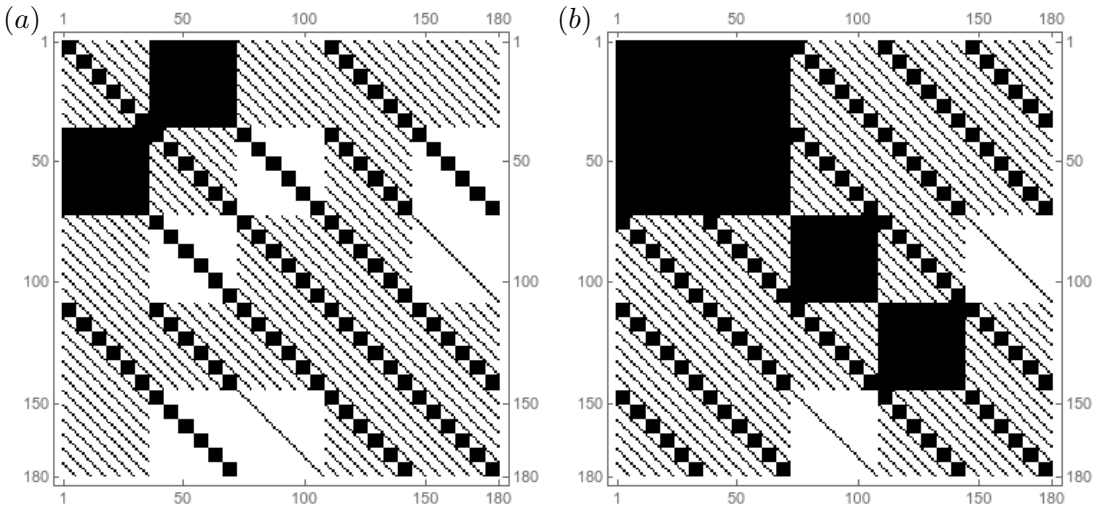

Figure 4.2: Sparsity patterns of the BiGlobal stability matrix: (a) two-dimensional Cartesian metric (Ex.: attachment-line flow (Gennaro et al. 2011)); (b) two-dimensional generalized metric (Ex: elliptic cone).

4.3. The controller (green) is responsible for initializing and distributing the matrices A and the necessary vectors (recall that matrix B is stored as a vector). The agent (red) are responsible for running the Arnoldi algorithm and sending the results back to the controller, where a serial eigenvalue routine from Lapack based on the QZ algorithm is used to recover the final results.

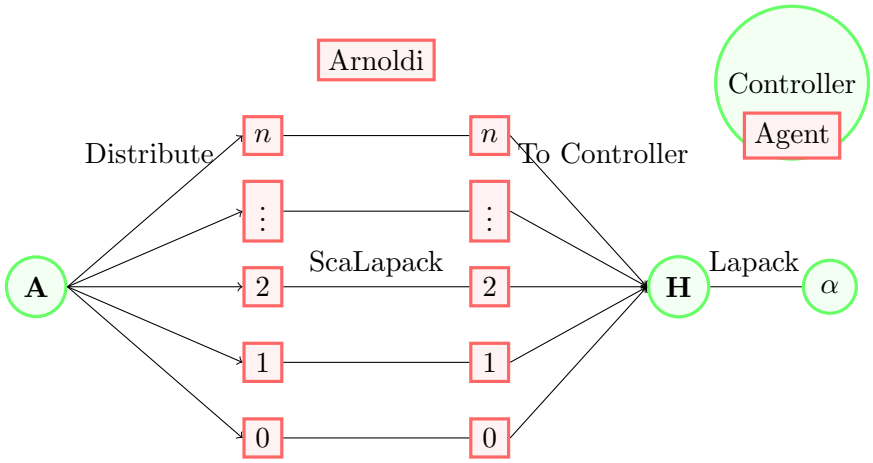

Figure 4.3: Scheme of matrix A distribution and the parallel solution of the Arnoldi algorithm with ScaLAPACK, followed by eigenvalue decomposition of the Hessenberg matrix H in a single node using Lapack.

In ScaLAPACK, the discretised block matrix generated is stored over several processors of a cluster, and, using distributed memory parallel computers, the maximum dimension of the problem is determined by the number of available processors. The two common issues in the matrix forming approach are expected to be alleviated with parallelization.

The first is the memory restriction due to the storage of the matrix. The second is the CPU time limitations imposed by a serial solution of the EVP. ScaLAPACK and PBLAS are used to perform linear algebra operations in parallel, while BLACS is used to set the communication (Blackford et al. 1997). These libraries have been documented to work scalable with dense matrices of leading dimension $O(10^5)$ on clusters featuring $O(10^4)$ processors (Borrill 1999).

ScaLAPACK is based on the BLACS layers, which handles MPI or PVM parallel communication and uses BLAS for linear algebra operations (PBLAS in the parallel form) (Theofilis 2007). Parallelization consists of three major steps. First, the BLACS library is initialized to be used in subsequent operations. Second, a rectangular processor grid is built using all available processors available. ScaLAPACK then creates an array descriptor vector for each global array and maps the global array elements among the processors following a two-dimensional block-cyclic distribution that gives the best load balance and maximum data locality of the ScaLAPACK algorithms (Blackford et al. 1997). The two-dimensional block-cyclic distribution is accomplished by dividing the global array into blocks with a specific number of rows and columns, given by a parameter so-called blocking factor (r), to be discussed shortly. This parameter can be different for rows and columns of an array, but normally, a unique value is used due to the square property of the matrix. The distribution algorithm works independently on rows and columns.

4.6.1 Block-cyclic element distribution

Following closely Theofilis (2020), let the (row, column) coordinates of an element of the (global) matrix be described by the pair of indices $(i_{\text{glob}}, j_{\text{glob}})$, with $0 \leq i_{\text{glob}} \leq M-1$ and $0 \leq j_{\text{glob}} \leq N-1$. The block-cyclic distribution scheme is discussed for a rectangular global matrix, $M \neq N$ because, although the eigenvalue problem is solved for square matrices, the singular value decomposition of matrices arising in the nonmodal global linear instability analysis is rectangular.

Let the number of available processes be arranged into a two-dimensional grid, $P \times Q$, and let (p, q) describe the coordinates of the processor within which global element $(i_{\text{glob}}, j_{\text{glob}})$ is found, with $0 \leq p < P-1$ and $0 \leq q < Q-1$. Again, the discussion of block-cyclic distribution is offered for $P \neq Q$, but the eigenvalue problem in ScaLAPACK will require $P = Q$.

Finally, let $r \times c$ be the row and column blocking factors, respectively, which determine the size of the blocks within each process, and let (b, d) be the local block coordinates within the process identified by the indices (p, q).

The local coordinates $(i_{\text{loc}}, j_{\text{loc}})$ of global element $(i_{\text{glob}}, j_{\text{glob}})$ within process (p, q) and block (b, d) are determined by the following mapping of the global index i_{glob} to a triplet $\langle p, b, i_{\text{loc}} \rangle$ and of global index j_{glob} to a triplet $\langle q, d, j_{\text{loc}} \rangle$, i.e.

$$(i_{\rm glob}, j_{\rm glob}) \;\; \mapsto \;\; \langle (p,q),(b,d),(i_{\rm loc}, j_{\rm loc})\rangle. \tag{4.36}$$

Here

$$(p,q) \;\; = \;\; \left(\left\lfloor \frac{i_{\rm glob}}{r} \right\rfloor \bmod (P), \left\lfloor \frac{j_{\rm glob}}{c} \right\rfloor \bmod (Q) \right), \tag{4.37}$$

$$(b,d) \;\; = \;\; \left(\left\lfloor \frac{i_{\rm glob}}{rP} \right\rfloor , \left\lfloor \frac{j_{\rm glob}}{cQ} \right\rfloor \right), \tag{4.38}$$

$$(i_{\rm loc}, j_{\rm loc}) \;\; = \;\; (i_{\rm glob} \bmod (r), j_{\rm glob} \bmod (c)), \tag{4.39}$$

$m \bmod (n)$ is the `modulo` function and $\lfloor m \rfloor$ is the integer `floor` function.
The inverse mapping of the triplet $\langle (p,q),(b,d),(i_{\rm loc}, j_{\rm loc})\rangle$ in the local coordinates to the global indices $(i_{\rm glob}, j_{\rm glob})$ is defined by

$$\langle (p,q),(b,d),(i_{\rm loc}, j_{\rm loc})\rangle \;\; \mapsto \;\; (r\,(p+bP)+i_{\rm loc}, c\,(q+dQ)+j_{\rm loc}) \tag{4.40}$$

$$\equiv \;\; (i_{\rm glob}, j_{\rm glob}) \tag{4.41}$$

An element $(i_{\rm glob}, j_{\rm glob})$ in a global rectangular matrix of dimension (M, N) acquires local coordinates $(i_{\rm loc}, j_{\rm loc})$ which depend on the number of processes, (P, Q), used to distribute the global matrix and on the (row, column) blocking factor values (r, c). Knowledge of these data permits computation of the local indices using equations (4.37-4.39). Conversely, if the local indices, as well as (P, Q) and (r, c) are known, equations (4.37-4.38) and (4.40) can be used to identify the global array indices pertinent to the element in question.
A simple example of block-cyclic distribution of a square array with leading dimension $M = N = 16$ over four processes arranged in a $(P, Q) = (2 \times 2)$ process grid and using a blocking factor $r = c = 5$ is shown in Fig. 4.4. The left figure shows the matrix elements as seen from a global perspective, while the right figure shows the elements held by each process, identified by a unique colour for each process.

4.6.2 Scalability study

The following results were computed on two different machines: a "small" cluster with 64 cores featuring an AMD Opteron 6366 HE processor with 1.8 GHz and 16 Mb Cache L3, 512 Gb RAM with maximum memory bandwidth 51.2 GB/s and a "large" cluster, namely the Copper Cray XE6m[2], with 460 nodes and 32 cores per node featuring an AMD Interlagos Opteron processor with 2.3 GHz and 16 Mb Cache L3, 60 GB of accessible memory per node and 51.2 GB/s of maximum memory bandwidth. The compiler used was GNU Fortran 4.8.3 (Red Hat 4.8.3-9).
The first task was to use the BLACS library to set the rectangular processor grid for instability analysis transparently to the cluster on which the code is running. The

[2]https://www.ors.hpc.mil

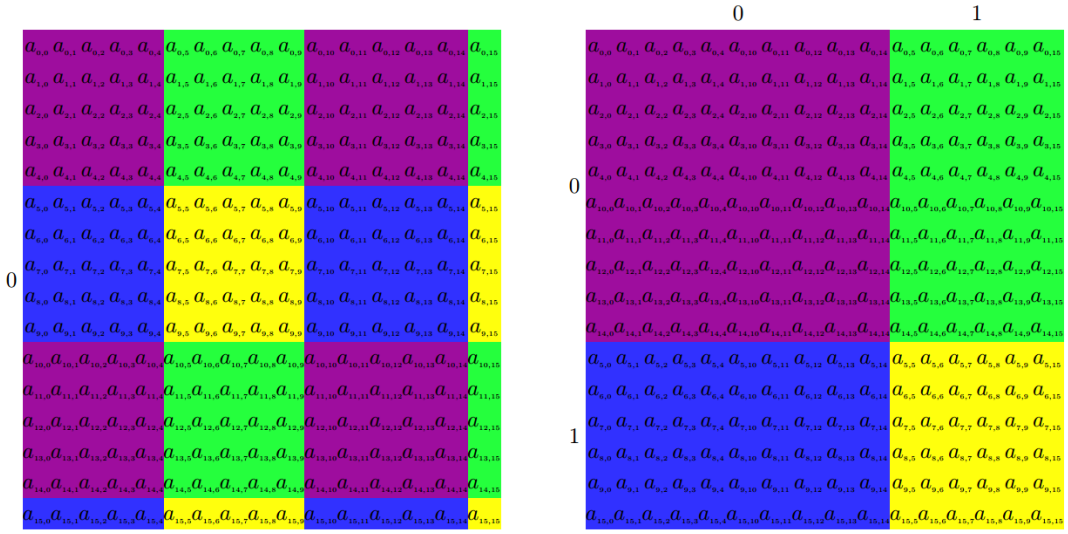

Figure 4.4: Distribution of a 16×16 array over a 2×2 processor grid using a block-cyclic scheme with a 5×5 blocking factor (Theofilis 2020).

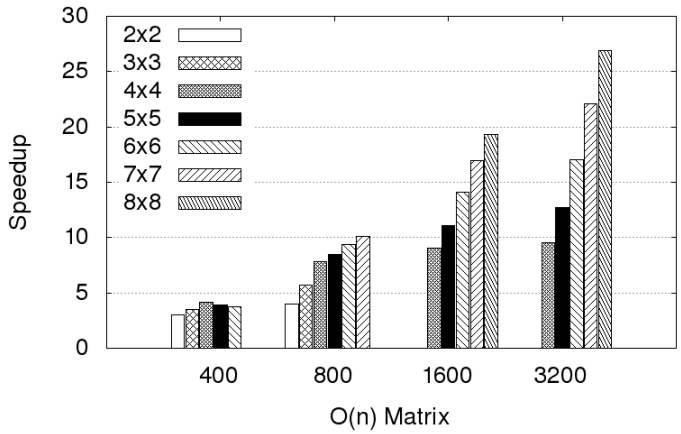

Figure 4.5: Speedup as function of the matrix order. The processors grid used are show in the graphic (Quintanilha Jr et al. 2017).

objective here was to distribute pieces of each matrix over the processors in the grid in an adequate manner, such that each process will always be busy doing roughly an equal number of calculations, meaning that load balancing is achieved (Blackford et al. 1997).

The local linear stability problem was first performed in the small cluster. The number of processors used was based on the processor grid (2x2, 3x3, 4x4, 5x5, 6x6, 7x7 and 8x8). Figure 4.5 shows a comparison between the number of processors by matrix length. As can be observed, the speedup increases, increasing the matrix order for all processors grid. This can be justified by the compensation between each process work and MPI communication. Different blocking factors were tested, varying between 2 and 20. The blocking factor which gives the better CPU time was 8 in all cases. Finally,

	Processor Grid	# CPUs	Element Distribution (s)	LU Decomposition (s)	Arnoldi Iteration (s)
201^2	8×8	64	182	140	80
	12×12	144	178	62	57
	16×16	256	172	47	50
	20×20	400	171	34	47
401^2	16×16	256	2800	1722	331
	20×20	400	2761	1142	256
	24×24	576	2735	956	229
	28×28	784	2710	698	206
	32×32	1024	2703	572	195
	36×36	1296	2690	431	195
	40×40	1600	2681	418	192
601^2	36×36	1296	13878	3985	514
	44×44	1936	13802	3421	505
	48×48	2304	13767	2389	435
	52×52	2704	13740	2144	433
	56×56	3136	13721	1885	416
	60×60	3600	13703	1814	409

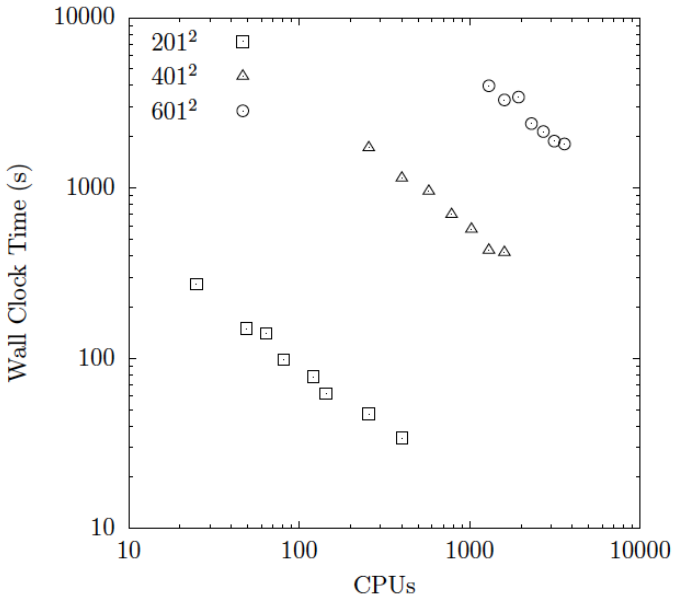

Figure 4.6: Scaling results for the solution of the two-dimensional Laplace EVP, discretised by $201^2, 401^2$ and 601^2 spectral collocation nodes and 128^2 blocks for the block cyclic distribution of matrix $\mathbf{A}$. *Resolution* 201^2: dim($\mathbf{A}$)=40401, size($\mathbf{A}$)=26.12 GB, min(#CPUs)= 14. *Resolution* 401^2: dim($\mathbf{A}$)=160801, size($\mathbf{A}$)=413.71 GB, min(#CPUs)= 220. *Resolution* 601^2:, dim($\mathbf{A}$)=361201, size($\mathbf{A}$)=2.087 TB, min(#CPUs)=1115 (Quintanilha Jr et al. 2017).

the two-dimensional Laplace equation was solved in the Cooper Cray XE6m machine, ensuring the correct computation of the analytically-known eigenvalues. Spectral collocation methods are used to discretise the square domain $x \in [-1, 1] \times y \in [-1, 1]$ using $N_x = N_y = 401$ Chebyshev Gauss Lobatto (CGL) nodes in each spatial direction. This results in a matrix with dim(A) = 160801, which occupies $\approx$ 413GB of memory in

double precision real arithmetic. The matrix is distributed using 1282 blocks over processor grids of different sizes, as shown in fig. 4.6. Once the matrix is LU-decomposed by ScaLAPACK, the distributed Arnoldi algorithm is used to construct a Krylov subspace of dimension $m_{\text{Kryl}} = 200$ and compute the leading Ritz values. In the same figure 4.6 the linear scaling of the numerical solution of the Laplace EVP is shown for the three different matrix sizes with the associated wall-clock time in seconds. Besides near-perfect linear scaling achieved for all resolutions when the number of CPUs is varied, the wall-clock time for the parallel numerical solution of the Laplace EVP (or a multi-dimensional flow stability EVP at analogous resolutions) is well accepted, falling below 15 mins when O(1000) CPUs are used.

Chapter 5

Code verification

In this chapter, the newly developed linear stability code will be benchmarked against well-known canonical cases: Plane Poiseulle Flow (PPF), Boundary-layer, 2D lid-driven cavity, and the swept attachment-line flow. Both modal and nonmodal stability results are verified for incompressible and compressible flows. This is an important step in order to gain confidence that the *LiGHT* code can solve multi-dimensional base flows (one-dimensional to three-dimensional) in both incompressible and high-speed regimes.

5.1 Local stability analysis

5.1.1 Plane Poiseulle Flow (PPF)

One of the most common benchmark problems to start any stability code verification is the plane Poiseulle flow. The geometry consists of two infinitely long plates parallel to each other at a constant distance. The flow is driven by a constant pressure gradient applied in the flow direction. If a profile is taken on the wall-normal direction, a parabolic velocity baseflow is obtained in the form of

$$\bar{u}(y) = 1 - y^2. \tag{5.1}$$

Because the plates are infinitely long, this is an example of a one-dimensional flow. The boundary conditions are no-slip $\bar{u} = 0$ and no penetration $\bar{u}' = 0$ at both plates.

Modal stability calculation

The temporal one-dimensional (local) eigenvalue problem (equation 2.12) is solved using two different algorithms, the QZ and the Arnoldi, explained in detail on §4.4. Since the PPF corresponds to a flow in a bounded domain, infinite discrete eigenvalues exist. Figure 5.1 illustrates the eigenspectrum calculated for two different Reynolds numbers based on the distance between the upper and the lower plates: (a) Re=3000 and (b) Re=10000. The streamwise wavenumber α is chosen to be 1 and the spanwise

wavenumber β is 0, corresponding to a two-dimensional mode. Both spectra were successfully recovered using the QZ and the Arnoldi algorithms. Figure 5.1(b) highlights in red the unstable Tollmien-Schlichting mode (Tollmien 1929, Schlichting 1932) found and published by Orszag (1971), with the eigenvalue corresponding to ω = (0.23752649 + 0.00373967 i). The amplitude functions of the Tollmien-Schlichting eigenmode is plotted in figure 5.2. The magnitude of the streamwise (a) and the wall-normal (b) velocities are characteristic of the so-called "wall modes". They are expected to be responsible for the instability at this choice of parameters. Both solutions recover the correct eigenfunctions shape.

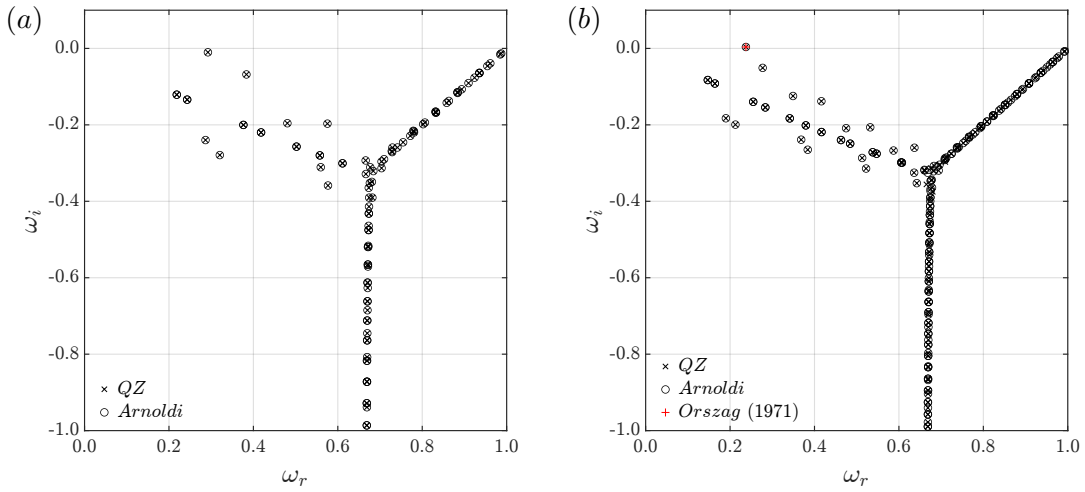

Figure 5.1: Eigenvalue spectra of plane Poiseuille flow for $\alpha = 1$, $\beta = 0$ and (a) Re=3000, (b) Re=10000. Both QZ and Arnoldi algorithms recover the same spectrum. The red plus symbol corresponds to the eigenvalue published by Orszag (1971).

Transient growth calculation

The plane Poiseuille flow is further interrogated in respect to the nonmodal stability theory, where the short time (transient phase) behaviour is also taken into account and is independent of the asymptotic stability of the flow. In other words, this calculation is responsible for giving the complete scenario:

- The growth or decay of the disturbance's energy at a short time (transient growth);
- The asymptotic behaviour responsible for the growth or decay of the disturbances at a long time ($t \to \infty$), also obtained by the EVP solution.

Therefore, all forthcoming results generated from the nonmodal stability code can also be verified in its asymptotic behaviour with the results obtained by the modal stability code.

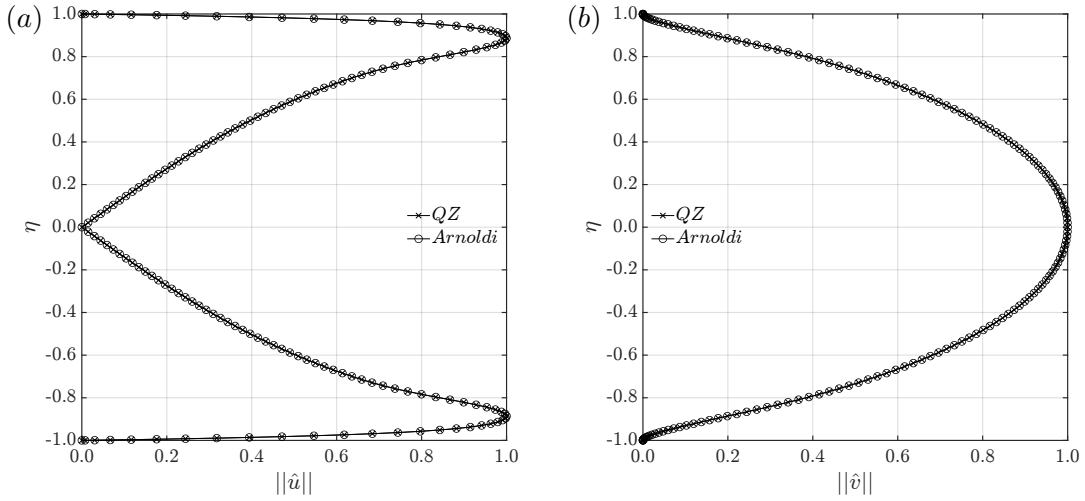

Figure 5.2: Plane Poiseuille flow eigenfuntions calculated with QZ and Arnoldi algorithms for Re = 10000, $\alpha = 1$ and $\beta = 0$. (a) Streamwise $|\hat{u}|$ and (b) wall-normal $|\hat{v}|$ velocity magnitude corresponding to the unstable Tollmien-Schlichting mode.

The first case analysed with the transient growth code is the plane Poiseuille flow for $\alpha = 1$, $\beta = 0$ and $Re = 3000$. The eigenvalues are shown in figure 5.1 (a). They all are situated in the lower half-plane of the spectrum, meaning that the flow is classified as modally **stable** at these conditions. Figure 5.3 plots the energy gain G(t) calculated with the nonmodal code and demonstrates that indeed the long time behaviour is of linear decay of energy, with the same rate given by the least stable eigenvalue calculated from the modal theory. However, during a short time, significant energy growth is reached. The QZ and the Arnoldi algorithms, used to recover the eigenfunctions necessary to calculate the transient growth, deliver the same results. Moreover, the maximum energy gain G(t) = 20.37 is the same as the one obtained by Reddy and Henningson (1993) and is shown by the red plus symbol.

A second verification case is the ability to recover the maximum energy growth achieved by the plane Poiseuille flow. Figure 5.4 (a) shows the energy curve for $\alpha = 0$, $\beta \approx 2.05$ and $Re = 1000$. The maximum value is compared with the result published by Reddy and Henningson (1993) and is shown by the red plus symbol. Excellent agreement is achieved, with G(t=76) $\approx$ 196. The last case is shown in figure 5.4 (b), where a modally stable ($Re = 5000$) and unstable ($Re = 8000$) flows are presented. Both cases correspond to a two-dimensional wave with streamwise wave-number $\alpha = 1$. Once again, excellent agreement of the maximum transient growth is recovered compared to the results reported by Reddy and Henningson (1993), showing that the local nonmodal code can correctly predict the transient growth of energy for different Reynolds numbers and both two-dimensional waves as well as streamwise aligned structures.

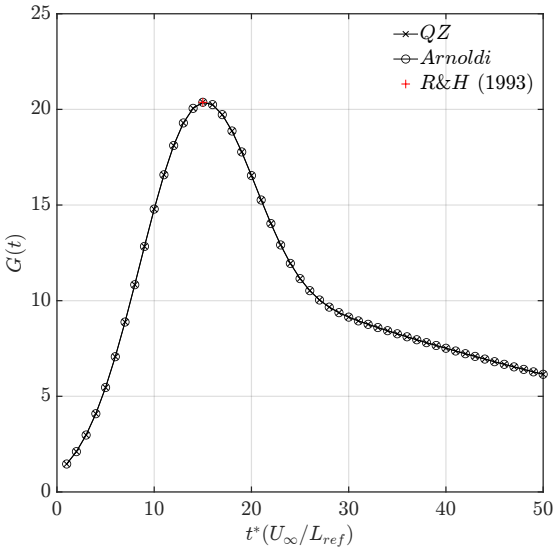

Figure 5.3: Energy growth of the plane Poiseuille flow for $\alpha = 1$, $\beta = 0$ and $Re = 3000$ calculated based on the QZ and Arnoldi eigenfunctions. The red plus symbol corresponds to G(t) = 20.37 reported as the optimal value by Reddy and Henningson (1993).

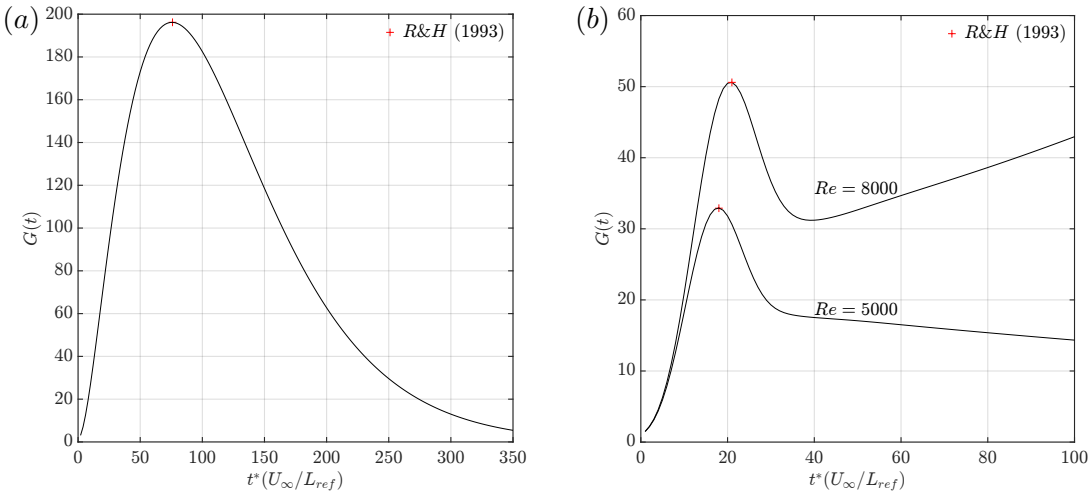

Figure 5.4: Energy growth of the plane Poiseuille flow for (a) $\alpha = 0$, $\beta \approx 2.05$ and $Re = 1000$ and (b) $\alpha = 1$, $\beta \approx 0$ and $Re = 8000$ and $Re = 5000$. In the later, both the asymptotic decay ($Re = 5000$) as well as the asymptotic growth ($Re = 8000$) have an energy growth at short time, in agreement with Reddy and Henningson (1993).

5.1.2 Blasius boundary layer

The second benchmark problem is the incompressible boundary layer, also known as the Blasius boundary layer (Blasius 1907). The geometry consists of a semi-infinite plate held parallel to a uniform flow U. Blasius derived a similarity solution for the case of no pressure gradient, i.e. $\frac{dU}{dx} = 0$. The baseflow can be calculated as a self-similar solution

given by

$$f''' + \frac{1}{2} f'' f = 0, \tag{5.2}$$

where prime denotes derivation with respect to the self-similar variable $\eta = y\sqrt{\frac{U}{\nu x}}$. The boundary conditions are no slip, no penetration on the wall, and constant free stream velocity outside the boundary layer. The boundary-value problem can be reduced to a system of initial value problem using the shooting method. The resulting baseflow generated can be used to verify the linear stability analysis code regarding an unbounded one-dimensional baseflow.

Modal stability calculation

The incompressible stability spectra of the Blasius boundary-layer profile is shown in figure 5.5 for the solution of the EVP using the QZ and Arnoldi algorithms. In this case of an unbounded domain, the continuous spectrum is represented by discrete modes. They are strongly dependent of resolution, domain truncation in the farfield and the associated boundary conditions. Figure 5.5 (a) shown the spectra for $\alpha = 0.179$, $\beta = 0$ and $Re = 580$. The unstable mode, also called a Tollmien-Schlichting mode, is in agreement with the literature value of $\omega = (0.3641 + 0.0080\ \mathrm{i})$ obtained by Mack (1976). Figure 5.5 (b) shows the spectra for a streamwise aligned disturbances $\alpha = 0$ and $\beta = 0.37$.

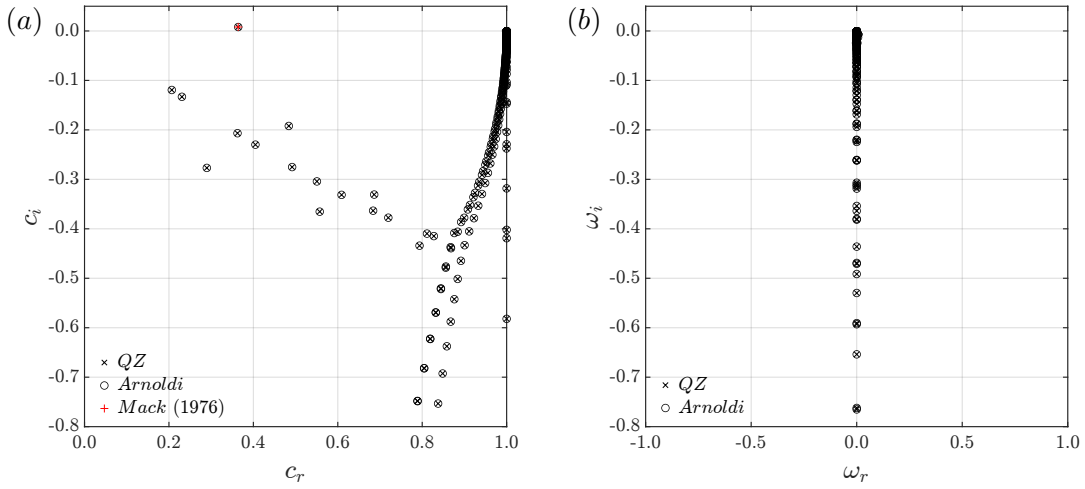

Figure 5.5: Eigenvalue spectra of Blasius boundary-layer flow for $Re = 580$ and (a) two-dimensional disturbance $\alpha = 0.179$ and (b) streamwise aligned disturbance with $\beta = 0.37$. The red plus symbol corresponds to the eigenvalue published by Mack (1976).

The eigenfunctions of the unstable Tollmien-Schlichting mode are shown in figure 5.6 for the streamwise $|\hat{u}|$ (a) and the wall-normal $|\hat{v}|$ (b) velocity magnitude. Due to its

low phase speed, the maximum amplitude is found close to the wall. Both QZ and Arnoldi methods recover the same amplitude functions.

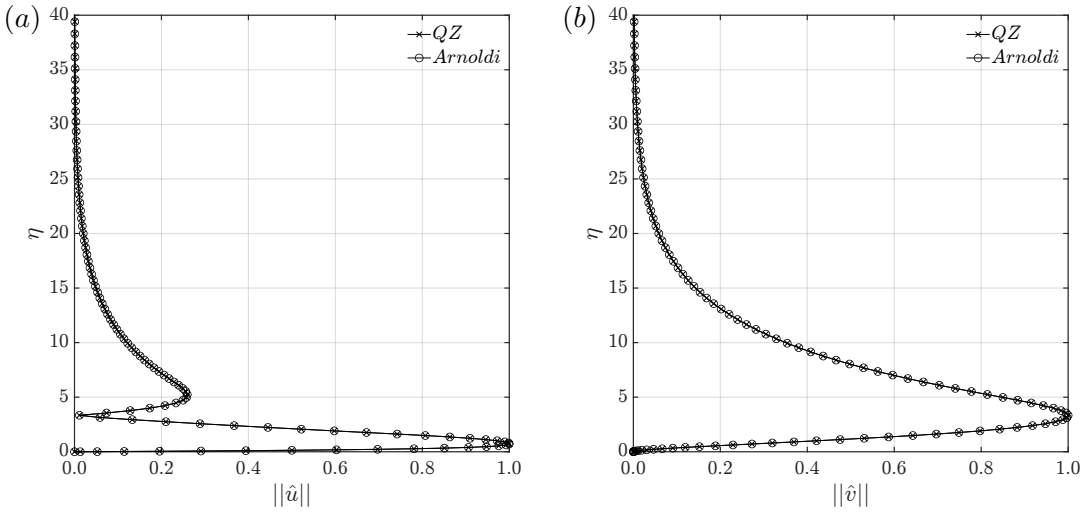

Figure 5.6: Blasius boundary layer flow eigenfuntions calculated with QZ and Arnoldi algorithms for $\alpha = 0.179$, $\beta = 0$ and $Re = 580$, (a) Streamwise $|\hat{u}|$ and (b) wall-normal $|\hat{v}|$ velocity magnitude corresponding to the unstable Tollmien-Schlichting mode.

Transient growth calculation

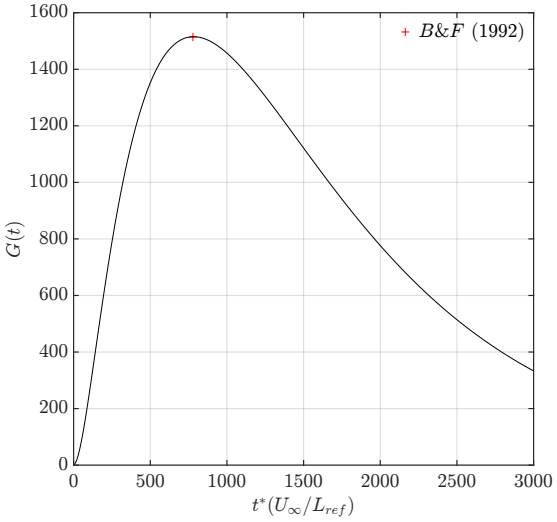

Figure 5.7: Energy growth of the Blasius boundary-layer flow for $\alpha = 0$, $\beta = 0.65$ and $Re = 1000$ based on the boundary-layer displacement thickness. The red plus symbol corresponds to G(t) = 1514, reported as the optimal value by Butler and Farrell (1992).

Local transient growth is calculated for the Blasius boundary-layer flow in the case of maximum energy permissible for $Re = 1000$, based on the boundary-layer displacement

thickness δ. In this case, the global optimal has $\alpha = 0$ and $\beta = 0.65$. Excellent agreement of the maximum energy growth value (G(t) = 1514) is found in comparison with the results of Butler and Farrell (1992) and is shown by the red plus symbol in figure 5.7.

5.1.3 Compressible boundary-layer

Moving on from incompressible to high-speed flows, the compressible boundary layer is used to verify the code due to compressibility effects. In this regime, the flow is of particular interest because, whereas viscous instability is dominant at low subsonic speeds, infinite viscous and inviscid instability modes can co-exist as the Mach number increases. The governing equations for the base flow may be written as (Mack 1984):

$$\begin{aligned} \frac{d}{d\eta}\left(\frac{d\bar{u}}{d\eta}\right) + \frac{g}{\bar{\mu}}\left(\bar{\mu}\frac{d\bar{u}}{d\eta}\right) &= 0, \\ \frac{d}{d\eta}\left(\frac{\bar{\mu}}{Pr}\frac{d\bar{T}}{d\eta}\right) + \frac{gPr}{\bar{\mu}}\left(\frac{\bar{\mu}}{Pr}\frac{d\bar{T}}{d\eta}\right) + 2\bar{\mu}\left(\frac{d\bar{u}}{d\eta}\right)^2 &= 0, \end{aligned} \tag{5.3}$$

where

$$g(\eta) = \frac{1}{2}\int_0^\eta \frac{\bar{u}}{\bar{T}} d\eta \tag{5.4}$$

with a calorically perfect gas, constant Prandtl number and Sutherland law for the viscosity assumed. The equations were solved with an inhouse compressible boundary layer solver.

Modal stability calculation

A classical verification case of the compressible boundary layer regarding modal instabilities is the $Ma = 4.5$ with two-dimensional waves, where the neutral curves present well-defined regions of instability for both the first and second (Mack) mode. The neutral stability curves are presented in figure 5.8. As seen here and published by Mack (1984), the onset Reynolds number for the second mode to become unstable is $Re = 235$. Moreover, the shape of the stability curves shows that viscosity has only stabilizing effects in high-order modes.

Two different spectra are computed with the QZ and the Arnoldi algorithms and are displayed in figure 5.9. The conditions used for the analysis are: (a) $Ma = 2.5$, $Re = 3000$, $\alpha = 0.06$, $\beta = 0.10$ and (b) $Ma = 2.5$, $Re = 300$, $\alpha = 0.0$, $\beta = 0.1$. Both methods are shown to recover the same spectrum when compressibility effects are added. For these calculations, the Prandtl number is assumed to be 0.7 and the stagnation temperature $T_{\text{stag}} = 333$ K. Whereas in the first case an unstable mode is found (therefore the flow is modally unstable), in the second case no eigenvalue cross to the positive ω_i part of the spectrum and the flow is considered modally stable.

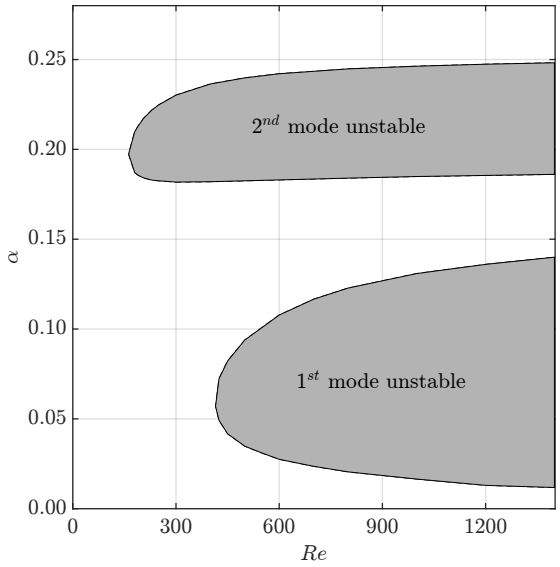

Figure 5.8: Neutral stability curves for $Ma = 4.5$ and two-dimensional wave. The wall is insulated at wind-tunnel temperatures (Mack 1984).

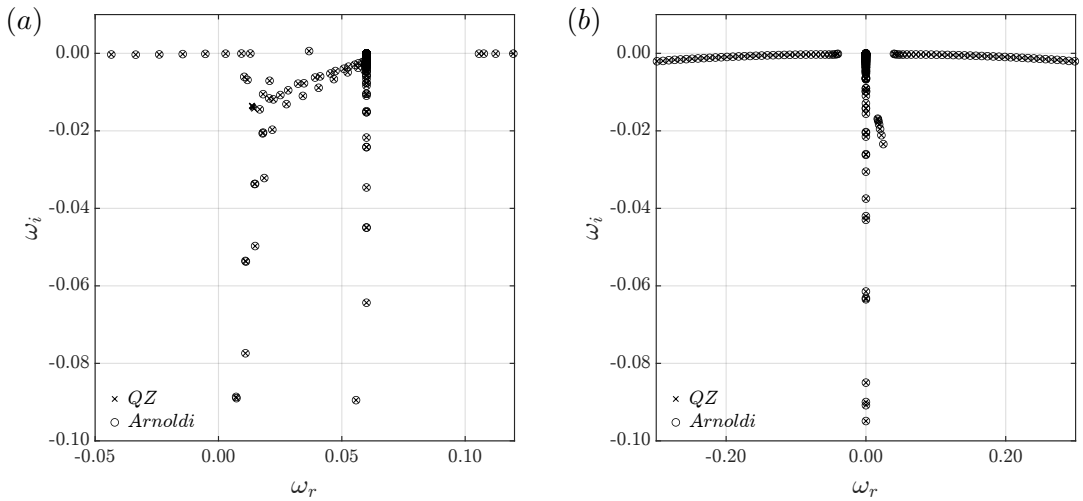

Figure 5.9: Eigenvalue spectra of compressible boundary-layer for (a) $Ma = 2.5$, $Re = 3000$, $\alpha = 0.06$, $\beta = 0.10$ and (b) $Ma = 2.5$, $Re = 300$, $\alpha = 0.0$, $\beta = 0.1$.

Transient growth calculation

Time evolution of the flow energy $G(t)$ is shown in figure 5.10 for the compressible flat-plate boundary layer. The gain curves correspond to the spectra shown in figure 5.9; (a) $Ma = 2.5$, $Re = 3000$, oblique waves with $\alpha = 0.06, \beta = 0.10$ and (b) $Ma = 2.5$, $Re = 300$, streamwise aligned periodic structures with $\alpha = 0, \beta = 0.1$ (Hanifi et al. 1996). The agreement between the present results (full lines) and the referenced work (red plus symbols) is excellent for both cases. Moreover, in figure 5.10 (a) an asymptotic growth is obtained due to the presence of the unstable mode seen in figure 5.9 (a). Even

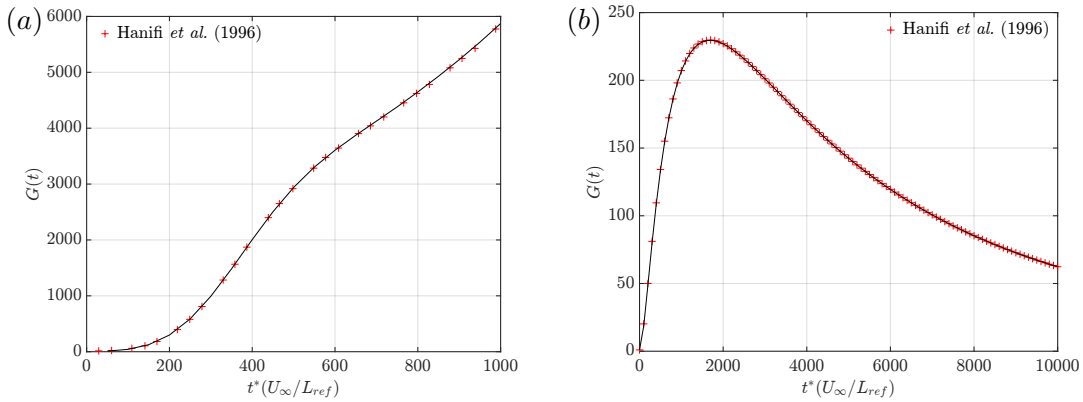

Figure 5.10: Energy growth of the compressible boundary-layer for (a) $Ma = 2.5$, $Re = 3000$, $\alpha = 0.06$, $\beta = 0.10$ and (b) $Ma = 2.5$, $Re = 300$, $\alpha = 0.0$, $\beta = 0.1$. The results published by Hanifi et al. (1996) are shown by the red plus symbols.

though the spectrum of figure 5.9 (b) does not contain any unstable modes, an energy peak of about $G(t) = 230$ at short time is achieved. Once the transient effects become less intense, the energy decays exponentially with a rate given by the corresponding least stable eigenvalue.

5.2 BiGlobal stability analysis

When the base flow is dependent on two spatial directions but can be relaxed in the third, a BiGlobal eigenvalue problem needs to be solved instead of the classical local approach. In order to do so, the Kronecker product discussed in §4.2 is first verified, solving the well-known two-dimensional Helmholtz eigenvalue problem in Cartesian coordinates. The generalised coordinate implementation necessary to analyse curvilinear systems, detailed in §2.4, is applied to compute the eigenvalues under an elliptic confocal coordinate transformation. After that, the local examples studied before (PPF and compressible boundary layer) are used to verify the complete BiGlobal stability code. To investigate one-dimensional flows in a BiGlobal stability context, the Fourier spectral collocation method presented in §4.1.2 is used to discretise the second homogeneous direction. This method allows the use of periodic boundary conditions maintaining spectral accuracy. Subsequently, the incompressible 2D square lid-driven cavity as well as both incompressible and compressible swept leading edge boundary layer flows are analysed to complete the verification of the code with existing literature.

5.2.1 Helmholtz EVP

The two-dimensional Helmholtz eigenvalue problem (EVP) can be written as

$$\left(\frac{\partial^2}{\partial x^2} + \frac{\partial^2}{\partial y^2}\right)\phi = -\lambda\phi, \tag{5.5}$$

and it is a useful example to assess the accurate implementation of the Kronecker product (4.18) necessary to build the spatial differentiation matrices in two-dimensional problems. The first case studied consists of a rectangular membrane domain ($\{x \in [0,1] \times y \in [0,1]\}$) subject to homogeneous Dirichlet boundary conditions. The analytical solution can be obtained by separation of variables, of the form

$$\sin(c_x(x+1))\,\sin(c_y(y+1)), \tag{5.6}$$

where c_x and c_y are integers multiples of $\pi/2$. The eigenvalues λ can be obtained as

$$\frac{\lambda^2}{\pi^2/4} = (i^2+j^2), \qquad \text{with} \quad i,j = 1,2,... \tag{5.7}$$

and can be used to verify the numerical calculations. Higher-order eigenvalues are converged with ≈ 12 digits with $N = N_x \times N_y = 41^2$ points due to spectral accuracy of the CGL collocation method implemented in the *LiGHT* code. Figure 5.11 (a) shows the eigenfunction corresponding to eigenvalue 34 recovered with N = 41^2 and interpolated on a $N = 101^2$ square grid to better represent the spatial structures.
The second step is associated with the correct implementation of the generalised coordinates detailed in §2.4 for both chain rule and metric factor methods. The two-dimensional Helmholtz EVP can be calculated on an orthogonal elliptic confocal domain, where the use of Fourier periodic conditions (4.1.2) is also verified. The transformation

$$\begin{aligned} x &= c\,\cosh(\xi)\,\cos(\eta), \\ y &= c\,\sinh(\xi)\,\sin(\eta) \end{aligned} \tag{5.8}$$

is implemented where $c = \mathrm{AR}/\sinh(\xi_0)$, AR is the ellipse aspect-ration (here set to 2) and $\xi_0 = \mathrm{atanh}(1/\mathrm{AR})$. The domain is discretised with $N_\eta = 60$ Fourier collocation points in the periodic direction η and $N_\xi = 61$ CGL collocation points in the wall-normal direction ξ. The eigenvalues are in agreement with the ones reported by Paredes (2014). The normalized eigenfuntion corresponding to the eigenvalue with index 7 is plotted in figure 5.11(b) together with the corresponding transformed grid.

5.2.2 Plane Poiseuille Flow (PPF)

The next verification is to recover the local analysis results within the BiGlobal version of the *LiGHT* code. In this case, the homogeneous streamwise direction is discretised using Fourier collocation points in order to consider a periodic domain. The plane Poiseuille flow (PPF) spectra recovered is plotted in figure 5.12(a), comparing the local and BiGlobal results. Excellent agreement is found overall. However, the spectrum generated using the BiGlobal stability code displays additional spurious stationary modes (the branch found at $\omega_r = 0$). These spurious modes need to be *neglected* to

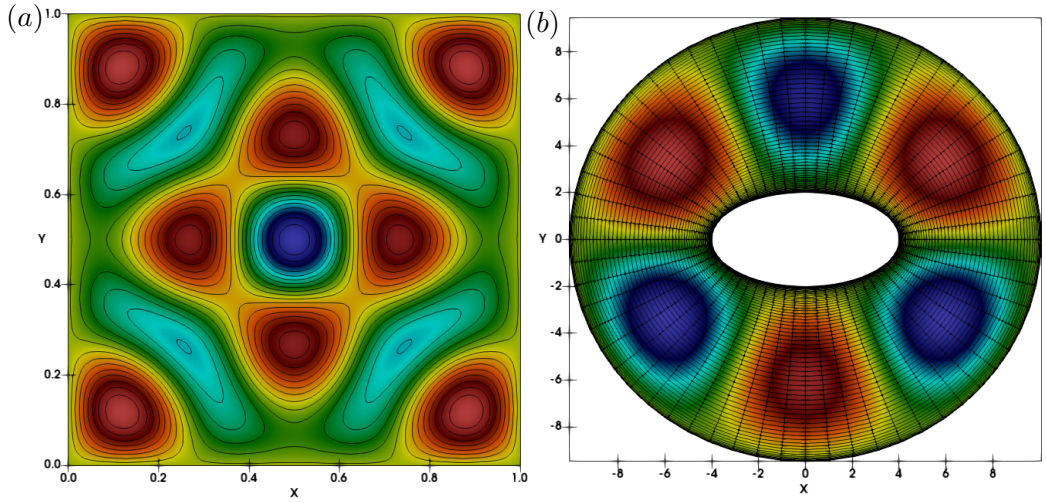

Figure 5.11: Iso-contours of normalized eigenfunctions of the two-dimensional Helmholtz EVP for (a) rectangular membrane and eigenvalue $\lambda^2/(\pi^2/4) = 34$ and (b) orthogonal elliptic confocal transformation with index 7.

recover the correct energy growth curves during the transient growth analysis. Figure 5.12(b) shows the perfect agreement between the one- and two-dimensional codes in capturing both the peak at a short time as well as the exponential decay.

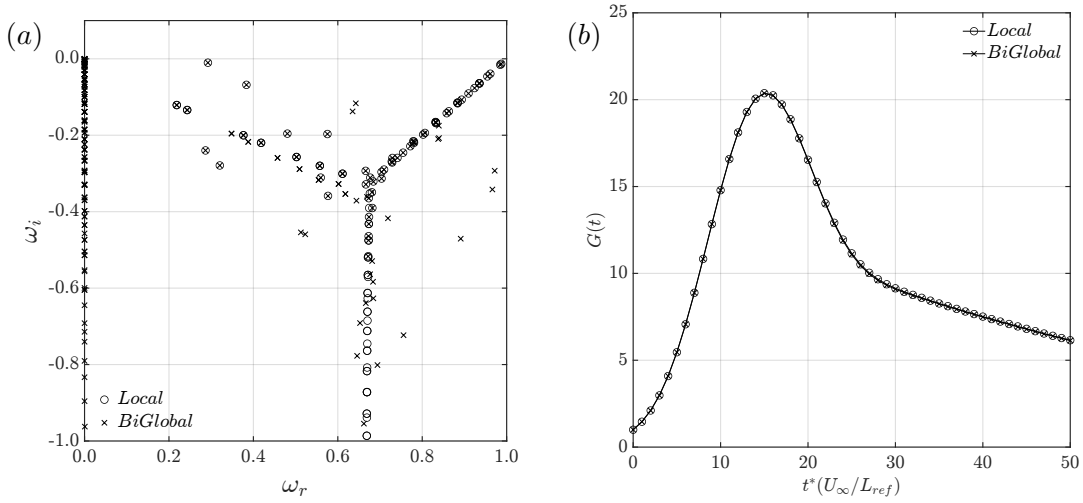

Figure 5.12: (a) Eigenvalue spectra and (b) energy growth of the plane Poiseuille flow for $\alpha = 1$, $\beta = 0$ and Re = 3000. Excellent agreement between the local and BiGlobal codes.

5.2.3 Compressible boundary-layer

The compressible boundary-layer flow is also verified, where again, Fourier collocation points are used in the streamwise direction of the flow. The local and global spectra

delivered by both cases are shown in figure 5.13(a) for $Ma = 2.5$, $Re = 300$ and streamwise aligned disturbance with $\beta = 0.1$. As it was previously discussed in the local analysis, in this case, only stationary ($\omega_r = 0$) modes are present. Transient growth analysis is performed, and figure 5.13(b) shows the associated energy gain. Excellent agreement is obtained between both Local and BiGlobal codes. This example concludes the verification of the two-dimensional code with respect to recovering the same results verified in the local stability framework and gives the confidence to study truly two-dimensional flows.

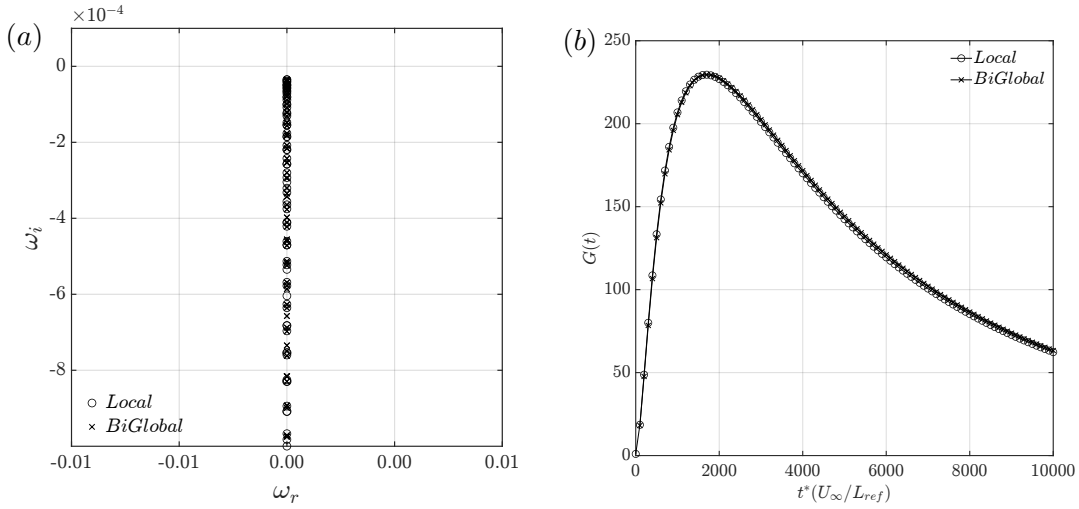

Figure 5.13: (a) Eigenvalue spectra and (b) energy growth of the compressible boundary-layer for $Ma = 2.5$, $Re = 300$, $\alpha = 0$, $\beta = 0.1$. Excellent agreement is seen between the local and BiGlobal results.

5.2.4 Square duct flow

Pressure-gradient driven flow in a rectangular square duct represents the two-dimensional extension of the plane Poiseuille flow. In this example, the base flow comprises only one velocity component along the homogeneous spatial direction, z. The solution satisfies the Poisson equation, and it is analytically known as (Lighthill and Rosenhead 1963, Theofilis, Duck and Owen 2004)

$$\bar{w}(x,y) = 1 - y^2 - 4\left(\frac{2}{\pi}\right)^3 \left[\sum_{n=0}^{\infty} \frac{(-1)^n}{(2n+1)^3} \frac{\cosh[(2n+1)\pi x/2]\cos[(2n+1)\pi y/2]}{\cosh[(2n+1)\pi A/2]}\right], \quad (5.9)$$

where A is the cross-section aspect ratio of the duct. Hence, the domain of interest can be defined as $\{x \in [-A, A] \times y \in [-1, 1]\}$. In the following analysis, the cross-section is taken to be square, and therefore A is 1.

Modal stability calculation

The complex eigenvalue problem was first solved by Tatsumi and Yoshimura (1990) using a generalisation of the Orr-Sommerfeld equation considering two inhomogeneous spatial directions. For verification of the *LiGHT* code, a subcritical Reynolds number of $Re = 1000$ and a wave-number $\beta = \pi$ is chosen to compare with the results of Paredes et al. (2016) using the same CGL spectral method to discretise both inhomogeneous spatial directions. Differently from Paredes et al. (2016), the LPPE boundary condition (eq. 4.25) is applied to the pressure at all four boundaries. The least stable eigenvalue obtained with the *LiGHT* code and a spatial resolution of $N = N_x \times N_y = 61^2$ is $\omega = (2.9027654538 - i\ 0.10352492613)$. For the same resolution, Paredes et al. (2016) reported an eigenvalue of $\omega = (2.9027654518 - i\ 0.10352492608)$. A Richardson-extrapolation of different grids gives $\omega = (2.9027654541 - i\ 0.10352492635)$. This results shown that eight and nine decimal digits are converged for the frequency and the growth rate, respectively. Moreover, the value of the frequency obtained herein is closer to the Richardson-extrapolation value on the 9th decimal digit compared with the results of Paredes et al. (2016). A reason for that could be the correct choice of the LPPE for the pressure boundary condition. Figure 5.14 presents colour contours of the real part of the least stable eigenmode. Figure 5.14 shows the real part of the amplitude functions.

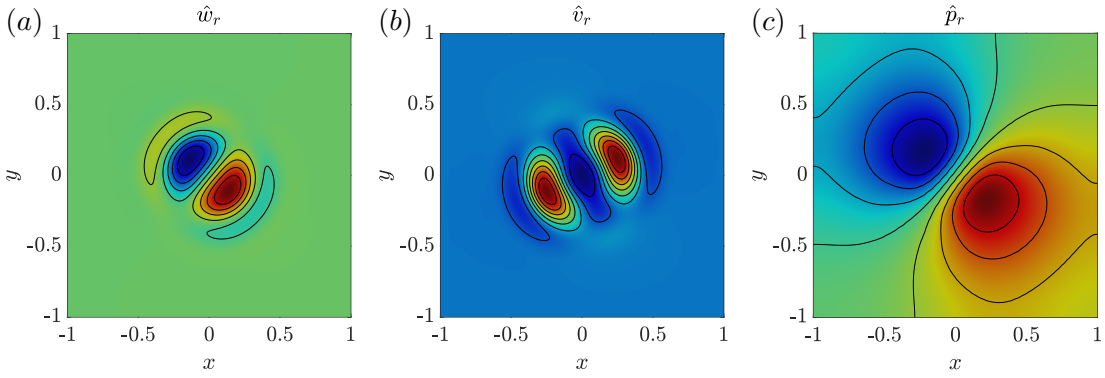

Figure 5.14: Eigenfunctions at $Re = 1000, \beta = \pi$ corresponding to the least stable eigenmode. Color contours of the real part of (a) $\hat{w}$, (b) $\hat{v}$ velocity components and (c) $\hat{p}$ pressure.

Transient growth calculation

In comparison with the vast modal stability literature (e.g. Tatsumi and Yoshimura 1990, Theofilis, Duck and Owen 2004), nonmodal stability analysis has been performed on a duct of square cross-section only more recently (Biau et al. 2008, Biau and Bottaro 2009, Boiko et al. 2010). Similarly to the pipe flow case (Gill 1965, Salwen et al. 1980), the flow is catalogued as linearly stable for all range of Reynolds number. Hence,

transient growth analysis becomes a natural candidate to be investigated as a possible mechanism responsible for the laminar-turbulent transition in this flow. Figure 5.15(a) shows a representative eigenspectrum of the square duct flow calculated for $Re = 3000$ and streamwise wave-number $\alpha = 1$ with three different Krylov subspace ($m = 501$, 1001 and 2001). The resolution of $N = 61^2$ is the same spatial resolution needed to converge the least stable mode. Already with the small subspace ($m = 501$), the least stable eigenvalue and various modes close to the origin are recovered. However, from the energy gain plot showed in figure 5.15(b), it is clear that this combination is insufficient to converge the initial value problem.

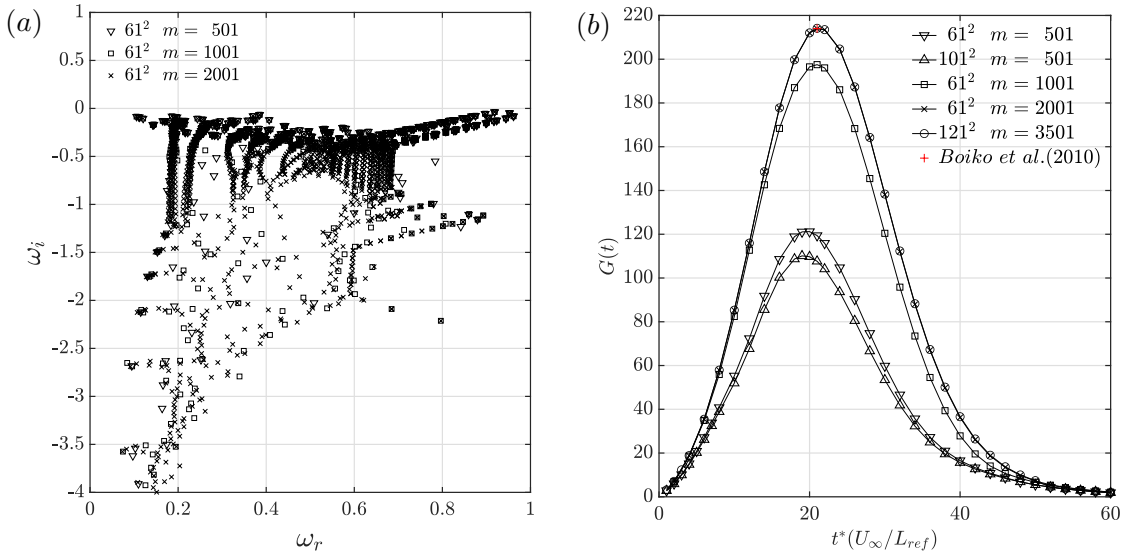

Figure 5.15: (a) Eigenvalue spectra and (b) energy growth convergence of the square cross-section duct for $Re = 3000$ and $\alpha = 1$. The maximum value of gain $G_{opt}(t \approx 21) \approx 214$ published by Boiko et al. (2010) is shown by the red plus symbol.

Increasing the subspace to $m = 1001$, more modes are included in the solution of the initial value problem and the gain curve shown in figure 5.15(b) approaches, but is still off, the literature value of $G_{opt}(t \approx 21) \approx 214$ (Boiko et al. 2010). Only with a Krylov subspace of $m = 2001$ the literature value is recovered, where more modes closer to the spectrums vertical branches are converged. Another test is performed, increasing the grid to $N = 101^2$ and keeping a Krylov subspace of $m = 501$ to examine whether the spatial discretisation could improve the gain curve for a smaller value of m. However, the result worsen, showing that the key parameter to check during transient growth analysis is the dimension of the Krylov subspace. The last result presented is with larger spatial discretisation $N = 121^2$ and Krylov subspace $m = 3501$ to confirm that the curve is converged in cases where no literature results are available. In fact, no change in the gain curve occurs, proving that $N = 61^2$ and $m = 2001$ is enough to converge the transient growth analysis, in this case. Interestingly, all the curves

shape look similar and the maximum value of $G(t)$ seems to appear at the same time $t = t_{opt} \approx 21$ for all cases. In other words, the maximum growth time is converged with a smaller choice of values, whereas the energy gain needs more modes to converge.

5.2.5 Swept leading edge boundary layer

Instability in the vicinity of the swept leading edge has been studied in a global modal analysis context in an incompressible and compressible regime to conclude the code verification. This last problem is interesting as a verification case of the eigenvalue problem solver since, even within the limitations of the simplified base flow model used in the analysis (Rosenhead 1963) and differently from the square duct case, all three base flow velocity components are present and no reductions of the Linearized Navier-Stokes equations are possible. Figure 5.16 shows a sketch of the swept leading edge flow.

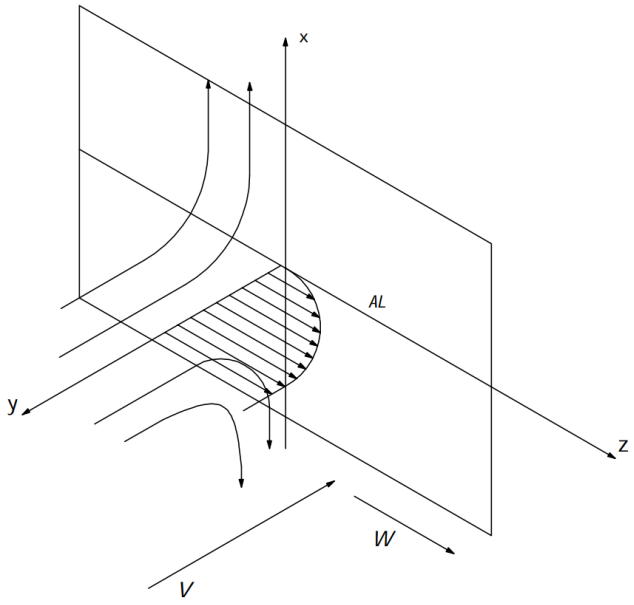

Figure 5.16: Sketch of the attachment-line flow showing the external velocity vectors (Gennaro 2008).

A similar solution proposed by Cohen and Reshotko (1955), Mack (1984) is used to model the base flow using the stream function and the Illingworth-Stewartson transformation. The velocity and temperature profiles can then be obtained by solving the

ODE system (Cohen and Reshotko 1955, Mack 1984)

$$\begin{aligned}
\bar{v}' &= -\bar{u} + \bar{v}\frac{\bar{T}'}{\bar{T}}, \\
\bar{u}'' &= \frac{1}{\bar{\mu}}\left(\frac{\bar{u}^2 + \bar{v}\bar{u}'}{\bar{T}} - 1 - \frac{\partial\bar{\mu}}{\partial\bar{T}}\bar{T}'\bar{u}'\right), \\
\bar{w}'' &= \frac{1}{\bar{\mu}}\left(\frac{\bar{v}\bar{w}'}{\bar{T}} - \frac{\partial\bar{\mu}}{\partial\bar{T}}\bar{T}'\bar{w}'\right), \\
\bar{T}'' &= \frac{Pr}{\bar{\mu}}\left(\frac{\bar{T}'\bar{v}}{\bar{T}} - (\gamma-1)Ma^2\bar{\mu}\bar{w}'^2 - \frac{\partial\bar{\mu}}{\partial\bar{T}}\frac{\bar{T}'^2}{Pr}\right),
\end{aligned} \tag{5.10}$$

where prime denotes derivatives in the wall-normal direction. The boundary-conditions necessary to close the problem are

$$\begin{aligned}
\bar{u} = \bar{w} = \bar{v} = 0, \quad &\text{at y} = 0, \\
\bar{u} = \bar{w} = \bar{T} = 1, \quad &\text{at y} = \infty.
\end{aligned} \tag{5.11}$$

The shooting method can be used to solve the ODE system with boundary conditions. The final three-dimensional base flow profiles are assumed to be only dependent on the wall-normal direction (y) except for the chordwise velocity component, which is also taken to be linearly dependent on the chordwise coordinate.

Modal stability calculation

The compressible global stability solver was applied to both incompressible and compressible cases. To reproduce the incompressible flow results with a compressible code, a low Mack number $Ma = 0.02$ was considered. For both cases, a linear mapping has been applied to the chordwise direction, while the boundary-layer mapping (4.2) has been used to discretise the wall-normal direction.

The boundary conditions are no-slip on the perturbation velocities and homogeneous Dirichlet for the temperature at the wall. A fast decay in the wall-normal direction is assumed for all disturbances at a sufficient large distance from the wall ($y_\infty = 100$). Along the chordwise direction, at a large distance from the attachment line (x = $\pm L_x$ = 100), linear extrapolation from the interior of the computational domain is used.

The first unstable eigenvalue, also known as the Görtler-Hämmerlin (GH) (Hall et al. 1984) was obtained in an incompressible global instability analysis by Lin and Malik (1996) and Theofilis (2003). Figure 5.17 (a) shows the global spectra obtained with the present BiGlobal code for $Ma = 0.02$, $Re = 800$, $\beta = 0.255$ and a resolution of $N = N_x \times N_y = 70^2$. The most unstable eigenvalues reported by Lin and Malik (1996) are also shown in circles. Excellent agreement with all four modes are found. Their frequency ω_r and growth rate ω_i are (0.0913, 0.00148), (0.0912, 0.00104), (0.0911, 0.00059) and (0.0910, 0.00016), respectively.

Moving on to the compressible regime, the swept leading edge boundary-layer has been studied in a global modal analysis context by Lin and Malik (1996), with several authors

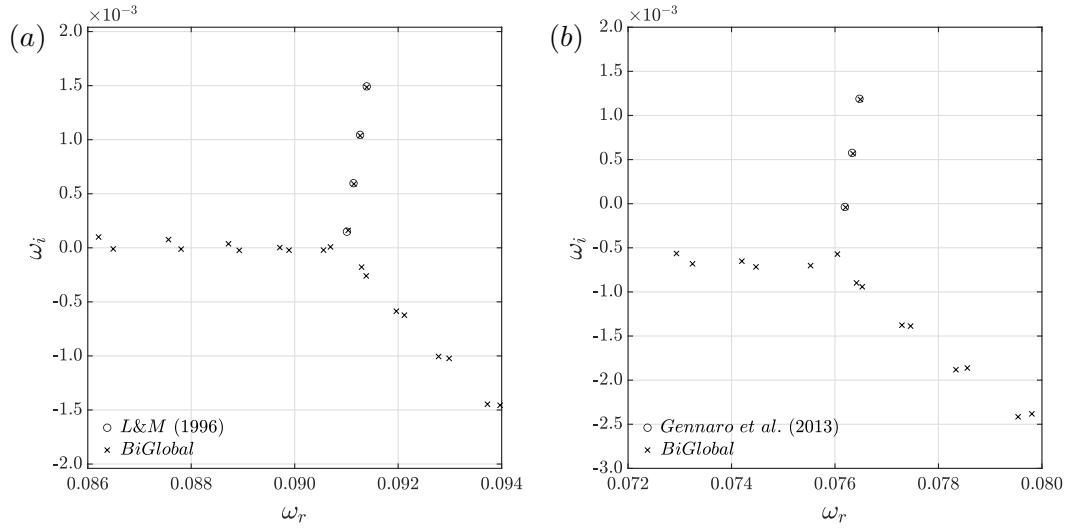

Figure 5.17: BiGlobal eigenvalue spectra obtained for $Re = 800$ and (a) incompressible ($Ma = 0.02$), $\beta = 0.255$ and (b) compressible $Ma = 0.9$ and $\beta = 0.19$.

having contributed aspects of flow instability physics since (Theofilis, Fedorov and Collis 2004, Mack et al. 2008, Gennaro et al. 2013). The compressible temporal BiGlobal stability analysis EVP has been solved for $Ma = 0.9$, $Re = 800$ and spanwise wave-number $\beta = 0.19$, indicating harmonic linear modal perturbations along the leading edge. The global eigenspectrum generated for this wave-number ($\beta = 0.19$) is found to deliver the most unstable Görtler-Hämmerlin (GH), first symmetric mode and is shown in figure 5.17 (b) along with the results provided by Gennaro et al. (2013). The eigenvalue of the GH mode is $\omega = (0.0765392 + i\ 0.00117793)$; the corresponding result of Gennaro et al. (2013) is $\omega = (0.0764718 + i\ 0.00118942)$, obtained using a spatial resolution of $N = N_x = N_y = 140$. Finally, figure 5.18 shows the real and imaginary parts of the amplitude functions $\hat{u}, \hat{w}$ and $\hat{T}$ recovered from the most unstable GH mode.

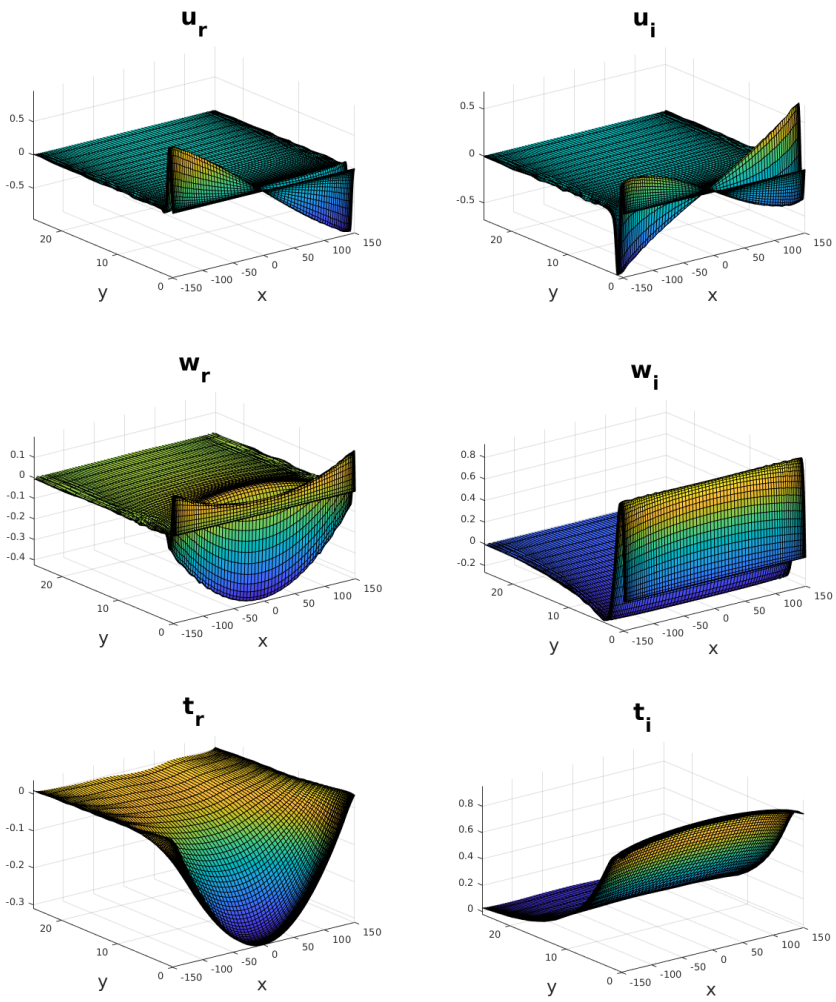

Figure 5.18: Amplitude functions at $Ma = 0.9, Re = 800$ and $\beta = 0.19$ corresponding to the most unstable (GH) mode. On the left-hand-side are the real and on the right-hand-side the imaginary components of $\hat{u}$, $\hat{w}$ and $\hat{T}$, respectively.

Chapter 6

Results

6.1 HIFiRE-5 elliptic cone model

The bulk of the results of this thesis have been obtained in the aspect ratio two elliptic cone model corresponding to the payload of the HiFIRE-5. The HIFiRE hypersonic flight test is a program lead by the Air Force Research Laboratory (AFRL) and the Australian Defence Science and Technology Organization (DSTO) (Dolvin 2008) aimed to demonstrate fundamental technologies critical to design of next generation aerospace systems, including boundary-layer laminar-turbulent transition prediction and control. The first configuration in the program, named HIFiRE-1, used a 7° half-angle cone to obtain in-flight transitional and turbulent boundary layer heating data on axisymmetric configurations. The design of this experiment, the associated pre-flight effort and actual flight data as well as transitional analysis have been discussed in detail in Kimmel et al. (2007), Kimmel (2008), Kimmel et al. (2011), Adamczak et al. (2011), Stanfield et al. (2012) and Li et al. (2011), further elaboration on the overview of earlier transition research on a circular base cone (Schneider 2004).

On the other hand, the last configuration to-date in the program, HIFiRE-5, was specifically designed to provide transition data in an essentially three-dimensional boundary-layer. This platform consists of an S-30 first stage, an improved Orion second stage and the transition section and can be better seen in figure 6.1 (Kimmel et al. 2010). The payload consists of a blunt-nosed elliptic cone of 2:1 aspect ratio and 0.86 m in length. The specific aspect ratio was chosen since it presents significant crossflow and second-mode instabilities that are expected to be the dominant instability mechanisms in three-dimensional boundary layers at hypersonic speeds. The minor axis of the cross-section is defined as the centreline, whereas the major axis is referred to as the attachment line. The blunted tip consists of a 2.5 mm radius circular arc, is tangent to the cone rays inscribed in the minor axis, while it retains a 2:1 elliptical cross-section to the tip.

Several efforts spanning over two decades have contributed to understanding hypersonic transition on elliptic cones. From an experimental point of view, Holden (1998)

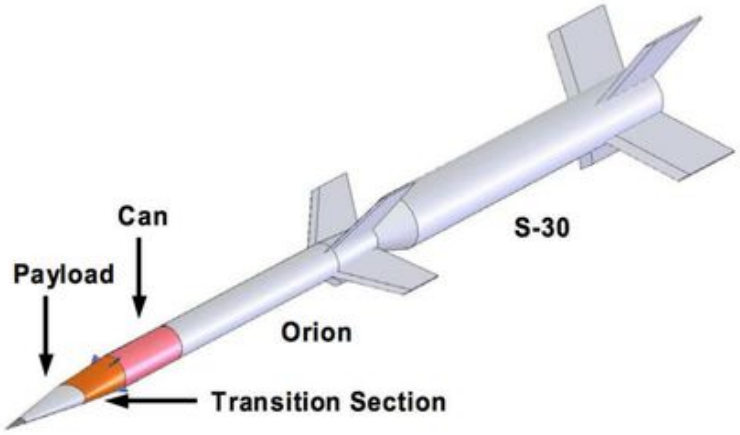

Figure 6.1: HIFiRE-5 stack (Kimmel et al. 2010).

obtained Schlieren images of hypersonic flow over a 4:1 aspect ratio elliptic cone at angles of attack from 0 to 5 degrees and reported that the transition front moves towards the base of the cone with increasing angle of attack. Schmisseur et al. (1998, 1999) measured the boundary-layer response to a laser-generated localized free-stream disturbance on the same 4:1 aspect ratio elliptic cone in a Mach 4 quiet tunnel at unit Reynolds number of 4.5×10^6 m^{-1}. At these conditions, the undisturbed flowfield was shown to be practically laminar in its entirety. The surface measurements also indicated that the boundary-layer response to disturbance is concentrated near the centreline. Kimmel et al. (1999) investigated the influence of base laminar crossflow on transition in the hypersonic boundary layer over a sharp-nosed 2:1 aspect ratio elliptic cone employing Schlieren imaging and surface oil-flow visualisation. Unlike hypersonic flow over planar and axisymmetric bodies, the transition front was found not to be driven by second mode instability. They found that the transition front was nonuniform with the earliest signs of boundary-layer transition being recorded in the vicinity of the centerline. Huntley and Smits (2000) studied in detail centerline boundary layer transition on a sharp-nosed 4:1 aspect ratio elliptic cone at Mach number 8 using CO2-enhanced Filtered Rayleigh Scattering. In line with the results of Kimmel et al. (1999), and despite the different cone aspect ratio, these authors also found transition to occur in the vicinity of the centerline and presented for the first time detailed results of the early stages of transition in this region. Juliano and Schneider (2010) performed experiments in the Boeing/AFOSR Mach-6 Quiet Tunnel (BMA6QT) facility with an aspect ratio 2 elliptic cone and showed that the dominant mechanism leading to transition are streamwise-aligned structures, identified as crossflow vortices between the centreline and the attachment line region. In the experiments of Borg et al. (2012) it was found that selective choice of spacing between roughness elements introduced can

excite wavelengths that would have been stable in the unperturbed boundary layer. Heat flux and boundary layer transition were measured by Juliano, Borg and Schneider (2015) in the BAM6QT facility, where two different transitional modes were found, the first one along the centreline and the second at the crossflow region. Moreover, these authors showed that both transitional modes were delayed when tunnel noise level was reduced and, conversely, the transition front moved forward when altitude was increased. Flight testing of the HiFIRE-5 commenced in 2012, although in that first flight the highest Mach number achieved in flight of 3, instead of the targeted 7 (Kimmel et al. 2013). Analysis of the flight data obtained revealed a transition pattern consistent with previous numerical and experimental studies, namely the presence of early transition at the centreline of the vehicle. Subsequently, Juliano et al. (2014) performed a full analysis of the flight data during the supersonic descent phase and reported two distinct boundary-layer transition mechanisms, the first causing transition at the centreline, while the second was related with transition at the leading edge and grows rapidly over a small range of free stream unit Reynolds numbers.

From a theoretical point of view, early work employing the parabolized Navier-Stokes equation was performed by Lyttle and Reed (1995), who analyzed flow on elliptic cone at zero angle of attack and different cross-sections and reported the existence of crossflow for all geometries investigated, but no crossflow transition in the range of parameters examined. One of the earliest inviscid linear global instability analyses was performed by Theofilis (2000c, 2002). Supersonic and hypersonic flow over elliptic cones of different aspect ratios was addressed, the two-dimensional Rayleigh equation was solved on a body-fitted coordinate system and distinct families of hydrodynamic and acoustic instabilities were discovered. Choudhari, Chang, Jentink, Li, Berger, Candler and Kimmel (2009) solved the corresponding two-dimensional viscous eigenvalue problem on a rectangle containing the main basic flow features around the centreline, for in-flight and wind tunnel conditions. The steady laminar three-dimensional base flows were calculated using a variety of structured and unstructured codes (Cheatwood and Gnoffo 1996, Baurle et al. 2020, Nompelis et al. 2005), while the main result of the eigenvalue problem solution was identification of unstable centreline global modes at all flow conditions examined. Paredes and Theofilis (2015), Paredes et al. (2016), also solved the global eigenvalue problem on a body-fitted elliptic coordinate system that extended from the centerline to the attachment line of an elliptic cone at zero angle of attack. They interrogated flow instability at 21.8 and 33km altitude, at Mach number of 7.45 and 7, and unit Reynolds numbers of 1.015×10^7 m^{-1} and 1.89×10^6 m^{-1}, respectively. They reported the existence of four classes of linear modal disturbances: symmetric and antisymmetric centerline instabilities associated with the shear-layer formed due to the lift-up effect at the centreline region, as seen in the analysis of Choudhari, Chang, Jentink, Li, Berger, Candler and Kimmel (2009), alongside high-frequency attachment-

line modes, oblique second (Mack) modes and cross-flow instabilities in the boundary layer between the centreline and attachment-line.

Large-scale numerical simulation of the HIFiRE-5 elliptic cone model was performed by Dinzl and Candler (2017) at the conditions of the Borg et al. (2012) experiment. These authors reported a Reynolds number dependence in the dominant stationary crossflow wavelength, with higher Reynolds numbers supporting instabilities corresponding to smaller wavelengths. Furthermore, streamwise-aligned structures were identified as streaks in agreement with experimental results and the formation of streamwise-aligned structures was attributed to the strong interaction between the streamwise velocity and the wall. On the other hand, Moyes et al. (2018) employed nonlinear Parabolised Stability Equations (PSE) and linear spatial (modal) BiGlobal instability analysis and demonstrated that coupling nonlinear PSE and global linear instability equations can provide a framework capable of predicting transition onset in flows with stationary crossflow as the dominant mechanism. Tufts et al. (2018) summarized work performed up to that point and discussed the strengths and weaknesses of using computation, ground test and flight test to predict laminar to turbulent transition over the HIFiRE-5 elliptic cone geometry. Very recently, Shi et al. (2020) developed an engineering model for transition prediction, based on new wind-tunnel experiments and flight data correlations. The proposed model is shown to agree well with the HiFIRE-5b flight data and with Purdue University wind-tunnel test data (Juliano and Schneider 2010). However, in the crossflow region closer to the centreline disagreements were observed between the experimental results of these authors when compared with flight testing data. Since classical linear stability analysis (Paredes et al. 2016, Moyes et al. 2018) predicts slow growth of disturbances in that region, no explanation of these differences could be provided on the basis of linear modal analysis. Finally, Choudhari et al. (2020) extended the analysis of the HIFiRE-5b flight experiment using local theory (Tufts et al. 2017) to study the linear stability of the boundary layer flow near the centreline of the elliptic cone and found an N-factor that peaks close to the value that correlates with Mack mode transition in the HIFiRE-1 circular cone experiment.

The present work aims at filling the knowledge gap regarding linear nonmodal instability on an aspect ratio two elliptic cone, and complements earlier modal analysis of the same problem discussed by Paredes and Theofilis (2015), Paredes et al. (2016). The base flow model and analysis parameters used are unit Reynolds numbers $Re' = 1.89 \times 10^6$ and 1.07×10^7 m^{-1}, at Mach number Ma = 8.05 and 7.45, corresponding to altitudes between the highest, 33 km and the lowest, 21 km, in cruise flight at zero angle of attack. By contrast to Paredes et al. (2016), the initial value problem is solved over time horizons sufficiently long for the modal analysis results to be recovered and the magnitude of transient energy growth is documented. Some guidance for the choice of parameters in the present global transient growth analysis is provided by a local

analysis (Quintanilha Jr et al. 2018), who addressed the potential of one-dimensional base flow profiles, at various streamwise stations and all azimuthal locations, from the centreline to the attachment-line, to sustain transient growth. Thus, the present work constructs a firm theoretical foundation for global transient growth to be performed on the geometry at hand, relaxing the approximation of azimuthal base flow homogeneity from the local analysis.

6.1.1 Base flow configuration

The HIFiRE-5 geometry is modeled by a blunt-nosed elliptic cone of 2:1 aspect ratio and 0.86m in length. The nose tip cross-section in the centreline of the model describes a circular arc with 2.5 mm radius, tangent to the cone ray describing the minor-axis, and retaining a 2:1 elliptical cross-section to the tip. Flight flow conditions were calculated for two different altitudes, 21 and 33km and Table 6.1 presents the corresponding free-stream velocity, U_∞, temperature, T_∞, and density, ρ_∞ as well as the unit Reynolds number, Re', and the Mach number, Ma, values at both altitudes. At 21 km the unit Reynolds number is one order-of-magnitude larger than at 33 km, due to the decrease of the density with increasing altitude; this difference will be seen to have an important qualitative effect on the results obtained in what follows. The wall temperature is defined using a prescribed temperature based on heat conduction analysis of an estimated trajectory for the vehicle. The wall temperature near the nose is approximately 650 K whereas the wall temperature over the rest of the surface varies between 300 K and 400 K. As discussed by Paredes et al. (2016), the ration between the wall temperature and the corresponding adiabatic wall temperature is $T_{\text{wall}}/T_{\text{adiabatic}} < 0.3$, resulting in a cold surface temperature over most of the cone surface downstream of the nose. In this case, no dissociation reactions were expected to influence the results. The steady laminar flow solution is the same used by Paredes et al. (2016) and has been calculated using the second order US3D non-equilibrium solver with shock capturing algorithm. High-enthalpy effect was not considered due to the relatively low hypersonic Mach number; a detailed description of the base flow computation can be found in Gosse et al. (2010, 2013).

Figure 6.2(a) shows contours of Mach number at 33km altitude and streamwise location $x^* = 0.36\ m$ from the tip of the elliptic cone. In this figure, it is possible to see the emergence of a bulge region at the centreline, $\zeta = \pi/2$, due to three-dimensionality of the flow. The boundary layer near the surface is deflected from the leading-edge towards the centreline producing a lift-up of low momentum boundary layer fluid, generating this mushroom-like structure, which was first seen in the experiments of Huntley and Smits (2000) and all subsequent experimental and numerical work. Figure 6.2(b) shows one-dimensional baseflow profiles extracted at three spanwise locations, $z^* = 0.00$, 0.02 and 0.04 m, normal to the elliptic cone wall. In what follows, these profiles have been

Altitude (km)	U_∞ (m/s)	T_∞ (K)	ρ_∞ (Kg/m^3)	Re' (m^{-1})	Ma
21	2207.1	218.45	0.0658	1.07x10^7	7.45
33	2452.1	230.97	0.0115	1.89x10^6	8.05

Table 6.1: Flow conditions for both altitudes analysed.

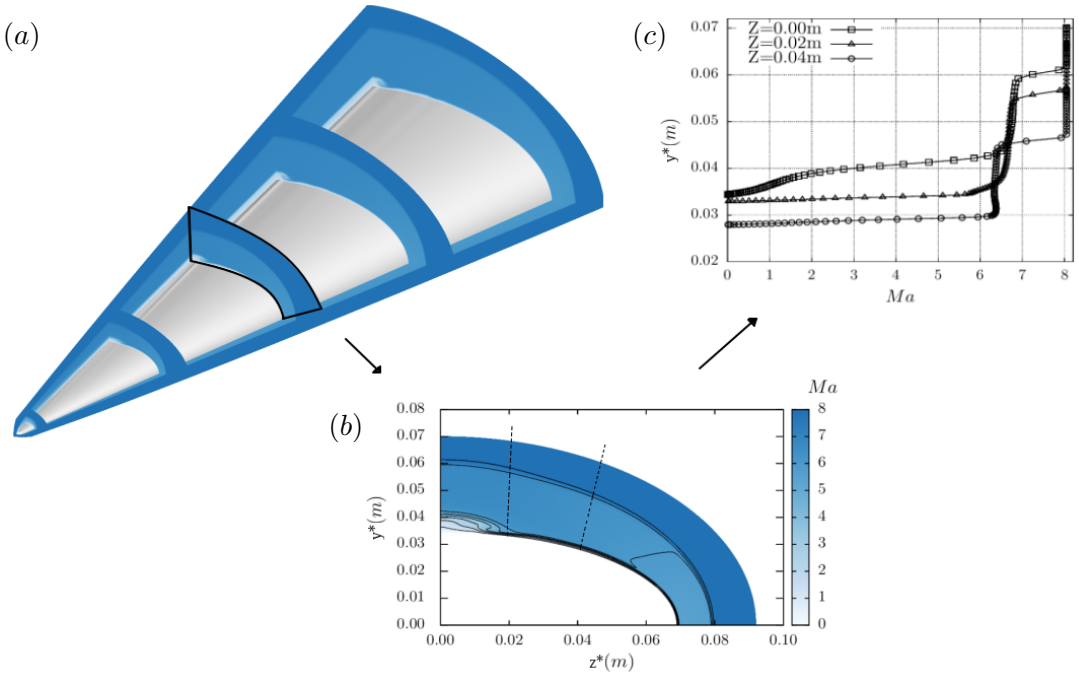

Figure 6.2: Mach number contours of the base flow at 33km altitude. (a) Full three-dimensional baseflow calculated with US3D solver (Gosse et al. 2010, 2013). An example of a two-dimensional base flow used in the BiGlobal stability analysis and (c) one-dimensional base flow profiles used in the local stability analysis.

used to perform local transient growth analysis, the results of which have guided the subsequent global transient growth analyses.

6.1.2 Elliptic cone transformation and spatial discretization

The transformation of the physical (x, y, z) to the computational (ξ, η, ζ) coordinate system is performed using the elliptic confocal transformation discussed by Theofilis (2000c) and Paredes et al. (2016),

$$\begin{aligned} x &= \xi \\ y &= c\,\xi\ \sinh(\eta_0+\eta)\ \sin\zeta \\ z &= c\,\xi\ \cosh(\eta_0+\eta)\ \cos\zeta, \end{aligned} \tag{6.1}$$

where c sets the half-angle of the cone minor-axis, $\theta = 7°$, through

$$c = \frac{\tan\theta}{\sinh\eta_0},$$

and

$$\eta_0 = \tanh^{-1}\frac{1}{AR}$$

is a parameter controlling the aspect ratio (AR) of the elliptic cone, here set as 2. Differently from the supersonic cylinder and the compression ramp, the two transformed spatial directions are η and ζ, where the homogeneous direction is ξ. The inhomogeneous spatial directions are appropriately discretized using Chebyshev-Gauss-Lobatto (CGL) spectral collocation points (§4.1.1),

$$\eta_j = \zeta_j = \cos\frac{j\pi}{N}, \quad j = 0, 1, ..., N. \tag{6.2}$$

The mapping used to resolve gradients inside the boundary-layer is

$$\eta_j = l\frac{1-\eta_j}{1+s+\eta_j}, \quad s = 2l, \quad l = \frac{\eta_h}{1-2\eta_h}, \tag{6.3}$$

where s is a scaling function, l is a parameter depending on the wall normal extent of the domain and η_h is the location in the domain below which half of the points are to be clustered, allowing control over the density of points near the wall. In the subsequent analysis, a η_h of 0.4 was employed. Along the spanwise direction, a linear mapping is used to capture the modes that exist along the crossflow region.

6.1.3 Domains studied

In the following analysis, the symmetries of the problem due to zero angles of attack and yaw are exploited in order to reduce the computational cost of numerical solution of the initial value problem. One quarter of the physical space ($0 \leq \zeta \leq \pi/2$) is discretized. Moreover, to guarantee convergence and correct capturing of the structure of the different modes, the domain analyzed is divided in two parts, as schematically shown in Figure 6.3. The first domain accounts for the centreline ($\zeta = \pi/2$) and the crossflow region ($\pi/2 < \zeta \leq \pi/4$) whereas in the second domain flow instability in the vicinity of the attachment line of the cone ($\zeta = 0$) is analyzed. The attachment-line region will be used to compare modal results with the work of Paredes et al. (2016) and the first domain, accounting for the centreline and crossflow, will be further interrogated in respect to nonmodal instabilities.

6.1.4 Boundary conditions

The boundary conditions to complement the elliptic eigenvalue and singular value problems are the following. For the first domain, in the azimuthal direction ζ, symmetric and antisymmetric boundary conditions are imposed at the centreline ($\zeta = \pi/2$; West boundary) and suffice to capture all instabilities present in the flow. At the opposite (East) boundary, linear extrapolation is imposed on all amplitude functions, allowing perturbations to exit the domain with minimal distortion. In the second domain,

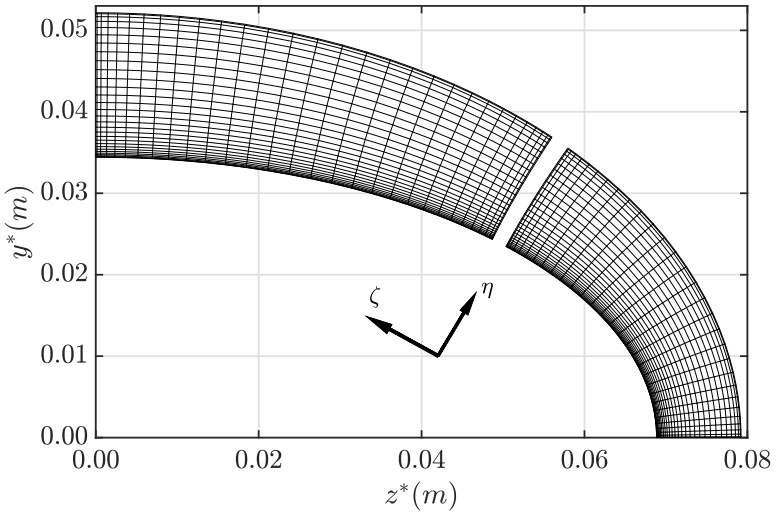

Figure 6.3: Example of the two domains used to perform the BiGlobal stability analysis. The first one is covering the centreline and the crossflow region ($\pi/2 \leq \zeta \leq \pi/4$) whereas the second one accounts for the region close to the attachment-line ($\zeta = 0$).

an analogous procedure is followed, namely symmetric and anti-symmetric boundary conditions are imposed at the attachment line ($\zeta = 0$) and linear extrapolation can be imposed at the opposite boundary. Along the wall-normal direction, the boundary conditions are the same for both domains: at the wall ($\eta = 0$; South) boundary, no-slip conditions are imposed on the perturbation velocity components. Homogeneous Dirichlet boundary condition is imposed for the perturbation temperature and the gradient of the pressure amplitude function is required to be zero at the wall. The location of the top (North) boundary is defined by the presence of the shock. At this boundary in both domains all perturbations are forced to decay through the imposition of a sponge region within which the local Reynolds number is artificially decreased by a smooth function (Meliga et al. 2012, Paredes et al. 2016) such that homogeneous Dirichlet boundary conditions can be imposed at this boundary.

6.1.5 Local transient growth computation

In order to investigate the potential to the HIFiRE-5 elliptic cone model to sustain algebraic growth of perturbations, a systematic local transient growth analysis is first performed. Both altitudes and conditions analysed are shown in table 6.1. As mentioned before, advantage was taken of the symmetry of the flow around an elliptic cone at zero angle of attack and only one quadrant of the cone was considered. Three axial locations along the streamwise direction have been monitored, $x^* = 0.42$ m, $x^* = 0.52$ m and $x^* = 0.62$ m. At each one of these locations, computations were performed for a relatively large number of azimuthal angles ζ, discretizing the range $0 \leq \zeta \leq 90^\circ$ in 5° increments. The profiles are taken in the wall-normal direction η (see fig. 6.3 and

fig. 6.4). In what follows, $\zeta = 0°$ refers to the attachment-line at the major semi-axis of the cone, $\zeta = 90°$ is the centerline at the minor semi-axis, while $0° < \zeta < 90°$ is the range in which crossflow instability may be encountered. The results are reported as a function of the wave-number parameters, α, in the streamwise direction and β in the azimuthal direction. The maximum $G(t)$ for this combination is plotted as a contour plot. Depending on the magnitude of the peaks of $G_{\max}$ conclusions will be drawn on the modal or nonmodal nature of linear instability of the flow.

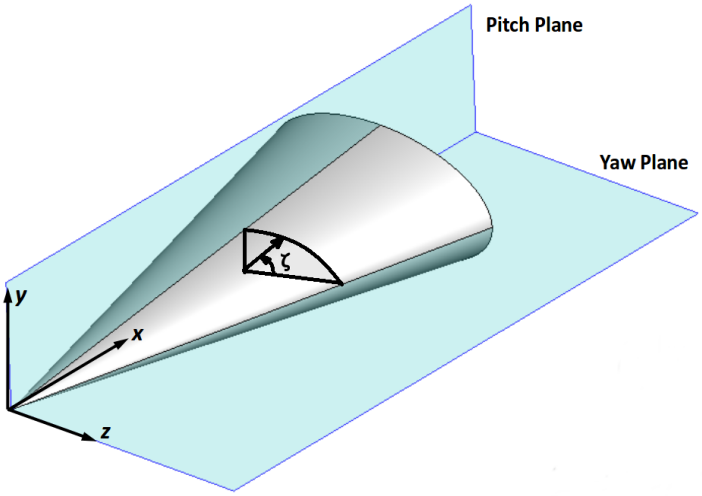

Figure 6.4: Elliptic cone coordinate system adapted from Juliano, Adamczak and Kimmel (2015)

.

Altitude: 33 km

The analysis starts at the highest altitude, where the unit Reynolds number is the smallest. Figures 6.5-6.7 present contour plots of transient growth analysis at the three axial locations examined as a function of the wave-number α and β. Out of the full set of azimuthal angles which the analysis was performed, six characteristic angles were chosen to represent the three main regions of the ellipse: the attachment-line $\zeta = 0°$, the crossflow region $\zeta = 15°$, $40°$, $60°$, $70°$ and the centreline $\zeta = 90°$.

Looking first at the centreline region, figures 6.5-6.7(f) show that transient growth results deliver asymptotic large values of $G(t)$, location at which previous modal analyses (Choudhari, Chang, Jentink, Li, Berger, Candler and Kimmel 2009, Paredes and Theofilis 2015) have predicted the largest amplified centreline global mode.

In the attachment-line region, figures 6.5-6.7(a) shows a smaller value of $G(t)$ in comparison with the exponential values achieved at the centreline. Nevertheless, the values of $G(t)$ are still considered high. These values correspond to the growth of modal instabilities with a growth rate weaker than the centreline case.

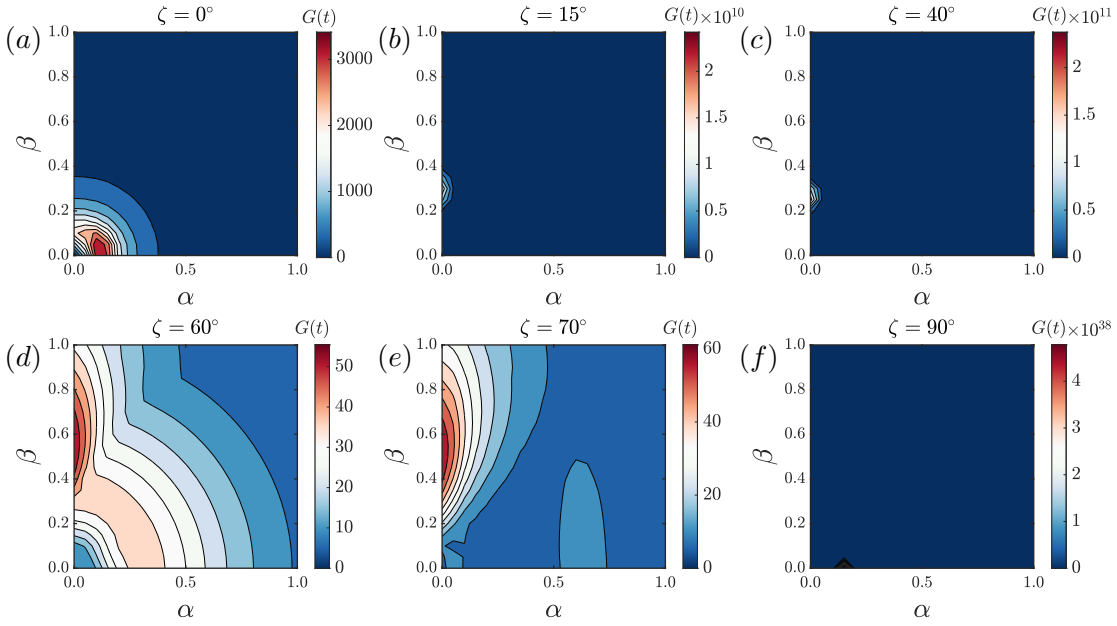

Figure 6.5: Contour plot of $G_{\max}$ at $h = 33$ km and $x^* = 0.42$ m as a function of the streamwise (α) and spanwise (β) wave numbers, at: (a) $\zeta = 0°$; (b) $\zeta = 15°$; (c) $\zeta = 40°$; (d) $\zeta = 60°$; (e) $\zeta = 70°$; and, (f) $\zeta = 90°$.

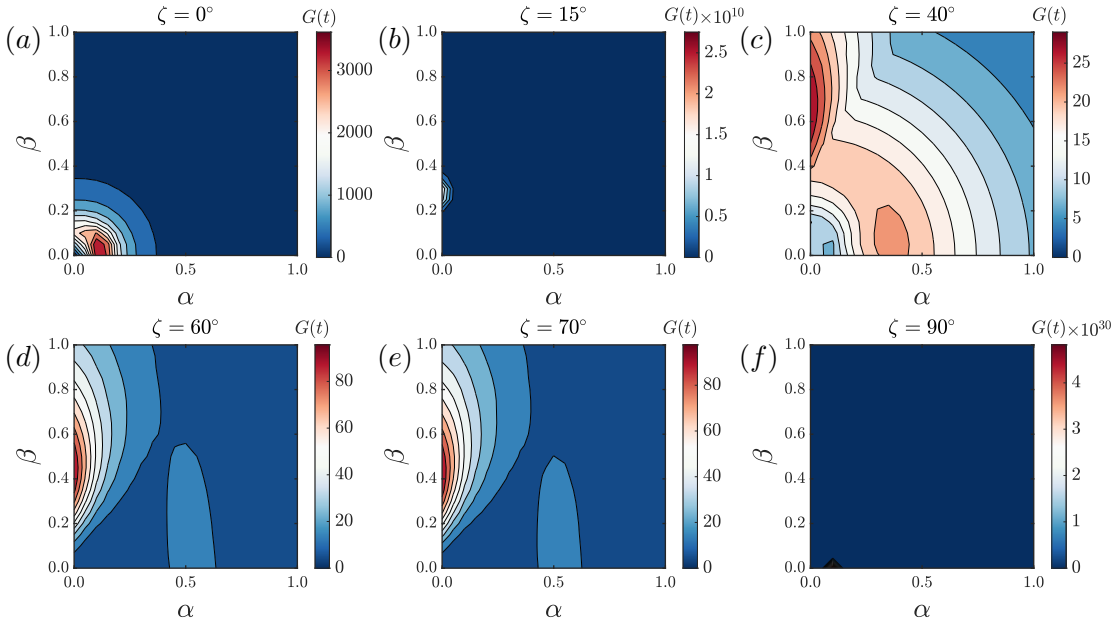

Figure 6.6: Contour plot of $G_{\max}$ at $h = 33$ km and $x^* = 0.52$ m as a function of the streamwise (α) and spanwise (β) wave numbers, at: (a) $\zeta = 0°$; (b) $\zeta = 15°$; (c) $\zeta = 40°$; (d) $\zeta = 60°$; (e) $\zeta = 70°$; and, (f) $\zeta = 90°$.

In the crossflow region of the results presented (fig. 6.5-6.7 (b)-(e)), different phenomena occur as the axial location x^* increases. At $x^* = 0.42$ m, figure 6.5(b) and (c) show exponentially high values of $G(t)$ peaking in the streamwise aligned direction $\beta \approx 0.3$ and $\alpha = 0$. This results corresponds to unstable crossflow disturbances. Interestingly,

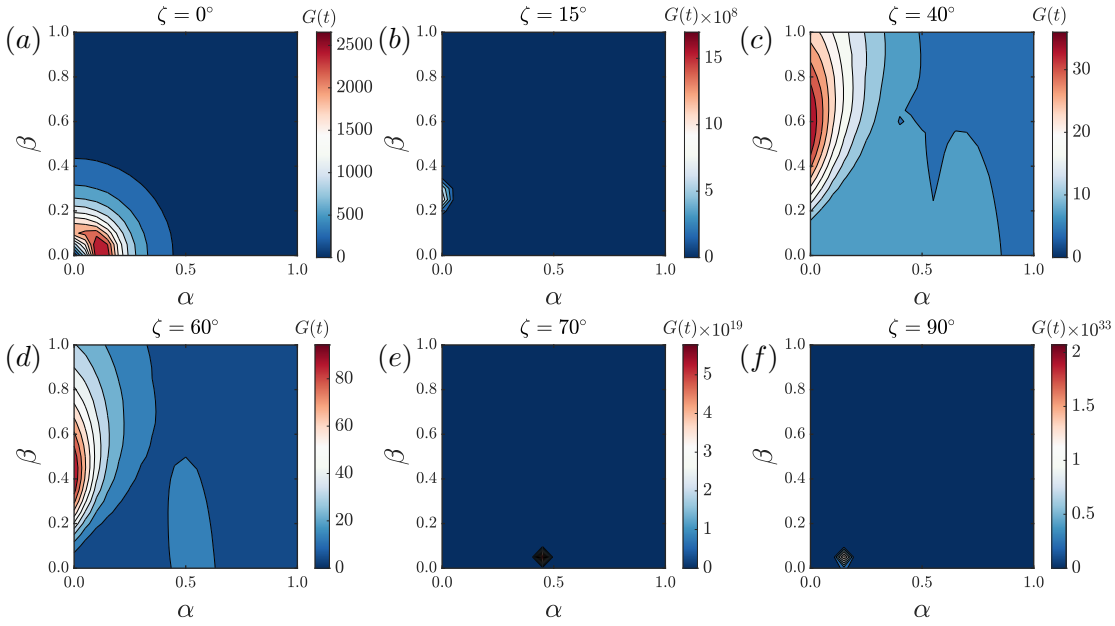

Figure 6.7: Contour plot of $G_{\max}$ at $h = 33$ km and $x^* = 0.62$ m as a function of the streamwise (α) and spanwise (β) wave numbers, at: (a) $\zeta = 0°$; (b) $\zeta = 15°$; (c) $\zeta = 40°$; (d) $\zeta = 60°$; (e) $\zeta = 70°$; and, (f) $\zeta = 90°$.

at $\zeta = 60°$ and $\zeta = 70°$ (fig. 6.5(d) and (e)) a different behaviour is found. No exponential growth exist and $G(t)$ has a finite value ≈ 60. The peak corresponds to a streamwise aligned structure with $\beta \approx 0.5$ and $\alpha = 0$ for both cases. In the next streamwise location, $x^* = 0.52$ m, figures 6.6 (c)-(e) show that one more angle generates finite values of $G(t)$ and therefore the nonmodal region is broaden. Similarly to the previous case, the $G(t)$ peak appears for $\alpha = 0$. However, in the last streamwise location investigated, $x^* = 0.62$ m, figure 6.7(e) presents a strong modal behaviour with non-zero values of α and β; this corresponds to an oblique disturbance. The finite values of $G(t)$ appears again in figures 6.7(c) and (d). The peak continues to exist for $\alpha = 0$. In other words, this case is a candidate to have algebraic nonmodal growth of instabilities in the crossflow region of the hypersonic flow on the elliptic cone and therefore needs to be further investigated in a global analysis.

Altitude: 21 km

For the sake of comparison with results at the higher altitude, Figures 6.8-6.10 present contour plots of transient growth analysis at 21 km altitude, at the same axial and azimuthal locations as results shown in the previous higher altitude. At this lower altitude, at which the modal global analysis of Paredes et al. (2016) was performed, the Reynolds number is an order of magnitude higher, and the first qualitative difference compared with the 33 km altitude case is at the attachment line, $\zeta = 0$. Figures 6.8-6.10(a) show that the maximum value of $G(t)$ corresponds to $\alpha = 0$ and $\beta = 1$. At the

first location, $x^* = 0.42$m (fig. 6.8(a)), the peak is for $G(t) \approx 25$ and it grows until $G(t) \approx 50$ at the last location, $x^* = 62$m (fig. 6.10(a)).

In the crossflow region, the first azimuthal location closest to the attachment-line (fig. 6.8-6.10(b)) provides the same qualitatively behaviour as encountered in the attachment-line, namely a peak in the growth for $\alpha = 0$, $\beta = 1$. The next three azimuthal locations investigated (fig. 6.8-6.10(c)-(e)) the type of the dominant structure changes completely. Their magnitude has increased to exponential values, showing that the modal scenario is the dominant one for more locations at this altitude. Moreover, the maximum value of $G(t)$ is associated with a oblique mode (α and $\beta \neq 0$). Finally, at the centreline $\zeta = 90°$ (fig. 6.8-6.10(f)), the gain is related to modal instability, with asymptotic large values of $G(t)$, as expected and found in the analysis of Paredes et al. (2016).

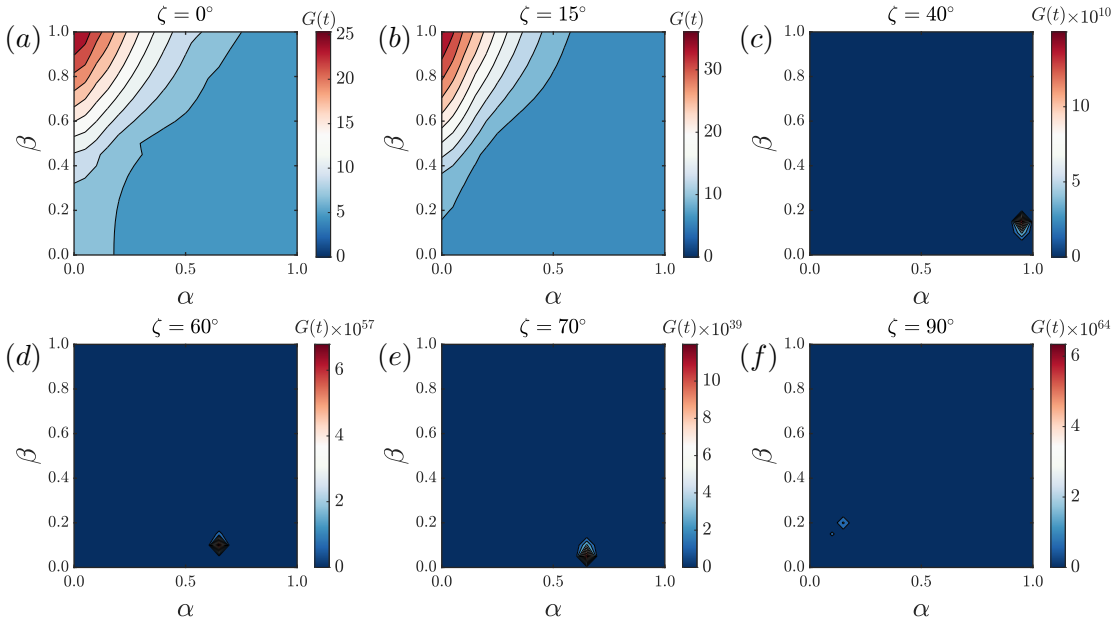

Figure 6.8: Contour plot of $G_{\max}$ at $h = 21$ km and $x^* = 0.42$ m as a function of the streamwise (α) and spanwise (β) wave numbers, at: (a) $\zeta = 0°$; (b) $\zeta = 15°$; (c) $\zeta = 40°$; (d) $\zeta = 60°$; (e) $\zeta = 70°$; and, (f) $\zeta = 90°$.

The strong assumption of streamwise and spanwise homogeneity that underlies local linear theory prevents drawing conclusions regarding whether linear instability will follow a modal or a nonmodal growth scenario at these altitudes. Motivation is thus provided to relax the assumption of homogeneity along the spanwise direction and perform transient growth of the two-dimensional base flows defined on planes normal to the elliptic cone axis, thus taking into account the cone curvature; this analysis will be presented in the next section.

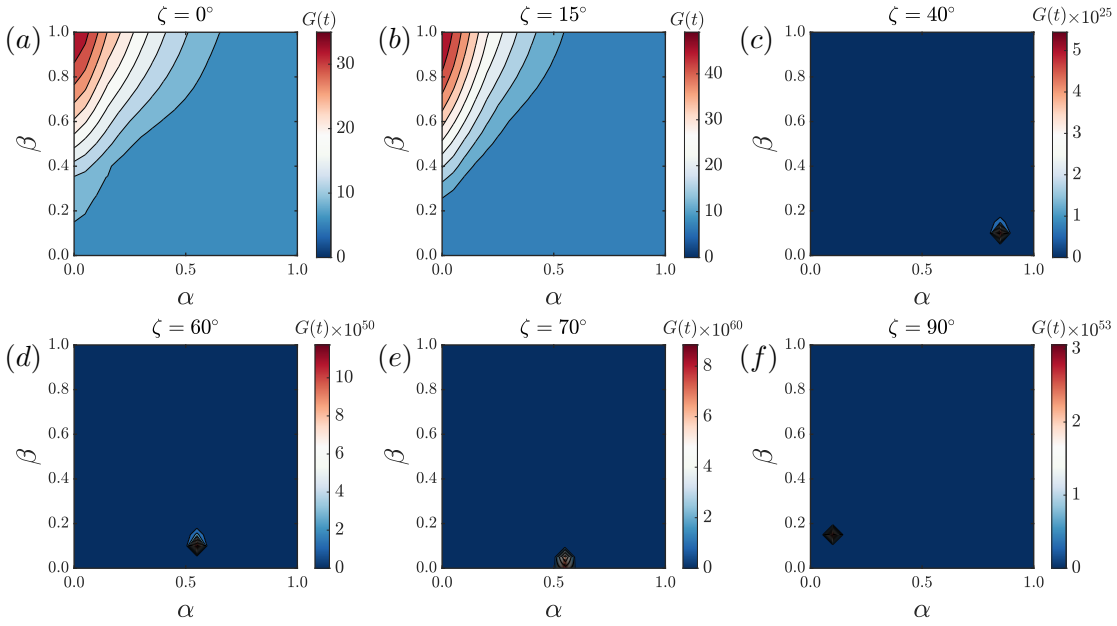

Figure 6.9: Contour plot of $G_{\max}$ at $h = 21$ km and $x^* = 0.52$ m as a function of the streamwise (α) and spanwise (β) wave numbers, at: (a) $\zeta = 0°$; (b) $\zeta = 15°$; (c) $\zeta = 40°$; (d) $\zeta = 60°$; (e) $\zeta = 70°$; and, (f) $\zeta = 90°$.

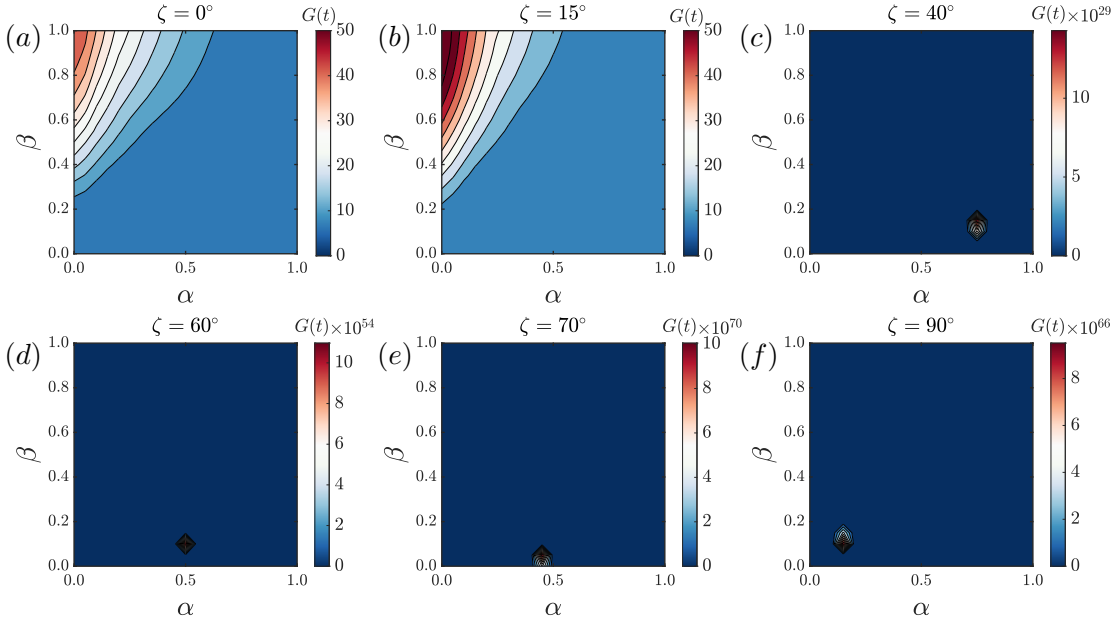

Figure 6.10: Contour plot of $G_{\max}$ at $h = 21$ km and $x^* = 0.62$ m as a function of the streamwise (α) and spanwise (β) wave numbers, at: (a) $\zeta = 0°$; (b) $\zeta = 15°$; (c) $\zeta = 40°$; (d) $\zeta = 60°$; (e) $\zeta = 70°$; and, (f) $\zeta = 90°$.

6.1.6 Modal linear stability calculation

Before discussing global nonmodal stability analysis, the two-dimensional eigenvalue problem solved by Paredes et al. (2016) is revisited. This was found to be necessary not only as verification of the results obtained herein, which used an altogether different

numerical strategy for the solution of the EVP and SVD problems compared with Paredes et al. (2016) but, equally importantly, in order to assess numerical parameters (such as the Krylov subspace size) used to access a large part of the global eigenspectrum besides its leading members, an aspect that was found to be essential for the convergence of nonmodal analysis results.

Table 6.2 presents grid convergence results for the complex eigenvalue ω of the most amplified eigenmode as a function of spatial resolution at both of the 21 km and 33 km altitudes. In addition, the logarithmic derivative of the gain function, $G(t)$, at a sufficient large time is presented at the highest resolution, in order to facilitate comparisons with the amplification/damping rate obtained in the solution of the EVP. Table 6.2 also presents the peak value of G at the respective time parameter, $t_{\text{opt}} = 250$ at 21 km altitude and $t_{\text{opt}} = 200$ at 33 km altitude. At both altitudes a convergence criterion of five significant digits has been imposed for the most unstable eigenvalue. The parameters have been non-dimensionalized by a length scale of $L_{\text{ref}} = \sqrt{0.5/Re'}$ and by the velocities presented in table 6.1.

Focusing on the modal result, ω, first, the results of table 6.2 shows the expected fact that substantially higher resolutions are required for the preset convergence criterion to be met at the lower altitude, where the Reynolds number is one order of magnitude higher than that at the higher altitude.

21 km					
Grid	$\omega_r \times 10$	$\omega_i \times 10^3$	$\frac{d \ln G(t)}{dt}\|_{t=t_\infty}$	G_{opt}	t_{opt}
161^2	0.8619	6.10		1016	270
171^2	0.8619	6.09		743	250
181^2	0.8619	6.09	0.00606	745	250

33 km					
Grid	$\omega_r \times 10$	$\omega_i \times 10^3$	$\frac{d \ln G(t)}{dt}\|_{t=t_\infty}$	G_{opt}	t_{opt}
81^2	1.0046	3.61		1714	-
91^2	1.0044	3.61		284	200
101^2	1.0044	3.61	0.00367	283	200

Table 6.2: Grid convergence for 33km altitude at streamwise location $x^* = 0.36$m from the elliptic cone tip using symmetric boundary conditions. The Krylov subspace was set to m = 3501 and the wave-number $\alpha = 0.11$.

Centreline instabilities

To further verify the EVP results delivered by the *LiGHT* code, color contours of the streamwise velocity magnitude of the most unstable centreline mode is presented in fig. 6.11 for both (a) symmetric and (b) antisymmetric centreline boundary conditions. The black isolines correspond to contours of the associated baseflow varying from 0

to 0.9 in 0.1 steps. The conditions chosen are the same as the conditions reported in Paredes et al. (2016), namely 21 km altitude and streamwise position $x^* = 0.52$ m from the elliptic cone tip. The latter authors performed a spatial BiGlobal analysis, while in this thesis a temporal framework is employed. For the sake of comparison, Gaster's transformation was used to transform the growth rate from temporal to spatial (Gaster 1962). Even though the transformation is only strictly valid close to neutral stability, good agreement is seen when comparing the temporal growth rate transformed to spatial $\alpha_{\mathrm{i,Sym}} = -0.0091$ and $\alpha_{\mathrm{i,Asym}} = -0.0088$ obtained in the present analysis with the spatial analysis results $\alpha_{\mathrm{i,Sym}} \approx -0.0998$ and $\alpha_{\mathrm{i,Asym}} \approx -0.0094$ of Paredes et al. (2016). The dimensional frequency of the most unstable symmetric and antisymmetric modes reported from the spatial analysis are $F = 230$ and 220 kHz, respectively. The temporal modes obtained herein can be obtained using the (dimensionless) result for ω_r by

$$F = \omega_r \frac{U_\infty}{2\pi L_{\mathrm{ref}}}, \tag{6.4}$$

giving $F = 200$ and 190 kHz for the most unstable symmetric and antisymmetric modes, respectively. The amplitude functions function of the leading centreline symmetric mode obtained in the present temporal analysis is shown in figure 6.11 (a) and that for the antisymmetric mode in figure 6.11 (b); respectively, they are seen to peak at the symmetry line and the immediate vicinity of the centreline. As already pointed out by Paredes et al. (2016), this feature is not observed in the lower Reynolds number behaviour near the centreline where the modes peak away from symmetric plane at z = 0.

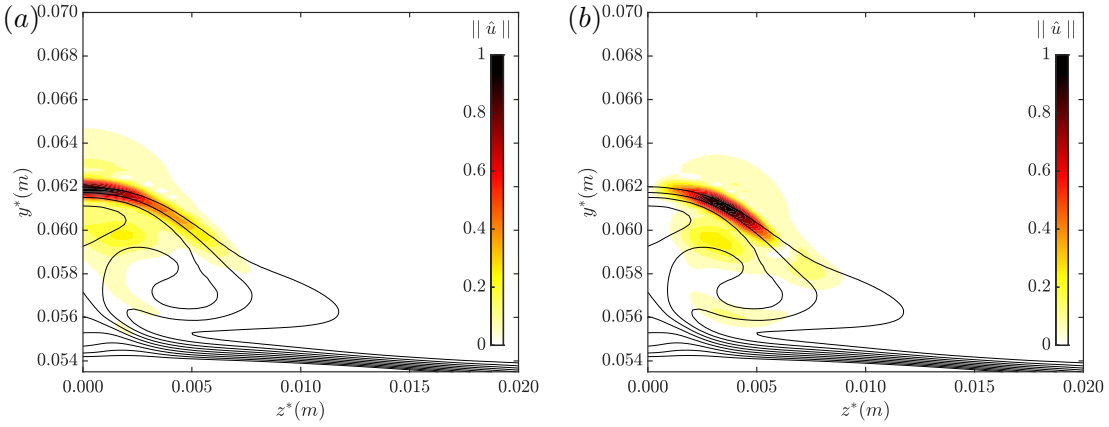

Figure 6.11: Streamwise velocity magnitude $|\hat{u}|$ of the leading symmetric (a) and antisymmetric (b) centreline modes at $x^* = 0.52$ m. The black lines are isocontours of the base flow ($\bar{u} = 0{:}(0.1){:}0.9$) (cf. Paredes et al. (2016)) .

Attachment line instabilities

As a final verification of the present implementation, the attachment line modes reported by Paredes et al. (2016) are recovered on the rightmost part of the mesh shown in Figure 6.3. Figure 6.12 presents the streamwise velocity magnitude of the most amplified symmetric and antisymmetric attachment line modes at $x^* = 0.52$ m. Following the same reasoning of the centreline mode, performing a Gaster's transformation in the present temporal results give a spatial growth rate of $\alpha_{\mathrm{i,S}} = -0.0172$ and $\alpha_{\mathrm{i,A}} = -0.0154$. These results are also in relatively good agreement with the results of $\alpha_{\mathrm{i,S}} \approx -0.0194$ and $\alpha_{\mathrm{i,A}} \approx -0.0168$ reported by Paredes et al. (2016). As in the comparison of centreline mode instabilities, an iteration on the wave-number parameter has revealed that the most unstable mode has a non-dimensional wave-number of 1.18 for both symmetric and antisymmetric mode, corresponding to a dimensional wave length of 1.2 mm. The non-dimensional frequency is close to unity, corresponding to the high-frequency results of ≈ 1700 kHz shown by Paredes et al. (2016) for both modes. The amplitude functions are concentrated inside the boundary layer. Qualitatively, the mode shapes of these attachment-line modes is analogous to that of the centreline modes, namely all components but the azimuthal peaks at the attachment line symmetry plane if symmetric boundary conditions are used and the opposite happens if antisymmetric boundary conditions are imposed at the symmetry plane.

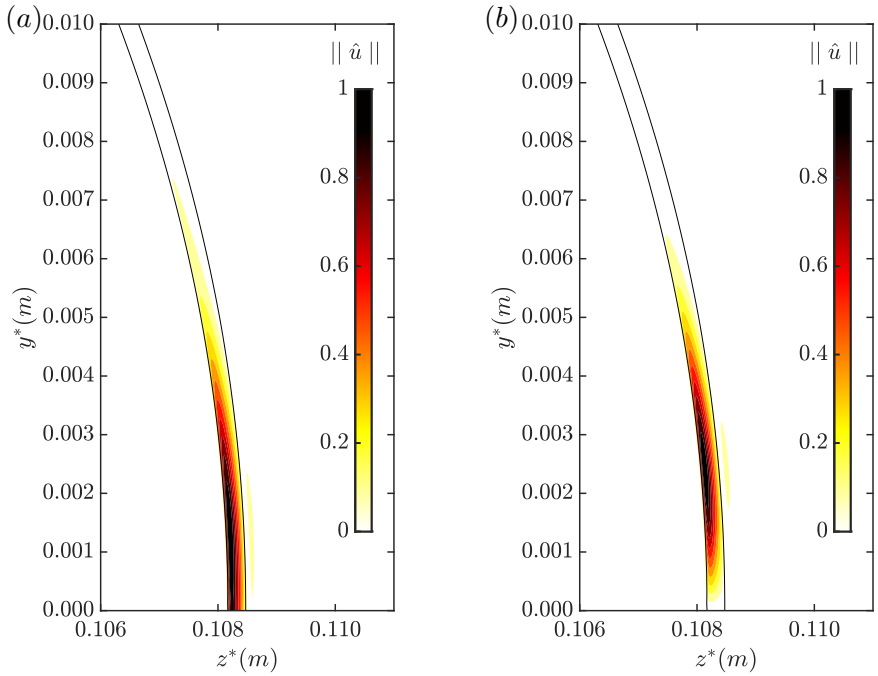

Figure 6.12: Streamwise velocity magnitude $|\hat{u}|$ of the leading symmetric (a) and antisymmetric (b) attachment line modes at $x^* = 0.52$ m. The black lines are isocontours of the base flow ($\bar{u} = 0$ and 0.9) (cf. Paredes et al. (2016)).

6.1.7 Global transient growth computation

Global transient growth analysis is performed at the two altitudes and the conditions presented in table 6.1. At each altitude, temporal global transient growth analysis is performed on base flows defined on planes normal to the cone axis at four streamwise locations, $x^* = 0.36$ m, 0.42 m, 0.52 m and 0.62 m, and homogeneity is assumed along the streamwise direction x.

The domain in which nonmodal stability analysis is performed has been reduced to include the centreline and the crossflow regions, $\pi/4 \leq \zeta \leq \pi/2$; as will be discussed in what follows; further numerical details have been presented in chapter 4. As observed by Paredes et al. (2016), symmetric disturbances are (modally) more unstable modes than their antisymmetric counterparts. This behaviour has also been confirmed by the present analysis, in both of the modal (long-time) and nonmodal (short-time) linear instability scenarios and henceforth, only results with symmetric boundary conditions will be presented; nonmodal growth of antisymmetric perturbations was found to be qualitatively identical with that exhibited by symmetric perturbations.

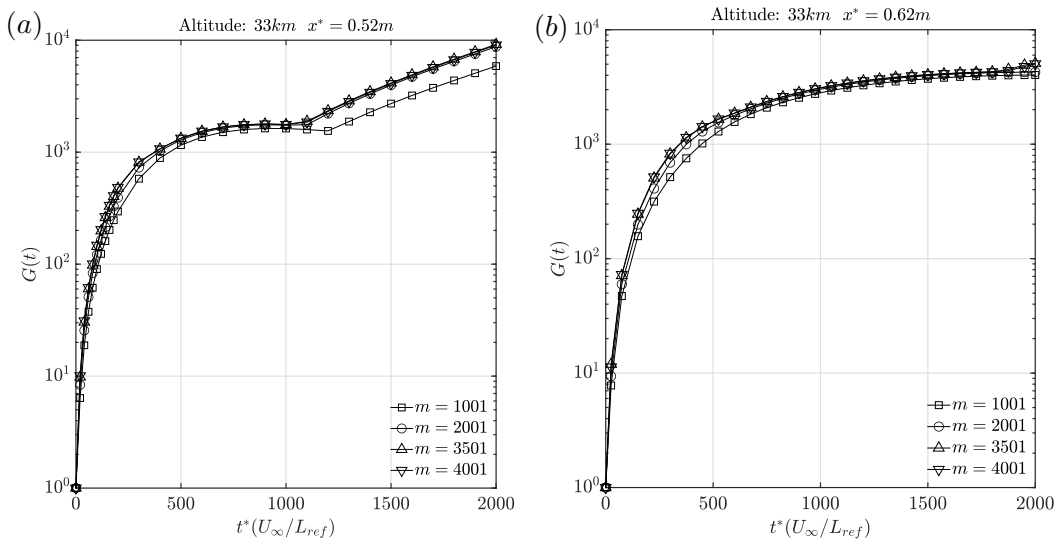

Figure 6.13: Comparison of the energy growth $G(t)$ for four different Krylov subspace m. The energy growth curves were obtained at (a) $x^* = 0.52$ m and (b) $x^* = 0.62$ m, at 33 km altitude and for $\alpha = 0$.

As discussed in chapter 3, transient growth calculation is restricted to a space spanned by a selected number of eigenfunctions. In what follows, at both altitudes studied, the Krylov subspace dimension m was varied between $m = 1001$ and 4001. Figure 6.13 shows examples of this variation for two different streamwise locations, $x^* = 0.52$ m and $x^* = 0.62$ m, at 33 km altitude. For the smallest subspace analysed, $m = 1001$, the correct shape of the energy gain curve is recovered, showing transient growth at short time, followed by exponential growth, for which the rate is also recovered. However, this

subspace *underpredicts* the energy gain values. Increasing the subspace to $m = 2001$, the exponential growth is already fully recovered and only at short time $t < 500$, the value of gain changes. Both curves for $m = 3501$ and $m = 4001$ overlap and therefore all subsequent calculations have been performed using $m = 3501$, to guarantee convergence of the transient growth results.

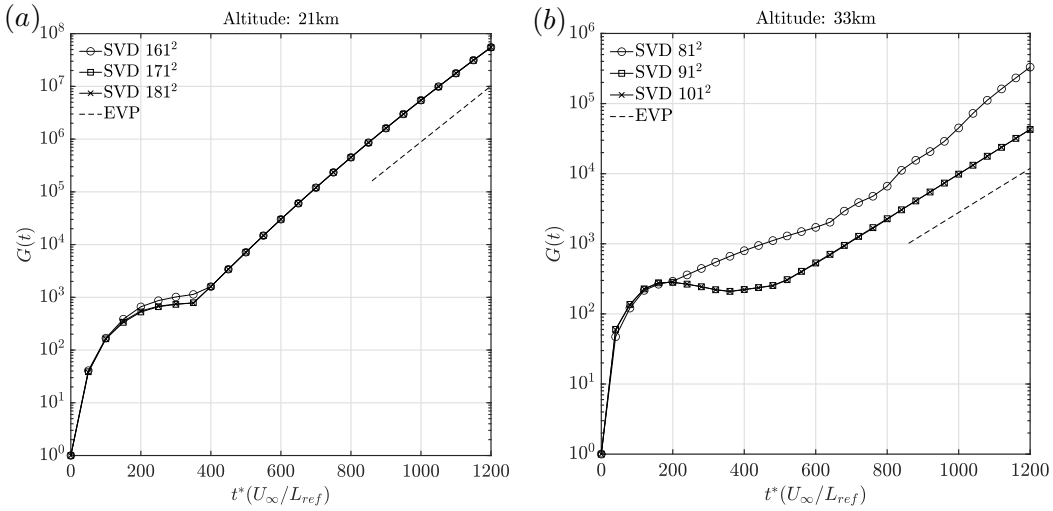

Figure 6.14: Comparison of the energy growth $G(t)$ for the three different grids analysed. The energy growth curves were obtained at (a) 21 and (b) 33km altitude, with $\alpha = 0.11$ and at x^*=0.36m. The dashed line represents the slop of the most unstable eigenvalue calculated from the EVP analysis.

In respect to grid convergence, table 6.2 presents the changes in the gain function for different grids. The resolutions used at the respective first grid, 161^2 for 21km altitude and 81^2 for 33km altitude, is insufficient to correctly predict the changes in the energy gain, even though these resolutions are adequate for reliable performance of modal analysis and prediction of the characteristics of the most unstable eigenmode. Figure 6.14 shows the energy gain over non-dimensional time for the three different grids at 21 km altitude and 33 km altitude. The notation here used for the maximum value of the energy gain at short time is G_{opt} and at asymptotically large time is G_∞. The results shown quantitatively in table 6.2 are visualised well in figure 6.14, where it can be seen that the resolutions of 171^2 spectral collocation nodes at the lower altitude, and 91^2 nodes at the higher altitude the entire respective $G(t)$ curves are identical with those corresponding to the more refined grids, 181^2 at 21 km and 101^2 at 33 km.
The final verification is regarding the ability of the present SVD implementation to recover the most unstable eigenvalue/growth rate delivered by solution of the EVP. The slope of the energy curve asymptotically grows at the rate of

$$G_\infty \approx e^{2\omega_i t_\infty} \tag{6.5}$$

and the values obtained are displayed in table 6.2. At the highest resolution at which

the SVD has been solved, excellent agreement is observed between the results of the IVP and EVP at both altitudes. This agreement is graphically shown in figure 6.14, where the slope corresponding to the EVP result is drawn by a dashed line and the fact that the respective $G(t)$ curves become parallel to these dashed lines graphically demonstrates the agreement shown numerically in table 6.2.

Parametric study

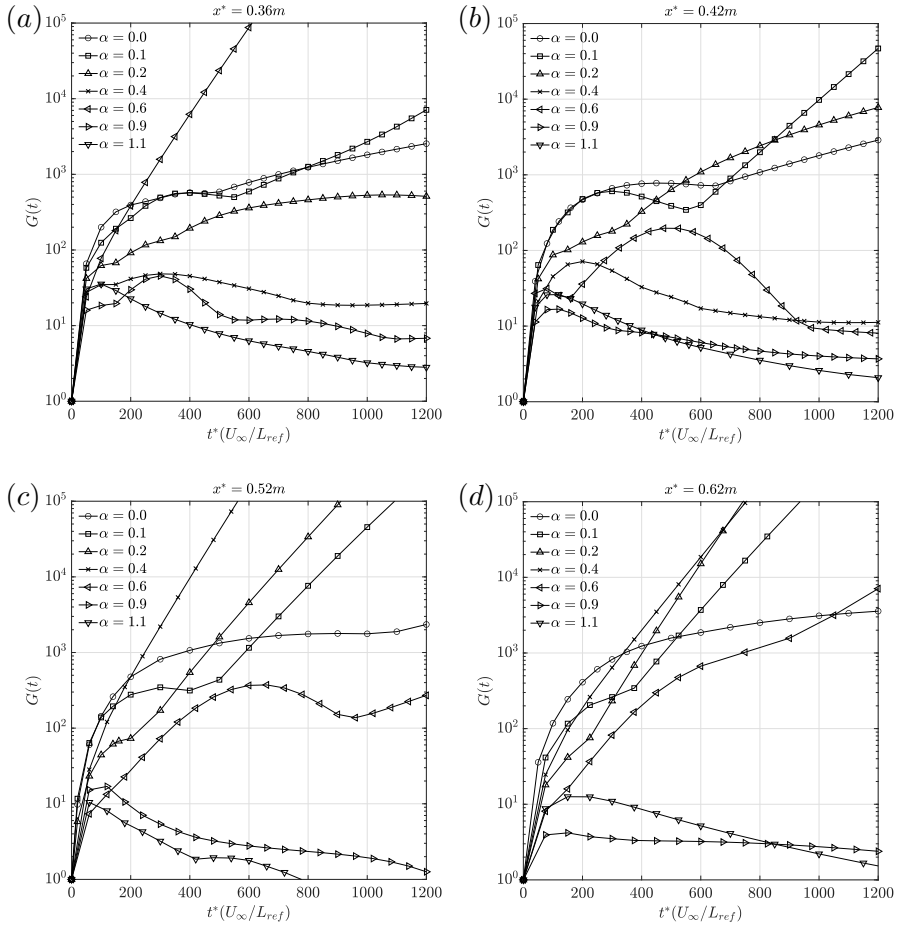

Figure 6.15: Variation in the streamwise wave-number α and the resulting transient energy growth at 33 km altitudes and streamwise locations (a) $x^* = 0.36$ m, (b) $x^* = 0.42$ m, (c) $x^* = 0.52$ m and $x^* = 0.62$ m

The streamwise wave-number α is studied to identify the perturbation responsible for the largest algebraic growth at short time, when the approximation of azimuthal base flow homogeneity from the local analysis is relaxed. Figure 6.15 shows an alpha loop iteration between $\alpha = 0$ to $\alpha = 1.1$, corresponding to a streak $\alpha = 0$ and wave-lengths varying from 32 mm to 3 mm, respectively. For all streamwise locations analysed, namely $x^* = 0.36$ m, $x^* = 0.36$ m, $x^* = 0.42$ m, $x^* = 0.52$ m and $x^* = 0.62$ m, the largest peak at short time appears for the structure aligned with the streamwise

direction $\alpha = 0$, as previously suggested by the local transient growth analysis. All the waves with $\alpha > 0.6$, and therefore wave-lengths smaller than 5.3 mm, decay after a small transient growth and even though other waves produce larger growth of the energy at short time, they are always smaller than the $\alpha = 0$ case.

Nonmodal linear stability analysis of streamwise-aligned perturbations

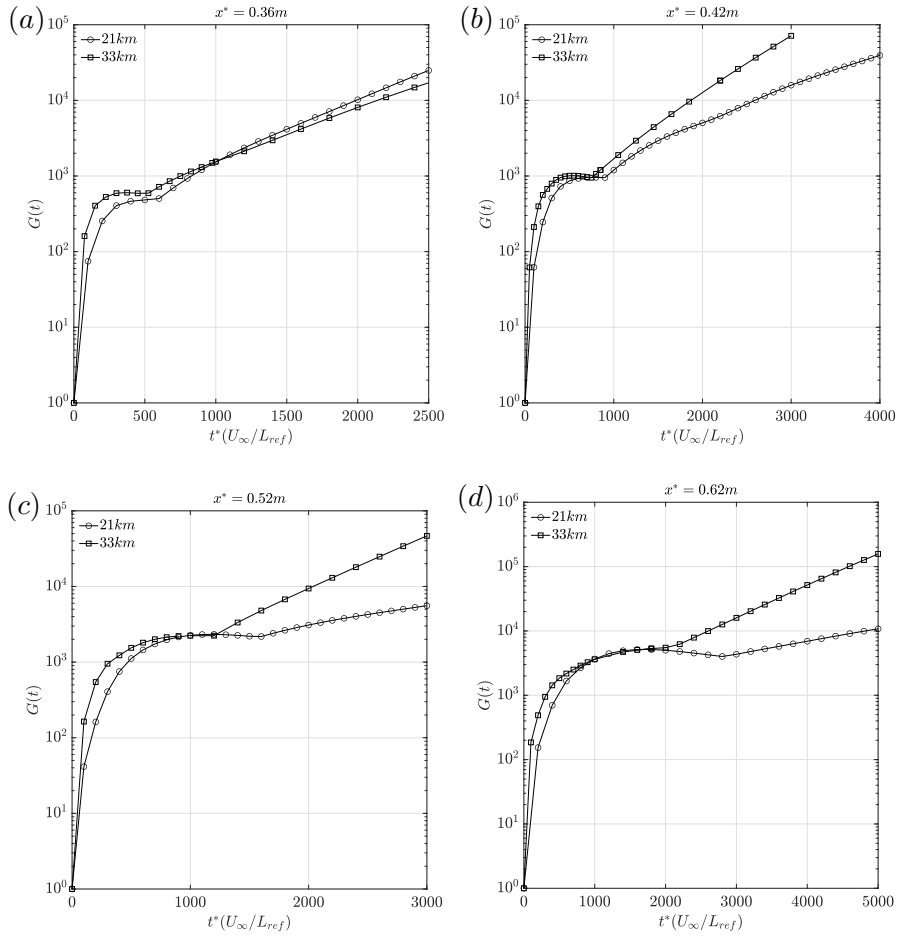

Figure 6.16: Comparison of transient energy growth at 21 km and 33 km altitudes with α=0 at streamwise locations (a) $x^* = 0.36$ m, (b) $x^* = 0.42$ m, (c) $x^* = 0.52$ m and $x^* = 0.62$ m

Recapitulating, the initial value problem (IVP) detailed in chapter 3 is solved in which time is a parameter. Different initial conditions will generate algebraic growth of energy $G(t)$ with its corresponding maximum value, however the optimal initial condition at one time is not necessarily that obtained by solution of the IVP at a different time. The gain curve can be interpreted as an envelope over all possible optimal initial conditions. Moreover, since at asymptotically large time it has been shown that the solutions of the IVP and the EVP coincide, it is to be expected that the structures of the optimal condition at large time will correlate well with the eigenfunctions of the

most unstable/least stable flow eigenmode.

Figure 6.16 shows transient growth of energy $G(t)$ as a function of non-dimensional time at the streamwise locations (a) $x^* = 0.36$ m, (b) $x^* = 0.52$ m, (c) $x^* = 0.42$ m and (d) $x^* = 0.62$ m. In each of the plots the transient growth of energy is shown at the two altitudes examined. The streamwise wave-number analysed is $\alpha = 0$, corresponding to structures aligned with the streamwise direction, that were found to sustain transient growth in the preceding local analysis. At all four locations, two qualitatively different behaviours of $G(t)$ are documented in these figures: at early times, energy grows algebraically up to levels of $O(10^3)$ before decaying; at longer times, modal growth overtakes the early nonmodal behaviour. At either of the two altitudes, the peak value of $G_{\max}$ grows monotonically with x, while the energy gain at short-time is always larger at 33 km altitude than the energy gain found at 21 km.

The dependence on Re_x of the maximum value reached by $G(t)$ during the stage of algebraic growth is plotted in figure 6.17 for both altitudes examined. Several significant observations may be made in these results. Firstly, as could already be seen in the results of 6.16, at the higher altitude the maximum value reached by G is larger: the value reached at $x^* = 0.72$ m at 33 km is $\sim 1.5\times10^4$, which corresponds to an equivalent $N-$factor (Barker et al. 2019) of

$$N_{\mathrm{TG}} = \frac{1}{2}\ln G_{\max} \approx 4.8. \tag{6.6}$$

	x^* (m)	0.36	0.42	0.52	0.62	0.72
21km	$Re_x \times 10^{-6}$	3.85	4.49	5.56	6.63	7.70
	$G(t_{opt})$	483.01	958.74	2167.40	5169.85	9276.20
	t_{opt}	500	772	1176	1700	2296
33km	$Re_x \times 10^{-6}$	0.68	0.79	0.98	1.17	1.36
	$G(t_{opt})$	602.98	1009.87	2233.78	5341.04	14198.90
	t_{opt}	356	531	1023	1827	3501

Table 6.3: Relationship between $G(t_{opt})$ and the different axial locations and respective Re_x along the elliptic cone model for both 21 km and 33 km altitude.

Such N-factor values are typically associated with laminar-turbulent transition of stationary crossflow vortices in the incompressible regime (Bippes 1999) and are certainly considered sufficiently high to lead the laminar flow to transition. In the present analysis, algebraically-growing perturbations are demonstrated to also reach $N_{\mathrm{TG}} \approx 5$ through the alternative nonmodal linear instability mechanism that can potentially be responsible for transition; we will return to the question of the associated structures, quantified as linear optimal perturbations, in what follows. Secondly, at the

lower altitude, where appreciable transient energy growth, $N_{\mathrm{TG}} \approx 4.6$, is also documented, a quadratic dependence of $G_{\max}$ on Re_x is found in the present hypersonic flow. However, at the higher altitude, this dependence is found to be closer to quartic,

$$G_{\max} \sim Re_x^4, \tag{6.7}$$

as can be seen in the curve fit of the 33 km results shown in figure 6.17. These results offer strong indications that the nonmodal laminar-turbulent transition scenario increases in significance as the flow altitude increases and the Reynolds number decreases. Ultimately, in all cases studied so far, after an initial algebraic growth, the energy gain curve grows exponentially at the same rate as the most unstable eigenvalue predicted by the modal theory. In this respect, the relative significance of the two linear laminar-turbulent transition scenarios will be determined by the level of environmental perturbations triggering either of the modal or nonmodal path to transition. When these perturbations are vanishingly small, modal growth, as first described by Paredes and Theofilis (2015) and Paredes et al. (2016) may prevail; however, when such perturbations are found at sufficiently large, though still linear, initial amplitudes, the $N-$factor values documented herein are capable of leading flow to transition through transient growth mechanisms that bypass the modal scenario.

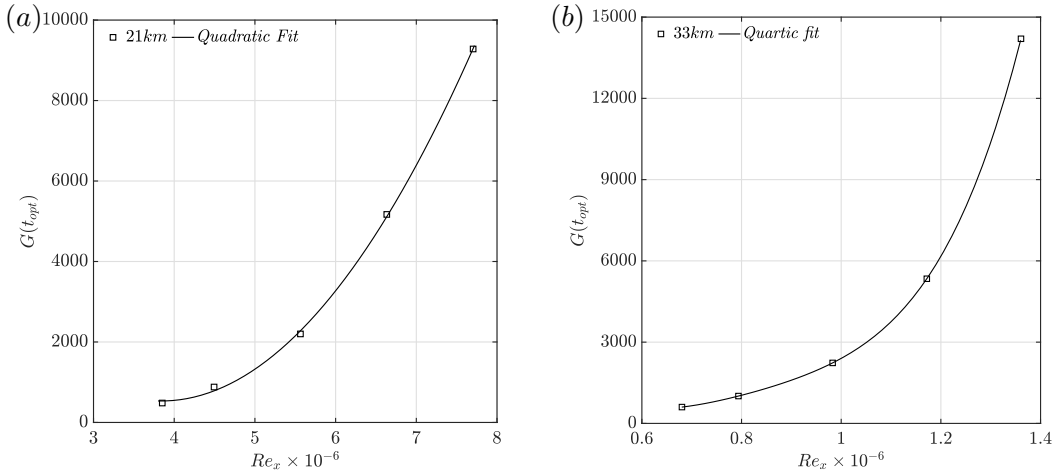

Figure 6.17: Best fit of the Gain function at $t = t_{opt}$ as function of Re_x: (a) 21 km altitude *quadratic* fit, (b) 33 km altitude *quartic* fit.

In what follows, an in-depth nonmodal analysis of flow is presented at the highest altitude 33 km altitude and $\alpha = 0$, which was seen in local analysis to correspond to maximum transient energy growth. The linear optimal initial conditions and the structures obtained at $t = t_{\mathrm{opt}}$, corresponding to maximum transient energy gain, are plotted as color contours of the real part of perturbation density, $\hat{\rho}$, in figure 6.18 and streamwise perturbation velocity component, $\hat{u}$, in figure 6.19. Other perturbation quantities are not shown for brevity, since they also show the exact same qualitative behaviour as the density and streamwise perturbation velocity components. In both

figures three columns, corresponding from left to right to $t = 0, t = t_{\text{opt}}$ and $t \to \infty$, and five rows, corresponding from upper to lower to $x^* = 0.36$ m, 0.42 m, 0.52 m, 0.62 m and 0.72 m are shown. The time $t = t_{\text{opt}}$ is the same at which the results of table 6.3 and figure 6.17 have been presented. Both $\hat{\rho}(y, z)$ and $\hat{u}(y, z)$ amplitude functions reveal a consistent picture of linear disturbance physics. The linear optimal initial condition corresponds to a structure located in the crossflow region on the cone. At the linear optimal time, t_{opt} this structure remains qualitatively at the same location, though it changes is magnitude. However, as $t \to \infty$, this transiently amplifying, streamwise aligned (owing to $\alpha = 0$) structure moves toward the centerline of the cone. The structure prevailing at asymptotically large times is indeed that recovered as the most unstable eigenvalue of modal analysis (Paredes et al. 2016). However, as the quantification of the $G_{\max}$ in equation (6.7) has indicated, it is likely that the two mechanisms may compete and the answer to which one will prevail may well depend on the level of environmental perturbations. In this context, comparisons with the ground-based experiments of Borg et al. (2012), which clearly documented streamwise-aligned structures in the flow, is in order here.

Qualitative comparisons with ground-based experiments

The present transient growth results reinforce the findings of local analysis (Quintanilha Jr et al. 2018) on the existence of algebraically growing, streamwise-aligned structures on the elliptic cone surface. In the absence of direct in-flight measurements on the HIFiRE-5 elliptic cone, information on these elongated structures is sought in the BAM6QT experiments of Borg et al. (2012). These experiments used a 38.1% scale model of the HIFiRE-5 elliptic cone with Mach number of $Ma = 6$ and an unit Reynolds number of $Re' = 8.1{\times}10^6$. Figure 6.20(a) shows the top view of the elliptic cone model.

A geometrical procedure is used to estimate length scales and the spacing between the vortical structures observed in the experiment. The known model length of $L_x \approx 0.25$ m and the angle of $\approx 14^\circ$ between the centreline and the attachment-line in the top view, leads to a trigonometric relationship to estimate the spanwise length $\Lambda \approx 0.06$ m. The number of streamwise structures visible within the length Λ can be counted as $N_z \approx 10 - 14$, from which the average spacing between the distinct structures seen in the experiment can be approximated as $\Delta_z \approx 4 - 7$ mm. Turning to the local transient growth analysis performed herein, the non-dimensional wave-number $\beta \approx 0.5$ shown in figures 6.5 and 6.6 is made dimensional by the reference length used in the analysis, yielding an approximation of the local theory spanwise spacing, $\Delta_z = 2\pi/\beta = 6.4$ mm. On the other hand, the spacing between the structures obtained in the transient growth analysis is shown in figures 6.18 and 6.19; the peak-to-peak distance between a full period of the structures in the crossflow region can also be estimated as

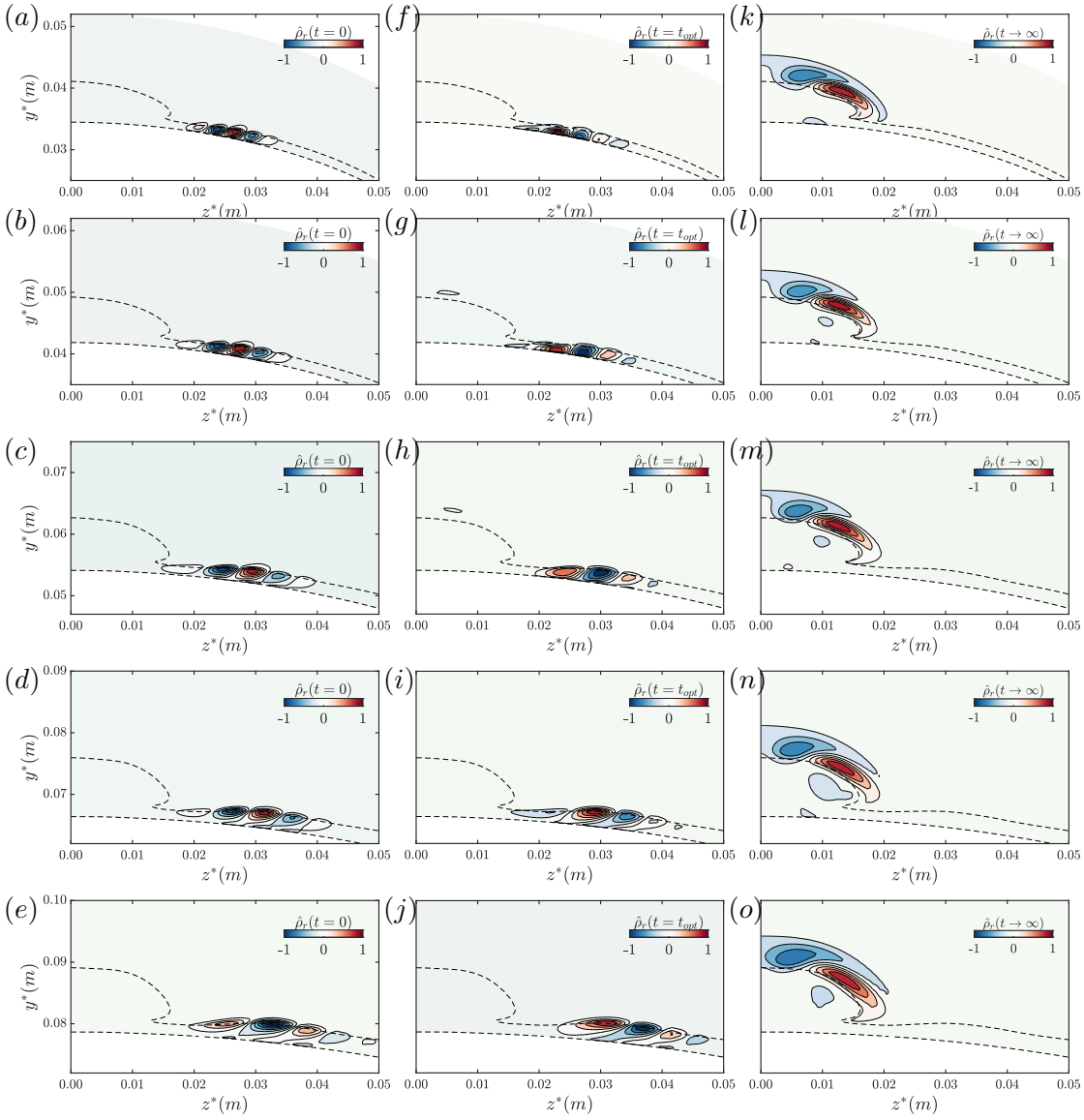

Figure 6.18: Real part of perturbation density $\hat{\rho}_r$ with $\alpha = 0$. The first column (a-e) corresponds to the optimal initial condition $t = 0$, the middle column (f-j) to the associated optimal perturbation $t = t_{\text{opt}}$ and the right column (k-o) to the long time behaviour $t \to \infty$. Each row corresponds to a different streamwise location along the elliptic cone surface, namely $x^* = 0.36$ m (a,f,k), $x^* = 0.42$ m (b,g,l), $x^* = 0.52$ m (c,h,m), $x^* = 0.62$ m (d,i,n) and $x^* = 0.72$ m (e,j,o). The blacks isolines correspond to contours of the steady base flow ($\bar{u} = 0$ and 0.95).

$\Delta_z \approx 6.5$ mm. As such, the estimated and computed spacing between the maximally amplified streamwise-aligned structures in local and two-dimensional transient growth analyses are practically identical and, interestingly, also coincide with the spacing of the structures seen in the experiments, despite the quantitative differences between the parameters (like Boundary-layer thickness and wall temperature, for instance) at which the experiments were performed and those of the present analyses. In other

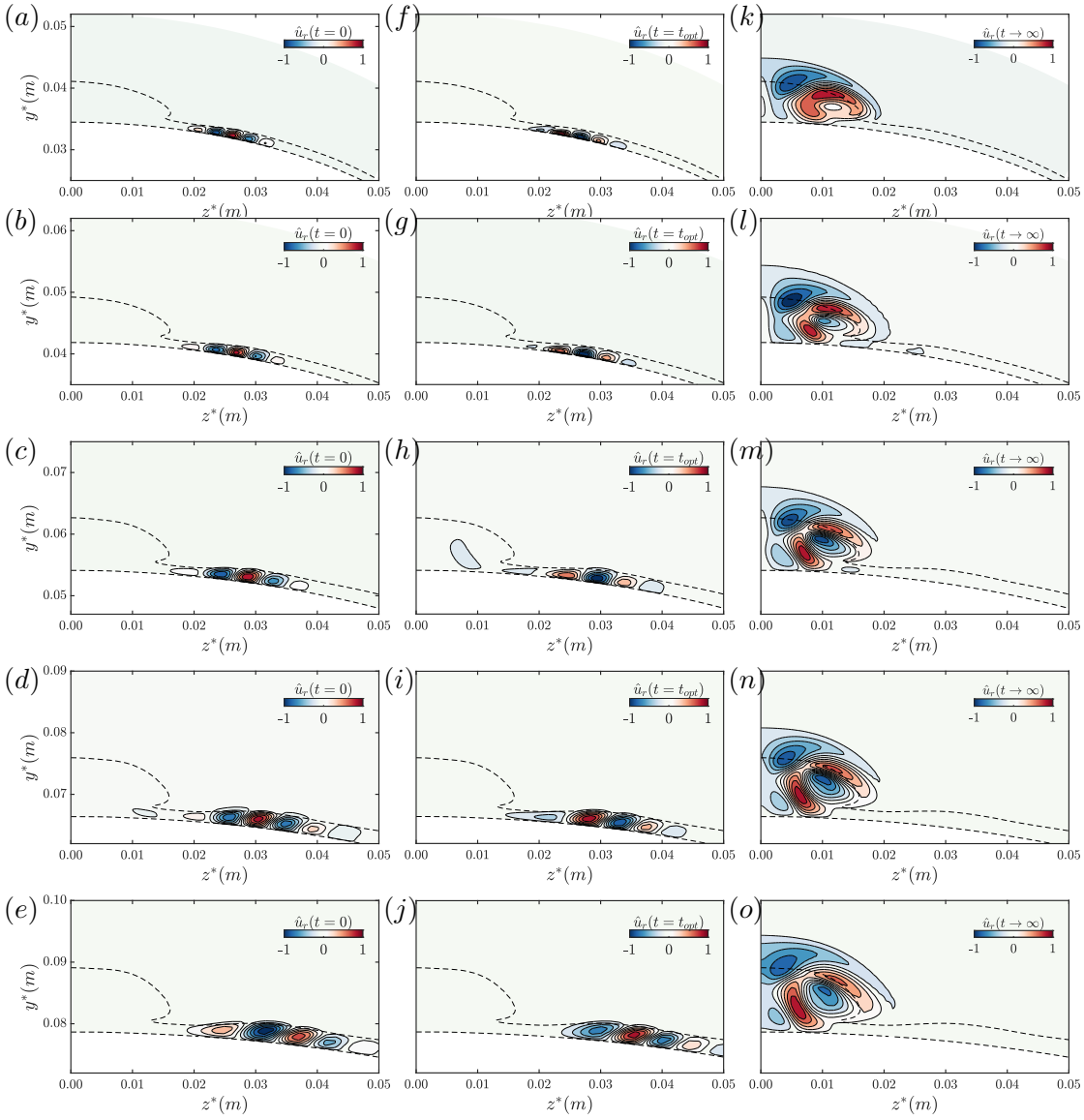

Figure 6.19: Real part of streamwise perturbation $\hat{u}_r$ with $\alpha = 0$. The first column (a-e) corresponds to the optimal initial condition $t = 0$, the middle column (f-j) to the associated optimal perturbation $t = t_{\text{opt}}$ and the right column (k-o) to the long time behaviour $t \to \infty$. Each row corresponds to a different streamwise location along the elliptic cone surface, namely $x^* = 0.36$ m (a,f,k), $x^* = 0.42$ m (b,g,l), $x^* = 0.52$ m (c,h,m), $x^* = 0.62$ m (d,i,n) and $x^* = 0.72$ m (e,j,o). The blacks isolines correspond to contours of the steady base flow ($\bar{u} = 0$ and 0.95).

words, the structures reported by Choudhari, Chang, Jentink, Li, Berger, Candler and Kimmel (2009) to arise from crossflow instability can be reinterpreted as algebraically growing linear optimal conditions that peak in the crossflow region and vanish towards the attachment-line. Such a conversion of linear optimal perturbations to crossflow modes has already been seen in the work of Tempelmann et al. (2010, 2012) in the incompressible boundary layer and completes the understanding of linear instability in

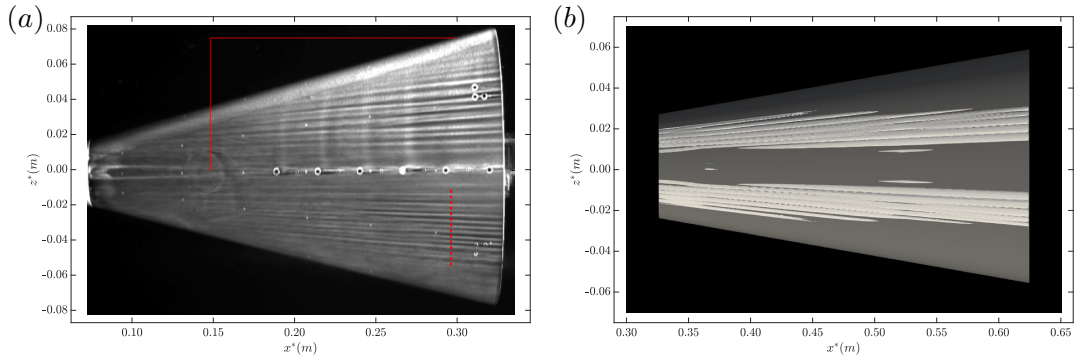

Figure 6.20: Top view of the elliptic cone model comparing: (a) oil flow visualization of experimental crossflow modes reported by Borg et al. (2012) at $Ma = 6$ and $Re' = 8.1{\times}10^6$ [1/m] and (b) three-dimensional reconstruction of the linear optimal streamwise velocity component calculated at 33km altitude, $Ma = 8.05$, $Re' = 1.89{\times}10^6$ [1/m] and $\alpha = 0$.

this hypersonic boundary layer.

Nonmodal analysis of streamwise periodic perturbations

Solutions of the initial value problem (3.13) have also been obtained at nonzero streamwise wavenumber parameters; of these, representative results obtained at $\alpha = 0.2$, corresponding to a non-dimensional wave-length of $2\pi/0.2 = 31.4$, the dimensional value being 6.8 mm at 21 km altitude and 16.1 mm at 33 km altitude, are discussed in what follows.

Results in figure 6.21 exhibit the same qualitative behaviour seen at $\alpha = 0$, namely that a non-negligible initial growth of energy is present, followed by exponential growth or decay of the signal according to modal theory. However, the maximum gain obtained at all parameters examined is $G_{\max} = O(10^2)$, one order of magnitude smaller than the maximum gain obtained in the case of streamwise-aligned structures, $\alpha = 0$.

Interestingly, while at all $x^* \geq 0.4$ m the ultimate behaviour of the $G(t)$ curve is one of modal growth, at x^*=0.36 m it can be seen that the IVP solution at 21 and 25 km yields qualitatively different results at asymptotically large times compared to the altitudes of 28 and 33 km: while at the lower two altitudes modal instability governs the large-time behaviour of the solution, at the higher two altitudes the flow is modally stable and only the transient energy growth may account for linear instability and laminar turbulent transition. In other words, at 21 km altitude the flow is modally unstable featuring the largest amplification rate. As altitude is increased and the density and Reynolds number decreases, the modal amplification rate also decreases, the flow being modally near-neutral at 28 km, while at the highest altitude of 33 km, all modal perturbations with $\alpha = 0.2$ are damped. As mentioned, this result is representative of others obtained at different wavenumbers, the quantitative difference being the altitude at which the

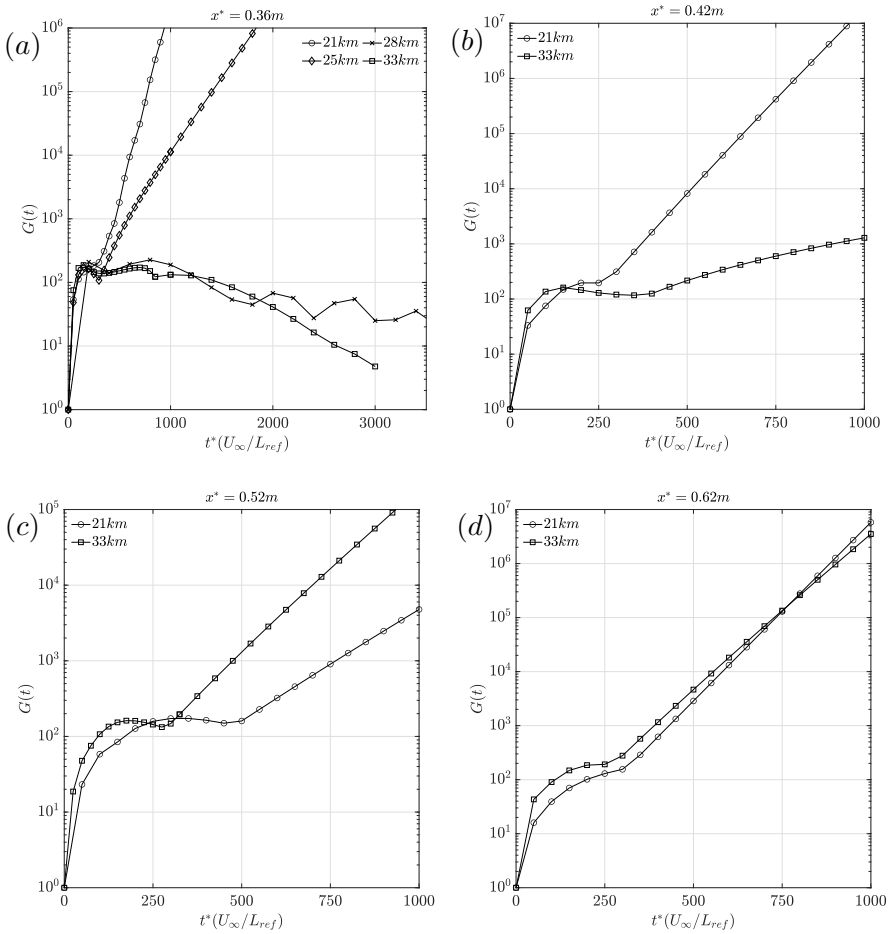

Figure 6.21: Comparison of energy gain between 21 km and 33 km altitudes with $\alpha = 0.2$ for different streamwise position. Namely, (a) $x^* = 0.36$ m, (b) $x^* = 0.42$ m, (c) $x^* = 0.52$ m and $x^* = 0.62$ m.

respective wavenumber becomes modally stable. This finding highlights the importance of performing not only a modal analysis but a full nonmodal analysis to interrogate the flow over the HiFIRE-5 elliptic cone model.

Figures 6.22 and 6.23 show the initial linear optimal conditions for the density and the streamwise velocity $\hat{u}$, respectively, at nondimensional wavenumber $\alpha = 0.2$, corresponding to a streamwise wavelength of $L_x = 16.1$ mm. Overall, analogous results with those at $\alpha = 0$ are obtained: the optimal structures at $t = 0$ and $t = t_{\text{opt}}$ are found to peak in the crossflow region of the cone, while at asymptotically large times the peak of the perturbations has moved to the cone centreline and can be related to the structures recovered from the solution of the EVP. While the $\alpha = 0$ and $\alpha \neq 0$ results are qualitatively identical at all α values examined, the major quantitative difference of the present results with those discussed in section 6.1.7 is in the level of maximum transient energy gain attained. The $G_{\max}$ of the streamwise aligned structures at any streamwise position along the cone is between two and three orders of magnitude larger

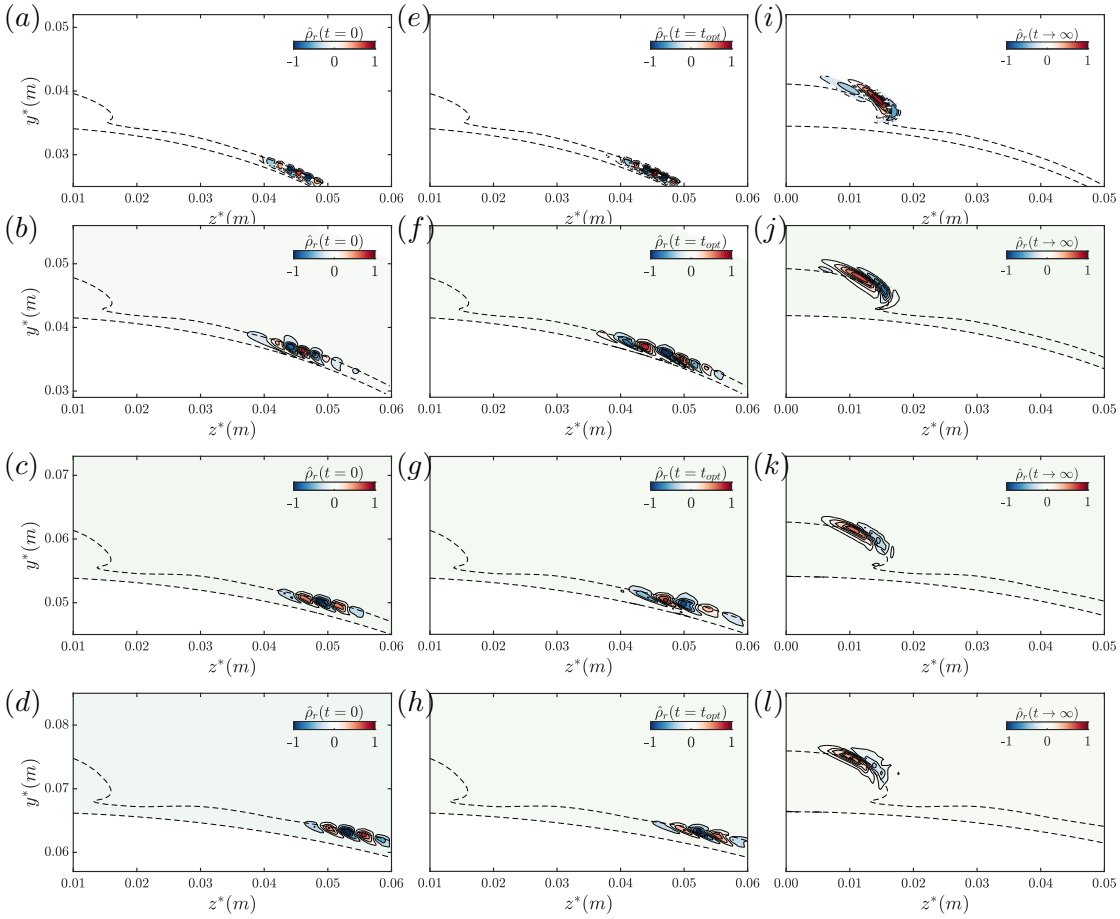

Figure 6.22: Real part of perturbation density $\hat{\rho}_r$ with $\alpha = 0.2$ ($L_x = 16.1$ mm). The first column (a-e) corresponds to the optimal initial condition $t = 0$, the middle column (f-j) to the associated optimal perturbation $t = t_{\text{opt}}$ and the right column (k-o) to the long time behaviour $t \to \infty$. Each row corresponds to a different streamwise location along the elliptic cone surface, namely $x^* = 0.36$ m (a,f,k), $x^* = 0.42$ m (b,g,l), $x^* = 0.52$ m (c,h,m), $x^* = 0.62$ m (d,i,n) and $x^* = 0.72$ m (e,j,o). The blacks isolines correspond to contours of the steady base flow ($\bar{u} = 0$ and 0.95).

than that corresponding to any $\alpha \neq 0$ structure. Consequently, nonmodal transition on the elliptic cone is expected to be associated with streamwise-aligned structures.

6.1.8 Summary of elliptic cone analysis

Linear transient growth analysis is presented on the aspect ratio two elliptic cone modeling the HIFiRE-5 geometry in hypersonic flow at Mach numbers between 7.45 and 8.05 (unit Reynolds number between 1.07×10^7 and 1.89×10^6) corresponding to cruise flight between altitudes of 21 and 33 km, respectively. Solutions of the initial value problem (IVP) are obtained by solving the Singular Value Decomposition of the matrices discretising the eigenvalue problem. Convergence of the IVP results was found to require eigenspectrum comprising orders of magnitude larger number of modes than

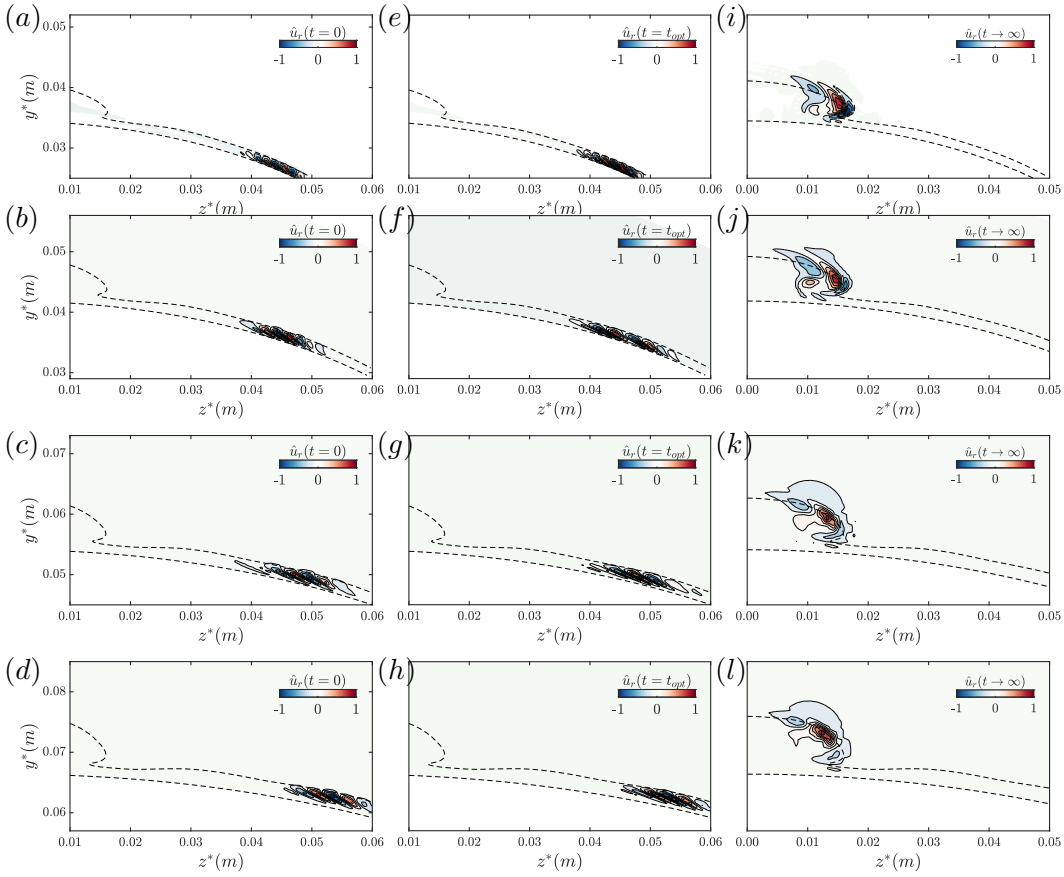

Figure 6.23: Real part of streamwise perturbation $\hat{u}_r$ with $\alpha = 0.2$ ($L_x = 16.1$ mm). The first column (a-e) corresponds to the optimal initial condition $t = 0$, the middle column (f-j) to the associated optimal perturbation $t = t_{\text{opt}}$ and the right column (k-o) to the long time behaviour $t \to \infty$. Each row corresponds to a different streamwise location along the elliptic cone surface, namely $x^* = 0.36$ m (a,f,k), $x^* = 0.42$ m (b,g,l), $x^* = 0.52$ m (c,h,m), $x^* = 0.62$ m (d,i,n) and $x^* = 0.72$ m (e,j,o). The blacks isolines correspond to contours of the steady base flow ($\bar{u} = 0$ and 0.95).

the corresponding modal analysis. A novel massively parallel solver for complex non-symmetric generalised eigenvalue problems in generalised coordinates was developed for the numerical work. Verification was performed by recovering, as leading members of the eigenspectrum used in the reconstruction of the solution to the initial value problem, modal stability analysis results known from the earlier analysis of Paredes et al. (2016). For reasons of numerical feasibility, the vicinity of the centerline and the crossflow region have been analysed separately from the attachment line region, such that numerical convergence could be ensured and the underlying physical phenomena be adequately captured.

Guided by solutions of the local analysis, which indicated that streamwise-aligned linear perturbations exhibit the highest energy gain, the two-dimensional IVP has been solved at streamwise stations 0.36 m $\leq x^* \leq$ 0.62 m along the cone, for *a-priori* un-

known time-horizons, until the slope of the energy gain curve locked onto the corresponding modal analysis result. In the centerline and crossflow region, substantially larger, $G_{\max} = O(10^4)$, transient energy growth is obtained for streamwise-aligned, $\alpha = 0$, perturbations at both extreme altitudes at the two flight altitudes compared to $G_{\max} = O(10^2)$ obtained for wave-like, $\alpha \neq 0$, perturbations. The linear optimal disturbances identified in the present analysis at $\alpha = 0$ peak in the region of crossflow and vanish towards the attachment-line. They take the form of a finite number of isolated elongated structures aligned with the streamwise direction and their spanwise wavelength compares favorably with that of the crossflow vortices reported in the BAM6QT experiment of Borg et al. (2012), despite quantitative differences in the parameters at which the experiment was performed. In the vicinity of the attachment line, solution of the initial value problem reveals modal growth around discrete streamwise wavenumber values and feeble algebraic energy growth between these wavenumbers.

A counter intuitive and relevant result of the present analysis is associated with the variation of the maximum transient energy gain on flight altitude: at any given streamwise location on the cone, $G_{\max}$ increases monotonically with increasing altitude and decreasing Reynolds number. At the lowest altitude (relatively modest) algebraic/transient energy growth is followed by exponential/modal *growth* of perturbations at all parameters examined; in other words, the linear instability of the flow is governed by the analysis of the modal scenario discussed by Paredes et al. (2016). By contrast, at 33 km transient growth is on occasion followed by modal/exponential *decay* of the perturbations in question, implying that, as the flight altitude increases, transient growth becomes the only physical linear instability mechanism leading the hypersonic boundary layer flow to laminar-turbulent transition. By contrast to the quadratic dependence of the maximum energy gain on the local Reynolds number, known from incompressible analysis (Schmid and Henningson 2001) and also verified at low-altitude/high Reynolds number nonmodal analyses herein, the quartic dependence $G_{\max} \sim Re_x^4$ found in our highest altitude results indicates that laminar-turbulent transition of hypersonic boundary layer flow may arise from nonmodal mechanisms, which presently remain unexplored for the majority of flows of interest.

6.2 Hypersonic flow past a circular cylinder

Flow over bluff bodies has been the focus of numerous numerical and experimental studies for decades. For instance, approximate solutions of the velocity potential in the irrotational compressible flow around a cylinder (Imai 1938, Tamada and Saito 1939) and sphere (Tamada 1939) were computed in the late '30s. From a linear stability analysis point of view, a lot of effort has been made to study the instability and its dynamics from incompressible to the low supersonic regime. However, complete knowledge of the related instabilities dynamics in high supersonic regimes is still lacking, particularly in the interaction of the mode structures and the shock.

In the incompressible limit, the state-of-the-art of flow instability physics is substantially more advanced. The celebrated work of Tomboulides and Orszag (2000) quantified (global) instability in the wake of a sphere. Giannetti and Luchini (2007) conducted direct and adjoint instability analysis of incompressible flow past a circular cylinder and used the adjoint eigenmodes to locate the so-called "wavemaker" core of the instability. These authors identified this region to be associated with two lobes placed symmetrically across the separation bubble, in line with the experimental results of Strykowski and Sreenivasan (1990) and the earlier analysis of Hill (1992). Giannetti and Luchini (2007) also introduced a novel technique to perform an analysis of the eigenvalue sensitivity to structural perturbations and used it to identify the region of maximum coupling among the velocity components at the end of the separation bubble. Abdessemed, Sharma, Sherwin and Theofilis (2009) investigated the transient nature of non-modal perturbations in incompressible flow past a circular cylinder at diameter-based Reynolds number $Re_D = 45, 50$ as well as 200 and 300. At lower Re_D two-dimensional optimum growth modes were found to appear in the near wake of the cylinder showing large transient growth that promotes the linear instability, which ultimately saturates into the von-Kármán street. The transient growth was attributed to amplification through a region of local absolute instability behind the cylinder at $Re_D > 20$ as identified by Monkewitz (1988).

In the compressible regime, approximate solutions of the velocity potential in the irrotational compressible flow around a cylinder (Imai 1938, Tamada and Saito 1939) and sphere (Tamada 1939) were computed in the late '30s. Including the effects of vorticity was found to have little influence on shock curvature but showed that the shock is further away from the body than predicted under the irrotational assumption (Hida 1953). More recently, two-dimensional viscous, compressible flow around a circular cylinder at $20 \leq Re_D \leq 100$ and $0 \leq Ma \leq 0.5$ was analysed by Canuto and Taira (2015). Compressibility effects were found to elongate the near wake for cases above and below the critical Reynolds number. It was observed that at a given Re, the growth rate of the primary wake instability decreases with increasing free-stream Mach number, suggesting that compressibility effects tend to stabilize the flow.

Schmidt and Rist (2014) experimentally examined the wake behind the supersonic cylinder at $2 \times 10^4 \leq Re_D \leq 5 \times 10^5$ and $Ma = 4$. Periodic oscillations of the slip lines in the wake were observed with Strouhal number increasing monotonically from 0.3 to 0.5 as Reynolds number is increased. These oscillations were likely driven by acoustic signals propagating back and forth through the subsonic region between the separation points on the cylinder and the neck, where the slip lines converge. Recently, Nagata et al. (2020) experimentally studied low Reynolds number flow over a circular cylinder at $1 \times 10^3 \leq Re_D \leq 5 \times 10^3$ and $0.1 \leq Ma \leq 0.5$. The Mach and Reynolds numbers were found to have non-linear effects on the frequency of vortex shedding that could be approximately characterized by the maximum width of the recirculation zone. It was shown that the trend of Ma effect on the release location of the Kármán vortices, the Strouhal number of vortex shedding and the maximum width of the recirculation is changed at approximately $Re_D = 3000$.

As can be seen, previous literature works in the compressible regime predominantly focused on the wake region, and little attention has been paid to the fore-body. Thus, the current linear stability analysis study is concentrated on the region ahead of the windward face of the body, with the bow shock included in the stability analysis domain (fig. 6.24). The aim of this study is to report an effort to compute and understand modal and non-modal instabilities in this region and the significance of the shock in such instabilities.

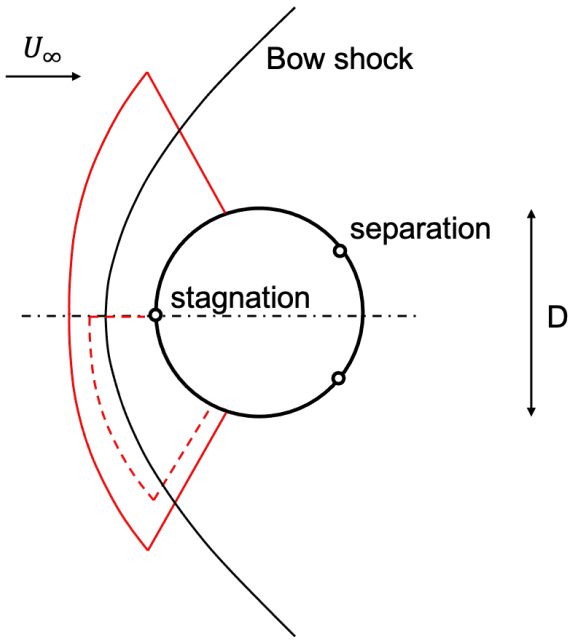

Figure 6.24: Sketch of the circular cylinder. The solid red line corresponds to the full DNS domain and the dashed red line corresponds to the stability analysis domain.

6.2.1 Base flow configuration

The analysis is carried out on a circular cylinder's windward face in a region containing both subsonic and supersonic flow as shown in figure 6.24. The free-stream conditions are $Ma = 6$ and $Re_D = 1000$, based on the cylinder diameter. The base flow was generated by Dr. Ricardo Santos during his PhD at Universidade Federal Fluminense, using a newly developed high-order finite-difference generalized coordinate DNS code[1] (Santos 2020). The steady-state solution was obtained by marching the two-dimensional compressible Navier-Stokes equations in time using SSPRK(3,3) scheme. The Lax-Friedrichs characteristic-wise flux difference scheme combined with a fifth-order accurate finite differences WENO-JS Jiang and Shu (1996) was used for the inviscid terms. For the viscous terms, however, a conservative sixth-order accurate centred finite difference scheme was applied. A more detailed explanation of the base flow calculation can be found in Santos (2020). Figure 6.25(a-d) presents color contours of normalized base flow velocity components $(\bar{u}, \bar{v})$, temperature $(\bar{T})$ and pressure $(\bar{p})$, respectively.

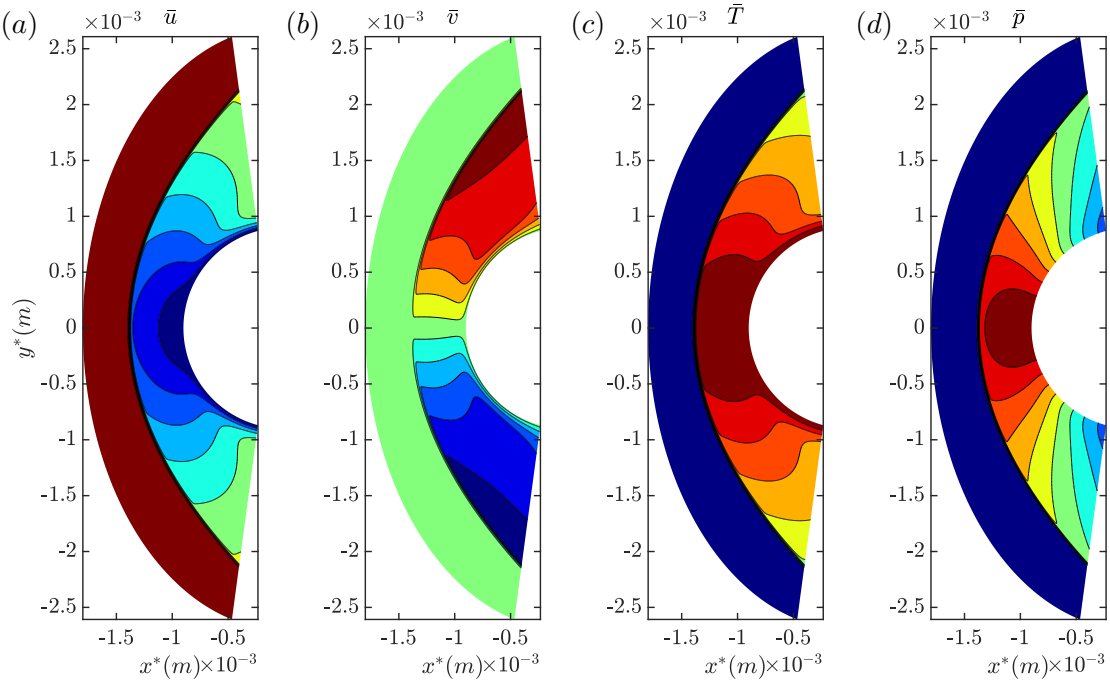

Figure 6.25: Steady base flow solutions obtained at $Re_D = 1000$ and $Ma = 6$ by DNS (Santos 2020); (a) streamwise velocity $\bar{u}$, (b) vertical velocity $\bar{v}$, (c) temperature $\bar{T}$ and (d) pressure $\bar{p}$. The components are normalized by their maximum absolute value.

[1] 3DSSSS - 3D Structured Steady-State Solver

6.2.2 Generalized transformation and spatial discretisation

The steady-state baseflow is interpolated into the *LiGHT* code using the same mesh used in the DNS calculation (Jiang and Shu 1996, Santos 2020). The two transformed spatial directions of this problem are ξ and η, and they are appropriately discretised using Chebyshev-Gauss-Lobatto (CGL) spectral collocation points (§4.1.1)

$$\xi_j = \eta_j = \cos\frac{j\pi}{N}, \quad j = 0, 1, ..., N. \tag{6.8}$$

When using Chebyshev spectral collocation method as spatial discretisation in a domain where the shock layer is included, the alignment between the grid and the shock is crucial, as is the refinement in that part of the domain. Considering the two-dimensional computational domain $(\xi, \eta) \in [0, 1] \times [0.1]$ the transformation to the physical domain (x, y) can be written as

$$\begin{aligned} x &= -(R_x - (R_x - r)\xi_A)\ \cos[\theta(2\eta - l)] \\ y &= \ \ (R_y - (R_y - r)\xi_A)\ \sin[\theta(2\eta - l)] \\ z &= \zeta \end{aligned} \tag{6.9}$$

where R_x and R_y are the cylinder's positions in respect to the axis, r is the cylinder radius, θ is the angle defining the fore-head of the cylinder, and l is a parameter to define symmetries. The auxiliary variable ξ_A can be obtained as

$$\xi_A = \frac{\xi_0}{A}\ (\sinh[(\xi - x_0)\phi] + A), \tag{6.10}$$

where ξ_0 is the location in ξ chosen to refine the mesh (for instance, in the shock layer, where strong gradients are present) and ϕ defines the clustering of points around ξ_0. The other parameters appearing in equation (6.9) can be defined as:

$$\begin{aligned} x_0 &= \frac{2\ \phi\ \log[(1 + e^{\phi} - 1) * \xi_0]}{1 + (e^{-\phi} - 1) * \xi_0)}, \\ A &= \sinh[\phi\ x_0]. \end{aligned} \tag{6.11}$$

In the following analysis, the symmetry of the problem is exploited to reduce the overall computational cost in the numerical solution of the initial value problem. The lower part of the baseflow shown in the figure 6.25 is discretised up to a sufficient angle θ to guarantee alignment between the grid and the shock, as schematically shown in Figure 6.26 for a low resolution grid. The parameters chosen for best alignment and cluster of the points in the shock are defined in table 2.

6.2.3 Boundary conditions

The boundary conditions to complement the EVP and the SVD are defined next. In the azimuthal direction η, symmetric or anti-symmetric boundary conditions can be imposed at $\eta = \pi$. In what follows, symmetric boundary conditions were found to recover

R_x	R_y	θ	l	ξ_0	ϕ
0.8	1.11	0.35	2	0.15	8

Table 6.4: Circular cylinder mesh parameters.

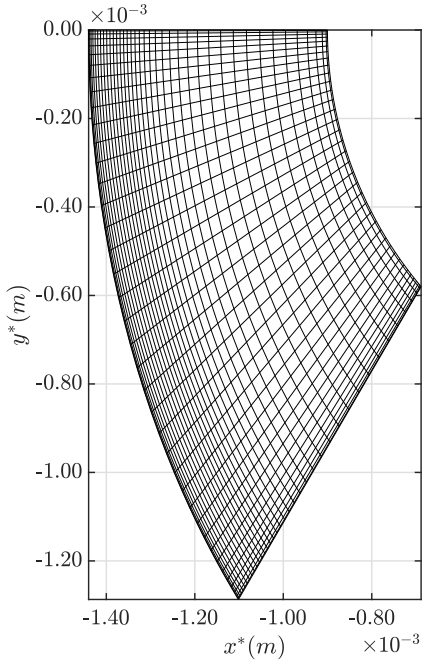

Figure 6.26: Example of a low resolution domain used to perform the BiGlobal stability analysis. The symmetry of the flow around the cylinder is exploited and the mesh is clustered at the shock layer using eq. 6.9.

the least stable two-dimensional mode (explained in the next section) and were imposed on all the following calculations. Nevertheless, an analysis of the full domain verified the correct implementation of symmetric/anti-symmetric boundary conditions. At the opposite boundary, linear extrapolation is imposed on all perturbation components, allowing them to exit the domain with minimal distortion. Along the wall-normal direction, at the wall ($\xi = 0$), no-slip conditions are imposed on the velocities and temperature amplitude functions. The gradient of the pressure amplitude function is required to be zero at the wall. Finally, since the domain includes the shock layer in the analysis and the flow is free of perturbations in the uniform free-stream, homogeneous Dirichlet boundary conditions can be imposed at the inlet.

6.2.4 Modal linear stability calculation

The BiGlobal stability problem (2.19) is solved using the chain rule and the metric factor methods described in section §2.4. Both approaches give similar results. From equation (6.9), x and y are the two inhomogeneous spatial directions and z is periodic.

Thus, the modal Ansatz can be written in terms of the computational domain as

$$\tilde{\mathbf{q}}(\xi,\eta,\zeta,t) = \hat{\mathbf{q}}(\xi,\eta)e^{[i(\beta\zeta-\omega t)]} \tag{6.12}$$

where β is the wave-number in $z = \zeta$ direction. A computational grid of $N_\xi = 141$ and $N_\eta = 161$ is used to discretise the problem along with two different dimensions of Krylov subspace, $m = 500$ and $m = 3500$. The spectra obtained for the two-dimensional case, i.e. when the spanwise wave-number β is 0, is presented in figure 6.27. Following the same reasoning of the square duct verification case, the least stable modes are already converged for a rather small number of m. However, a large subspace dimension is needed to converge the initial value problem (3.13) and will be justified in the transient growth calculation presented in the next section. The DNS residual's decay rate in the time marching to steady state is shown as a red plus symbol in figure 6.27. Excellent agreement is found when comparing the decay rate of the least damped mode calculated with the *LiGHT* code ($\omega_i = -0.313238$) with that of the DNS residual ($\omega_i = -0.318333$). In both cases, the mode has $\omega_r = 0$, meaning that the least stable mode is stationary. This result highlights the *LiGHT* code's capabilities to accurately recover the damping rate of flows even when high gradients are present due to the inclusion of the shock layer in the stability analysis calculations.

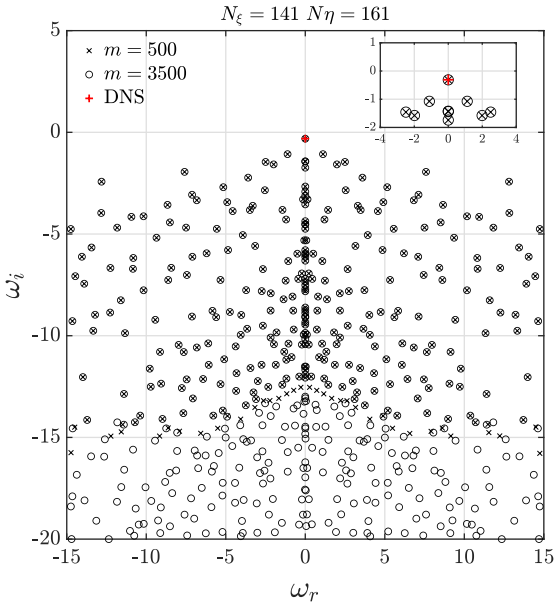

Figure 6.27: Eigenvalue spectra of the circular cylinder for $Ma = 6$, $Re_D = 1000$ and two different Krylov subspace ($m = 500$ and $m = 3500$). The top right corner highlights the excellent agreement obtained in the least damped mode calculated with the *LiGHT* code ($\omega_i = -0.313238$) and with the DNS residual ($\omega_i = -0.318333$).

The normalized amplitude functions of the least stable mode are presented in figure 6.28. Since this is a two-dimensional mode, the spanwise component $\hat{w}$ along z-direction

is zero. All perturbations are shown to peak at the shock layer, reflecting the importance of the grid alignment and refinement in that region. Interestingly, no perturbation components peak inside the boundary layer or close to the stagnation region.

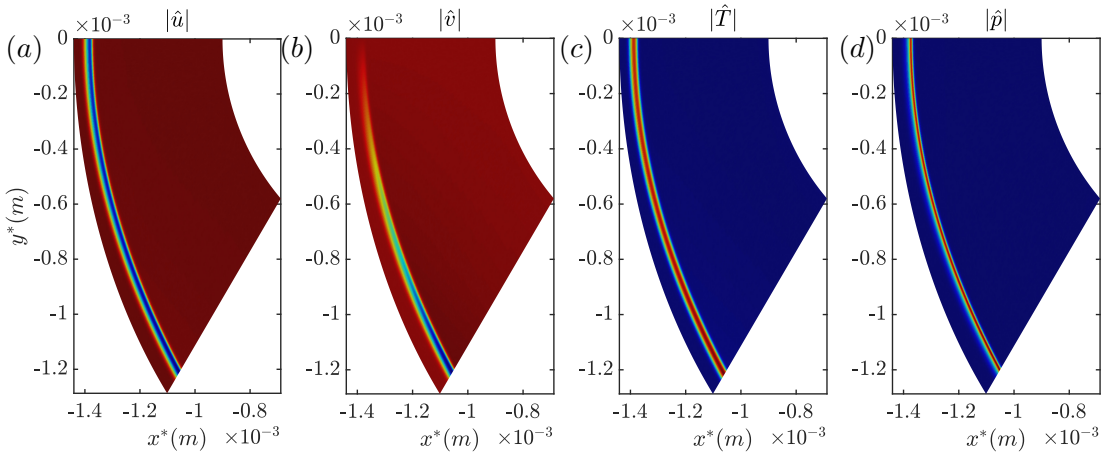

Figure 6.28: Amplitude functions peaking at the shock layer for all components; (a) streamwise velocity $\hat{u}$, (b) vertical velocity $\hat{v}$, (c) temperature $\hat{T}$ and (d) pressure $\hat{p}$. The components are normalized by their maximum absolute value.

Figure 6.29 shows the comparison of the least damped mode obtained from the linear stability analysis with the structure obtained from the residuals algorithm (Theofilis 2000b) applied to the DNS result. The profile is taken at an angle of $\eta = 210°$ in the radial direction (r) starting from the cylinder wall (where the radius is $r = 0.5$). A rather surprising agreement can be seen in all four components through the whole profile, especially in the peak, where no difference can be noticed.

6.2.5 Transient growth calculation

Non-modal stability analysis is performed on the same base flow and conditions described before. The measurement of a perturbation's energy growth at a short time is of particular interest, especially when all eigenvalues are found to be stable in the asymptotic regime. This is the case of the eigenspectrum shown in figure 6.27. The gain curve is plotted in a semi-log graph in figure 6.30 for four different Krylov subspace: $m = 501$, $m = 2001$, $m = 3501$ and $m = 4001$. The gain curve is completely off for the smallest subspace, showing intermittent growth in the time interval. For $m = 2001$, the gain curve takes the correct shape but only converges the first peak appearing at a non-dimensional time $t \approx 0.9$. For the next two subspaces $m = 3501$ and $m = 4001$, the curves fall on top of each other, also predicting the second peak at $t \approx 2.6$. Moreover, the present SVD implementation's ability to recover the asymptotic behaviour given by the most unstable/least stable eigenvalue has been examined. The slope of the energy

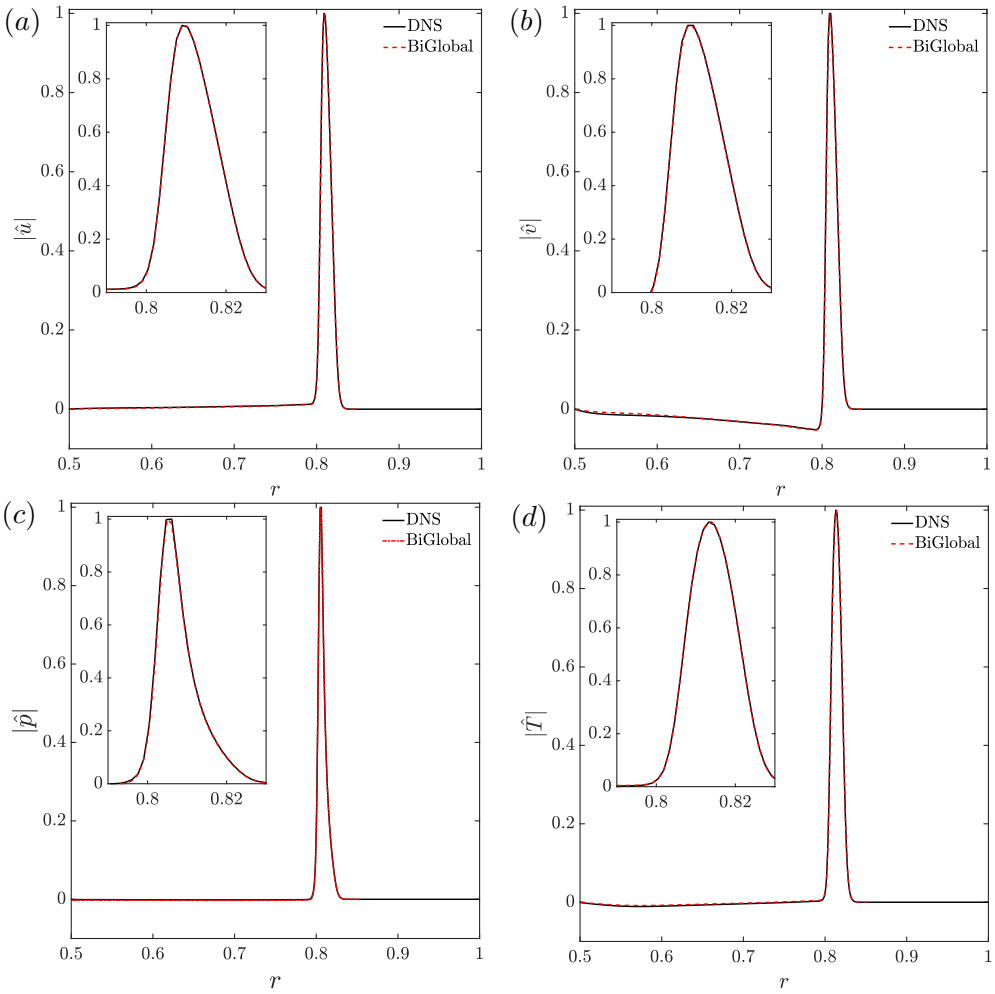

Figure 6.29: Comparison between the amplitude functions obtained with the *LiGHT* code and the residual algorithm (Theofilis 2000b) on a profile taken at $\theta = 135°$. Excellent agreement is obtained in capturing the peak at the shock layer.

curve asymptotically grows at the rate of

$$G_\infty \approx e^{2\omega_i t_\infty} \tag{6.13}$$

This agreement is graphically shown in figure 6.30, where a dashed line indicates the slope corresponding to the EVP result. Since the respective $G(t)$ curves become parallel to the dashed line, they demonstrate the agreement in predicting the ultimately asymptotic decay.

Figure 6.31 shows the optimal initial condition obtained at both periods of time $t = 0.9$ and $t = 2.6$ where a peak in the gain function is obtained. It is important to keep in mind that different initial conditions will generate algebraic growth of energy $G(t)$ with its corresponding maximum value; however, the optimal initial condition at one time is not necessarily the same at a different time. The gain curve can be interpreted as an envelope over all possible optimal initial conditions. Moreover, since the solutions of

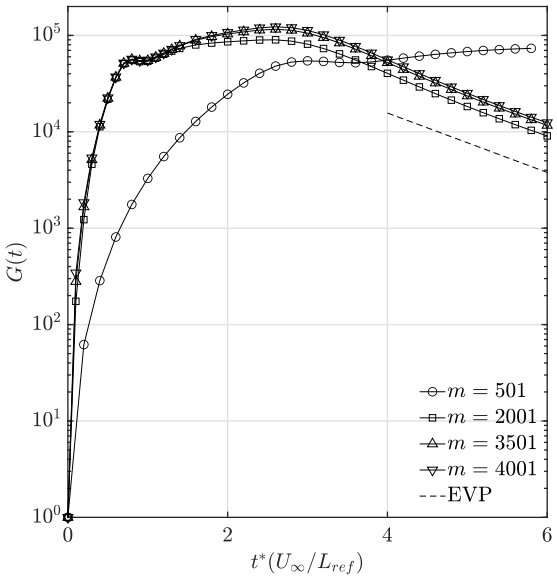

Figure 6.30: Energy growth dependence of the Krylov subspace size for $Ma = 6$, $Re_D = 1000$ and $\beta = 0$. The two energy peaks appear at $t \approx 0.9$ and $t \approx 2.6$.

the IVP and the EVP coincide at an asymptotically large time, it is expected that the optimal condition will correlate well with the eigenfunctions of the most unstable/least stable eigenmode in that time. The first row of figure 6.31 (a-d) shows the optimal initial condition at non-dimensional time $t = 0.9$. In comparison with the least damped mode structure shown in figure 6.28, the peaks are still in the shock; however, for $|\hat{u}|, |\hat{T}|$ and $|\hat{p}|$, the peak is not continuous through the shock anymore. They seem to weaken as they go away from the symmetry plane. In the $|\hat{v}|$ velocity component, the behaviour is the opposite, where the peak is high along a larger portion of the shock compared to the least damped mode. Moreover, a darker region can be seen near the cylinder wall, which does not occur in the least damped structure. At $t = 2.6$ the optimal already took the same form of the eigenfunction recovered from the EVP solution. This overall behaviour suggests that high energy is found at the shock layer during a short period of time when the shock oscillates. During this period, small perturbations imposed on the shock can be amplified with rather large energy. After this time, the shock stabilizes and stays steady, and the perturbations will ultimately decay at the same rate as predicted by the eigenvalue analysis.

6.2.6 Summary of circular cylinder analysis

The linear global modal and non-modal instability of the two-dimensional hypersonic flow past a circular cylinder was investigated. The free-stream flow conditions were $Ma = 6$ and diameter-based Reynolds number $Re_D = 1000$. The analysis focused on the region ahead of the body's windward face to investigate the bow shock contribution

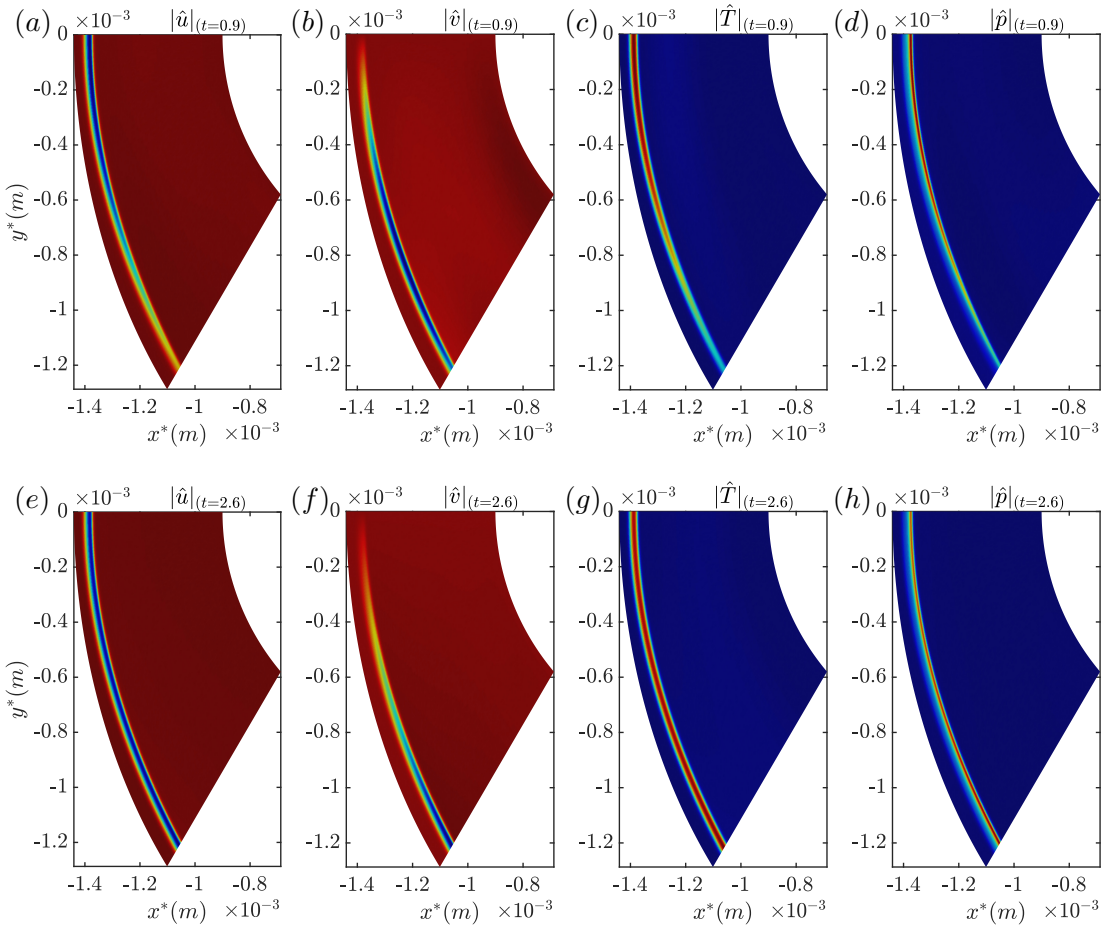

Figure 6.31: Optimal initial condition at $t = 0.9$ (first row: (a) - (d)) and at $t = 2.6$ (second row: (e) - (h)) peaking at the shock layer for all components; (a) streamwise velocity $|\hat{u}|$, (b) vertical velocity $|\hat{v}|$, (c) temperature $|\hat{T}|$ and (d) pressure $|\hat{p}|$. All components are normalized by their maximum absolute value.

in the linear stability analysis. In that matter, the analysis included the shock in the stability domain, where an accurate grid alignment was shown to be necessary to avoid spurious results. By doing so, the BiGlobal stability analysis showed excellent agreement in capturing the least damped mode in comparison with the DNS. Moreover, all amplitude functions present peak only in the shock layer. Finally, a transient growth analysis was performed for $\beta = 0$, revealing two strong peaks at short time. The first was associated with the shock motion, where strong amplification of the energy exists. The second was associated with the least damped mode when the shock stabilizes. After that, the gain curve decays at the same rate as predicted by the DNS and the modal stability theory. In order to account for three-dimensional instabilities, the analysis must be extended considering $\beta \neq 0$.

6.3 Compression ramp

In supersonic flows, the interaction between a shock and the boundary-layer (SBLI) is of much interest. Flow separation can be generated in supersonic flows by the strong adverse pressure gradient associated with various-shaped deviations from the flat geometry, such as the compression ramp schematically depicted in figure 6.32. This type of flow has been the subject of intense investigation ever since the early experimental works of (Chapman et al. 1958) recognized the significance of separation to the laminar-turbulent transition process at high speeds.

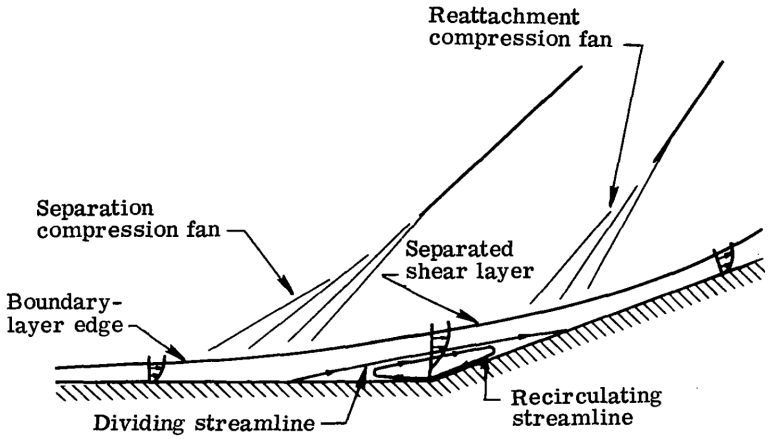

Figure 6.32: Schematic representation of the compression corner (Carter 1972).

In turn, correct prediction of the instability dynamics of flow separation is key to determining the relative portions of laminar and turbulent flow on a vehicle travelling at supersonic speeds. The consequent correct prediction of heat transfer is critical to aerodynamic performance. Canonical cases studied in this context include separation induced by shocks impinging on laminar or turbulent boundary layers on the flat plate, separation caused by forward- or backwards-facing steps, roughness elements embedded inside the boundary layer, as well as separation localized at small- and finite-angle, two-dimensional or oblique wedges. Edney (1968) documented experimentally and classified several patterns arising from shock-induced separation. Babinsky and Harvey (2011) presented an overview of the observed phenomena, while Gaitonde (2015) recently discussed the progress made in understanding this class of flows. A key issue identified is the low-frequency shock oscillation, purported in the literature to be associated with some form of linear flow instability. Understanding the precise nature of this instability and its dependence on the underlying base or mean flow parameters would close the currently open debate on this topic and open up avenues to pursue flow control via the control of flow instabilities. The first modal global linear instability analysis of interest to shock-induced separation has been the two-dimensional global

mode analyses of Crouch et al. (2007, 2009) who monitored the separated flow generated by two-dimensional shock/turbulent boundary-layer interaction over an airfoil at transonic conditions. Results obtained by these authors could successfully associate the buffeting phenomenon observed on airfoils with the frequency of the most-amplified two-dimensional global mode of the underlying turbulent mean flow, the latter obtained by solution of the Reynolds Averaged Navier-Stokes equations. On the other hand, the work of Robinet (2007) has been the first documented global linear instability analysis of a separation bubble generated by the shock wave / laminar boundary layer interaction. It was asserted that the analogue of the stationary three-dimensional global mode discovered by Theofilis et al. (2000) in incompressible flow is also the most amplified instability at the supersonic conditions examined. In other words, Robinet (2007) sustains that the separation bubble in this flow acts as an oscillator. A similar result regarding the existence of self-excited stationary three-dimensional eigenmodes has been obtained in the recent work of Nichols et al. (2017), who analyzed a mean turbulent, as opposed to a steady laminar separation bubble and also found an amplified spectrum corresponding to both supersonic and incompressible separated flow. The clearest evidence to-date regarding the existence of self-excited oscillator-type spanwise-periodic disturbances generated inside the laminar separation zone and extending along the downstream ramp wall comes from the DNS work of Egorov et al. (2011). They clearly show three-dimensional structures appearing in the ramp's vicinity at a finite simulation time. Detailed analysis of the DNS signal was shown at Mach number value $Ma = 5$ and Reynolds numbers around $Re = 6 \times 10^4$. The growth in time of these structures, referred to as deviations, has been documented in terms of the time-dependence of the r.m.s. values of the velocity components and the thermodynamic variables. They all exhibit linear growth of magnitude over several decades on a semi-logarithmic scale, thereby confirming the exponential amplification of a self-excited global mode. More recently, global linear stability theory concepts applied to DSMC simulation results demonstrated strong coupling between the shock structure and linear instability of a laminar two-dimensional separation bubble in $Ma = 16$ axisymmetric flows over a $25°-55°$ double-cone, as well as in $Ma = 7$ flows over a $30°-55°$ double-wedge configuration (Tumuklu, Levin and Theofilis 2018, Tumuklu, Theofilis and Levin 2018, Tumuklu et al. 2019). On double-cones, the presence of λ-shocks and oscillations of the detached and separation shocks at a Strouhal number, St, of 0.078 has been documented by Tumuklu, Theofilis and Levin (2018). Subsequent extension of the analysis to 3D, spanwise-homogeneous flow over the same double-wedge configuration by Sawant et al. (2019, 2021) showed the presence of linearly growing, self-excited, small-amplitude, 3D perturbations inside the separation bubble as well as in the interior of separation and detached shock layers.

The current effort is to report the *LiGHT* code's capabilities in recovering global modes

in an example with complex flow physics and show the inter-dependence of shock motion with linear global instabilities.

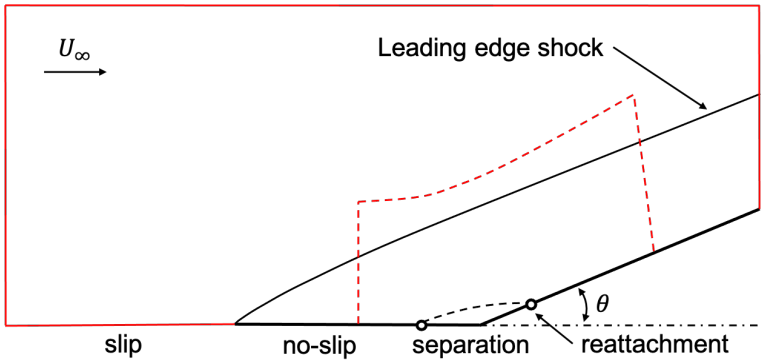

Figure 6.33: Sketch of the compression ramp with the important parameters. The dashed red line indicates the linear stability domain.

6.3.1 Base flow configuration

The compression ramp is an interesting problem to investigate from a physical point of view due to the presence of a separated shear layer, the subsequent separation and re-attachment shocks as well as its interactions. The free-stream conditions are $Ma = 3$ and $Re = 50000$ based on the flat-plate length prior the ramp. The ramp deflection angle showed in 6.33 is fixed in $\theta = 10°$. In order to simulate the leading edge, a change between slip and no-slip boundary conditions is imposed at the wall. Similarly to the flow over a supersonic cylinder investigated before, for the compression ramp, the base flow was also generated by Santos (2020) using the 3DSSSS - 3D Structured Steady-State Solver. The results were obtained by marching the two-dimensional compressible Navier-Stokes equations in time using SSPRK(3,3) scheme. For the inviscid terms, the Lax-Friedrichs characteristic-wise flux difference scheme combined with a fifth-order accurate finite differences WENO-JS Jiang and Shu (1996) was used. For the viscous terms, a conservative sixth-order accurate centred finite difference scheme was applied. Figure 6.34 shows the laminar steady-state base flow solutions obtained for the velocities $\bar{u}$, $\bar{v}$, temperature $\bar{T}$ and pressure $\bar{p}$. The domain shown is the same domain used to perform the linear stability analysis and will be explained in details shortly. The leading-edge, separation and re-attachment shock can be better seen from the wall-normal velocity component $\bar{v}$.

6.3.2 Generalized transformation and spatial discretization

The same transformation used to simulate the laminar steady base flow was used in the subsequent stability analysis where the two transformed spatial directions of this

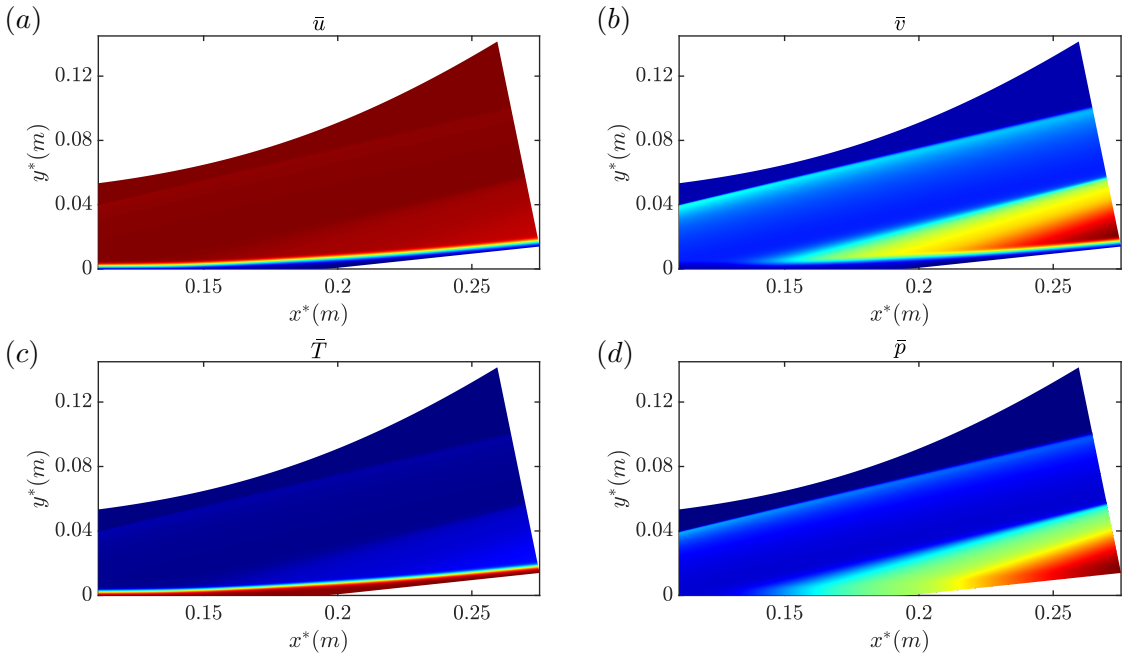

Figure 6.34: Compression ramp laminar steady base flow for $Ma = 3$, $Re = 50000$ obtained by DNS by Santos (2020); (a) streamwise velocity $\bar{u}$, (b) wall-normal velocity $\bar{v}$, (c) temperature $\bar{T}$ and (d) pressure $\bar{p}$. The components are normalized by its maximum absolute value.

problem are ξ and η, and they can be appropriately discretized using Chebyshev-Gauss-Lobatto (CGL) spectral collocation points (§4.1.1)

$$\xi_j = \eta_j = \cos\frac{j\pi}{N}, \quad j = 0, 1, ..., N. \tag{6.14}$$

We have seen that the use of Chebyshev spectral collocation method to discretize a domain with a shock needs a sharp alignment between the grid and the shock itself. The transformation used to help control the alignment parameters is based on the work of Adams (1998, 2000), Martin et al. (2003) and Pagella et al. (2004), where the key idea is to use the following mapping between computational and physical space

$$\begin{aligned} x &= (x_{\min} + (x_{\max} - x_{\min})\ \xi) \\ y &= a\left(x + \frac{\ln(\cosh(x_k))}{c(\eta)} - \frac{\ln(\cosh(x_n))}{c(\eta)}\right) + y_{\max}\ \eta \\ z &= \zeta \end{aligned} \tag{6.15}$$

where $x_{\min}$ and $x_{\max}$ is the inlet and outlet locations, respectively and $y_{\max}$ is the domain height. These equations are used to interpolate between the minimum and maximum values of the grid according to the transformations

$$
\begin{aligned}
x &= (1 - r(\eta))\ x_w(\xi) + r(\eta)\ x_\infty(\xi) \\
y &= (1 - r(\eta))\ y_w(\xi) + r(\eta)\ y_\infty(\xi) \\
z &= \zeta
\end{aligned}
\tag{6.16}
$$

where now both limits of $c(\eta)$ can be defined as $c(0) = C_{\text{wall}}$ and $c(1) = C_\infty$. In this form r(η) is an interpolation factor that interpolates the grid along the wall-normal direction from the wall (subscript w) and the upper free-stream boundary (subscript ∞). The interpolation factor is defined as follows

$$
r(\eta) = \frac{e^{d\ \eta'} - 1}{e^d - 1}, \tag{6.17}
$$

where $\eta' = \eta/(M-1)\ \Delta\eta$. Here, d is an imposed factor to space the grid in the desired manner, where small d values approach a linearly spaced grid. M is the number of elements, and $\Delta\eta$ is the spacing of the mesh. It is important to note that the grid shown above requires the imposition of a c value at the wall and free-stream, and both y_w and y_∞ are obtained by evaluating eq. (6.15) for $\eta = 0$ and $\eta = y_\infty$, respectively. With this transformation, an analytical form of the Jacobian (eq. 2.27) can be derived to relate the flow derivatives between the physical and computational domain (see Santos (2020)). Similarly to the supersonic cylinder case, the shock needs special treatment and the parameters are tuned to better align the separation shock with the grid. A schematic of the mesh is shown in figure 6.35 for a low resolution grid.

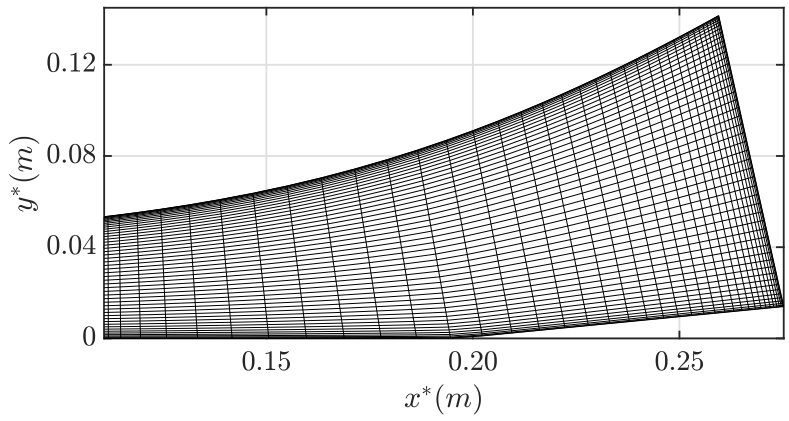

Figure 6.35: Example of the compression ramp discretisation at a low resolution using eqs. (6.15 - 6.16) for visualization purposes.

6.3.3 Boundary conditions

The boundary conditions necessary to solve the EVP are the following; in the wall-normal direction at the wall ($\eta = 0$), no-slip conditions are imposed to all velocities and

temperature amplitude functions. The pressure amplitude function gradient is set to be zero at the wall. Since the domain includes all the shocks in the wall-normal direction, no perturbations exist in the farfield and homogeneous Dirichlet boundary conditions can be imposed. Along the streamwise direction ξ, no perturbation is expected to enter the domain from the inlet and a homogeneous Dirichlet condition is imposed to all perturbations. At the opposite boundary, linear extrapolation is imposed for all amplitude functions in the outflow, allowing them to exit the domain with minimal distortion.

6.3.4 Modal linear stability calculation

Global modal stability analysis is performed for a two-dimensional wave, i.e. the wave number in the spanwise direction is set to be 0. The main objective is to recover the DNS residual's decay rate using the *LiGHT* code. The resulting eigenspectrum is shown in figure 6.36.

BiGlobal modal stability analysis (2.19) is performed using the chain rule 2.25 formulation. From equation (6.15) we see that x and y are the two inhomogeneous directions accounting for the streamwise and wall-normal directions, respectively. The spanwise spatial direction z is homogeneous, and the modal Ansatz can be written in terms of the computational domain as

$$\tilde{\mathbf{q}}(\xi, \eta, \zeta, t) = \hat{\mathbf{q}}(\xi, \eta) e^{[i(\beta\zeta - \omega t)]} \tag{6.18}$$

where β is the wave-number in $z = \zeta$ direction and is assumed to be zero to direct comparison with DNS results. A computational grid of $N_\xi = 255$ and $N_\eta = 151$ is used to discretize the problem and the eigenspectrum obtained can be seen in figure 6.36. The zoomed region in this plot shows the DNS residual decay rate as a red plus symbol falling on top of the least stable eigenvalue calculated with the *LiGHT* code. The respective decay rates are $\omega = -0.0027449$ (DNS) and $\omega = -0.0028156$ (*LiGHT*). In accordance with the previous supersonic cylinder case, where the *LiGHT* code showed its capabilities to recover the damping rate of flows in the presence of a shock layer, now the code has also been proved to correctly predict modes in such complex flows where a separation bubble exists, and the shock interacts with the boundary layer.

Figure 6.37 shows the spatial structure of the least damped mode in terms of the streamwise (a) and wall-normal (b) velocity components, the temperature (c) and the pressure (d) perturbations (the spanwise velocity component $\hat{w} = 0$) obtained with the *LiGHT* code. The structures are normalized by their maximum absolute value. Results are shown in the vicinity of the compression corner since, significantly, it was found that the leading edge region, including the leading edge shock, is steady and does not contribute to the amplitude functions of the global mode. In contrast, what is clearly visible in the results presented is the intimate connection between the separation shock

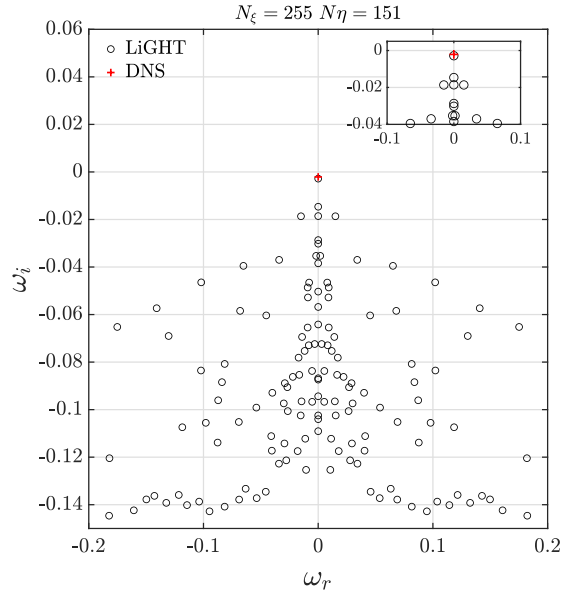

Figure 6.36: Eigenvalue spectrum of the compression ramp for $Ma = 3$ and $Re = 50000$ based on the flat-plate length. A zoom of the plot in the top right corner highlights the excellent agreement obtained in the decay rate calculated with the *LiGHT* code ($\omega = -0.0028156$) and with the DNS residual ($\omega = -0.0027449$).

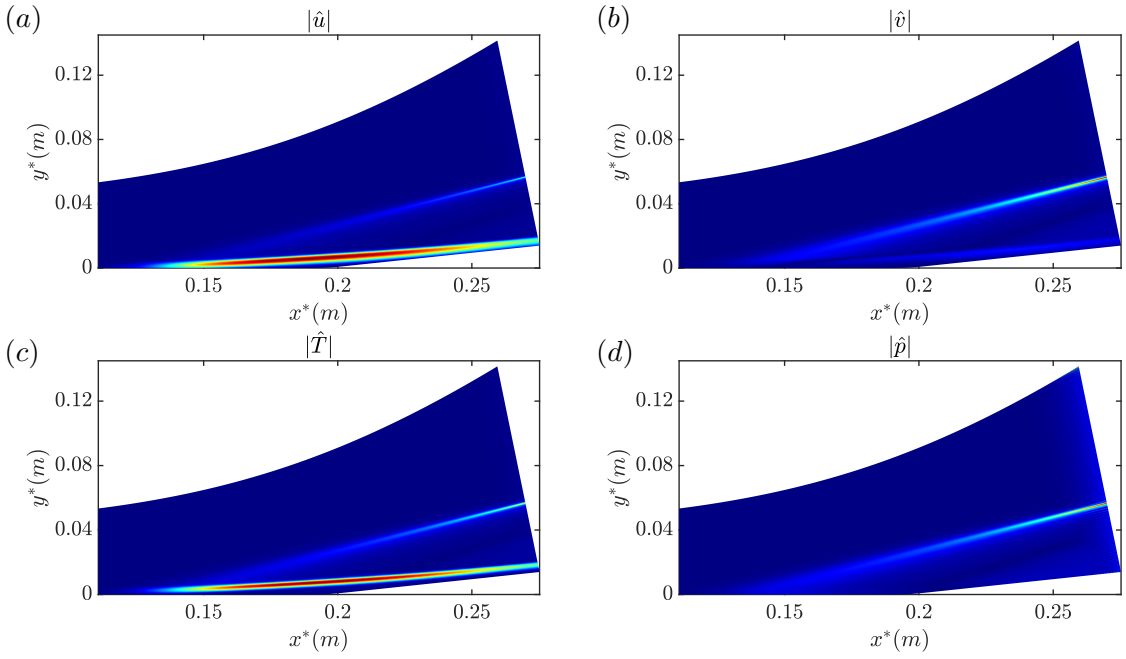

Figure 6.37: Amplitude functions of the least-damped two-dimensional mode for $Ma = 3$ and $Re = 50000$ based on the flat-plate length; (a) streamwise velocity $\hat{u}$, (b) wall-normal velocity $\hat{v}$, (c) temperature $\hat{T}$ and (d) pressure $\hat{p}$. The components magnitudes are normalized by their maximum absolute value.

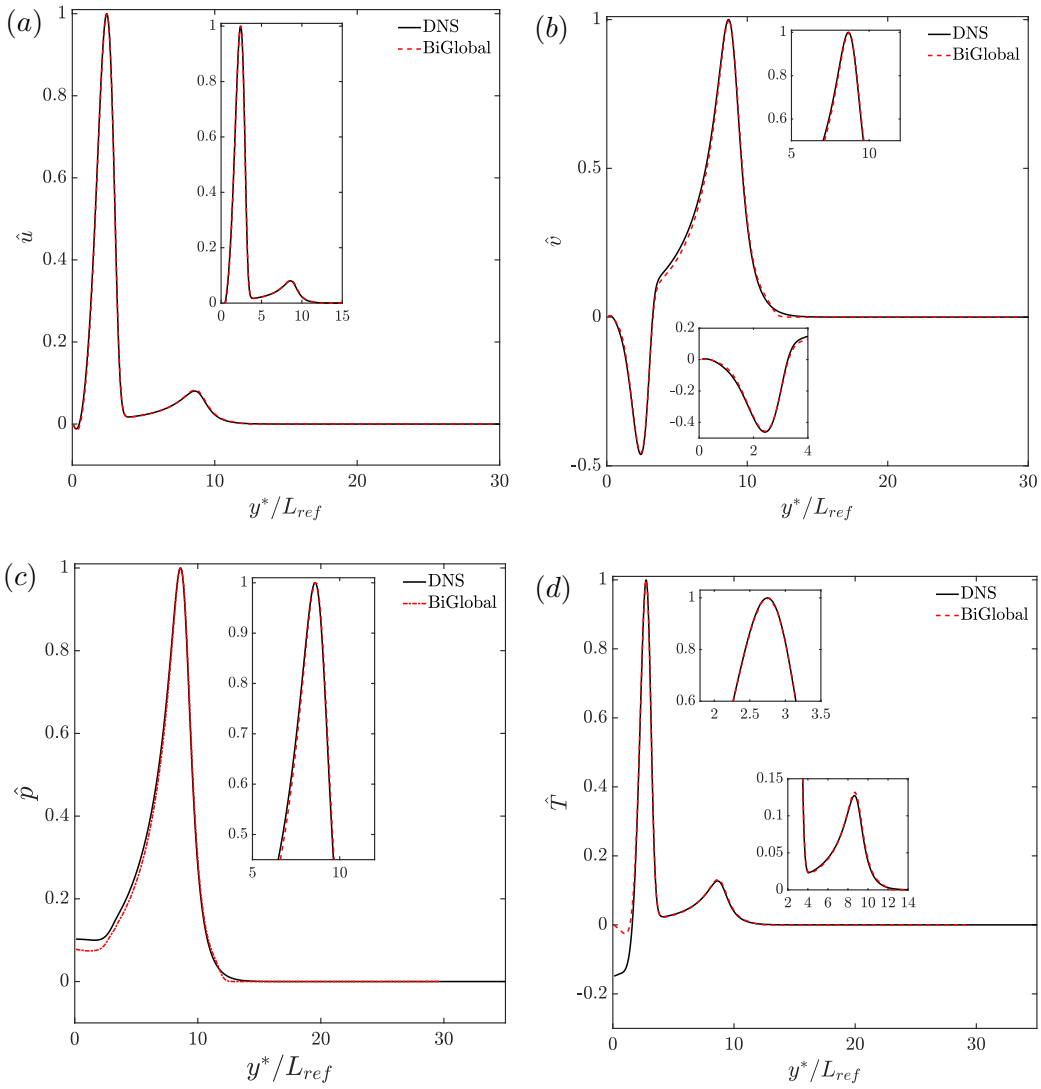

Figure 6.38: Comparison between compression ramp amplitude functions obtained with the *LiGHT* code and the residuals algorithm (Theofilis 2000b) on a vertical profile taken at the corner.

and the laminar separation bubble: the peaks of the global mode's amplitude function are to be found at these locations. In other words, instability in the laminar separation will affect shock motion and vice-versa. This result is in line with the findings of the celebrated work of Crouch et al. (2007) on the origins of buffeting in turbulent transonic flow on two-dimensional wings, where shock oscillations have been associated with linear amplification of a global mode having its peak at precisely the shock and (mean) separation location. The same result regarding the inter-dependence of shock motion and global instability in a laminar separation bubble has also been documented in the analysis of $Ma = 16$ hypersonic flow in the double-cone junction by Tumuklu, Levin and Theofilis (2018), Tumuklu, Theofilis and Levin (2018). The present results

indicate that instability analysis of supersonic flow in the compression corner needs to consider the separation shock as an integral part of the analysis.
Finally, a vertical profile is taken at the corner, including the separation bubble and the shock. Figure 6.38 shows the profiles obtained for the velocities $\hat{u}$ and $\hat{v}$, temperature $\hat{T}$ and pressure $\hat{p}$. For both velocities, an excellent agreement is found for both peaks appearing in the separation bubble and at the separation shock. However, for the thermodynamic variables $\hat{p}$ and $\hat{T}$, there is only an agreement after some distance from the wall. The peak at the separation shock matches for both methods, but there is still some residual in the DNS results close to the wall, which makes the temperature value nonzero. Nevertheless, this small discrepancy does not affect the solution's damping rate.

6.3.5 Transient growth calculation

Similarly to the hypersonic cylinder case, when all eigenvalues are found to be stable in the asymptotic regime, a measurement of the energy gain at short time is of particular interest. The gain curve of the compression ramp for $\beta = 0$ is plotted in a semi-log graph in figure 6.39. Three different Krylov subspace are investigated: $m = 1001$, $m = 2501$, $m = 3501$. In the smallest subspace, the time in which the peak appears is converged. However, the value of $G_{\max}$ is underpredicted, as well as the rest of the curve. Increasing the subspace size to $m = 2501$ and comparing with $m = 3501$, all points in the curve fall on top of each other. The maximum peak occurs at $t_{\text{opt}} \approx 7$ for a gain of $G_{\max} \approx 29$. This negligible value of gain clarifies that for the two-dimensional compression ramp ($\beta = 0$), nonmodal stability is not relevant for transition.
Moreover, recalling that the slope of the energy curve asymptotically grows at the rate of

$$G_\infty \approx e^{2\omega_i t_\infty}. \tag{6.19}$$

In figure 6.39, a dashed line indicates the slope corresponding to the EVP solution. Since all three $G(t)$ gain curves become parallel to this dashed line, they demonstrate that even the smallest subspace agrees in predicting the ultimately asymptotic decay.

6.3.6 Summary of compression ramp analysis

Linear modal and nonmodal stability analysis have been performed on the supersonic flow over a compression ramp at $Ma = 3$ and Reynolds number $Re = 50000$, based on the flat plate length. The separation bubble and the associated separation and reattachment shock interactions were investigated in a global modal stability analysis framework. The global mode's amplitude functions peaked at the separation shock and in the laminar separation bubble. This finding highlights the intimate connection between them and the importance of including the shock in the stability analysis

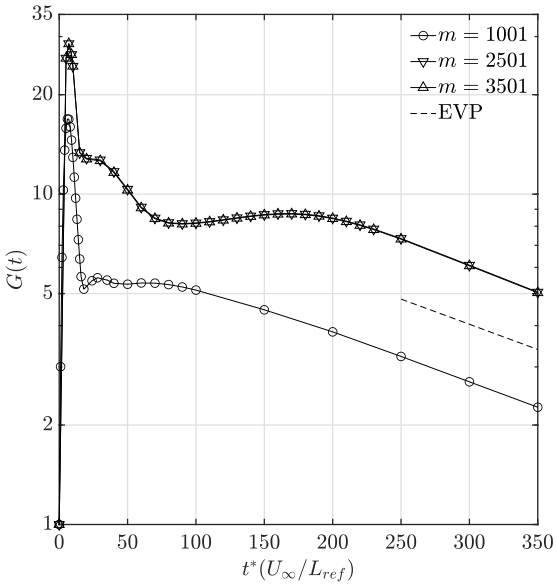

Figure 6.39: Energy growth dependence of the Krylov subspace size of the compression ramp for $Ma = 3$, $Re = 50000$ and $\beta = 0$. The negligible energy peak appears at $t \approx 7$.

calculation. The damping rate of the two-dimensional mode ($\beta = 0$) is in close agreement with the DNS residual's decay rate. A profile taken at the corner for both DNS and BiGlobal shape functions shows excellent agreement for the velocity components. Furthermore, nonmodal stability analysis found negligible transient growth for the parameter investigated.

6.4 Supersonic flat plate boundary layer

Renewed interest in manoeuvrable sustained hypersonic flight at altitudes around 50 km inside the earth's atmosphere brings to the fore the question of laminar-turbulent transition prediction on any part of the vehicle surface, and especially on axisymmetric vehicle forebodies and on lifting surfaces, typically modelled as circular-base cones and flat plates, respectively. Intense experimental and numerical efforts are underway (Chynoweth et al. 2017, Schneider 2004), mostly employing classic boundary layer linear stability theory (Mack 1965, 1969, 1984, Fedorov 2011) to predict and control linear instability mechanisms leading boundary layer flow to transition and turbulence and prevent a multifold increase in the thermal protection requirements and decrease of vehicle range. Such linear stability analysis approaches either altogether exclude the shock from the analysis or include it in the underlying (steady) base flow by appropriate modifications of the boundary conditions used at the boundary-layer edge (Stuckert and Reed 1994, Malik and Anderson 1991). In doing so, the internal shock layer structure (which is inaccessible to the Navier-Stokes equations) and its potential effect on boundary layer stability is either neglected or modelled through the boundary conditions. It would thus appear natural to apply kinetic theory methods to address linear flow instability; however, to-date it has not been demonstrated that kinetic theory methods can meet the long known stringent requirements on the quality of the base flow (and its first and second derivatives) for reliable stability analysis results to be obtained (Mack 1984). At such high altitudes, rarefied gas flows are encountered (Kennard 1938, Chambre and Schaaf 1961, Liu and Fang 2006). In these cases, the Knudsen number is of particular interest when assessing the boundary of fluid flows. This dimensionless parameter relates the mean free path $\overline{\lambda}$ and a characteristic length scale. Depending on the exact value of the Knudsen number, Kn, modifications to the boundary conditions used in the compressible Navier-Stokes equations are required for the latter to capture flow physics properly. Flows in which $0.01 \leq Kn \leq 0.1$ belong to the slip regime and require appropriate treatment of the wall boundary conditions to account for velocity slip and temperature jump (W.M. Zhang and X.Wei 2012). At $Kn > 0.1$ alternative methodologies based on kinetic theory, such as DSMC (Bird 1994), moment equations (Gu and Emerson 2009) or numerical solutions of the full Boltzmann equation (Evans et al. 2011), are required. Although kinetic theory methods can be applied to all flow regimes (W.M. Zhang and X.Wei 2012, Evans et al. 2011), their use in continuum and slip flow regimes is computationally very intensive methods based on the Navier-Stokes equations are preferable. However, the main drawback of the PDE-based description of compressible flows remains its inadequate description of the shock layer structure, as already discussed by Liepmann et al. (1962).

The objective of this work is to apply linear stability analysis on a canonical boundary layer over a semi-infinite flat plate using a steady base flow obtained from Direct Sim-

ulation Monte Carlo (DSMC) and compare the results with a base flow generated from the classical boundary-layer theory imposing slip and no-slip as boundary conditions.

6.4.1 Wall boundary conditions

The results were obtained for a Knudsen number of $Kn = 0.019$, and therefore slip exists at the wall boundary. The system of equations (5.3) require to be closed using wall boundary conditions accounting for the velocity slip and temperature jump. In this work, the conditions proposed by von Smoluchowski (1898) are used with a correction to the Maxwell conditions (Maxwell 1879), improved by Beskok et al. (1996), who modified these boundary conditions to include higher order terms,

$$\begin{aligned} u^*_{\text{slip}} &= \frac{1}{2}\left[u^*_\lambda + (1-\sigma_v)u^*_\lambda + \sigma_v u^*_{\text{wall}}\right] + \frac{3\sigma_v}{8}\frac{\mu^*}{\rho^* T^*}\frac{\partial T^*}{\partial x^*}, \\ T^*_{\text{slip}} &= \frac{\frac{2-\sigma_T}{Pr}\frac{\gamma}{\gamma+1}T^*_\lambda + \sigma_T T^*_{\text{wall}}}{\sigma_T + \frac{2-\sigma_T}{Pr}}. \end{aligned} \tag{6.20}$$

Here u^*_λ and T^*_λ denote the values of the streamwise velocity and temperature, respectively, at a distance of one mean free path, $\overline{\lambda}$, from the wall. As reported by the authors, this form of the equations allows these boundary conditions to obtain numerical solutions of the Navier-Stokes equations in the slip regime and up to very high Knudsen numbers, $Kn \sim 0.5$ (Beskok et al. 1996). The accommodation coefficients for velocity and temperature (Chambre and Schaaf 1961, Beskok and Karniadakis 1999, Klothakis et al. 2017) are denoted by σ_v and σ_T, respectively, and are both taken equal to unity. The wall values delivered by equations (6.20) have been found to be in general agreement with the slip velocities, and temperature jumps computed in the DSMC.

6.4.2 Base flow computation

All flow conditions and parameters are presented in table 6.5. Two approaches were followed: First, a baseflow was computed using the compressible boundary layer equations shown in 5.3. Second, a steady state baseflow was computed by Mr. Angelos Klothakis using the massively parallel open-source DSMC code SPARTA (Gallis et al. 2014, Plimpton et al. 2019) developed in Sandia National Laboratories. A snapshot of the streamwise velocity $\bar{u}$ at the last simulation time computed using SPARTA can be seen in figure 6.40, where a steady state solution is obtained. The base flow profiles were compared against each other and results can be found in Klothakis et al. (2021).

6.4.3 Local linear stability analysis computation

Eigenspectrum pertaining to the DMSC- and boundary-layer profiles obtained for air at a given two-dimensional wave-number $\alpha = 0.2$ are shown in figure 6.41; the amplitude functions of the least damped mode can be found in figures 6.42. In this plot, the generalised inflexion point (GIP) location is also indicated by a dashed horizontal

Table 6.5: Flow conditions analysed (Klothakis et al. 2021).

Gas constants, plate geometry and pre-shock free-stream conditions	
Fluid	Air
Knudsen number, Kn	0.0187
Mach number, M_∞, [-]	4.74
Reynolds number, Re_L, [-]	60354
Free-stream velocity, u_∞ [m s^{-1}]	1310
Free-stream temperature, T_∞ [K]	190
Free-stream density, ρ_∞ [kg m^{-3}]	6.04×10^{-4}
Reference temperature, T_{ref} [K]	273
Wall temperature, T_w [K]	Adiabatic

Boundary layer parameters	
Mach number, M_e, [-]	4.55
$Re = \sqrt{Re_x}$, [-]	214.0
Streamwise location, x, [m]	0.70
Slip velocity, u_{slip}, [m s^{-1}]	24.28
Edge velocity, u_e, [m s^{-1}]	1301.7
Edge temperature, T_e, [K]	202.90
Edge density, ρ_e, [kg m^{-3}]	6.91×10^{-4}
Edge pressure, p_e, [Pa]	40.296
Edge viscosity, μ_e, [N s m^{-2}]	1.376×10^{-5}
Wall temperature, T_w [K]	887.77

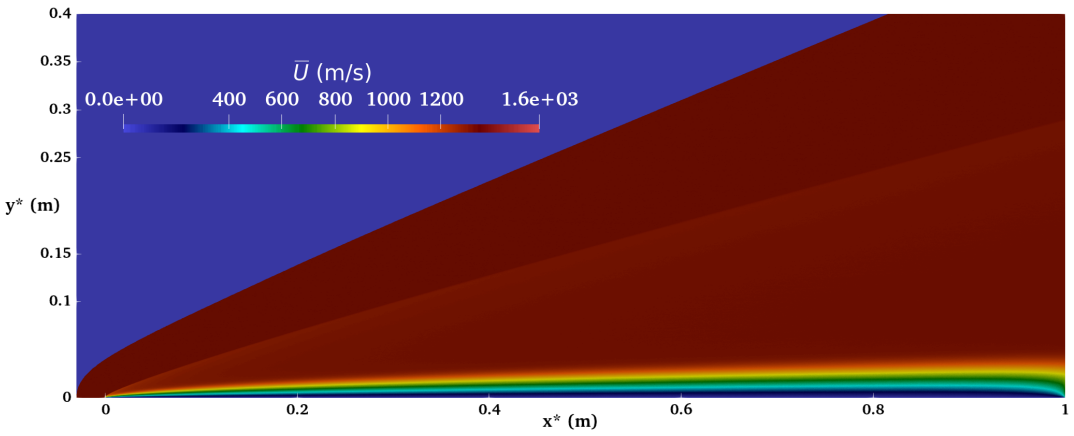

Figure 6.40: Steady base flow solution obtained by DSMC using SPARTA (Klothakis et al. 2021).

line. The results show that the linear instability properties of the profile extracted from the DSMC simulations and those computed in the corresponding boundary layer approximation are qualitatively identical and actually in close quantitative agreement. Only damped eigenvalues have been found at all sets of parameters, as expected from the relatively low values of $Re = \sqrt{Re_x}$.

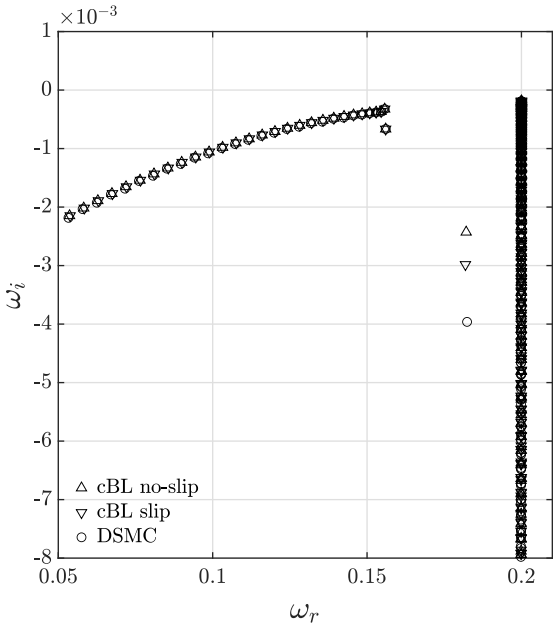

Figure 6.41: Eigenvalue spectrum of DSMC data, compared with compressible boundary layer (cBL) spectra under slip and no-slip boundary conditions. The discrete eigenvalue obtained on the profiles including velocity slip and temperature jump for the boundary layer is $\omega_{\text{cBL}} = 0.181859 - 0.00298i$, while that corresponding to the DSMC data is $\omega_{\text{DSMC}} = 0.182390 - 0.00396i$ (Klothakis et al. 2021).

Interestingly, figure 6.41 also includes the eigenspectra of compressible boundary layer profiles in which the classic no-slip boundary condition is imposed. The least damped discrete mode corresponding to the no-slip boundary layer profile is *less stable* than that pertaining to the profile in which the slip boundary conditions (6.20) have been imposed. The implication is that the imposition of the no-slip boundary condition in the base flow profile leads to the theoretical prediction of *earlier boundary layer transition*. The acoustic branches pertaining to both base flow profiles are practically identical, as are (rather surprisingly) the frequencies of the leading discrete modes of the raw DSMC profile and that of the boundary layer subject to boundary conditions (6.20).

6.4.4 Summary of flat plate analysis

Laminar hypersonic flow over a flat plate has been computed by highly-resolved DSMC simulations for boundary-layer edge Mach number of $Ma_e = 4.55$ and Reynolds number of $Re = 60354$, based on the flat plate length. A boundary layer profile extracted from the DSMC simulations has been analysed with respect to their linear modal instability. Results have been compared with those pertinent to the corresponding boundary layer profiles, in which wall slip was taken into consideration. In both gases, the acoustic branches obtained in the DSMC and the boundary layer analyses were indistinguish-

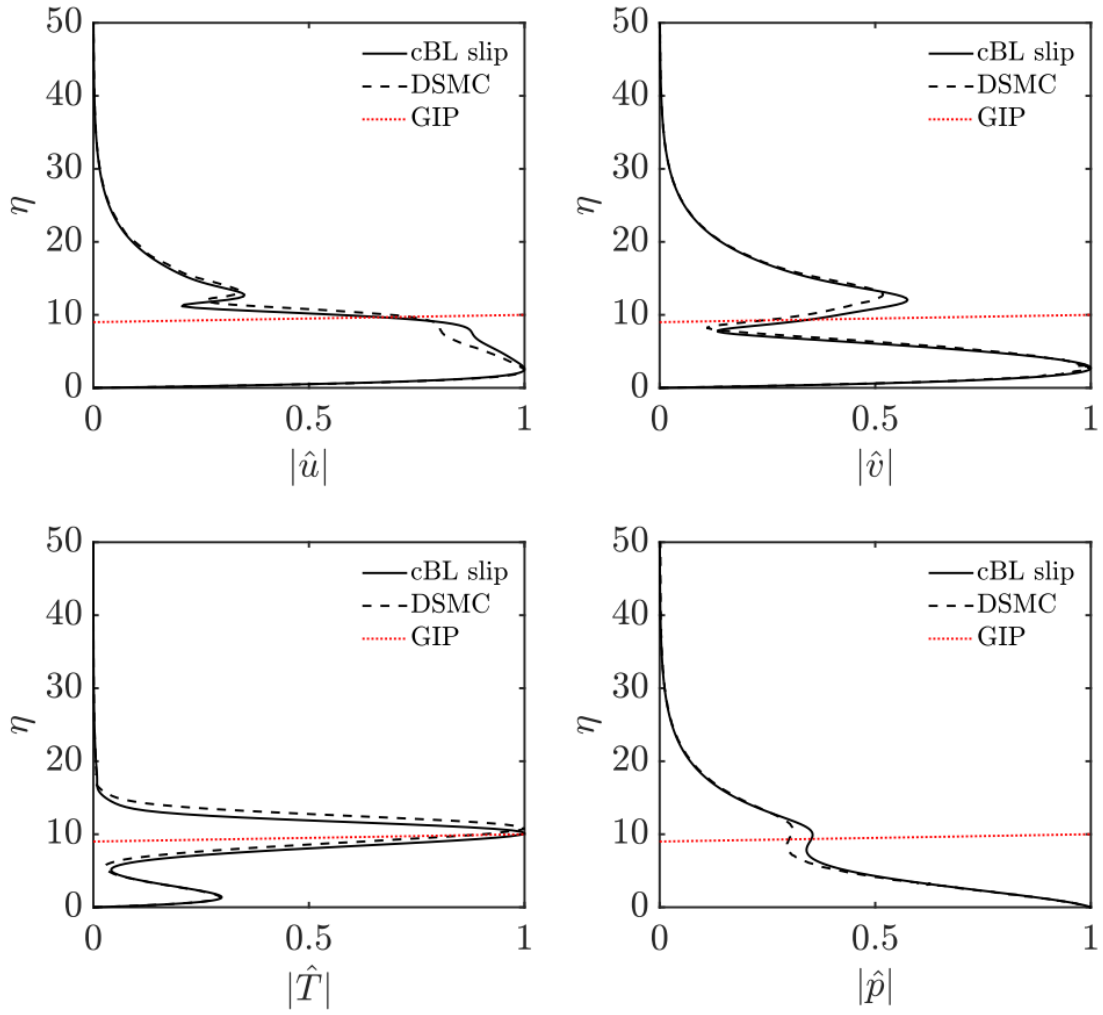

Figure 6.42: Normalized amplitude functions of linear perturbations for DSMC data and compressible boundary layer (cBL) with slip boundary conditions, at the parameters of figure 6.41. The location of the generalized inflection point (GIP) is indicated by a horizontal red line (Klothakis et al. 2021).

able. In contrast, the leading members of the discrete spectrum of the DSMC profiles were found to have practically identical frequencies with their boundary layer counterparts. To the authors best knowledge, these novel results establish, for the first time, the ability of the kinetic-theory based DSMC approach to predict steady laminar base flows of sufficient quality to be in close agreement with the established Navier-Stokes/boundary-layer-equations-based linear stability theory Mack (1965, 1969, 1984). Moreover, the results also demonstrate that imposition of the no-slip boundary condition on the base flow profiles leads to the prediction of less damped/more unstable leading discrete eigenmodes than those found when the slip boundary condition is imposed.

Chapter 7

Thesis summary and future recommendations

A newly developed Fortran code for the massively parallel solution of multi-dimensional complex non-symmetric eigenvalue problems (EVP) and Singular Value Decomposition (SVD) problems arising in global linear fluid flow instability has been developed. After a strict verification of the code with the literature, four different cases have been investigated. A summary, together with possible future works, is outlined next.

First, linear local and BiGlobal nonmodal stability analysis is presented on the hypersonic flow over an aspect ratio two elliptic cone model. Two different altitudes, namely 21 km and 33 km, are investigated. Guided by solutions to the local transient growth problem, which indicated that streamwise aligned linear perturbations exhibit the highest energy gain, the two-dimensional IVP has been solved until the slope of the energy gain curve locked onto the corresponding modal analysis result. Substantially more significant transient energy growth is obtained for streamwise-aligned perturbations at both altitudes, with optimal linear perturbations peaking in the crossflow region. They take the form of a finite number of isolated elongated structures aligned with the streamwise direction, and their spanwise wavelength compares qualitatively with the crossflow vortices reported in the BAM6QT experiment of Borg et al. (2012). By contrast to the quadratic dependence of the maximum energy gain on the local Reynolds number at the lower altitude, a quartic reliance is found in the highest altitude results indicates that laminar-turbulent transition of hypersonic boundary-layer flow may arise from nonmodal mechanisms, which presently remain unexplored for the majority of flows of interest. In the short term, nonmodal stability analysis can be carried out on the hypersonic flow over the HiFIRE-5 elliptic cone model in intermediate altitudes between 21 km and 33 km to investigate the threshold of the quadratic to quartic change in the energy gain relation. Moreover, higher altitudes can be analysed, where transient growth is the likely mechanism responsible for the laminar-turbulent transition.

Modal and nonmodal global stability analysis was performed in the hypersonic flow over the windward face of a circular cylinder. The baseflow was obtained using a high-order finite-difference generalised coordinates DNS code (Santos 2020). The bow shock generated ahead of the cylinder was included in the stability analysis domain. Modal results are in excellent agreement with the DNS least damped mode calculated with the Residuals Algorithm Theofilis (2000b). Moreover, a nonmodal analysis of the two-dimensional flow shows that strong transient growth can occur with the optimal conditions peaking in the shock. The immediate next step in the work related to the hypersonic cylinder and the compression ramp is the imposition of three-dimensional perturbations ($\beta \neq 0$) in the two-dimensional base flow to verify if the flow remains stable. After that, the neutral curve can be calculated, performing a parametric study for different Reynolds numbers. In this case, the regions of stability or amplification of the perturbations can be catalogued.

To investigate the shock boundary-layer interaction (SBLI) role in the global mode, a modal and nonmodal linear stability analysis has been carried out in the supersonic flow over a 10° compression ramp. The base flow was also generated using the high-order finite-difference 3DSSS code. The results obtained pointed out the strong relationship between the recompression shock and the laminar separation bubble. The least damped two-dimensional mode obtained from the *LiGHT* code is in excellent agreement with the DNS. On the other hand, negligible transient growth was found in the two-dimensional flow. The future work would aim in the same direction as the previous cylinder case, studying three-dimensional perturbations that would lead to modal instability.

Finally, the local linear stability analysis of the hypersonic flow over a semi-infinite flat-pate is investigated using Direct Simulation Monte Carlo (DSMC) to generate a steady base flow. Results are compared against the classical base flow obtained from the compressible boundary-layer theory, imposing both slip and no-slip conditions on the wall. All three profiles agree well in the continuous and acoustic branches of the eigenspectrum. Moreover, the results also demonstrate that imposition of the no-slip boundary condition on the base flow profiles leads to the prediction of less damped/more unstable leading discrete eigenmodes than those found when the slip boundary condition is imposed. After showing the linear stability analysis capability to be performed on DSMC base flows, a future endeavour related to the flow over a flat-plate would be the analysis of high Mach numbers, where the continuous approach adopted by the Navier-Stokes equations does not hold.

The newly developed global transient growth can also be used to investigate different three-dimensional geometries with one homogeneous spatial direction, as for example the Cerminara's configuration (Cerminara 2017, Cerminara and Sandham 2020) or the BOLT configuration (Wheaton et al. 2018, Thome et al. 2018, Moyes and Reed 2021).

Appendix A

Compressible Local LNSE in Cartesian coordinates

The coefficients of the matrices $\mathcal{A}$ and $\mathcal{B}$ for local stability analysis can be written explicitly as

$$\left(A_j^i \frac{\partial^2}{\partial y^2} + B_j^i \frac{\partial}{\partial y} + C_j^i \right) \hat{q}_j = \omega \; D_j^i \; \hat{q}_j. \tag{A.1}$$

Here, A, B, C and D are vectors with size $(N1 \times 1)$ and the superscript $i = (1, 2, 3, 4, 5)$ corresponds to the linearized equations of motion, 1 referring to the momentum equation in x, 2 to the momentum equation in y , 3 to the momentum equation in z, 4 to the energy and 5 to the continuity equation. The subscript $j = (1, 2, 3, 4, 5) \equiv (\hat{u}, \hat{v}, \hat{w}, \hat{T}, \hat{p})$ corresponds to the five disturbances variables. This formulation was also shown by Malik (1990). Mack (1969, 1984), Macaraeg and Streett (1988) show the equations for density and temperature formulation.
The nonzero elements are given by

Momentum - x equation

$$
\begin{aligned}
A^1_{\hat{u}} &= -\frac{\mu}{Re} \\
B^1_{\hat{u}} &= +\gamma \mathrm{Ma}^2 \bar{v} \frac{\bar{p}}{\bar{T}} - \frac{1}{Re}\frac{d\bar{\mu}}{d\bar{T}}\frac{\partial \bar{T}}{\partial y} \\
C^1_{\hat{u}} &= +i\gamma \mathrm{Ma}^2 \frac{\bar{p}}{\bar{T}}(\alpha \bar{u} + \beta \bar{w}) + \frac{1}{Re}\left(\bar{\lambda}\alpha^2 + \bar{\mu}(2\alpha^2 + \beta^2)\right) \\
D^1_{\hat{u}} &= +i\gamma \mathrm{Ma}^2 \frac{\bar{p}}{\bar{T}}
\end{aligned}
$$

$$
\begin{aligned}
B^1_{\hat{v}} &= -i\alpha \frac{1}{Re}(\mu + \lambda) \\
C^1_{\hat{v}} &= +\gamma \mathrm{Ma}^2 \frac{\bar{p}}{\bar{T}}\frac{\partial \bar{u}}{\partial y} - i\alpha \frac{1}{Re}\frac{d\bar{\mu}}{d\bar{T}}\frac{\partial \bar{T}}{\partial y}
\end{aligned}
\tag{A.2}
$$

$$
C^1_{\hat{w}} = +\alpha\beta \frac{1}{Re}(\mu + \lambda)
$$

$$
\begin{aligned}
B^1_{\hat{T}} &= -\frac{1}{Re}\frac{d\bar{\mu}}{d\bar{T}}\frac{\partial \bar{u}}{\partial y} \\
C^1_{\hat{T}} &= -\gamma \mathrm{Ma}^2 \bar{v}\frac{\partial \bar{u}}{\partial y}\frac{\bar{p}}{\bar{T}^2} - \frac{1}{Re}\left(\frac{d\bar{\mu}}{d\bar{T}}\frac{\partial^2 \bar{u}}{\partial y^2} + i\alpha \frac{d\bar{\lambda}}{d\bar{T}}\frac{\partial \bar{v}}{\partial y} + \frac{d^2\bar{\mu}}{d\bar{T}^2}\frac{\partial \bar{T}}{\partial y}\frac{\partial \bar{u}}{\partial y}\right)
\end{aligned}
$$

$$
C^1_{\hat{p}} = +\gamma \mathrm{Ma}^2 \bar{v}\frac{1}{\bar{T}}\frac{\partial \bar{u}}{\partial y} + i\alpha
$$

Momentum - y equation

$$
\begin{aligned}
B^2_{\hat{u}} &= -i\alpha\frac{1}{Re}(\mu+\lambda)\\
C^2_{\hat{u}} &= -i\alpha\frac{1}{Re}\frac{d\bar{\lambda}}{d\bar{T}}\frac{\partial\bar{T}}{\partial y}
\end{aligned}
$$

$$
\begin{aligned}
A^2_{\hat{v}} &= -\frac{1}{Re}(2\bar{\mu}+\bar{\lambda})\\
B^2_{\hat{v}} &= +\gamma\mathrm{Ma}^2\bar{v}\frac{\bar{p}}{\bar{T}} - \frac{1}{Re}\left(2\frac{d\bar{\mu}}{d\bar{T}}+\frac{d\bar{\lambda}}{d\bar{T}}\right)\frac{\partial\bar{T}}{\partial y}\\
C^2_{\hat{v}} &= +\gamma\mathrm{Ma}^2\frac{\bar{p}}{\bar{T}}\left(i(\alpha\bar{u}+\beta\bar{w})+\frac{\partial\bar{v}}{\partial y}\right)+\frac{1}{Re}\left(\bar{\mu}(\alpha^2+\beta^2)\right)\\
D^2_{\hat{v}} &= +i\gamma\mathrm{Ma}^2\frac{\bar{p}}{\bar{T}}
\end{aligned}
$$

$$
\begin{aligned}
B^2_{\hat{w}} &= -i\beta\frac{1}{Re}(\mu+\lambda)\\
C^2_{\hat{w}} &= -i\beta\frac{1}{Re}\frac{d\bar{\lambda}}{d\bar{T}}\frac{\partial\bar{T}}{\partial y}
\end{aligned}
\tag{A.3}
$$

$$
\begin{aligned}
B^2_{\hat{T}} &= -\frac{1}{Re}\left(2\frac{d\bar{\mu}}{d\bar{T}}+\frac{d\bar{\lambda}}{d\bar{T}}\right)\frac{\partial\bar{v}}{\partial y}\\
C^2_{\hat{T}} &= -\gamma\mathrm{Ma}^2\bar{v}\frac{\partial\bar{v}}{\partial y}\frac{\bar{p}}{\bar{T}^2} - \frac{1}{Re}\left[\frac{d\bar{\mu}}{d\bar{T}}\left(i\alpha\frac{\partial\bar{u}}{\partial y}+i\beta\frac{\partial\bar{w}}{\partial y}+2\frac{\partial^2\bar{v}}{\partial y^2}\right)+\frac{d\bar{\lambda}}{d\bar{T}}\frac{\partial^2\bar{v}}{\partial y^2}\right.\\
&\quad\left.+\left(2\frac{d^2\bar{\mu}}{d\bar{T}^2}+\frac{d^2\bar{\lambda}}{d\bar{T}^2}\right)\frac{\partial\bar{v}}{\partial y}\frac{\partial\bar{T}}{\partial y}\right]
\end{aligned}
$$

$$
\begin{aligned}
B^2_{\hat{p}} &= +1\\
C^2_{\hat{p}} &= +\gamma\mathrm{Ma}^2\bar{v}\frac{1}{\bar{T}}\frac{\partial\bar{v}}{\partial y}
\end{aligned}
$$

Momentum - z equation

$$
\begin{aligned}
A^3_{\hat{w}} &= -\frac{\mu}{Re} \\
B^3_{\hat{w}} &= +\gamma \mathrm{Ma}^2 \bar{v}\frac{\bar{p}}{\bar{T}} - \frac{1}{Re}\frac{d\bar{\mu}}{d\bar{T}}\frac{\partial \bar{T}}{\partial y} \\
C^3_{\hat{w}} &= +i\gamma \mathrm{Ma}^2 \frac{\bar{p}}{\bar{T}}(\alpha\bar{u}+\beta\bar{w}) + \frac{1}{Re}\left(\bar{\lambda}\beta^2 + \bar{\mu}(\alpha^2+2\beta^2)\right) \\
D^3_{\hat{w}} &= +i\gamma \mathrm{Ma}^2 \frac{\bar{p}}{\bar{T}}
\end{aligned}
$$

$$
\begin{aligned}
B^3_{\hat{v}} &= -i\beta\frac{1}{Re}(\mu+\lambda) \\
C^3_{\hat{v}} &= +\gamma \mathrm{Ma}^2 \frac{\bar{p}}{\bar{T}}\frac{\partial \bar{w}}{\partial y} - i\beta\frac{1}{Re}\frac{d\bar{\mu}}{d\bar{T}}\frac{\partial \bar{T}}{\partial y}
\end{aligned}
\tag{A.4}
$$

$$
C^3_{\hat{u}} = +\alpha\beta\frac{1}{Re}(\mu+\lambda)
$$

$$
\begin{aligned}
B^3_{\hat{T}} &= -\frac{1}{Re}\frac{d\bar{\mu}}{d\bar{T}}\frac{\partial \bar{w}}{\partial y} \\
C^3_{\hat{T}} &= -\gamma \mathrm{Ma}^2 \bar{v}\frac{\partial \bar{w}}{\partial y}\frac{\bar{p}}{\bar{T}^2} - \frac{1}{Re}\left(\frac{d\bar{\mu}}{d\bar{T}}\frac{\partial^2 \bar{w}}{\partial y^2} + i\beta\frac{d\bar{\lambda}}{d\bar{T}}\frac{\partial \bar{v}}{\partial y} + \frac{d^2\bar{\mu}}{d\bar{T}^2}\frac{\partial \bar{T}}{\partial y}\frac{\partial \bar{w}}{\partial y}\right)
\end{aligned}
$$

$$
C^3_{\hat{p}} = +\gamma \mathrm{Ma}^2 \bar{v}\frac{1}{\bar{T}}\frac{\partial \bar{w}}{\partial y} + i\beta
$$

Energy equation

$$
\begin{aligned}
B^4_{\hat{u}} &= -2\bar{\mu}\frac{Ec}{Re}\frac{\partial \bar{u}}{\partial y} \\
C^4_{\hat{u}} &= -2i\alpha\bar{\lambda}\frac{Ec}{Re}\frac{\partial \bar{v}}{\partial y}
\end{aligned}
$$

$$
\begin{aligned}
B^4_{\hat{v}} &= -2\frac{Ec}{Re}\frac{\partial \bar{v}}{\partial y}(2\bar{\mu}+\bar{\lambda}) \\
C^4_{\hat{v}} &= +\gamma \mathrm{Ma}^2 c_p \frac{\bar{p}}{\bar{T}}\frac{\partial \bar{T}}{\partial y} - Ec\frac{\partial \bar{p}}{\partial y} - 2\bar{\mu}\frac{Ec}{Re}\left(i\alpha\frac{\partial \bar{u}}{\partial y} + i\beta\frac{\partial \bar{w}}{\partial y}\right)
\end{aligned}
$$

$$
\begin{aligned}
B^4_{\hat{w}} &= -2\bar{\mu}\frac{Ec}{Re}\frac{\partial \bar{w}}{\partial y} \\
C^4_{\hat{w}} &= -2i\beta\bar{\lambda}\frac{Ec}{Re}\frac{\partial \bar{v}}{\partial y}
\end{aligned}
$$

$$
\begin{aligned}
A^4_{\hat{T}} &= -\frac{1}{RePr}\bar{k} \\
B^4_{\hat{T}} &= +\gamma \mathrm{Ma}^2 c_p \bar{v}\frac{\bar{p}}{\bar{T}} - \frac{2}{RePr}\frac{d\bar{k}}{d\bar{T}}\frac{\partial \bar{T}}{\partial y} \\
C^4_{\hat{T}} &= +\gamma \mathrm{Ma}^2 c_p \frac{\bar{p}}{\bar{T}^2}\left(\bar{T}(i\alpha\bar{u}+i\beta\bar{w}) - \bar{v}\frac{\partial \bar{T}}{\partial y}\right) \\
&\quad - \frac{Ec}{Re}\left[\frac{d\bar{\mu}}{d\bar{T}}\left(\left(\frac{\partial \bar{u}}{\partial y}\right)^2 + 2\left(\frac{\partial \bar{v}}{\partial y}\right)^2 + \left(\frac{\partial \bar{w}}{\partial y}\right)^2\right)\right] \\
&\quad + \frac{1}{RePr}\left[\bar{k}(\alpha^2+\beta^2) - \frac{d\bar{k}}{d\bar{T}}\frac{\partial^2 \bar{T}}{\partial y^2} - \frac{d^2\bar{k}}{d\bar{T}^2}\left(\frac{\partial \bar{T}}{\partial y}\right)^2\right] \\
D^4_{\hat{T}} &= +i\gamma \mathrm{Ma}^2 c_p \frac{\bar{p}}{\bar{T}}
\end{aligned}
\tag{A.5}
$$

$$
\begin{aligned}
B^4_{\hat{p}} &= -Ec\ \bar{v} \\
C^4_{\hat{p}} &= +\gamma \mathrm{Ma}^2 c_p \bar{v}\frac{1}{\bar{T}}\frac{\partial \bar{T}}{\partial y} - Ec(i\alpha\bar{u}+i\beta\bar{w}) \\
D^4_{\hat{p}} &= -iEc
\end{aligned}
$$

Continuity equation

$$
\begin{aligned}
C^5_{\hat{u}} &= +\, i\alpha\bar{p} \\
\\
B^5_{\hat{v}} &= \bar{p} \\
C^5_{\hat{v}} &= +\, \frac{\partial \bar{p}}{\partial y} - \frac{\bar{p}}{\bar{T}}\frac{\partial \bar{T}}{\partial y} \\
\\
C^5_{\hat{w}} &= +\, i\beta\bar{p} \\
\\
B^5_{\hat{T}} &= -\, \frac{\bar{p}}{\bar{T}}\bar{v} \\
C^5_{\hat{T}} &= -\, \bar{v}\frac{1}{\bar{T}}\frac{\partial \bar{p}}{\partial y} - \frac{\bar{p}}{\bar{T}}\left(i\alpha\bar{u} + i\beta\bar{w} + \frac{\partial \bar{v}}{\partial y} - 2\bar{v}\frac{1}{\bar{T}}\frac{\partial \bar{T}}{\partial y}\right) \\
D^5_{\hat{T}} &= -\, i\frac{\bar{p}}{\bar{T}} \\
\\
B^5_{\hat{p}} &= +\, \bar{v} \\
C^5_{\hat{p}} &= +\, i\alpha\bar{u} + i\beta\bar{w} + \frac{\partial \bar{v}}{\partial y} - \bar{v}\frac{1}{\bar{T}}\frac{\partial \bar{T}}{\partial y} \\
D^5_{\hat{p}} &= +\, i
\end{aligned}
\tag{A.6}
$$

Appendix B

Compressible BiGlobal LNSE in Cartesian coordinates

The coefficients of the matrices $\mathcal{A}$ and $\mathcal{B}$ shown in (2.21) are (see Paredes (2014) for density and temperature formulation)

$$\begin{pmatrix} \mathcal{A}_{11} & \mathcal{A}_{12} & \mathcal{A}_{13} & \mathcal{A}_{14} & \mathcal{A}_{15} \\ \mathcal{A}_{21} & \mathcal{A}_{22} & \mathcal{A}_{23} & \mathcal{A}_{24} & \mathcal{A}_{25} \\ \mathcal{A}_{31} & \mathcal{A}_{32} & \mathcal{A}_{33} & \mathcal{A}_{34} & \mathcal{A}_{35} \\ \mathcal{A}_{41} & \mathcal{A}_{42} & \mathcal{A}_{43} & \mathcal{A}_{44} & \mathcal{A}_{45} \\ \mathcal{A}_{51} & \mathcal{A}_{52} & \mathcal{A}_{53} & \mathcal{A}_{54} & \mathcal{A}_{55} \end{pmatrix} \begin{pmatrix} \hat{u} \\ \hat{v} \\ \hat{w} \\ \hat{T} \\ \hat{p} \end{pmatrix} = \omega \begin{pmatrix} \mathcal{B}_{11} & 0 & 0 & 0 & 0 \\ 0 & \mathcal{B}_{22} & 0 & 0 & 0 \\ 0 & 0 & \mathcal{B}_{33} & 0 & 0 \\ 0 & 0 & 0 & \mathcal{B}_{44} & \mathcal{B}_{45} \\ 0 & 0 & 0 & \mathcal{B}_{54} & \mathcal{B}_{55} \end{pmatrix} \begin{pmatrix} \hat{u} \\ \hat{v} \\ \hat{w} \\ \hat{T} \\ \hat{p} \end{pmatrix}$$

Momentum x equation

$$\begin{aligned}
\mathcal{A}_{11} =& -\frac{4}{3}\frac{\bar{\mu}}{Re}D_{xx} + \left[-\frac{4}{3}\frac{1}{Re}\frac{d\bar{\mu}}{dT}\bar{T}_x + \bar{\rho}\bar{u}\right]D_x - \frac{\bar{\mu}}{Re}D_{yy} + \left[-\frac{1}{Re}\frac{d\bar{\mu}}{dT}\bar{T}_y + \bar{\rho}\bar{v}\right]D_y \\
&+ \frac{\beta^2\bar{\mu}}{Re} + \bar{\rho}\bar{u}_x + i\beta\bar{\rho}\bar{w} \\
\mathcal{A}_{12} =& -\frac{1}{3}\frac{\bar{\mu}}{Re}D_{xy} - \frac{1}{Re}\frac{\bar{\mu}}{dT}\bar{T}_y D_x + \frac{2}{3}\frac{1}{Re}\frac{d\bar{\mu}}{dT}\bar{T}_x D_y + \bar{\rho}\bar{u}_y \\
\mathcal{A}_{13} =& -\frac{i}{3}\frac{\beta}{Re}\bar{\mu}D_x + \frac{2}{3}\frac{i\beta}{Re}\frac{d\bar{\mu}}{dT}\bar{T}_x \\
\mathcal{A}_{14} =& -\frac{1}{Re}\frac{d\bar{\mu}}{dT}\left(\frac{4}{3}\bar{u}_x - \frac{2}{3}\bar{v}_y\right)D_x - \frac{1}{Re}\frac{d\bar{\mu}}{dT}(\bar{u}_y + \bar{v}_x)D_y \\
&- \frac{1}{Re}\frac{d\bar{\mu}}{dT}\left(i\beta\bar{w}_x + \frac{4}{3}\bar{u}_{xx} + \bar{u}_{yy} + \frac{1}{3}\bar{v}_{xy}\right) \\
&- \frac{1}{Re}\frac{d^2\bar{\mu}}{dT^2}\left(\frac{4}{3}\bar{T}_x\bar{u}_x + \bar{T}_y(\bar{u}_y + \bar{v}_x) - \frac{2}{3}\bar{T}_x\bar{v}_y\right) - \frac{\bar{\rho}}{\bar{T}}(\bar{u}\bar{u}_x + \bar{v}\bar{u}_y) \\
\mathcal{A}_{15} =& D_x + \frac{\gamma Ma^2}{\bar{T}}(\bar{u}\bar{u}_x + \bar{v}\bar{u}_y) \\
\mathcal{B}_{11} =& i\bar{\rho}
\end{aligned} \tag{B.1}$$

Momentum y equation

$$
\begin{aligned}
\mathcal{A}_{21} =& -\frac{1}{3}\frac{\bar{\mu}}{Re}D_{xy} + \frac{2}{3}\frac{1}{Re}\frac{d\bar{\mu}}{dT}\bar{T}_y D_x - \frac{1}{Re}\frac{d\bar{\mu}}{dT}\bar{T}_x D_y + \bar{\rho}\bar{v}_x \\
\mathcal{A}_{22} =& -\frac{\bar{\mu}}{Re}D_{xx} + \left[-\frac{1}{Re}\frac{d\bar{\mu}}{dT}\bar{T}_x + \bar{\rho}\bar{u}\right]D_x - \frac{4}{3}\frac{\bar{\mu}}{Re}D_{yy} + \left[-\frac{4}{3}\frac{1}{Re}\frac{d\bar{\mu}}{dT}\bar{T}_y + \bar{\rho}\bar{v}\right]D_y \\
&+ \frac{\beta^2\bar{\mu}}{Re} + \bar{\rho}\bar{v}_y + i\beta\bar{\rho}\bar{w} \\
\mathcal{A}_{23} =& -\frac{i}{3}\frac{\beta}{Re}\bar{\mu}D_y + \frac{2}{3}\frac{i\beta}{Re}\frac{d\bar{\mu}}{dT}\bar{T}_y \\
\mathcal{A}_{24} =& -\frac{1}{Re}\frac{d\bar{\mu}}{dT}(\bar{u}_y + \bar{v}_x)D_x - \frac{1}{Re}\frac{d\bar{\mu}}{dT}\left(\frac{4}{3}\bar{v}_y - \frac{2}{3}\bar{u}_x\right)D_y \\
&- \frac{1}{Re}\frac{d\bar{\mu}}{dT}\left(i\beta\bar{w}_y + \frac{4}{3}\bar{v}_{yy} + \frac{1}{3}\bar{u}_{xy} + \bar{v}_{xx}\right) \\
&- \frac{1}{Re}\frac{d^2\bar{\mu}}{dT^2}\left(\frac{4}{3}\bar{T}_y\bar{v}_y + \bar{T}_x(\bar{u}_y + \bar{v}_y) - \frac{2}{3}\bar{T}_y\bar{u}_x\right) - \frac{\bar{\rho}}{\bar{T}}(\bar{u}\bar{v}_x + \bar{v}\bar{v}_y) \\
\mathcal{A}_{25} =& D_y + \frac{\gamma Ma^2}{\bar{T}}(\bar{u}\bar{v}_x + \bar{v}\bar{v}_y) \\
\mathcal{B}_{22} =& i\bar{\rho}
\end{aligned}
\tag{B.2}
$$

Momentum z equation

$$
\begin{aligned}
\mathcal{A}_{31} =& -\frac{i}{3}\frac{\beta}{Re}\bar{\mu}D_x - \frac{i\beta}{Re}\frac{d\bar{\mu}}{dT}\bar{T}_x + \bar{\rho}\bar{w}_x \\
\mathcal{A}_{32} =& \mathcal{A}_{31} = -\frac{i}{3}\frac{\beta}{Re}\bar{\mu}D_y - \frac{i\beta}{Re}\frac{d\bar{\mu}}{dT}\bar{T}_y + \bar{\rho}\bar{w}_y \\
\mathcal{A}_{33} =& -\frac{\bar{\mu}}{Re}D_{xx} - \frac{\bar{\mu}}{Re}D_{yy} + \left[-\frac{1}{Re}\frac{d\bar{\mu}}{dT}\bar{T}_x + \bar{\rho}\bar{u}\right]D_x + \left[-\frac{1}{Re}\frac{d\bar{\mu}}{dT}\bar{T}_y + \bar{\rho}\bar{v}\right]D_y \\
&+ \frac{4}{3}\frac{\beta^2\bar{\mu}}{Re} + i\beta\bar{\rho}\bar{w} \\
\mathcal{A}_{34} =& -\frac{1}{Re}\frac{d\bar{\mu}}{dT}\bar{w}_x D_x - \frac{1}{Re}\frac{d\bar{\mu}}{dT}\bar{w}_y D_y \\
&- \frac{1}{Re}\frac{d\bar{\mu}}{dT}\left(\bar{w}_{xx} + \bar{w}_{yy} - \frac{2}{3}i\beta(\bar{u}_x + \bar{v}_y)\right. \\
&- \frac{1}{Re}\frac{d^2\bar{\mu}}{dT^2}(\bar{T}_x\bar{w}_x + \bar{T}_y(\bar{w}_y) - \frac{\bar{\rho}}{\bar{T}}(\bar{u}\bar{w}_x + \bar{v}\bar{w}_y) \\
\mathcal{A}_{35} =& i\beta + \frac{\gamma Ma^2}{\bar{T}}(\bar{u}\bar{w}_x + \bar{v}\bar{w}_y) \\
\mathcal{B}_{33} =& i\bar{\rho}
\end{aligned}
\tag{B.3}
$$

Energy equation

$$
\begin{aligned}
\mathcal{A}_{41} =& \Bigg[- 2\frac{(\gamma-1)Ma^2}{Re}\bar{\mu}\left(\frac{4}{3}\bar{u}_x - \frac{2}{3}\bar{v}_y\right) + \gamma Ma^2\bar{p}D_x - 2\frac{(\gamma-1)Ma^2}{Re}\bar{\mu}(\bar{u}_y + \bar{v}_x)D_y \\
& - 2\frac{(\gamma-1)Ma^2}{Re}\bar{\mu}\bar{w}_x + Ma^2\bar{p}_x \\
\mathcal{A}_{42} =& - 2\frac{(\gamma-1)Ma^2}{Re}\bar{\mu}(\bar{u}_y + \bar{v}_x)D_x + \Bigg[- 2\frac{(\gamma-1)Ma^2}{Re}\bar{\mu}\left(- \frac{2}{3}\bar{u}_x + \frac{4}{3}\bar{v}_y\right) \\
& + \gamma Ma^2\bar{p}\Bigg]D_y - 2\frac{(\gamma-1)Ma^2}{Re}\bar{\mu}\bar{w}_y + Ma^2\bar{p}_y \\
\mathcal{A}_{43} =& - 2\frac{(\gamma-1)Ma^2}{Re}\bar{\mu}\bar{w}_x D_x - 2\frac{(\gamma-1)Ma^2}{Re}\bar{\mu}\bar{w}_y D_y + \frac{4}{3}\frac{i\beta(\gamma-1)Ma^2}{Re}\bar{\mu}(\bar{u}_x + \bar{v}_y) \\
& + i\beta\gamma Ma^2\bar{p} \\
\mathcal{A}_{44} =& - \frac{\bar{k}}{RePr}D_{xx} - \frac{2}{RePr}\frac{d\bar{k}}{dT}\bar{T}_x D_x - \frac{\bar{k}}{RePr}D_{yy} - \frac{2}{RePr}\frac{d\bar{k}}{dT}\bar{T}_y D_y \\
& + \frac{\beta^2\bar{k}}{RePr} - \frac{1}{RePr}\frac{d\bar{k}}{dT}(\bar{T}_{xx} + \bar{T}_{yy}) - \frac{1}{RePr}\frac{d^2\bar{k}}{dT^2}(\bar{T}_x^2 + \bar{T}_y^2) \\
& + \frac{(\gamma-1)Ma^2}{Re}\frac{d\bar{\mu}}{dT}\left(\frac{2}{3}(\bar{u}_x + \bar{v}_y)^2 - (\bar{u}_y + \bar{v}_x)^2 - 2(\bar{u}_x^2 + \bar{v}_y^2) - \bar{w}_x^2 - \bar{w}_y^2\right) \\
\mathcal{A}_{45} =& Ma^2\bar{u}D_x + Ma^2\bar{v}D_y + i\beta Ma^2\bar{w} + \gamma Ma^2(\bar{u}_x + \bar{v}_y) \\
\mathcal{B}_{45} =& iMa^2
\end{aligned}
\tag{B.4}
$$

Continuity equation

$$
\begin{aligned}
\mathcal{A}_{51} =& \bar{\rho}D_x + \bar{\rho}_x \\
\mathcal{A}_{52} =& \bar{\rho}D_y + \bar{\rho}_y \\
\mathcal{A}_{53} =& i\beta\bar{\rho} \\
\mathcal{A}_{54} =& - \frac{\bar{\rho}}{\bar{T}}\bar{u}D_x - \frac{\bar{\rho}}{\bar{T}}\bar{v}D_y + \frac{\bar{\rho}}{\bar{T}}(-\bar{u}_x - \bar{v}_y - i\beta\bar{w}) + \frac{\bar{\rho}}{\bar{T}^2}(\bar{u}\bar{T}_x + \bar{v}\bar{T}_y) - \frac{1}{\bar{T}}(\bar{u}\bar{\rho}_x + \bar{v}\bar{\rho}_y) \\
\mathcal{A}_{55} =& \gamma Ma^2\frac{\bar{u}}{\bar{T}}D_x + \gamma Ma^2\frac{\bar{v}}{\bar{T}}D_y - \frac{\gamma Ma^2}{\bar{T}^2}(\bar{u}\bar{T}_x + \bar{v}\bar{T}_y) + \frac{\gamma Ma^2}{\bar{T}}(\bar{u}_x + \bar{v}_y + i\beta\bar{w}) \\
\mathcal{B}_{54} =& - \frac{i\bar{\rho}}{\bar{T}} \\
\mathcal{B}_{55} =& \gamma Ma^2\frac{i}{\bar{T}}
\end{aligned}
\tag{B.5}
$$

Appendix C

Compressible TriGlobal LNSE in Cartesian coordinates

The coefficients of the matrices $\mathcal{A}$ and $\mathcal{B}$ for TriGlobal stability analysis can be written explicitly as

$$\left(A_j^i \frac{\partial^2}{\partial x^2} + B_j^i \frac{\partial^2}{\partial y^2} + C_j^i \frac{\partial^2}{\partial z^2} + D_j^i \frac{\partial^2}{\partial x \partial y} + E_j^i \frac{\partial^2}{\partial x \partial z} + F_j^i \frac{\partial^2}{\partial y \partial z} + G_j^i \frac{\partial}{\partial x} + H_j^i \frac{\partial}{\partial y} + I_j^i \frac{\partial}{\partial z} + J_j^i\right) \hat{q}_j = \omega \; K_j^i \; \hat{q}_j. \tag{C.1}$$

Here, $A, B, C, D, E, F, G, H, I, J$ and K are vectors with size $(NxNyNz \times 1)$ and the superscript $i = (1, 2, 3, 4, 5)$ corresponds to the linearized equations of motion, 1 referring to the momentum equation in x, 2 to the momentum equation in y , 3 to the momentum equation in z, 4 to the energy and 5 to the continuity equation. The subscript $j = (1, 2, 3, 4, 5) \equiv (\hat{u}, \hat{v}, \hat{w}, \hat{T}, \hat{p})$ corresponds to the five disturbances variables.
The nonzero elements are given by

Momentum - x equation

$$
\begin{aligned}
A^1_{\hat{u}} &= -\frac{1}{Re}\left(\bar{\lambda}+2\bar{\mu}\right)\\
B^1_{\hat{u}} &= -\frac{1}{Re}\bar{\mu}\\
C^1_{\hat{u}} &= -\frac{1}{Re}\bar{\mu}\\
G^1_{\hat{u}} &= +\gamma \mathrm{Ma}^2\frac{\bar{p}}{\bar{T}}\bar{u}-\frac{1}{Re}\left(\frac{d\bar{\lambda}}{d\bar{T}}+2\frac{d\bar{\mu}}{d\bar{T}}\right)\frac{\partial\bar{T}}{\partial x}\\
H^1_{\hat{u}} &= +\gamma \mathrm{Ma}^2\frac{\bar{p}}{\bar{T}}\bar{v}-\frac{1}{Re}\frac{d\bar{\mu}}{d\bar{T}}\frac{\partial\bar{T}}{\partial y}\\
I^1_{\hat{u}} &= +\gamma \mathrm{Ma}^2\frac{\bar{p}}{\bar{T}}\bar{w}-\frac{1}{Re}\frac{d\bar{\mu}}{d\bar{T}}\frac{\partial\bar{T}}{\partial z}\\
J^1_{\hat{u}} &= +\gamma \mathrm{Ma}^2\frac{\bar{p}}{\bar{T}}\frac{\partial\bar{u}}{\partial x}\\
K^1_{\hat{u}} &= +i\gamma \mathrm{Ma}^2\frac{\bar{p}}{\bar{T}}
\end{aligned}
\tag{C.2}
$$

$$
\begin{aligned}
D^1_{\hat{v}} &= -\frac{1}{Re}(\bar{\lambda}+\bar{\mu})\\
G^1_{\hat{v}} &= -\frac{1}{Re}\frac{d\bar{\mu}}{d\bar{T}}\frac{\partial\bar{T}}{\partial y}\\
H^1_{\hat{v}} &= -\frac{1}{Re}\frac{d\bar{\lambda}}{d\bar{T}}\frac{\partial\bar{T}}{\partial x}\\
J^1_{\hat{v}} &= +\gamma \mathrm{Ma}^2\frac{\bar{p}}{\bar{T}}\frac{\partial\bar{u}}{\partial y}
\end{aligned}
$$

$$
\begin{aligned}
E^1_{\hat{w}} &= -\frac{1}{Re}(\bar{\lambda}+\bar{\mu})\\
G^1_{\hat{w}} &= -\frac{1}{Re}\frac{d\bar{\mu}}{d\bar{T}}\frac{\partial\bar{T}}{\partial z}\\
I^1_{\hat{w}} &= -\frac{1}{Re}\frac{d\bar{\lambda}}{d\bar{T}}\frac{\partial\bar{T}}{\partial x}\\
J^1_{\hat{w}} &= +\gamma \mathrm{Ma}^2\frac{\bar{p}}{\bar{T}}\frac{\partial\bar{u}}{\partial z}
\end{aligned}
$$

$$
\begin{aligned}
G^1_{\hat{T}} =& -\frac{1}{Re}\left[\left(\frac{d\bar{\lambda}}{d\bar{T}}+2\frac{d\bar{\mu}}{d\bar{T}}\right)\frac{\partial\bar{u}}{\partial x}+\frac{d\bar{\lambda}}{d\bar{T}}\left(\frac{\partial\bar{v}}{\partial y}+\frac{\partial\bar{w}}{\partial z}\right)\right]\\
H^1_{\hat{T}} =& -\frac{1}{Re}\frac{d\bar{\mu}}{d\bar{T}}\left(\frac{\partial\bar{u}}{\partial y}+\frac{\partial\bar{v}}{\partial x}\right)\\
I^1_{\hat{T}} =& -\frac{1}{Re}\frac{d\bar{\mu}}{d\bar{T}}\left(\frac{\partial\bar{u}}{\partial z}+\frac{\partial\bar{w}}{\partial x}\right)\\
J^1_{\hat{T}} =& -\gamma\mathrm{Ma}^2\frac{\bar{p}}{\bar{T}^2}\left(\bar{u}\frac{\partial\bar{u}}{\partial x}+\bar{v}\frac{\partial\bar{u}}{\partial y}+\bar{w}\frac{\partial u}{\partial z}\right)\\
&-\frac{1}{Re}\left[\frac{d\bar{\mu}}{d\bar{T}}\left(\frac{\partial^2\bar{v}}{\partial x\,\partial y}+\frac{\partial^2\bar{w}}{\partial x\,\partial z}+2\frac{\partial^2\bar{u}}{\partial x^2}+\frac{\partial^2\bar{u}}{\partial y^2}+\frac{\partial^2\bar{u}}{\partial z^2}\right)\right.\\
&+\frac{d^2\bar{\mu}}{d\bar{T}^2}\left(\frac{\partial\bar{T}}{\partial y}\left(\frac{\partial\bar{u}}{\partial y}+\frac{\partial\bar{v}}{\partial x}\right)+\frac{\partial\bar{T}}{\partial z}\left(\frac{\partial\bar{u}}{\partial z}+\frac{\partial\bar{w}}{\partial x}\right)+2\frac{\partial\bar{T}}{\partial x}\frac{\partial\bar{u}}{\partial x}\right)\\
&\left.+\frac{d\bar{\lambda}}{d\bar{T}}\left(\frac{\partial^2\bar{v}}{\partial x\,\partial y}+\frac{\partial^2\bar{w}}{\partial x\,\partial z}+\frac{\partial^2\bar{u}}{\partial x^2}\right)+\frac{d^2\bar{\lambda}}{d\bar{T}^2}\frac{\partial\bar{T}}{\partial x}\left(\frac{\partial\bar{u}}{\partial x}+\frac{\partial\bar{v}}{\partial y}+\frac{\partial\bar{w}}{\partial z}\right)\right]
\end{aligned}
$$

$$
\begin{aligned}
G^1_{\hat{p}} =& 1\\
J^1_{\hat{p}} =& -\gamma\mathrm{Ma}^2\frac{1}{\bar{T}}\left(\bar{u}\frac{\partial\bar{u}}{\partial x}+\bar{v}\frac{\partial\bar{u}}{\partial y}+\bar{w}\frac{\partial\bar{u}}{\partial z}\right)
\end{aligned}
$$

Momentum - y equation

$$
\begin{aligned}
D_{\hat{u}}^2 &= -\frac{1}{Re}(\bar{\lambda}+\bar{\mu}) \\
G_{\hat{u}}^2 &= -\frac{1}{Re}\frac{d\bar{\lambda}}{d\bar{T}}\frac{\partial\bar{T}}{\partial y} \\
H_{\hat{u}}^2 &= -\frac{1}{Re}\frac{d\bar{\mu}}{d\bar{T}}\frac{\partial\bar{T}}{\partial x} \\
J_{\hat{u}}^2 &= +\gamma \mathrm{Ma}^2\frac{\bar{p}}{\bar{T}}\frac{\partial\bar{v}}{\partial x}
\end{aligned}
$$

$$
\begin{aligned}
A_{\hat{v}}^2 &= -\frac{1}{Re}\bar{\mu} \\
B_{\hat{v}}^2 &= -\frac{1}{Re}\left(\bar{\lambda}+2\bar{\mu}\right) \\
C_{\hat{v}}^2 &= -\frac{1}{Re}\bar{\mu} \\
G_{\hat{v}}^2 &= +\gamma \mathrm{Ma}^2\frac{\bar{p}}{\bar{T}}\bar{u} - \frac{1}{Re}\frac{d\bar{\mu}}{d\bar{T}}\frac{\partial\bar{T}}{\partial x} \\
H_{\hat{v}}^2 &= +\gamma \mathrm{Ma}^2\frac{\bar{p}}{\bar{T}}\bar{v} - \frac{1}{Re}\left(\frac{d\bar{\lambda}}{d\bar{T}}+2\frac{d\bar{\mu}}{d\bar{T}}\right)\frac{\partial\bar{T}}{\partial y} \\
I_{\hat{v}}^2 &= +\gamma \mathrm{Ma}^2\frac{\bar{p}}{\bar{T}}\bar{w} - \frac{1}{Re}\frac{d\bar{\mu}}{d\bar{T}}\frac{\partial\bar{T}}{\partial z} \\
J_{\hat{v}}^2 &= +\gamma \mathrm{Ma}^2\frac{\bar{p}}{\bar{T}}\frac{\partial\bar{v}}{\partial y} \\
K_{\hat{v}}^2 &= +i\gamma \mathrm{Ma}^2\frac{\bar{p}}{\bar{T}}
\end{aligned}
\tag{C.3}
$$

$$
\begin{aligned}
F_{\hat{w}}^2 &= -\frac{1}{Re}(\bar{\lambda}+\bar{\mu}) \\
H_{\hat{w}}^2 &= -\frac{1}{Re}\frac{d\bar{\mu}}{d\bar{T}}\frac{\partial\bar{T}}{\partial z} \\
I_{\hat{w}}^2 &= -\frac{1}{Re}\frac{d\bar{\lambda}}{d\bar{T}}\frac{\partial\bar{T}}{\partial y} \\
J_{\hat{w}}^2 &= +\gamma \mathrm{Ma}^2\frac{\bar{p}}{\bar{T}}\frac{\partial\bar{v}}{\partial z}
\end{aligned}
$$

$$
\begin{aligned}
G^2_{\hat{T}} =& -\frac{1}{Re}\frac{d\bar{\mu}}{d\bar{T}}\left(\frac{\partial \bar{u}}{\partial y}+\frac{\partial \bar{v}}{\partial x}\right)\\
H^2_{\hat{T}} =& -\frac{1}{Re}\left[\left(\frac{d\bar{\lambda}}{d\bar{T}}+2\frac{d\bar{\mu}}{d\bar{T}}\right)\frac{\partial \bar{v}}{\partial y}+\frac{d\bar{\lambda}}{d\bar{T}}\left(\frac{\partial \bar{u}}{\partial x}+\frac{\partial \bar{w}}{\partial z}\right)\right]\\
I^2_{\hat{T}} =& -\frac{1}{Re}\frac{d\bar{\mu}}{d\bar{T}}\left(\frac{\partial \bar{v}}{\partial z}+\frac{\partial \bar{w}}{\partial y}\right)\\
J^2_{\hat{T}} =& -\gamma \mathrm{Ma}^2\frac{\bar{p}}{\bar{T}^2}\left(\bar{u}\frac{\partial \bar{v}}{\partial x}+\bar{v}\frac{\partial \bar{v}}{\partial y}+\bar{w}\frac{\partial v}{\partial z}\right)\\
&-\frac{1}{Re}\left[\frac{d\bar{\mu}}{d\bar{T}}\left(\frac{\partial^2 \bar{u}}{\partial x\,\partial y}+\frac{\partial^2 \bar{w}}{\partial y\,\partial z}+2\frac{\partial^2 \bar{v}}{\partial y^2}+\frac{\partial^2 \bar{v}}{\partial x^2}+\frac{\partial^2 \bar{v}}{\partial z^2}\right)\right.\\
&+\frac{d^2\bar{\mu}}{d\bar{T}^2}\left(\frac{\partial \bar{T}}{\partial x}\left(\frac{\partial \bar{u}}{\partial y}+\frac{\partial \bar{v}}{\partial x}\right)+\frac{\partial \bar{T}}{\partial z}\left(\frac{\partial \bar{v}}{\partial z}+\frac{\partial \bar{w}}{\partial y}\right)+2\frac{\partial \bar{T}}{\partial y}\frac{\partial \bar{v}}{\partial y}\right)\\
&\left.+\frac{d\bar{\lambda}}{d\bar{T}}\left(\frac{\partial^2 \bar{u}}{\partial x\,\partial y}+\frac{\partial^2 \bar{w}}{\partial y\,\partial z}+\frac{\partial^2 \bar{v}}{\partial y^2}\right)+\frac{d^2\bar{\lambda}}{d\bar{T}^2}\frac{\partial \bar{T}}{\partial y}\left(\frac{\partial \bar{u}}{\partial x}+\frac{\partial \bar{v}}{\partial y}+\frac{\partial \bar{w}}{\partial z}\right)\right]
\end{aligned}
$$

$$
\begin{aligned}
H^2_{\hat{p}} =& 1\\
J^2_{\hat{p}} =& -\gamma \mathrm{Ma}^2\frac{1}{\bar{T}}\left(\bar{u}\frac{\partial \bar{v}}{\partial x}+\bar{v}\frac{\partial \bar{v}}{\partial y}+\bar{w}\frac{\partial \bar{v}}{\partial z}\right)
\end{aligned}
$$

Momentum - z equation

$$
\begin{aligned}
E^3_{\hat{u}} &= -\frac{1}{Re}(\bar{\lambda}+\bar{\mu}) \\
G^3_{\hat{u}} &= -\frac{1}{Re}\frac{d\bar{\lambda}}{d\bar{T}}\frac{\partial \bar{T}}{\partial z} \\
I^3_{\hat{u}} &= -\frac{1}{Re}\frac{d\bar{\mu}}{d\bar{T}}\frac{\partial \bar{T}}{\partial x} \\
J^3_{\hat{u}} &= +\gamma \mathrm{Ma}^2 \frac{\bar{p}}{\bar{T}}\frac{\partial \bar{w}}{\partial x}
\end{aligned}
$$

$$
\begin{aligned}
A^3_{\hat{w}} &= -\frac{1}{Re}\bar{\mu} \\
B^3_{\hat{w}} &= -\frac{1}{Re}\bar{\mu} \\
C^3_{\hat{w}} &= -\frac{1}{Re}\left(\bar{\lambda}+2\bar{\mu}\right) \\
G^3_{\hat{w}} &= +\gamma \mathrm{Ma}^2 \frac{\bar{p}}{\bar{T}}\bar{u} - \frac{1}{Re}\frac{d\bar{\mu}}{d\bar{T}}\frac{\partial \bar{T}}{\partial x} \\
H^3_{\hat{w}} &= +\gamma \mathrm{Ma}^2 \frac{\bar{p}}{\bar{T}}\bar{v} - \frac{1}{Re}\frac{d\bar{\mu}}{d\bar{T}}\frac{\partial \bar{T}}{\partial y} \\
I^3_{\hat{w}} &= +\gamma \mathrm{Ma}^2 \frac{\bar{p}}{\bar{T}}\bar{w} - \frac{1}{Re}\left(\frac{d\bar{\lambda}}{d\bar{T}}+2\frac{d\bar{\mu}}{d\bar{T}}\right)\frac{\partial \bar{T}}{\partial z} \\
J^3_{\hat{w}} &= +\gamma \mathrm{Ma}^2 \frac{\bar{p}}{\bar{T}}\frac{\partial \bar{w}}{\partial z} \\
K^3_{\hat{w}} &= +i\gamma \mathrm{Ma}^2 \frac{\bar{p}}{\bar{T}}
\end{aligned}
$$

(C.4)

$$
\begin{aligned}
F^3_{\hat{v}} &= -\frac{1}{Re}(\bar{\lambda}+\bar{\mu}) \\
H^3_{\hat{v}} &= -\frac{1}{Re}\frac{d\bar{\lambda}}{d\bar{T}}\frac{\partial \bar{T}}{\partial z} \\
I^3_{\hat{v}} &= -\frac{1}{Re}\frac{d\bar{\mu}}{d\bar{T}}\frac{\partial \bar{T}}{\partial y} \\
J^3_{\hat{v}} &= +\gamma \mathrm{Ma}^2 \frac{\bar{p}}{\bar{T}}\frac{\partial \bar{w}}{\partial y}
\end{aligned}
$$

$$
\begin{aligned}
G^3_{\hat{T}} =& -\frac{1}{Re}\frac{d\bar{\mu}}{d\bar{T}}\left(\frac{\partial \bar{u}}{\partial z}+\frac{\partial \bar{w}}{\partial x}\right)\\
H^3_{\hat{T}} =& -\frac{1}{Re}\frac{d\bar{\mu}}{d\bar{T}}\left(\frac{\partial \bar{v}}{\partial z}+\frac{\partial \bar{w}}{\partial y}\right)\\
I^3_{\hat{T}} =& -\frac{1}{Re}\left[\left(\frac{d\bar{\lambda}}{d\bar{T}}+2\frac{d\bar{\mu}}{d\bar{T}}\right)\frac{\partial \bar{w}}{\partial z}+\frac{d\bar{\lambda}}{d\bar{T}}\left(\frac{\partial \bar{u}}{\partial x}+\frac{\partial \bar{v}}{\partial y}\right)\right]\\
J^3_{\hat{T}} =& -\gamma \mathrm{Ma}^2\frac{\bar{p}}{\bar{T}^2}\left(\bar{u}\frac{\partial \bar{w}}{\partial x}+\bar{v}\frac{\partial \bar{w}}{\partial y}+\bar{w}\frac{\partial w}{\partial z}\right)\\
&-\frac{1}{Re}\left[\frac{d\bar{\mu}}{d\bar{T}}\left(\frac{\partial^2 \bar{u}}{\partial x\,\partial z}+\frac{\partial^2 \bar{v}}{\partial y\,\partial z}+2\frac{\partial^2 \bar{w}}{\partial z^2}+\frac{\partial^2 \bar{w}}{\partial x^2}+\frac{\partial^2 \bar{w}}{\partial y^2}\right)\right.\\
&+\frac{d^2\bar{\mu}}{d\bar{T}^2}\left(\frac{\partial \bar{T}}{\partial x}\left(\frac{\partial \bar{u}}{\partial z}+\frac{\partial \bar{w}}{\partial x}\right)+\frac{\partial \bar{T}}{\partial y}\left(\frac{\partial \bar{v}}{\partial z}+\frac{\partial \bar{w}}{\partial y}\right)+2\frac{\partial \bar{T}}{\partial z}\frac{\partial \bar{w}}{\partial z}\right)\\
&\left.+\frac{d\bar{\lambda}}{d\bar{T}}\left(\frac{\partial^2 \bar{u}}{\partial x\,\partial z}+\frac{\partial^2 \bar{v}}{\partial y\,\partial z}+\frac{\partial^2 \bar{w}}{\partial z^2}\right)+\frac{d^2\bar{\lambda}}{d\bar{T}^2}\frac{\partial \bar{T}}{\partial z}\left(\frac{\partial \bar{u}}{\partial x}+\frac{\partial \bar{v}}{\partial y}+\frac{\partial \bar{w}}{\partial z}\right)\right]
\end{aligned}
$$

$$
\begin{aligned}
I^3_{\hat{p}} =& 1\\
J^3_{\hat{p}} =& -\gamma \mathrm{Ma}^2\frac{1}{\bar{T}}\left(\bar{u}\frac{\partial \bar{w}}{\partial x}+\bar{v}\frac{\partial \bar{w}}{\partial y}+\bar{w}\frac{\partial \bar{w}}{\partial z}\right)
\end{aligned}
$$

Energy equation

$$
\begin{aligned}
G^4_{\hat{u}} &= -2\frac{\mathrm{Ec}}{Re}\left[\frac{\partial \bar{u}}{\partial x}\left(\bar{\lambda}+2\bar{\mu}\right)+\bar{\lambda}\left(\frac{\partial \bar{v}}{\partial y}+\frac{\partial \bar{w}}{\partial z}\right)\right] \\
H^4_{\hat{u}} &= -2\bar{\mu}\frac{\mathrm{Ec}}{Re}\left(\frac{\partial \bar{u}}{\partial y}+\frac{\partial \bar{v}}{\partial x}\right) \\
I^4_{\hat{u}} &= -2\bar{\mu}\frac{\mathrm{Ec}}{Re}\left(\frac{\partial \bar{u}}{\partial z}+\frac{\partial \bar{w}}{\partial x}\right) \\
J^4_{\hat{u}} &= +\gamma \mathrm{Ma}^2 c_p \frac{\bar{p}}{\bar{T}}\frac{\partial \bar{T}}{\partial x}-\mathrm{Ec}\frac{\partial \bar{p}}{\partial x}
\end{aligned}
$$

$$
\begin{aligned}
G^4_{\hat{v}} &= -2\bar{\mu}\frac{\mathrm{Ec}}{Re}\left(\frac{\partial \bar{u}}{\partial y}+\frac{\partial \bar{v}}{\partial x}\right) \\
H^4_{\hat{v}} &= -2\frac{\mathrm{Ec}}{Re}\left[\frac{\partial \bar{v}}{\partial y}\left(\bar{\lambda}+2\bar{\mu}\right)+\bar{\lambda}\left(\frac{\partial \bar{u}}{\partial x}+\frac{\partial \bar{w}}{\partial z}\right)\right] \\
I^4_{\hat{u}} &= -2\bar{\mu}\frac{\mathrm{Ec}}{Re}\left(\frac{\partial \bar{v}}{\partial z}+\frac{\partial \bar{w}}{\partial y}\right) \\
J^4_{\hat{v}} &= +\gamma \mathrm{Ma}^2 c_p \frac{\bar{p}}{\bar{T}}\frac{\partial \bar{T}}{\partial y}-\mathrm{Ec}\frac{\partial \bar{p}}{\partial y}
\end{aligned}
\qquad \text{(C.5)}
$$

$$
\begin{aligned}
G^4_{\hat{w}} &= -2\bar{\mu}\frac{\mathrm{Ec}}{Re}\left(\frac{\partial \bar{u}}{\partial z}+\frac{\partial \bar{w}}{\partial x}\right) \\
H^4_{\hat{w}} &= -2\bar{\mu}\frac{\mathrm{Ec}}{Re}\left(\frac{\partial \bar{v}}{\partial z}+\frac{\partial \bar{w}}{\partial y}\right) \\
I^4_{\hat{w}} &= -2\frac{\mathrm{Ec}}{Re}\left[\frac{\partial \bar{w}}{\partial z}\left(\bar{\lambda}+2\bar{\mu}\right)+\bar{\lambda}\left(\frac{\partial \bar{u}}{\partial x}+\frac{\partial \bar{v}}{\partial y}\right)\right] \\
J^4_{\hat{w}} &= +\gamma \mathrm{Ma}^2 c_p \frac{\bar{p}}{\bar{T}}\frac{\partial \bar{T}}{\partial z}-\mathrm{Ec}\frac{\partial \bar{p}}{\partial z}
\end{aligned}
$$

$$
\begin{aligned}
A^4_{\hat{T}} =& -\frac{1}{RePr}\bar{k}\\
B^4_{\hat{T}} =& -\frac{1}{RePr}\bar{k}\\
C^4_{\hat{T}} =& -\frac{1}{RePr}\bar{k}\\
G^4_{\hat{T}} =& +\gamma \mathrm{Ma}^2 c_p \frac{\bar{p}}{\bar{T}}\bar{u} - \frac{2}{RePr}\frac{d\bar{k}}{d\bar{T}}\frac{\partial \bar{T}}{\partial x}\\
H^4_{\hat{T}} =& +\gamma \mathrm{Ma}^2 c_p \frac{\bar{p}}{\bar{T}}\bar{v} - \frac{2}{RePr}\frac{d\bar{k}}{d\bar{T}}\frac{\partial \bar{T}}{\partial y}\\
I^4_{\hat{T}} =& +\gamma \mathrm{Ma}^2 c_p \frac{\bar{p}}{\bar{T}}\bar{w} - \frac{2}{RePr}\frac{d\bar{k}}{d\bar{T}}\frac{\partial \bar{T}}{\partial z}\\
J^4_{\hat{T}} =& -\gamma \mathrm{Ma}^2 c_p \frac{\bar{p}}{\bar{T}^2}\left(\bar{u}\frac{\partial \bar{T}}{\partial x} + \bar{v}\frac{\partial \bar{T}}{\partial y} + \bar{w}\frac{\partial \bar{T}}{\partial z}\right) - \frac{1}{RePr}\left[\frac{d\bar{k}}{d\bar{T}}\left(\frac{\partial^2 \bar{T}}{\partial x^2} + \frac{\partial^2 \bar{T}}{\partial y^2} + \frac{\partial^2 \bar{T}}{\partial z^2}\right)\right.\\
&\left. + \frac{d^2\bar{k}}{d\bar{T}^2}\left(\left(\frac{\partial \bar{T}}{\partial x}\right)^2 + \left(\frac{\partial \bar{T}}{\partial y}\right)^2 + \left(\frac{\partial \bar{T}}{\partial z}\right)^2\right)\right]\\
&- \frac{\mathrm{Ec}}{Re}\left\{\frac{d\bar{\mu}}{d\bar{T}}\left[\left(\frac{\partial \bar{u}}{\partial y} + \frac{\partial \bar{v}}{\partial x}\right)^2 + 2\left(\left(\frac{\partial \bar{u}}{\partial y}\right)^2 + \left(\frac{\partial \bar{v}}{\partial x}\right)^2 + \left(\frac{\partial \bar{w}}{\partial z}\right)^2\right)\right.\right.\\
&\left.\left. + \left(\frac{\partial \bar{u}}{\partial z} + \frac{\partial \bar{w}}{\partial x}\right)^2 + \left(\frac{\partial \bar{v}}{\partial z} + \frac{\partial \bar{w}}{\partial y}\right)^2\right] + \frac{d\bar{\lambda}}{\bar{T}}\left(\frac{\partial \bar{u}}{\partial x} + \frac{\partial \bar{v}}{\partial y} + \frac{\partial \bar{w}}{\partial z}\right)^2\right\}\\
K^4_{\hat{T}} =& -i\gamma \mathrm{Ma}^2 c_p \frac{\bar{p}}{\bar{T}}
\end{aligned}
$$

$$
\begin{aligned}
G^4_{\hat{p}} =& -\mathrm{Ec}\bar{u}\\
H^4_{\hat{p}} =& -\mathrm{Ec}\bar{v}\\
I^4_{\hat{p}} =& -\mathrm{Ec}\bar{w}\\
J^4_{\hat{p}} =& +\gamma \mathrm{Ma}^2 c_p \frac{1}{\bar{T}}\left(\bar{u}\frac{\partial \bar{T}}{\partial x} + \bar{v}\frac{\partial \bar{T}}{\partial y} + \bar{w}\frac{\partial \bar{T}}{\partial z}\right)\\
K^4_{\hat{p}} =& -i\mathrm{Ec}
\end{aligned}
$$

Continuity equation

$$
\begin{aligned}
G^5_{\hat{u}} &= +\bar{p} \\
J^5_{\hat{u}} &= +\frac{\partial \bar{p}}{\partial x} - \frac{\bar{p}}{\bar{T}}\frac{\partial \bar{T}}{\partial x}
\end{aligned}
$$

$$
\begin{aligned}
H^5_{\hat{v}} &= +\bar{p} \\
J^5_{\hat{v}} &= +\frac{\partial \bar{p}}{\partial y} - \frac{\bar{p}}{\bar{T}}\frac{\partial \bar{T}}{\partial y}
\end{aligned}
$$

$$
\begin{aligned}
I^5_{\hat{w}} &= +\bar{p} \\
J^5_{\hat{w}} &= +\frac{\partial \bar{p}}{\partial z} - \frac{\bar{p}}{\bar{T}}\frac{\partial \bar{T}}{\partial z}
\end{aligned}
$$

$$
\begin{aligned}
G^5_{\hat{T}} &= -\frac{\bar{p}}{\bar{T}}\bar{u} \\
H^5_{\hat{T}} &= -\frac{\bar{p}}{\bar{T}}\bar{v} \\
I^5_{\hat{T}} &= -\frac{\bar{p}}{\bar{T}}\bar{w} \\
J^5_{\hat{T}} &= -\frac{\bar{p}}{\bar{T}}\left(\frac{\partial \bar{u}}{\partial x} + \frac{\partial \bar{v}}{\partial y} + \frac{\partial \bar{w}}{\partial z}\right) - \frac{1}{\bar{T}}\left(\bar{u}\frac{\partial \bar{p}}{\partial x} - \bar{v}\frac{\partial \bar{p}}{\partial y} - \bar{w}\frac{\partial \bar{p}}{\partial z}\right) \\
&\quad + 2\frac{\bar{p}}{\bar{T}^2}\left(\bar{u}\frac{\partial \bar{T}}{\partial x} + \bar{v}\frac{\partial \bar{T}}{\partial y} + \bar{w}\frac{\partial \bar{T}}{\partial z}\right) \\
K^5_{\hat{T}} &= -i\frac{\bar{p}}{\bar{T}}
\end{aligned}
\tag{C.6}
$$

$$
\begin{aligned}
G^5_{\hat{p}} &= +\bar{u} \\
H^5_{\hat{p}} &= +\bar{v} \\
I^5_{\hat{p}} &= +\bar{w} \\
J^5_{\hat{p}} &= -\frac{1}{\bar{T}}\left(\bar{u}\frac{\partial \bar{T}}{\partial x} + \bar{v}\frac{\partial \bar{T}}{\partial y} + \bar{w}\frac{\partial \bar{T}}{\partial z}\right) + \frac{\partial \bar{u}}{\partial x} + \frac{\partial \bar{v}}{\partial y} + \frac{\partial \bar{w}}{\partial z} \\
K^5_{\hat{p}} &= +i
\end{aligned}
$$

Appendix D

Compressible BiGlobal LNSE in tensor form

The complex non-symmetric generalised eigenvalue problem written using the metric factor

$$\mathcal{A}\hat{\mathbf{q}} = \omega\mathcal{B}\hat{\mathbf{q}}, \tag{D.1}$$

can be written explicitly in tensor form as

$$\left(A_j^i \frac{1}{h_2^2}\frac{\partial^2}{\partial\eta^2} + B_j^i \frac{1}{h_3^2}\frac{\partial^2}{\partial\zeta^2} + C_j^i \frac{1}{h_2 h_3}\frac{\partial^2}{\partial\eta\partial\zeta} + D_j^i \frac{1}{h_2}\frac{\partial}{\partial\eta} + E_j^i \frac{1}{h_3}\frac{\partial}{\partial\zeta} + F_j^i\right)\hat{q}_j = \omega\, G_j^i\, \hat{q}_j. \tag{D.2}$$

Here A, B, C, D, E, F and G are vectors with size $(N\eta N\zeta \times 1)$ and the superscript $i = (1, 2, 3, 4, 5)$ corresponds to the linearized equations of motion, 1 referring to the momentum equation in ξ, 2 to the momentum equation in η , 3 to the momentum equation in ζ, 4 to the energy and 5 to the continuity equation. The subscript $j = (1, 2, 3, 4, 5) \equiv (\hat{u}, \hat{v}, \hat{w}, \hat{T}, \hat{p})$ corresponds to the five disturbances variables.
The nonzero elements are given by

Momentum - ξ equation

$$A^1_{\hat{u}} = -\frac{\bar{\mu}}{Re}$$

$$B^1_{\hat{u}} = -\frac{\bar{\mu}}{Re}$$

$$D^1_{\hat{u}} = -\frac{1}{Re}\frac{d\bar{\mu}}{d\bar{T}}\frac{1}{h_2}\frac{\partial\bar{T}}{\partial\eta} - (m_{12} - m_{22} + m_{32})\frac{\bar{\mu}}{Re} + \gamma Ma^2\frac{\bar{p}}{\bar{T}}\bar{v}$$

$$E^1_{\hat{u}} = -\frac{1}{Re}\frac{d\bar{\mu}}{d\bar{T}}\frac{1}{h_3}\frac{\partial\bar{T}}{\partial\zeta} - (m_{13} + m_{23} - m_{33})\frac{\bar{\mu}}{Re} + \gamma Ma^2\frac{\bar{p}}{\bar{T}}\bar{w}$$

$$\begin{aligned}F^1_{\hat{u}} =& \gamma Ma^2\frac{\bar{p}}{\bar{T}}\left(\frac{1}{h_1}i\alpha\bar{u} + m_{12}\bar{v} + m_{13}\bar{w}\right) + \frac{1}{Re}\left\{\frac{d\bar{\mu}}{d\bar{T}}\left(m_{12}\frac{1}{h_2}\frac{\partial\bar{T}}{\partial\eta} + m_{13}\frac{1}{h_3}\frac{\partial\bar{T}}{\partial\zeta}\right)\right.\\
&+ \bar{\mu}\left[\frac{1}{h_2}\frac{\partial m_{12}}{\partial\eta} + \frac{1}{h_3}\frac{\partial m_{13}}{\partial\zeta} + 2\frac{1}{h_1^2}\alpha^2 + 2\frac{1}{h_1}i\alpha(m_{11} - m_{21} - m_{31})\right.\\
&\left.+ m_{12}\ m_{32} + m_{13}\ m_{23} + 2\left(m_{12}^2 + m_{13}^2 + m_{21}^2 + m_{31}^2\right)\right]\\
&\left.+ \bar{\lambda}\left[\frac{1}{h_1^2}\alpha^2 - \frac{1}{h_1}\left(i\alpha(m_{11} - m_{21} - m31) - \frac{\partial m_{21}}{\partial\xi} - \frac{\partial m_{31}}{\partial\xi}\right)\right]\right\}\end{aligned}$$

$$G^1_{\hat{u}} = i\gamma Ma^2\frac{\bar{p}}{\bar{T}}$$

$$D^1_{\hat{v}} = \frac{1}{Re}\left[\bar{\mu}\left(3m_{21} - \frac{1}{h_1}i\alpha\right) + \bar{\lambda}\left(m_{21} - \frac{1}{h_1}i\alpha\right)\right]$$

$$\begin{aligned}F^1_{\hat{v}} =& \gamma Ma^2\left(\frac{\bar{p}}{\bar{T}}\frac{1}{h_2}\frac{\partial\bar{u}}{\partial\eta} + \frac{\bar{p}}{\bar{T}}m_{12}\bar{u} - 2\frac{\bar{p}}{\bar{T}}m_{21}\bar{v}\right) + \frac{1}{Re}\left[\frac{d\bar{\mu}}{d\bar{T}}\left(m_{21}\frac{1}{h_2}\frac{\partial\bar{T}}{\partial\eta} - i\alpha\frac{1}{h_1h_2}\frac{\partial\bar{T}}{\partial\eta}\right)\right.\\
&+ \bar{\mu}\left(-2\frac{1}{h_1}\frac{\partial m_{12}}{\partial\xi} + \frac{1}{h_2}\frac{\partial m_{21}}{\partial\eta} - \frac{1}{h_1}i\alpha(3m_{12} + m_{32}) + 2m_{31}(m_{32} - m_{12}) + m_{21}m_{32}\right)\\
&\left.- \bar{\lambda}\left(\frac{1}{h_1}\frac{\partial m_{12}}{\partial\xi} + \frac{1}{h_1}\frac{\partial m_{32}}{\partial\xi} + \frac{1}{h_1}i\alpha(m_{12} + m_{32})\right)\right]\end{aligned}$$

$$E^1_{\hat{w}} = \frac{1}{Re}\left[\bar{\mu}\left(3m_{31} - \frac{1}{h_1}i\alpha\right) + \bar{\lambda}\left(m_{31} - \frac{1}{h_1}i\alpha\right)\right]$$

$$\begin{aligned}F^1_{\hat{w}} =& \gamma Ma^2\left(\frac{\bar{p}}{\bar{T}}\frac{1}{h_3}\frac{\partial\bar{u}}{\partial\zeta} + \frac{\bar{p}}{\bar{T}}m_{13}\bar{u} - 2\frac{\bar{p}}{\bar{T}}m_{31}\bar{w}\right) + \frac{1}{Re}\left[\frac{d\bar{\mu}}{d\bar{T}}\left(m_{31}\frac{1}{h_3}\frac{\partial\bar{T}}{\partial\zeta} - i\alpha\frac{1}{h_1h_3}\frac{\partial\bar{T}}{\partial\zeta}\right)\right.\\
&+ \bar{\mu}\left(-2\frac{1}{h_1}\frac{\partial m_{13}}{\partial\xi} + \frac{1}{h_3}\frac{\partial m_{31}}{\partial\zeta} - \frac{1}{h_1}i\alpha(3m_{13} + m_{23}) + 2m_{21}(m_{23} - m_{13}) + m_{23}m_{31}\right)\\
&\left.- \bar{\lambda}\left(\frac{1}{h_1}\frac{\partial m_{13}}{\partial\xi} + \frac{1}{h_1}\frac{\partial m_{23}}{\partial\xi} + \frac{1}{h_1}i\alpha(m_{13} + m_{23})\right)\right]\end{aligned}$$

$$
\begin{aligned}
D^1_{\hat{T}} =& + \frac{1}{Re}\frac{d\bar{\mu}}{d\bar{T}}\left(m_{12}\bar{u} + m_{21}\bar{v} - \frac{1}{h_2}\frac{\partial \bar{u}}{\partial \eta}\right)\\
E^1_{\hat{T}} =& + \frac{1}{Re}\frac{d\bar{\mu}}{d\bar{T}}\left(m_{13}\bar{u} + m_{31}\bar{w} - \frac{1}{h_3}\frac{\partial \bar{u}}{\partial \zeta}\right)\\
F^1_{\hat{T}} =& - \gamma Ma^2\left[\bar{v}\frac{\bar{p}}{\bar{T}^2}\frac{1}{h_2}\frac{\partial \bar{u}}{\partial \eta} + \bar{w}\frac{\bar{p}}{\bar{T}^2}\frac{1}{h_3}\frac{\partial \bar{u}}{\partial \zeta} + \frac{\bar{p}}{\bar{T}^2}\left(\bar{u}\left(m_{12}\bar{v} + m_{13}\bar{w}\right) + m_{21}\bar{v}^2 + m_{31}\bar{w}^2\right)\right]\\
& - \frac{1}{Re}\left\{\frac{d\bar{\mu}}{d\bar{T}}\left[\bar{u}\left(\frac{1}{h_2}\frac{\partial m_{12}}{\partial \eta} - \frac{1}{h_3}\frac{\partial m_{13}}{\partial \zeta} + 2(m_{12}^2 + m_{13}^2 + m_{21}^2 + m_{31}^2) + m_{12}m_{32} + m_{13}m_{23}\right)\right.\right.\\
& + \bar{v}\left(\frac{1}{h_2}\frac{\partial m_{21}}{\partial \eta} - \frac{1}{h_1}2(i\alpha m_{12} + \frac{\partial m_{12}}{\partial \xi}) - 2m_{31}(m_{12} - m_{32}) + m_{21}m_{32}\right)\\
& + \bar{w}\left(\frac{1}{h_3}\frac{\partial m_{31}}{\partial \zeta} - \frac{1}{h_1}2(i\alpha m_{13} + \frac{\partial m_{13}}{\partial \xi}) - 2m_{21}(m_{13} - m_{23}) + m_{23}m_{31}\right)\\
& - (m_{12} - m_{22} + m_{32})\frac{1}{h_2}\frac{\partial \bar{u}}{\partial \eta} - (m_{13} + m_{23} - m_{33})\frac{1}{h_3}\frac{\partial \bar{u}}{\partial \zeta} - \frac{1}{h_2}\frac{\partial^2 \bar{u}}{\partial \eta^2} - \frac{1}{h_3}\frac{\partial^2 \bar{u}}{\partial \zeta^2}\\
& \left. + 3m_{21}\frac{1}{h_2}\frac{\partial \bar{v}}{\partial \eta} + 3m_{31}\frac{1}{h_3}\frac{\partial \bar{w}}{\partial \zeta}\right] + \frac{d\bar{\lambda}}{d\bar{T}}\left[- \bar{u}\frac{1}{h_1}\left(\frac{\partial m_{21}}{\partial \xi} + \frac{\partial m_{31}}{\partial \xi} + i\alpha(m_{21} + m_{31})\right)\right.\\
& - \bar{v}\frac{1}{h_1}\left(\frac{\partial m_{12}}{\partial \xi} + \frac{\partial m_{32}}{\partial \xi} + i\alpha(m_{12} + m_{32})\right) - \bar{w}\frac{1}{h_1}\left(\frac{\partial m_{13}}{\partial \xi} + \frac{\partial m_{23}}{\partial \xi} + i\alpha(m_{13} + m_{23})\right)\\
& \left.(m_{21} - \frac{1}{h_1}i\alpha)\frac{1}{h_2}\frac{\partial \bar{v}}{\partial \eta} + (m_{31} - \frac{1}{h_1}i\alpha)\frac{1}{h_3}\frac{\partial \bar{w}}{\partial \zeta}\right] + \frac{d^2\bar{\mu}}{d\bar{T}^2}\left[\frac{\partial \bar{T}}{\partial \eta}\left(\frac{1}{h_2^2}\frac{\partial \bar{u}}{\partial \eta} - \frac{1}{h_2}\left(m_{12}\bar{u} - m_{21}\bar{v}\right)\right)\right.\\
& \left.\left. + \frac{\partial \bar{T}}{\partial z}\left(\frac{1}{h_3^2}\frac{\partial \bar{u}}{\partial \zeta} - \frac{1}{h_3}\left(m_{13}\bar{u} - m_{31}\bar{w}\right)\right)\right]\right\}
\end{aligned}
$$

$$
F^1_{\hat{p}} = \frac{1}{h_1}i\alpha + \frac{\gamma Ma^2}{\bar{T}}\left(\bar{v}\frac{1}{h_2}\frac{\partial \bar{u}}{\partial \eta} + \bar{w}\frac{1}{h_3}\frac{\partial \bar{u}}{\partial \zeta} + \bar{u}\left(m_{12}\bar{v} + m_{13}\bar{w}\right) - m_{21}\bar{v}^2 - m_{31}\bar{w}^2\right) \tag{D.3}
$$

Momentum - η equation

$$
D^2_{\hat{u}} = - \frac{1}{Re}\left[\bar{\lambda}\left(\frac{1}{h1}i\alpha + m_{21} + m_{31}\right) + \bar{\mu}\left(\frac{1}{h1}i\alpha + 3m_{21} + m_{31}\right)\right]
$$

$$
\begin{aligned}
F^2_{\hat{u}} =& \gamma Ma^2\frac{\bar{p}}{\bar{T}}\left(m_{21}\bar{v} - 2m_{12}\bar{u}\right) + \bar{\lambda}\left[\frac{1}{h_1}i\alpha m_{12} - \frac{1}{h_2}\left(\frac{\partial m_{21}}{\partial \eta} + \frac{\partial m_{31}}{\partial \eta}\right)\right]\\
& + \frac{1}{Re}\left\{\bar{\mu}\left[\frac{1}{h1}\left(3i\alpha m_{12} + \frac{\partial m_{12}}{\partial \xi}\right) - 2\frac{1}{h_2}\frac{\partial m_{21}}{\partial \eta} + 2m_{32}(m_{31} - m_{21}) + m_{12}m_{31}\right]\right.\\
& \left. - 2m_{21}\frac{d\bar{\mu}}{d\bar{T}}\frac{1}{h_2}\frac{\partial \bar{T}}{\partial \eta} - \frac{d\bar{\lambda}}{d\bar{T}}\frac{1}{h_2}\frac{\partial \bar{T}}{\partial \eta}\left(\frac{1}{h_1}i\alpha + m_{21} + m_{31}\right)\right\}
\end{aligned}
$$

$$
\begin{aligned}
A^2_{\hat{v}} =& -\frac{1}{Re}\left(2\bar{\mu}+\bar{\lambda}\right)\\
B^2_{\hat{v}} =& -\frac{1}{Re}\bar{\mu}\\
D^2_{\hat{v}} =& \gamma Ma^2\frac{\bar{p}}{\bar{T}}\bar{v}-\frac{1}{Re}\Bigg[2\bar{\mu}\big(m_{12}-m_{22}+m_{32}\big)+\bar{\lambda}\big(m_{12}-m_{22}+m_{32}\big)\\
&-\frac{1}{h_2}\frac{\partial\bar{T}}{\partial\eta}\left(2\frac{d\bar{\mu}}{d\bar{T}}+\frac{d\bar{\lambda}}{d\bar{T}}\right)\Bigg]\\
E^2_{\hat{v}} =& +\gamma Ma^2\frac{\bar{p}}{\bar{T}}\bar{w}-\frac{1}{Re}\left[\bar{\mu}\big(m_{13}+m_{23}-m_{33}\big)+\frac{1}{h_3}\frac{\partial\bar{T}}{\partial\zeta}\frac{d\bar{\mu}}{d\bar{T}}\right]\\
F^2_{\hat{v}} =& \gamma Ma^2\frac{\bar{p}}{\bar{T}}\left[\bar{u}\left(\frac{1}{h_1}i\alpha+m_{21}\right)+\bar{w}m_{23}+\frac{1}{h_2}\frac{\partial\bar{v}}{\partial\eta}\right]+\frac{1}{Re}\Bigg\{\frac{d\bar{\mu}}{d\bar{T}}m_{23}\frac{1}{h_3}\frac{\partial\bar{T}}{\partial\zeta}\\
&+\bar{\mu}\Bigg[\frac{1}{h_1}\frac{\partial m_{21}}{\partial\xi}+\frac{1}{h_3}\frac{\partial m_{23}}{\partial\zeta}+\frac{1}{h_1^2}\alpha^2+\frac{1}{h_1}i\alpha(m_{11}-m_{21}-m_{31})+\\
&+m_{13}\ m_{23}+m_{21}\ m_{31}+2\left(m_{12}^2+m_{21}^2+m_{23}^2+m_{32}^2\right)\Bigg]-\frac{1}{h_2}\frac{\partial\bar{T}}{\partial\eta}\frac{d\bar{\lambda}}{d\bar{T}}(m_{12}+m_{32})\\
&-\bar{\lambda}\frac{1}{h_2}\left(\frac{\partial m_{12}}{\partial\eta}+\frac{\partial m_{32}}{\partial\eta}\right)\Bigg\}\\
G^2_{\hat{v}} =& i\gamma Ma^2\frac{\bar{p}}{\bar{T}}
\end{aligned}
$$

$$
\begin{aligned}
C^2_{\hat{w}} =& -\frac{1}{Re}\big(\bar{\lambda}+\bar{\mu}\big)\\
D^2_{\hat{w}} =& -\frac{1}{Re}\left[\bar{\mu}(m_{13}+3m_{23})+\bar{\lambda}(m_{13}+m_{23})+\frac{d\bar{\mu}}{d\bar{T}}\frac{1}{h_3}\frac{\partial\bar{T}}{\partial\zeta}\right]\\
E^2_{\hat{w}} =& +\frac{1}{Re}\left[m_{32}(3\bar{\mu}+\bar{\lambda})-\frac{d\bar{\lambda}}{d\bar{T}}\frac{1}{h_3}\frac{\partial\bar{T}}{\partial\eta}\right]\\
F^2_{\hat{w}} =& \gamma Ma^2\frac{\bar{p}}{\bar{T}}\left[m_{23}\bar{v}-2m_{32}\bar{w}+\frac{1}{h_3}\frac{\partial\bar{v}}{\partial\zeta}\right]+\frac{1}{Re}\Bigg\{\frac{d\bar{\mu}}{d\bar{T}}\left[m_{32}\frac{1}{h_3}\frac{\partial\bar{T}}{\partial\zeta}-2m_{23}\frac{1}{h_2}\frac{\partial\bar{T}}{\partial\eta}\right]\\
&+\bar{\mu}\left[\frac{1}{h_3}\frac{\partial m_{32}}{\partial\zeta}-\frac{1}{h_2}2\frac{\partial m_{23}}{\partial\eta}+2m_{12}(m_{13}-m_{23})+m_{13}m_{32}\right]\\
&-\bar{\lambda}\left[\frac{1}{h_2}\left(\frac{\partial m_{13}}{\partial\eta}+\frac{\partial m_{23}}{\partial\eta}\right)\right]-\frac{d\bar{\lambda}}{d\bar{T}}\left[\frac{1}{h_2}\frac{\partial\bar{T}}{\partial\eta}(m_{13}+m_{23})\right]\Bigg\}
\end{aligned}
$$

$$
\begin{aligned}
D^2_{\hat{T}} =& -\frac{1}{Re}\Bigg[\frac{d\bar{\lambda}}{d\bar{T}}\Big(\bar{u}(m_{21}+m_{31})+\bar{v}(m_{12}+m_{32})+\bar{w}(m_{13}+m_{23})\\
&+\frac{1}{h_2}\frac{\partial\bar{v}}{\partial\eta}+\frac{1}{h_3}\frac{\partial\bar{w}}{\partial\zeta}\Big)+2\frac{d\bar{\mu}}{d\bar{T}}\left(\bar{u}m_{21}+\bar{w}m_{23}+\frac{1}{h_2}\frac{\partial\bar{v}}{\partial\eta}\right)\Bigg]\\
E^2_{\hat{T}} =& -\frac{1}{Re}\frac{d\bar{\mu}}{d\bar{T}}\left(\frac{1}{h_2}\frac{\partial\bar{w}}{\partial\eta}-\bar{v}m_{23}-\bar{w}m_{32}+\frac{1}{h_3}\frac{\partial\bar{v}}{\partial\zeta}\right)
\end{aligned}
$$

$$
\begin{aligned}
F^2_{\hat{T}} =&\gamma Ma^2\frac{\bar{p}}{\bar{T}^2}\left[\bar{u}^2 m_{12}-\bar{v}\left(\bar{u}m_{21}+\bar{w}m_{23}+\frac{1}{h_2}\frac{\partial\bar{v}}{\partial\eta}\right)+\bar{w}\left(\bar{w}m_{32}-\frac{1}{h_3}\frac{\partial\bar{v}}{\partial\zeta}\right)\right]\\
&+\frac{1}{Re}\left\{\frac{d\bar{\mu}}{d\bar{T}}\left[\bar{u}\left(\frac{1}{h_1}\left(i\alpha m_{12}+\frac{\partial m_{12}}{\partial d\xi}\right)-2\frac{1}{h_2}\frac{\partial m_{21}}{\partial\eta}+2m_{32}(m_{31}-m_{21})+m_{12}m_{31}\right)\right.\right.\\
&+\bar{v}\left(\frac{1}{h_1}\left(i\alpha m_{21}+\frac{\partial m_{21}}{\partial\xi}\right)+\frac{1}{h_3}\frac{\partial m_{23}}{\partial\zeta}+2(m_{12}^2+m_{21}^2+m_{23}^2+m_{32}^2)\right.\\
&\left.+m_{13}m_{23}+m_{21}m_{31}\right)-\bar{w}\left(2\frac{1}{h_2}\frac{\partial m_{23}}{\partial\eta}-\frac{1}{h_3}\frac{\partial m_{32}}{\partial\zeta}-2m_{12}(m_{13}-m_{23})-m_{13}m_{32}\right)\\
&-\frac{1}{h_2}\frac{\partial\bar{u}}{\partial\eta}\left(\frac{1}{h_1}i\alpha+(3m_{21}+m_{31})\right)-2\frac{1}{h_2}\frac{\partial\bar{v}}{\partial\eta}(m_{12}-m_{22}+m_{32})\\
&-\frac{1}{h_3}\frac{\partial\bar{v}}{\partial\zeta}(m_{13}+m_{23}-m_{33})-2\frac{1}{h_2^2}\frac{\partial^2\bar{v}}{\partial\eta^2}-\frac{1}{h_3^2}\frac{\partial^2\bar{v}}{\partial\zeta^2}-\frac{1}{h_2}\frac{\partial\bar{w}}{\partial\eta}(m_{13}+3m_{23})\\
&+3m_{32}\frac{1}{h_3}\frac{\partial\bar{w}}{\partial\zeta}-\frac{1}{h_2h_3}\frac{\partial^2\bar{w}}{\partial\eta\zeta}\Big]-\frac{d\bar{\lambda}}{d\bar{T}}\left[\bar{u}\frac{1}{h_2}\left(\frac{\partial m_{21}}{\partial\eta}+\frac{\partial m_{31}}{\partial\eta}\right)+\bar{v}\frac{1}{h_2}\left(\frac{\partial m_{12}}{\partial\eta}+\frac{\partial m_{32}}{\partial\eta}\right)\right.\\
&+\bar{w}\frac{1}{h_2}\left(\frac{\partial m_{13}}{\partial\eta}+\frac{\partial m_{23}}{\partial\eta}\right)+\frac{1}{h_2}\frac{\partial\bar{u}}{\partial\eta}(m_{21}+m_{31})+\frac{1}{h_2}\frac{\partial\bar{v}}{\partial\eta}(m_{12}-m_{22}+m_{32})\\
&\left.+\frac{1}{h_2^2}\frac{\partial^2\bar{v}}{\partial\eta^2}+\frac{1}{h_2}\frac{\partial\bar{w}}{\partial\eta}(m_{13}+m_{23})-m_{32}\frac{1}{h_3}\frac{\partial\bar{w}}{\partial\zeta}+\frac{1}{h_2h_3}\frac{\partial^2\bar{w}}{\partial\eta\zeta}\right]-\frac{d^2\bar{\mu}}{d\bar{T}^2}\left[\right.\\
&\left.2\frac{1}{h_2}\frac{\partial\bar{T}}{\partial\eta}\left(\frac{1}{h_2}\left(\frac{\partial\bar{v}}{\partial\eta}+\bar{u}m_{21}+\bar{w}m_{23}\right)\right)+\frac{1}{h_3}\frac{\partial\bar{T}}{\partial\zeta}\left(\frac{1}{h_2}\frac{\partial\bar{w}}{\partial\eta}+\frac{1}{h_3}\frac{\partial\bar{v}}{\partial\zeta}-\bar{v}m_{23}-\bar{w}m_{32}\right)\right]\\
&-\frac{d^2\bar{\lambda}}{d\bar{T}^2}\ \frac{1}{h_2}\frac{\partial\bar{T}}{\partial\eta}\left[\frac{1}{h_2}\frac{\partial\bar{v}}{\partial\eta}+\frac{1}{h_3}\frac{\partial\bar{w}}{\partial\zeta}+\bar{u}(m_{21}+m_{31})+\bar{v}(m_{12}+m_{32})+\bar{w}(m_{13}+m_{23})\right]\Big\}\\
D^2_{\hat{p}} =&1\\
F^2_{\hat{p}} =&\gamma Ma^2\frac{1}{\bar{T}}\left[\bar{u}\left(\bar{v}m_{21}-\bar{u}m_{12}\right)+\bar{w}\left(\bar{v}m_{23}-\bar{w}m_{32}+\frac{1}{h_3}\frac{\partial\bar{v}}{\partial\zeta}\right)+\bar{v}\frac{1}{h_2}\frac{\partial\bar{v}}{\partial\eta}\right]
\end{aligned}
\tag{D.4}
$$

Momentum - ζ equation

$$
\begin{aligned}
E^3_{\hat{u}} =&-\frac{1}{Re}\left[\bar{\lambda}\left(\frac{1}{h1}i\alpha+m_{21}+m_{31}\right)+\bar{\mu}\left(\frac{1}{h1}i\alpha+3m_{31}+m_{21}\right)\right]\\
F^3_{\hat{u}} =&\gamma Ma^2\frac{\bar{p}}{\bar{T}}\left(m_{31}\bar{w}-2m_{13}\bar{u}\right)+\bar{\lambda}\left[\frac{1}{h_1}i\alpha m_{13}-\frac{1}{h_3}\left(\frac{\partial m_{21}}{\partial\zeta}+\frac{\partial m_{31}}{\partial\zeta}\right)\right]\\
&+\frac{1}{Re}\left\{\bar{\mu}\left[\frac{1}{h1}\left(3i\alpha m_{13}+\frac{\partial m_{13}}{\partial\xi}\right)-2\frac{1}{h_3}\frac{\partial m_{31}}{\partial\zeta}+2m_{23}(m_{21}-m_{31})+m_{13}m_{21}\right]\right.\\
&\left.-2m_{31}\frac{d\bar{\mu}}{d\bar{T}}\frac{1}{h_3}\frac{\partial\bar{T}}{\partial\zeta}-\frac{d\bar{\lambda}}{d\bar{T}}\frac{1}{h_3}\frac{\partial\bar{T}}{\partial\zeta}\left(\frac{1}{h_1}i\alpha+m_{21}+m_{31}\right)\right\}
\end{aligned}
$$

$$
\begin{aligned}
C^3_{\hat{v}} =& -\frac{1}{Re}\big(\bar{\lambda}+\bar{\mu}\big)\\
D^3_{\hat{v}} =& +\frac{1}{Re}\left[m_{23}(3\bar{\mu}+\bar{\lambda})-\frac{d\bar{\lambda}}{d\bar{T}}\frac{1}{h_3}\frac{\partial\bar{T}}{\partial\zeta}\right]\\
E^3_{\hat{v}} =& -\frac{1}{Re}\left[\bar{\mu}\bigg((m_{12}+3m_{32})\bigg)+\bar{\lambda}\bigg((m_{12}+m_{32})\bigg)+\frac{d\bar{\mu}}{d\bar{T}}\frac{1}{h_2}\frac{\partial\bar{T}}{\partial\eta}\right]\\
F^3_{\hat{v}} =&\gamma Ma^2\frac{\bar{p}}{\bar{T}}\left[m_{32}\bar{w}-2m_{23}\bar{v}+\frac{1}{h_2}\frac{\partial\bar{w}}{\partial\eta}\right]+\frac{1}{Re}\left\{\frac{d\bar{\mu}}{d\bar{T}}\left[m_{23}\frac{1}{h_2}\frac{\partial\bar{T}}{\partial\eta}-2m_{32}\frac{1}{h_3}\frac{\partial\bar{T}}{\partial\zeta}\right]\right.\\
&+\bar{\mu}\left[\frac{1}{h_2}\frac{\partial m_{23}}{\partial\eta}-\frac{1}{h_3}2\frac{\partial m_{32}}{\partial\zeta}+2m_{13}(m_{12}-m_{32})+m_{12}m_{23}\right]\\
&\left.-\bar{\lambda}\left[\frac{1}{h_3}\bigg(\frac{\partial m_{12}}{\partial\zeta}+\frac{\partial m_{32}}{\partial\zeta}\bigg)\right]-\frac{d\bar{\lambda}}{d\bar{T}}\left[\frac{1}{h_3}\frac{\partial\bar{T}}{\partial\zeta}(m_{12}+m_{32})\right]\right\}
\end{aligned}
$$

$$
\begin{aligned}
A^3_{\hat{w}} =& -\frac{\bar{\mu}}{Re}\\
B^3_{\hat{w}} =& -\frac{1}{Re}\bigg(2\bar{\mu}+\bar{\lambda}\bigg)\\
D^3_{\hat{w}} =& +\gamma Ma^2\frac{\bar{p}}{\bar{T}}\bar{v}-\frac{1}{Re}\left[\bar{\mu}\big(m_{12}-m_{22}+m_{32}\big)+\frac{1}{h_2}\frac{\partial\bar{T}}{\partial\eta}\frac{d\bar{\mu}}{d\bar{T}}\right]\\
E^3_{\hat{w}} =&\gamma Ma^2\frac{\bar{p}}{\bar{T}}\bar{w}-\frac{1}{Re}\left[2\bar{\mu}\big(m_{13}+m_{23}-m_{33}\big)+\bar{\lambda}\big(m_{13}+m_{23}-m_{33}\big)\right.\\
&\left.-\frac{1}{h_3}\frac{\partial\bar{T}}{\partial\zeta}\bigg(2\frac{d\bar{\mu}}{d\bar{T}}+\frac{d\bar{\lambda}}{d\bar{T}}\bigg)\right]\\
F^3_{\hat{w}} =&\gamma Ma^2\frac{\bar{p}}{\bar{T}}\left[\bar{u}\bigg(\frac{1}{h_1}i\alpha+m_{31}\bigg)+\bar{v}m_{32}+\frac{1}{h_3}\frac{\partial\bar{w}}{\partial\zeta}\right]+\frac{1}{Re}\left\{\frac{d\bar{\mu}}{d\bar{T}}m_{32}\frac{1}{h_2}\frac{\partial\bar{T}}{\partial\eta}\right.\\
&+\bar{\mu}\left[\frac{1}{h_1}\frac{\partial m_{31}}{\partial\xi}+\frac{1}{h_2}\frac{\partial m_{32}}{\partial\eta}+\frac{1}{h_1^2}\alpha^2+\frac{1}{h_1}i\alpha(m_{11}-m_{21}-m_{31})+\right.\\
&\left.+m_{12}\ m_{32}+m_{21}\ m_{31}+2\left(m_{13}^2+m_{23}^2+m_{31}^2+m_{32}^2\right)\right]-\frac{1}{h_3}\frac{\partial\bar{T}}{\partial\zeta}\frac{d\bar{\lambda}}{d\bar{T}}(m_{13}+m_{23})\\
&\left.-\bar{\lambda}\frac{1}{h_3}\bigg(\frac{\partial m_{13}}{\partial\zeta}+\frac{\partial m_{23}}{\partial\zeta}\bigg)\right\}\\
G^3_{\hat{w}} =&i\gamma Ma^2\frac{\bar{p}}{\bar{T}}
\end{aligned}
$$

$$
\begin{aligned}
D^3_{\hat{T}} =& -\frac{1}{Re}\frac{d\bar{\mu}}{d\bar{T}}\bigg(\frac{1}{h_2}\frac{\partial\bar{w}}{\partial\eta}-\bar{v}m_{23}-\bar{w}m_{32}+\frac{1}{h_3}\frac{\partial\bar{v}}{\partial\zeta}\bigg)\\
E^3_{\hat{T}} =& -\frac{1}{Re}\left[\frac{d\bar{\lambda}}{d\bar{T}}\bigg(\bar{u}(m_{21}+m_{31})+\bar{v}(m_{12}+m_{32})+\bar{w}(m_{13}+m_{23})\right.\\
&\left.+\frac{1}{h_3}\frac{\partial\bar{w}}{\partial\zeta}+\frac{1}{h_2}\frac{\partial\bar{v}}{\partial\eta}\bigg)+2\frac{d\bar{\mu}}{d\bar{T}}\bigg(\bar{u}m_{31}+\bar{v}m_{32}+\frac{1}{h_3}\frac{\partial\bar{w}}{\partial\zeta}\bigg)\right]
\end{aligned}
$$

$$
\begin{aligned}
F^3_{\hat{T}} =& \gamma Ma^2 \frac{\bar{p}}{\bar{T}^2}\left[\bar{u}^2 m_{13} - \bar{v}\left(\bar{w}m_{32} - \bar{v}m_{23} + \frac{1}{h_2}\frac{\partial \bar{w}}{\partial \eta}\right) - \bar{w}\left(\bar{u}m_{31} + \frac{1}{h_3}\frac{\partial \bar{w}}{\partial \zeta}\right)\right] \\
&+ \frac{1}{Re}\Bigg\{\frac{d\bar{\mu}}{d\bar{T}}\left[\bar{u}\left(\frac{1}{h_1}\left(i\alpha m_{13} + \frac{\partial m_{13}}{\partial d\xi}\right) - 2\frac{1}{h_3}\frac{\partial m_{31}}{\partial \zeta} + 2m_{23}(m_{21} - m_{31}) + m_{13}m_{21}\right)\right. \\
&+ \bar{w}\left(\frac{1}{h_1}\left(i\alpha m_{31} + \frac{\partial m_{31}}{\partial \xi}\right) + \frac{1}{h_2}\frac{\partial m_{32}}{\partial \eta} + 2(m_{13}^2 + m_{23}^2 + m_{31}^2 + m_{32}^2)\right. \\
&\left.+ m_{21}m_{31} + m_{12}m_{32}\right) - \bar{v}\left(2\frac{1}{h_3}\frac{\partial m_{32}}{\partial \zeta} - \frac{1}{h_2}\frac{\partial m_{23}}{\partial \eta} - 2m_{13}(m_{12} - m_{32}) - m_{12}m_{23}\right) \\
&- \frac{1}{h_3}\frac{\partial \bar{u}}{\partial \zeta}\left(\frac{1}{h_1}i\alpha + (3m_{31} + m_{21})\right) - 2\frac{1}{h_3}\frac{\partial \bar{w}}{\partial \zeta}(m_{13} + m_{23} - m_{33}) \\
&- \frac{1}{h_2}\frac{\partial \bar{w}}{\partial \eta}(m_{12} - m_{22} + m_{32}) - 2\frac{1}{h_3^2}\frac{\partial^2 \bar{w}}{\partial \zeta^2} - \frac{1}{h_2^2}\frac{\partial^2 \bar{w}}{\partial \eta^2} - \frac{1}{h_3}\frac{\partial \bar{v}}{\partial \zeta}(m_{12} + 3m_{32}) \\
&+ 3m_{23}\frac{1}{h_2}\frac{\partial \bar{v}}{\partial \eta} - \frac{1}{h_2 h_3}\frac{\partial^2 \bar{v}}{\partial \eta \zeta}\Bigg] - \frac{d\bar{\lambda}}{d\bar{T}}\left[\bar{u}\frac{1}{h_3}\left(\frac{\partial m_{21}}{\partial \zeta} + \frac{\partial m_{31}}{\partial \zeta}\right) + \bar{v}\frac{1}{h_3}\left(\frac{\partial m_{12}}{\partial \zeta} + \frac{\partial m_{32}}{\partial \zeta}\right)\right. \\
&+ \bar{w}\frac{1}{h_3}\left(\frac{\partial m_{13}}{\partial \zeta} + \frac{\partial m_{23}}{\partial \zeta}\right) + \frac{1}{h_3}\frac{\partial \bar{u}}{\partial \zeta}(m_{21} + m_{31}) + \frac{1}{h_3}\frac{\partial \bar{w}}{\partial \zeta}(m_{13} + m_{23} - m_{33}) + \frac{1}{h_3^2}\frac{\partial^2 \bar{w}}{\partial \zeta^2} \\
&\left.+ \frac{1}{h_3}\frac{\partial \bar{v}}{\partial \zeta}(m_{12} + m_{32}) - m_{23}\frac{1}{h_2}\frac{\partial \bar{v}}{\partial \eta} + \frac{1}{h_2 h_3}\frac{\partial^2 \bar{v}}{\partial \eta \zeta}\right] - \frac{d^2\bar{\mu}}{d\bar{T}^2}\left[\right. \\
&2\frac{1}{h_3}\frac{\partial \bar{T}}{\partial \zeta}\left(\frac{1}{h_3}\left(\frac{\partial \bar{w}}{\partial \zeta} + \bar{u}m_{31} + \bar{v}m_{32}\right)\right) + \frac{1}{h_2}\frac{\partial \bar{T}}{\partial \eta}\left(\frac{1}{h_3}\frac{\partial \bar{v}}{\partial \zeta} + \frac{1}{h_2}\frac{\partial \bar{w}}{\partial \eta} - \bar{v}m_{23} - \bar{w}m_{32}\right)\Bigg] \\
&- \frac{d^2\bar{\lambda}}{d\bar{T}^2}\ \frac{1}{h_3}\frac{\partial \bar{T}}{\partial \zeta}\left[\frac{1}{h_3}\frac{\partial \bar{w}}{\partial \zeta} + \frac{1}{h_2}\frac{\partial \bar{v}}{\partial \eta} + \bar{u}(m_{21} + m_{31}) + \bar{v}(m_{12} + m_{32}) + \bar{w}(m_{13} + m_{23})\right]\Bigg\} \\
E^3_{\hat{p}} =& 1 \\
F^3_{\hat{p}} =& \gamma Ma^2 \frac{1}{\bar{\bar{T}}}\left[\bar{u}\left(\bar{w}m_{31} - \bar{u}m_{13}\right) + \bar{v}\left(\bar{w}m_{32} - \bar{v}m_{23} + \frac{1}{h_2}\frac{\partial \bar{w}}{\partial \eta}\right) + \bar{w}\frac{1}{h_3}\frac{\partial \bar{w}}{\partial \zeta}\right]
\end{aligned}
\tag{D.5}
$$

Energy equation

$$
\begin{aligned}
D^4_{\hat{u}} &= + \frac{Ec}{Re}2\bar{\mu}\left(m_{12}\bar{u} + m_{21}\bar{v} - \frac{1}{h_2}\frac{\partial \bar{u}}{\partial \eta}\right) \\
E^4_{\hat{u}} &= + \frac{Ec}{Re}2\bar{\mu}\left(m_{13}\bar{u} + m_{31}\bar{w} - \frac{1}{h_3}\frac{\partial \bar{u}}{\partial \zeta}\right)
\end{aligned}
$$

$$
\begin{aligned}
F^4_{\hat{u}} =& -\frac{Ec}{Re}\Bigg\{2\bar{\mu}\Bigg[\bar{u}(m_{12}^2+m_{13}^2+2m_{21}^2+2m_{31}^2)+\bar{v}\Bigg(2\frac{1}{h_1}i\alpha m_{12}+m_{12}m_{21}+2m_{31}m_{32}\Bigg)\\
&+\bar{w}\Bigg(2\frac{1}{h_1}i\alpha m_{13}+m_{13}m_{31}+2m_{21}m_{23}\Bigg)+\frac{1}{h_2}\Bigg(2m_{21}\frac{\partial\bar{v}}{\partial\eta}-m_{12}\frac{\partial\bar{u}}{\partial\eta}\Bigg)\\
&+\frac{1}{h_3}\Bigg(2m_{31}\frac{\partial\bar{w}}{\partial\zeta}-m_{13}\frac{\partial\bar{u}}{\partial\zeta}\Bigg)\Bigg]+2\bar{\lambda}\Bigg[\bar{u}\Bigg(\frac{1}{h_1}i\alpha(m_{21}+m_{31})+(m_{21}-m_{31})^2\Bigg)\\
&+\bar{v}\Bigg(\frac{1}{h_1}i\alpha(m_{12}+m_{32})+(m_{12}+m_{32})(m_{21}+m_{31})\Bigg)\\
&+\bar{w}\Bigg(\frac{1}{h_1}i\alpha(m_{13}+m_{23})+(m_{13}+m_{23})(m_{21}+m_{31})\Bigg)\\
&+\frac{1}{h_2}\frac{\partial\bar{v}}{\partial\eta}\Bigg(\frac{1}{h_1}i\alpha+m_{21}+m_{31}\Bigg)+\frac{1}{h_3}\frac{\partial\bar{w}}{\partial\zeta}\Bigg(\frac{1}{h_1}i\alpha+m_{21}+m_{31}\Bigg)\Bigg]\Bigg\}\\
D^4_{\hat{v}} =& -\frac{Ec}{Re}\Bigg[4\bar{\mu}\Bigg(\frac{1}{h_2}\frac{\partial\bar{v}}{\partial\eta}+m_{21}\bar{u}+m_{23}\bar{w}\Bigg)\\
&+2\bar{\lambda}\Bigg(\frac{1}{h_2}\frac{\partial\bar{v}}{\partial\eta}+\frac{1}{h_3}\frac{\partial\bar{w}}{\partial\zeta}+\bar{u}(m_{21}+m_{31})+\bar{v}(m_{12}+m_{32})+\bar{w}(m_{13}+m_{23})\Bigg)\Bigg]\\
E^4_{\hat{v}} =& -\frac{Ec}{Re}2\bar{\mu}\Bigg(\frac{1}{h_2}\frac{\partial\bar{w}}{\partial\eta}+\frac{1}{h_3}\frac{\partial\bar{v}}{\partial\zeta}-m_{23}-m_{32}\Bigg)\\
F^4_{\hat{v}} =& \gamma Ma^2\frac{\bar{p}}{\bar{T}}\frac{1}{h_2}\frac{\partial\bar{T}}{\partial\eta}-Ec\frac{1}{h_2}\frac{\partial\bar{p}}{\partial\eta}+\frac{Ec}{Re}\Bigg\{2\bar{\mu}\Bigg[\bar{u}\Bigg(\frac{1}{h_1}i\alpha m_{12}-m_{12}m_{21}-2m_{31}m_{32}\Bigg)\\
&+\bar{v}\Bigg(\frac{1}{h_1}i\alpha m_{21}-m_{21}^2-m_{23}^2-2m_{12}^2-2m_{32}^2\Bigg)-\bar{w}\Bigg(m_{23}m_{32}+2m_{12}m_{13}\Bigg)\\
&-\frac{1}{h_2}\frac{\partial\bar{u}}{\partial\eta}\Bigg(\frac{1}{h_1}i\alpha-m_{21}\Bigg)+m_{23}\Bigg(\frac{1}{h_3}\frac{\partial\bar{v}}{\partial\zeta}+\frac{1}{h_2}\frac{\partial\bar{w}}{\partial\eta}\Bigg)-2m_{32}\frac{1}{h_3}\frac{\partial\bar{w}}{\partial\zeta}\Bigg]\\
&-2\bar{\lambda}\Bigg[\bar{u}\Bigg((m_{12}+m_{32})(m_{21}+m_{31})\Bigg)+\bar{v}(m_{12}+m_{32})^2\\
&+\bar{w}\Bigg((m_{12}+m_{32})(m_{13}+m_{23})\Bigg)+\frac{1}{h_2}\frac{\partial\bar{v}}{\partial\eta}\Bigg(m_{12}+m_{32}\Bigg)+\frac{1}{h_3}\frac{\partial\bar{w}}{\partial\zeta}\Bigg(m_{12}+m_{32}\Bigg)\Bigg]\Bigg\}
\end{aligned}
$$

$$
\begin{aligned}
D^4_{\hat{w}} =& -\frac{Ec}{Re}2\bar{\mu}\Bigg(\frac{1}{h_3}\frac{\partial\bar{v}}{\partial\zeta}+\frac{1}{h_2}\frac{\partial\bar{w}}{\partial\eta}-m_{23}-m_{32}\Bigg)\\
E^4_{\hat{w}} =& -\frac{Ec}{Re}\Bigg[4\bar{\mu}\Bigg(\frac{1}{h_3}\frac{\partial\bar{w}}{\partial\zeta}+m_{31}\bar{u}+m_{32}\bar{v}\Bigg)\\
&+2\bar{\lambda}\Bigg(\frac{1}{h_2}\frac{\partial\bar{v}}{\partial\eta}+\frac{1}{h_3}\frac{\partial\bar{w}}{\partial\zeta}+\bar{u}(m_{21}+m_{31})+\bar{v}(m_{12}+m_{32})+\bar{w}(m_{13}+m_{23})\Bigg)\Bigg]
\end{aligned}
$$

$$
\begin{aligned}
F^4_{\hat{w}} =& \gamma Ma^2 \frac{\bar{p}}{\bar{T}} \frac{1}{h_3} \frac{\partial \bar{T}}{\partial \zeta} - Ec \frac{1}{h_3} \frac{\partial \bar{p}}{\partial \zeta} + \frac{Ec}{Re} \Bigg\{ 2\bar{\mu} \Bigg[\bar{u} \Bigg(\frac{1}{h_1} i\alpha m_{13} - m_{13} m_{31} - 2 m_{21} m_{23} \Bigg) \\
& - \bar{v} \Bigg(m_{23} m_{32} + 2 m_{12} m_{13} \Bigg) + \bar{w} \Bigg(\frac{1}{h_1} i\alpha m_{31} - m_{31}^2 - m_{23}^2 - 2 m_{13}^2 - 2 m_{32}^2 \Bigg) \\
& - \frac{1}{h_3} \frac{\partial \bar{u}}{\partial \zeta} \Bigg(\frac{1}{h_1} i\alpha - m_{31} \Bigg) + m_{32} \Bigg(\frac{1}{h_2} \frac{\partial \bar{w}}{\partial \eta} + \frac{1}{h_3} \frac{\partial \bar{v}}{\partial \zeta} \Bigg) - 2 m_{23} \frac{1}{h_2} \frac{\partial \bar{v}}{\partial \eta} \Bigg] \\
& - 2\bar{\lambda} \Bigg[\bar{u} \Bigg((m_{13} + m_{23})(m_{21} + m_{31}) \Bigg) + \bar{w} (m_{13} + m_{23})^2 \\
& + \bar{v} \Bigg((m_{12} + m_{32})(m_{13} + m_{23}) \Bigg) + \frac{1}{h_2} \frac{\partial \bar{v}}{\partial \eta} \Bigg(m_{13} + m_{23} \Bigg) + \frac{1}{h_3} \frac{\partial \bar{w}}{\partial \zeta} \Bigg(m_{13} + m_{23} \Bigg) \Bigg] \Bigg\}
\end{aligned}
$$

$$
\begin{aligned}
A^4_{\hat{T}} =& - \frac{1}{RePr} \bar{k} \\
B^4_{\hat{T}} =& - \frac{1}{RePr} \bar{k} \\
D^4_{\hat{T}} =& + \Bigg[\gamma Ma^2 \frac{\bar{p}}{\bar{T}} \bar{v} - \frac{1}{RePr} \Bigg(2 \frac{\partial \bar{k}}{\partial \bar{T}} \frac{1}{h_2} \frac{\partial \bar{T}}{\partial \eta} + \bar{k} (m_{12} - m_{22} + m_{32}) \Bigg) \Bigg] \\
E^4_{\hat{T}} =& + \Bigg[\gamma Ma^2 \frac{\bar{p}}{\bar{T}} \bar{w} - \frac{1}{RePr} \Bigg(2 \frac{\partial \bar{k}}{\partial \bar{T}} \frac{1}{h_3} \frac{\partial \bar{T}}{\partial \zeta} + \bar{k} (m_{13} + m_{23} - m_{33}) \Bigg) \Bigg]
\end{aligned}
$$

$$
\begin{aligned}
F^4_{\hat{T}} = &+ \gamma Ma^2 \frac{\bar{p}}{\bar{\bar{T}}}\left(\bar{u}\frac{1}{h_1}i\alpha - \frac{\bar{v}}{\bar{T}}\frac{1}{h_2}\frac{\partial \bar{T}}{\partial \eta} - \frac{\bar{w}}{\bar{T}}\frac{1}{h_3}\frac{\partial \bar{T}}{\partial \zeta}\right) - \frac{1}{RePr}\left[\frac{\partial^2 \bar{k}}{\partial \bar{T}^2}\left(\frac{1}{h_2^2}\frac{\partial^2 \bar{T}}{\partial \eta^2} + \frac{1}{h_3^2}\frac{\partial^2 \bar{T}}{\partial \zeta^2}\right)\right. \\
&+ \frac{\partial \bar{k}}{\partial \bar{T}}\left(\frac{1}{h_2}\frac{\partial \bar{T}}{\partial \eta}(m_{12} - m_{22} + m_{32}) + \frac{1}{h_3}\frac{\partial \bar{T}}{\partial \zeta}(m_{13} + m_{23} - m_{33}) + \frac{1}{h_2^2}\frac{\partial^2 \bar{T}}{\partial \eta^2} + \frac{1}{h_3^2}\frac{\partial^2 \bar{T}}{\partial \zeta^2}\right) \\
&\left. + \bar{k}\left(\frac{1}{h_1}i\alpha(m_{21} + m_{31} - m_{11}) - \frac{1}{h_1^2}\alpha^2\right)\right] - \frac{Ec}{Re}\left\{\frac{\partial \bar{\lambda}}{\partial \bar{T}}\left[\bar{u}^2(m_{21} + m_{31})^2\right.\right. \\
&+ \bar{v}^2(m_{12} + m_{32})^2 + \bar{w}^2(m_{13} + m_{23})^2 + 2\bar{u}\left(\bar{v}((m_{12} + m_{32}) + (m_{21} + m_{31}))\right. \\
&\left. + \bar{w}((m_{13} + m_{23}) + (m_{21} + m_{31})) + \frac{1}{h_2}\frac{\partial \bar{v}}{\partial \eta}(m_{21} + m_{31}) + \frac{1}{h_3}\frac{\partial \bar{w}}{\partial \zeta}(m_{21} + m_{31})\right) \\
&+ \bar{v}\left(\bar{w}((m_{12} + m_{32}) + (m_{13} + m_{23})) + \frac{1}{h_2}\frac{\partial \bar{v}}{\partial \eta}(m_{12} + m_{32}) + \frac{1}{h_3}\frac{\partial \bar{w}}{\partial \zeta}(m_{12} + m_{32})\right) \\
&+ \bar{w}\left(\frac{1}{h_2}\frac{\partial \bar{v}}{\partial \eta}(m_{13} + m_{23}) + \frac{1}{h_3}\frac{\partial \bar{w}}{\partial \zeta}(m_{13} + m_{23})\right) + \left(\frac{1}{h_2}\frac{\partial \bar{v}}{\partial \eta} + \frac{1}{h_3}\frac{\partial \bar{w}}{\partial \zeta}\right)^2\Big] \\
&+ \frac{\partial \bar{\mu}}{\partial \bar{T}}\left[\bar{u}^2(m_{12}^2 + m_{13}^2 + 2m_{21}^2 + 2m_{31}^2) + \bar{v}^2(2m_{12}^2 + m_{21}^2 + m_{23}^2 + 2m_{32}^2)\right. \\
&+ \bar{w}^2(2m_{13}^2 + 2m_{23}^2 + m_{31}^2 + m_{32}^2) + 2\bar{u}\left(\bar{v}(m_{12}m_{21} + 2m_{31}m_{32})\right. \\
&\left. + \bar{w}(m_{13}m_{31} + 2m_{21}m_{23}) + 2m_{21}\frac{1}{h_2}\frac{\partial \bar{v}}{\partial \eta} - m_{12}\frac{1}{h_2}\frac{\partial \bar{u}}{\partial \eta} - m_{13}\frac{1}{h_3}\frac{\partial \bar{u}}{\partial \zeta} + 2m_{31}\frac{1}{h_3}\frac{\partial \bar{w}}{\partial \zeta}\right) \\
&+ 2\bar{v}\left(\bar{w}(2m_{12}m_{13} + m_{23}m_{32}) - m_{21}\frac{1}{h_2}\frac{\partial \bar{u}}{\partial \eta} - m_{23}\left(\frac{1}{h_2}\frac{\partial \bar{w}}{\partial \eta} + \frac{1}{h_3}\frac{\partial \bar{v}}{\partial \zeta}\right) + 2m_{32}\frac{1}{h_3}\frac{\partial \bar{w}}{\partial \zeta}\right) \\
&+ 2\bar{w}\left(2m_{23}\frac{1}{h_2}\frac{\partial \bar{v}}{\partial \eta} - m_{32}\left(\frac{1}{h_2}\frac{\partial \bar{w}}{\partial \eta} + \frac{1}{h_3}\frac{\partial \bar{v}}{\partial \zeta}\right) - m_{31}\frac{1}{h_3}\frac{\partial \bar{u}}{\partial \zeta}\right) + \left(\frac{1}{h_2}\frac{\partial \bar{w}}{\partial \eta} + \frac{1}{h_3}\frac{\partial \bar{v}}{\partial \zeta}\right)^2 \\
&\left.\left. + \left(\frac{1}{h_2}\frac{\partial \bar{u}}{\partial \eta}\right)^2 + 2\left(\frac{1}{h_2}\frac{\partial \bar{v}}{\partial \eta}\right)^2 + \left(\frac{1}{h_3}\frac{\partial \bar{u}}{\partial \zeta}\right)^2 + 2\left(\frac{1}{h_3}\frac{\partial \bar{w}}{\partial \zeta}\right)^2\right]\right\} \\
G^4_{\hat{T}} = &+ i\gamma Ma^2 \frac{\bar{p}}{\bar{\bar{T}}}
\end{aligned}
$$

$$
\begin{aligned}
D^4_{\hat{p}} &= - Ec\ \bar{v} \\
E^4_{\hat{p}} &= - Ec\ \bar{w} \\
F^4_{\hat{p}} &= + \gamma Ma^2 \frac{1}{\bar{\bar{T}}}\left(\bar{v}\frac{1}{h_2}\frac{\partial \bar{T}}{\partial \eta} + \bar{w}\frac{1}{h_3}\frac{\partial \bar{T}}{\partial \zeta}\right) - Ec\ \bar{u}\frac{1}{h_1}i\alpha \\
G^4_{\hat{p}} &= - i\ Ec
\end{aligned}
\tag{D.6}
$$

Continuity equation

$$
\begin{aligned}
F^5_{\hat{u}} &= + \frac{1}{h_1}\, i\alpha\bar{p} + (m_{21} + m_{31})\bar{p} \\
\\
E^5_{\hat{v}} &= + \bar{p} \\
F^5_{\hat{v}} &= - \frac{\bar{p}}{\bar{T}}\frac{1}{h_2}\frac{\partial \bar{T}}{\partial \eta} + \frac{1}{h_2}\frac{\partial \bar{p}}{\partial \eta} + (m_{12} + m_{32})\bar{p} \\
\\
D^5_{\hat{w}} &= + \bar{p} \\
F^5_{\hat{w}} &= - \frac{\bar{p}}{\bar{T}}\frac{1}{h_3}\frac{\partial \bar{T}}{\partial \zeta} + \frac{1}{h_3}\frac{\partial \bar{p}}{\partial \zeta} + (m_{13} + m_{23})\bar{p} \\
\\
D^5_{\hat{T}} &= - \frac{\bar{p}}{\bar{T}}\bar{v} \\
E^5_{\hat{T}} &= - \frac{\bar{p}}{\bar{T}}\bar{w} \\
F^5_{\hat{T}} &= + \frac{\bar{p}}{\bar{T}}\Bigg[- (m_{21} + m_{31})\,\bar{u} - (m_{12} + m_{32})\bar{v} - (m_{13} + m_{23})\bar{w} - \frac{1}{h_1} i\alpha\bar{u} \\
&\qquad + \frac{1}{\bar{T}}\left(2\bar{v}\frac{1}{h_2}\frac{\partial \bar{T}}{\partial \eta} + 2\bar{w}\frac{1}{h_3}\frac{\partial \bar{T}}{\partial \zeta} \right) \Bigg] - \frac{1}{\bar{T}}\left(\bar{v}\frac{1}{h_2}\frac{\partial \bar{p}}{\partial \eta} - \bar{w}\frac{1}{h_3}\frac{\partial \bar{p}}{\partial \zeta} \right) - \frac{\bar{p}}{\bar{T}}\left(\frac{1}{h_2}\frac{\partial \bar{v}}{\partial \eta} + \frac{1}{h_3}\frac{\partial \bar{w}}{\partial \zeta} \right) \\
G^5_{\hat{T}} &= - i\frac{\bar{p}}{\bar{T}} \\
\\
D^5_{\hat{p}} &= - \bar{v} \\
E^5_{\hat{p}} &= - \bar{w} \\
F^5_{\hat{p}} &= + \frac{1}{h_1} i\alpha\bar{u} + (m_{21} + m_{31})\,\bar{u} - \frac{1}{\bar{T}}\left(\bar{v}\frac{1}{h_2}\frac{\partial \bar{T}}{\partial \eta} + (m_{12} + m_{32})\bar{v} - \bar{w}\frac{1}{h_3}\frac{\partial \bar{T}}{\partial \zeta} + (m_{13} + m_{23})\bar{w} \right) \\
&\qquad + \frac{1}{h_2}\frac{\partial \bar{v}}{\partial \eta} + \frac{1}{h_3}\frac{\partial \bar{w}}{\partial \zeta} \\
G^5_{\hat{p}} &= i
\end{aligned}
\tag{D.7}
$$

In the previous equations, m and h are defined as

$$\begin{aligned}
m_{11} &= \frac{1}{h_1^2}\frac{\partial h_1}{\partial \xi}, & m_{12} &= \frac{1}{h_1 h_2}\frac{\partial h_1}{\partial \eta}, & m_{13} &= \frac{1}{h_1 h_3}\frac{\partial h_1}{\partial \zeta}, \\
m_{21} &= \frac{1}{h_1 h_2}\frac{\partial h_2}{\partial \xi}, & m_{22} &= \frac{1}{h_2^2}\frac{\partial h_2}{\partial \eta}, & m_{23} &= \frac{1}{h_2 h_3}\frac{\partial h_2}{\partial \zeta}, \\
m_{31} &= \frac{1}{h_1 h_3}\frac{\partial h_3}{\partial \xi}, & m_{32} &= \frac{1}{h_2 h_3}\frac{\partial h_3}{\partial \eta}, & m_{33} &= \frac{1}{h_3^2}\frac{\partial h_3}{\partial \zeta},
\end{aligned} \tag{D.8}$$

and

$$h_i = \sqrt{g_{ii}} = \sqrt{\left(\frac{\partial x}{\partial \chi_i}\right)^2 + \left(\frac{\partial y}{\partial \chi_i}\right)^2 + \left(\frac{\partial z}{\partial \chi_i}\right)^2}, \qquad i = (1,2,3) \tag{D.9}$$

with $\chi = (\xi, \eta, \zeta)$.

Bibliography

Abdessemed, N., Sharma, A. S., Sherwin, S. J. and Theofilis, V.: 2009, Transient growth analysis of the flow past a circular cylinder, *Physics of Fluids* **21**(4), 044103.

Abdessemed, N., Sherwin, S. and Theofilis, V.: 2009, Linear instability analysis of low pressure turbine flows, *Journal of Fluid Mechanics* **628**, 57–83.

Adamczak, D., Kimmel, R., Paull, A. and Alesi, H.: 2011, HIFiRE-1 flight trajectory estimation and initial experimental results, *17th AIAA International Space Planes and Hypersonic Systems and Technologies Conference*, AIAA Paper 2011-2358.

Adams, N. A.: 1998, Direct numerical simulation of turbulent compression ramp flow, *Theoretical and Computational Fluid Dynamics* **12**(2), 109–129.

Adams, N. A.: 2000, Direct simulation of the turbulent boundary layer along a compression ramp at M = 3 and Reθ= 1685, *Journal of Fluid Mechanics* **420**, 47–83.

Adams, N. and Kleiser, L.: 1996, Subharmonic transition to turbulence in a flat-plate boundary layer at Mach number 4.5, *Journal of Fluid Mechanics* **317**, 301–335.

Airiau, C. and Casalis, G.: 1994, Weakly non linear instability of the laminar boundary layer calculated by a parabolic system of equations, *Asymptotic Modelling in Fluid Mechanics*, Springer, Berlin, Heidelberg, pp. 99–106.

Albensoeder, S., Kuhlmann, H. C. and Rath, H. J.: 2001, Three-dimensional centrifugal-flow instabilities in the lid-driven-cavity problem, *Physics of fluids* **13.1**, 121–135.

Alizard, F. and Robinet, J.-C.: 2007, Spatially convective global modes in a boundary layer, *Physics of fluids* **19**(11), 114105.

Andersson, P., Berggren, M. and Henningson, D. S.: 1999, Optimal disturbances and bypass transition in boundary layers., *Physics of Fluids* **11**(1), 134–150.

Andersson, P., Brandt, L., Bottaro, A. and Henningson, D.: 2001, On the breakdown of boundary layer streaks., *Journal of Fluid Mechanics* **428**, 29–60.

Anyiwo, J. C. and Bushnell, D. M.: 1982, Turbulence amplification in shock-wave boundary-layer interaction, *AIAA Journal* **20**(7), 893–899.

Aris, R.: 1962, *Vectors, tensors and the basic equations of fluid mechanics*, Prentice-Hall, Inc., Englewood Cliffs, NJ.

Arkevik, E., Hoepffner, J. and Henningson, D.: 2007, Optimal growth, model reduction and control in a separated boundary-layer flow using global eigenmodes, *Journal of Fluid Mechanics* **579**, 223–241.

Arnoldi, W. E.: 1951, The principle of minimized iterations in the solution of the matrix eigenvalue problem, *Quarterly of Applied Mathematics* **9**, 17–29.

Babinsky, H. and Harvey, J. K.: 2011, *Shock wave-boundary-layer interactions*, Vol. 32, Cambridge University Press.

Bagheri, S., Schlatter, P., Schmid, P. and Henningson, D.: 2009, Global stability of a jet in crossflow, *Journal of Fluid Mechanics* **624**, 33 – 44.

Balakumar, P. and Malik, M.: 1992, Discrete modes and continuous spectra in supersonic boundary layers, *Journal of Fluid Mechanics* **239**, 631–656.

Balakumar, P. and Reed, H. L.: 1991, Stability of three-dimensional supersonic boundary layers, *Physics of Fluids A: Fluid Dynamics* **3**(4), 617–632.

Barker, P., Choudhari, M., Li, F., Jewell, J., Kimmel, R., Marineau, E. and Gossir, G.: 2019, Nosetip bluntness effects on transition at hypersonic speeds: experimental and numerical analysis, *Journal of Spacecrafts and Rockets* **56**(2), 369–387.

Barkley, D.: 2006, Linear analysis of the cylinder wake mean flow, *EPL (Europhysics Letters)* **75**(5), 750.

Barkley, D., Blackburn, H. M. and Sherwin, S. J.: 2008, Direct optimal growth analysis for timesteppers, *International journal for numerical methods in fluids* **57**(9), 1435–1458.

Barkley, D., Gomes, M. G. M. and Henderson, R. D.: 2002, Three-dimensional instability in flow over a backward-facing step, *Journal of fluid mechanics* **473**, 167–190.

Barkley, D. and Henderson, R.: 1996, Three-dimensional Floquet stability analysis of the wake of a circular cylinder, *Journal of Fluid Mechanics* **322**, 215–241.

Baurle, R. A., White, J. A., Drozda, T. G. and Norris, A. T.: 2020, Vulcan-cfd theory manual: Ver. 7.1. 0, *Technical report*, NTRS Report Number TM-2020-5000766, Hampton, VA.

Beaudoin, J.-F., Cadot, O., Aider, J.-L. and Wesfreid, J. E.: 2004, Three-dimensional stationary flow over a backward-facing step, *European Journal of Mechanics-B/Fluids* **23**(1), 147–155.

Beneddine, S., Sipp, D., Arnault, A., Dandois, J. and Lesshafft, L.: 2016, Conditions for validity of mean flow stability analysis, *Journal of Fluid Mechanics* **798**, 485.

Berlin, S.: 1998, *Oblique waves in boundary layer transition*, PhD thesis, Royal Institute of Technology, Stockholm.

Bertolotti, F.: 1991, Linear and nonliear stability of boundary layers with streamwise varying properties, *Technical report*, The Ohio State University.

Bertolotti, F., Herbert, T. and Spalart, P.: 1992, Linear and nonlinear stability of the Blasius boundary layer, *Journal of Fluid Mechanics* **242**, 441–474.

Beskok, A. and Karniadakis, G. E.: 1999, Report: a model for flows in channels, pipes, and ducts at micro and nano scales, *Microscale Thermophysical Engineering* **3**(1), 43–77.

Beskok, A., Karniadakis, G. E. and Trimmer, W.: 1996, Rarefaction and compressibility effects in gas microflows, *Journal of Fluids Engineering* **118**(3), 448–456.

Biau, D. and Bottaro, A.: 2009, An optimal path to transition in a duct, *Philosophical Transactions of the Royal Society A: Mathematical, Physical and Engineering Sciences* **367**(1888), 529–544.

Biau, D., Soueid, H. and Bottaro, A.: 2008, Transition to turbulence in duct flow, *Journal of Fluid Mechanics* **596**, 133–142.

Bippes, H.: 1990, Instability features appearing on swept wing configurations, *Proc. IUTAM Symp. on Laminar Turbulent Transition*, (D. Arnal and R. Michel, eds.), Springer-Verlag, Berlin, pp. 419–430.

Bippes, H.: 1999, Basic experiments on transition in three-dimensional boundary layers dominated by crossflow instability, *Progress in Aerospace Sciences* **35**, 363–412.

Bippes, H. and Nitschke-Kowsky, P.: 1990, Experimental study of instability modes in a three-dimensional boundary layer, *AIAA journal* **28**(10), 1758–1763.

Bird, G.: 1994, *Molecular gas dynamics and the direct simulation of gas flows*, Oxford University Press, Oxford.

Bishop, R. L. and Goldberg, S. I.: 2012, *Tensor analysis on manifolds*, Courier Corporation.

Blackburn, H., Barkley, D. and Sherwin, S.: 2008, Convective instability and transient growth in flow over a backward-facing step, *Journal of Fluid Mechanics* **603**, 271–304.

Blackburn, H., Sherwin, S. and Barkley, D.: 2008, Convective instability and transient growth in steady and pulsatile stenotic flows, *Journal of Fluid Mechanics* **607**, 267–277.

Blackford, L. S., Choi, J., Cleary, A., D'Azevedo, E., Demmel, J., Dhillon, I., Dongarra, J., Hammarling, S., Henry, G., Petitet, A. et al.: 1997, *ScaLAPACK users' guide*, Vol. 4, Siam.

Blasius, H.: 1907, Grenzschichten in flüssigkeiten mit kleiner reibung, *Z. Math. u. Phys* **56**, 1–37.

Boberg, L. and Brosa, U.: 1988, Onset of turbulence in a pipe, *Z. Naturforsch* **43a**, 697–726.

Boiko, A. V., Nechepurenko, Y. M. and Sadkane, M.: 2010, Fast computation of optimal disturbances for duct flows with a given accuracy, *Computational Mathematics and Mathematical Physics* **50**(11), 1914–1924.

Borg, M., Kimmel, R. and Stanfield, S.: 2012, Traveling crossflow instability for HIFiRE-5 in a quiet hypersonic wind tunnel, *43rd AIAA Fluid Dynamics Conference*, AIAA Paper 2012-2737.

Borg, M. P. and Schneider, S. P.: 2008, Effect of freestream noise on roughness-induced transition for the x-51a forebody, *Journal of Spacecraft and Rockets* **45**(6), 1106–1116.

Borrill, J.: 1999, Madcap-the microwave anisotropy dataset computational analysis package, *arXiv preprint astro-ph/9911389* .

Boyd, J.: 1989, *Chebyshev & Fourier Spectral Methods*, Springer-Verlag.

Bres, G. A. and Colonius, T.: 2008, Three-dimensional instabilities in compressible flow over open cavities, *Journal of Fluid Mechanics* **599**, 309–339.

Bridges, T. and Morris, P.: 1984, Differential eigenvalue problems in which the parameter appears nonlinearly, *Journal of Computational Physics* **55**(3), 437–460.

Briggs, R. J.: 1964, Electron-stream interaction with plasmas, Cambridge, Ma: MIT Press.

Butler, K. and Farrell, B.: 1992, Three-dimensional optimal perturbations in viscous shear flow, *Physics of Fluids* **4(8)**.

Byström, M. G., Pralits, J. O., Hanifi, A., Luchini, P. and Henningson, D.: 2007, Optimal disturbances in three-dimensional boundary-layer flows, *6th ERCOFTAC SIG 33 workshop, Laminar-Turbulent Transition Mechanisms, Prediction and Control. June 17-20, 2007, Kleinwalsertal, Austria.*

Cantwell, C., Barkley, D. and Blackburn, H.: 2010, Transient growth analysis of flow through a sudden expansion in a circular pipe, *Physics of Fluids* **22**(3), 034101.

Canuto, C., Hussaini, M., Quarteroni, A. and Zang, T.: 1988, *Spectral Methods*, Springer-Verlag, Berlin.

Canuto, C., Hussaini, M. Y., Quarteroni, A. and Thomas Jr, A.: 2012, *Spectral methods in fluid dynamics*, Springer-Verlag, Berlin.

Canuto, C., Hussaini, M. Y., Quarteroni, A. and Zang, T. A.: 2006, *Spectral methods: fundamentals in single domains*, Springer-Verlag, Berlin.

Canuto, D. and Taira, K.: 2015, Two-dimensional compressible viscous flow around a circular cylinder, *Journal of Fluid Mechanics* **785**, 349–371.

Carpenter, A., Saric, W. and Reed, H.: 2008, Laminar flow control on a swept wing with distributed roughness, *26th AIAA Applied Aerodynamics Conference*, AIAA Paper 2008-7335.

Carter, J. E.: 1972, Numerical solutions of the navier-stokes equations for the supersonic laminar flow over a two-dimensional compression corner, *Technical report*, NASA TR R-385.

Cerminara, A.: 2017, *Boundary-layer receptivity and breakdown mechanisms for hypersonic flow over blunt leading-edge configurations*, PhD thesis, University of Southampton.

Cerminara, A. and Sandham, N.: 2020, Transition mechanisms in cross-flow-dominated hypersonic flows with free-stream acoustic noise, *Journal of Fluid Mechanics* **896**(A21).

Chambre, P. A. and Schaaf, S. A.: 1961, *Flow of rarefied gases*, Princeton Aeronautical Paperbacks, Princeton Legacy Library.

Chang, C.-L., Malik, M. and Hussaini, M.: 1990, Effects of shock on the stability of hypersonic boundary layers, *21st Fluid Dynamics, Plasma Dynamics and Lasers Conference*, p. 1448.

Chapman, D. R., Kuehn, D. M. and Larson, H. K.: 1958, Investigation of separated flows in supersonic and subsonic streams with emphasis on the effect of transition, *Technical report*, NACA Report 1356.

Cheatwood, F. M. and Gnoffo, P. A.: 1996, User's manual for the langley aerothermodynamic upwind relaxation algorithm (LAURA), *Technical report*, NASA TM-4764.

Chiba, S.: 1998, Global stability analysis of incompressible viscous flow, *J. Jpn. Soc. Comput. Fluid Dyn* **7**, 20–48.

Chomaz, J., Huerre, P. and Redekopp, L.: 1988, Bifurcations to local and global modes in spatially developing flows, *Physical review letters* **60**(1), 25.

Chomaz, J.-M.: 2005, Global instabilities in spatially developing flows: non-normality and nonlinearity, *Annu. Rev. Fluid Mech.* **37**, 357–392.

Choudhari, M., Chang, C.-L., Jentink, T., Li, F., Berger, K., Candler, G. and Kimmel, R.: 2009, Transition analysis for the HIFiRE-5 vehicle, *39th AIAA Fluid Dynamics Conference*. AIAA Paper 2009–4056.

Choudhari, M., Li, F., Chang, C.-L., Edwards, J., Kegerise, M. and King, R.: 2010, Laminar-turbulent transition behind discrete roughness elements in a high-speed boundary layer, *48th AIAA aerospace sciences meeting including the new horizons forum and aerospace exposition*, AIAA paper 2012-1575.

Choudhari, M., Li, F. and Edwards, J.: 2009, Stability analysis of roughness array wake in a high-speed boundary layer, *47th AIAA Aerospace Sciences Meeting including The New Horizons Forum and Aerospace Exposition*, AIAA paper 2009-170.

Choudhari, M. M., Li, F. and Paredes, P.: 2020, Streak instabilities on HIFiRE-5 elliptic cone, *AIAA Scitech 2020 Forum*, AIAA paper 2020-0828.

Choudhari, M., Norris, A., Li, F., Chang, C.-L. and Edwards, J.: 2013, Wake instabilities behind discrete roughness elements in high speed boundary layers, *51st AIAA aerospace sciences meeting including the new horizons forum and aerospace exposition*, AIAA paper 2013-0081.

Chu, B.-T.: 1965, On the energy transfer to small disturbances in fluid flow (part i), *Acta Mechanica* **1**(3), 215–234.

Chynoweth, B. C., Edelman, J., Gray, K., McKiernan, G. and Schneider, S. P.: 2017, Measurements in the boeing/afosr mach-6 quiet tunnel on hypersonic boundary-layer transition, *47th AIAA Fluid Dynamics Conference*, AIAA paper 2017-3632.

Cohen, C. B. and Reshotko, E.: 1955, Similar solutions for the compressible laminar boundary layer with heat transfer and pressure gradient, *Technical report*, NACA report 1293, Flight Propulsion Research Lab, Cleveland Oh.

Corbett, P. and Bottaro, A.: 2001, Optimal linear growth in swept boundary layers, *Journal of Fluid Mechanics* **435**, 1–23.

Corke, T., Bar-Sever, A. and Morkovin, M.: 1986, Experiments on transition enhancement by distributed roughness, *The Physics of fluids* **29**(10), 3199–3213.

Cossu, C. and Brandt, L.: 2002, Stabilization of Tollmien-Schlichting waves by finite amplitude optimal streaks in the Blasius boundary layer, *Physics of Fluids* **14**, L57.

Cossu, C., Chomaz, J.-M., Huerre, P. and Costa, M.: 2000, Maximum spatial growth of görtler vortices, *Flow, turbulence and combustion* **65**(3), 369–392.

Cossu, C., Pujals, G. and Depardon, S.: 2009, Optimal transient growth and very large-scale structures in turbulent boundary layers, *Journal of Fluid Mechanics* **619**, 79.

Crouch, J., Garbaruk, A. and Magidov, D.: 2007, Predicting the onset of flow unsteadiness based on global instability, *Journal of Computational Physics* **224**(2), 924–940.

Crouch, J., Garbaruk, A., Magidov, D. and Travin, A.: 2009, Origin of transonic buffet on aerofoils, *Journal of fluid mechanics* **628**, 357.

De Tullio, N.: 2013, *Receptivity and transition to turbulence of supersonic boundary layers with surface roughness*, PhD thesis, University of Southampton.

De Tullio, N., Paredes, P., Sandham, N. and Theofilis, V.: 2013, Laminar–turbulent transition induced by a discrete roughness element in a supersonic boundary layer, *Journal of Fluid Mechanics* **735**, 613–646.

De Tullio, N. and Sandham, N. D.: 2015, Influence of boundary-layer disturbances on the instability of a roughness wake in a high-speed boundary layer, *Journal of Fluid Mechanics* **763**(10), 136–165.

De Vicente, J., Basley, J., Meseguer-Garrido, F., Soria, J. and Theofilis, V.: 2014, Three-dimensional instabilities over a rectangular open cavity: from linear stability analysis to experimentation, *Journal of Fluid Mechanics* **748**, 189.

Dijkstra, H.: 1992, On the structure of cellular solutions in rayleigh-benard-marangoni flows in small-aspect-ratio containers, *Journal of Fluid Mechanics* **243**, 73–102.

Dinzl, D. J. and Candler, G. V.: 2017, Direct simulation of hypersonic crossflow instability on an elliptic cone, *AIAA journal* **55**(6), 1769–1782.

Dolvin, D.: 2008, Hypersonic international flight research and experimentation (HiFIRE) fundamental science and technology development strategy, *15th AIAA International Space Planes and Hypersonic Systems and Technologies Conference*, p. 2581.

Downs, R., White, E. and Denissen, N.: 2008, Transient growth and transition induced by random distributed roughness, *AIAA Journal* **46**(2), 451–462.

Drazin, P. and Reid, W.: 1981, *Hydrodynamic Stability*, Cambridge University Press.

Duan, L. and Choudhari, M.: 2012, Effects of riblets on skin friction and heat transfer in high-speed turbulent boundary layers, *50th AIAA Aerospace Sciences Meeting Including the New Horizons Forum and Aerospace Exposition*, AIAA paper 2012-1108.

Edney, B.: 1968, Anomalous heat transfer and pressure distributions on blunt bodies at hypersonic speeds in the presence of an impinging shock., *Technical report*, No. FFA-115, Flygtekniska Forsoksanstalten, Stockholm (Sweden).

Edwards, W., Tuckerman, L., Friesner, R. and Sorensen, D.: 1994, Krylov methods for the incompressible Navier-Stokes equations, *Journal of Computational Physics* **110**, 82–102.

Egorov, I., Neiland, V. and Shredchenko, V.: 2011, Three-dimensional flow structures at supersonic flow over the compression ramp, *49th AIAA Aerospace Sciences Meeting*. AIAA paper 2011-730.

Ehrenstein, U. and Gallaire, F.: 2008, Two-dimensional global low-frequency oscillations in a separating boundary-layer flow, *Journal of Fluid Mechanics* **614**, 315.

Ellingsen, T. and Palm, E.: 1975, Stability of linear flow, *The Physics of Fluids* **18**(4), 487–488.

Eriksson, L. and Rizzi, A.: 1985, Computer-aided analysis of the convergence to steady state of discrete approximations to the euler equations, *Journal of Computational Physics* **57**, 90–128.

Erlebacher, G. and Hussaini, M.: 1990, Numerical experiments in supersonic boundary-layer stability, *Physics of Fluids A: Fluid Dynamics* **2**(1), 94–104.

Evans, B., Morgan, K. and Hassan, O.: 2011, A discontinuous finite element solution of the boltzmann kinetic equation in collisionless and bgk forms for macroscopic gas flows, *Applied Mathematical Modelling* **35**(3), 996–1015.

Farrell, B. F. and Ioannou, P. J.: 1996, Generalized stability theory. Part I: Autonomous operators, *Journal of the atmospheric sciences* **53**(14), 2025–2040.

Farrell, B. and Ioannou, P.: 2000, Transient and asymptotic growth of two-dimensional perturbations in viscous compressible shear flow, *Physics of Fluids* **12**(11), 3021–3028.

Fasel, H.: 1976, Investigation of the stability of boundary layers by a finite-difference model of the navier—stokes equations, *Journal of Fluid Mechanics* **78**(2), 355–383.

Fasel, H., Thumm, A. and Bestek, H.: 1993, Direct numerical simulation of transition in supersonic boundary layers: oblique breakdown, *Fluids Engineering Conference*, Publ by ASME, pp. 77–92.

Fedorov, A.: 2011, Transition and stability of high-speed boundary layers, *Annual Review of Fluid Mechanics* **43**, 79–95.

Feldman, Y. and Gelfgat, A.: 2010, Oscillatory instability in a 3d lid-driven flow in a cube, *Physics of Fluids* **22**, 093602.

Fischer, M. C. and Weinstein, L. M.: 1972, Cone transitional boundary-layer structure at Me= 14, *AIAA Journal* **10**(5), 699–701.

Fransson, J., Brandt, L., Talamelli, A. and Cossu, C.: 2005, Experimental study of the stabilization of Tollmien-Schlichting waves by finite amplitude streaks, *Physics of Fluids* **17**(054110).

Fujii, K.: 2006, Experiment of the two-dimensional roughness effect on hypersonic boundary-layer transition, *Journal of Spacecraft Rockets* **43**(4), 731–738.

Gaitonde, D. V.: 2015, Progress in shock wave/boundary layer interactions, *Progress in Aerospace Sciences* **72**, 80–99.

Gallis, M. A., Torczynski, J. R., Plimpton, S. J., Rader, D. J. and Koehler, T.: 2014, Direct simulation monte carlo: The quest for speed, *AIP Conference Proceedings*, Vol. 1628, American Institute of Physics, pp. 27–36.

Gasperas, G.: 1987, The stability of the compressible boundary layer on a sharp cone at zero angle of attack, *25th AIAA Aerospace Sciences Meeting*, AIAA paper 1987-0494.

Gaster, M.: 1962, A note on the relation between temporally increasing and spatially increasing disturbances in hydrodynamic instability, *J. Fluid Mech.* **14**, 222–224.

Gennaro, E. M.: 2008, *Análise da instabilidade hidrodinâmica de uma esteira assimétrica*, PhD thesis, Universidade de São Paulo.

Gennaro, E., Rodriguez, D., Medeiros, M. and Theofilis, V.: 2011, Linear instability of orthogonal compressible leading-edge boundary layer flow, *6th AIAA Theoretical Fluid Mechanics Conference*, AIAA paper 2011-3751.

Gennaro, E., Rodríguez, D., Medeiros, M. and Theofilis, V.: 2013, Sparse techniques in global flow instability with application to compressible leading-edge flow, *AIAA journal* **51.9**, 2295–2303.

Giannetti, F. and Luchini, P.: 2007, Structural sensitivity of the first instability of the cylinder wake, *Journal of Fluid Mechanics* **581**, 167–197.

Giannetti, F., Luchini, P. and Marino, L.: 2009, Linear stability analysis of three-dimensional lid-driven cavity flow., *Atti del XIX Congresso AIMETA di Meccanica Teorica e Applicata*, Aras Edizioni, Ancona, Italy, Ancona 14-17 Sep. 2009, pp. 738.1–10.

Gill, A.: 1965, On the behaviour of small disturbances to poiseuille flow in a circular pipe, *Journal of Fluid Mechanics* **21**(1), 145–172.

Golub, G. and van Loan, C.: 1996, *Matrix Computations*, 3 edn, The Johns Hopkins University Press.

Gomez, F., Gómez, R. and Theofilis, V.: 2014, On three-dimensional global linear instability analysis of flows with standard aerodynamics codes, *Aerospace Science and Technology* **32**(1), 223–234.

Gómez, F., Paredes, P., Gómez, R. and Theofilis, V.: 2012, Global stability of cubic and large aspect ratio three-dimensional lid-driven cavities, AIAA paper 2012-3274.

González, L. M., Theofilis, V. and Gómez-Blanco, R.: 2007a, Finite element methods for viscous incompressible biglobal instability analysis on unstructured meshes, *AIAA journal* **45**(4), 840–854.

González, L., Theofilis, V. and Gomez-Blanco, R.: 2007b, Finite element methods for viscous incompressible BiGlobal instability analysis on unstructured meshes, *AIAA Journal* **45**(4), 840–854.

Görtler, H.: 1941, Instabilität laminarer Grenzschichten an konkaven Wänden gegenüber gewissen dreidimensionalen Störungen, *ZAMM-Journal of Applied Mathematics and Mechanics/Zeitschrift für Angewandte Mathematik und Mechanik* **21**(4), 250–252.

Görtler, H.: 1955, Dreidimensionale Instabilität der ebenen Staupunktströmung gegenüber wirbelartigen Störungen, *in* H. Görtler and W. Tollmien (eds), *50 Jahre Grenzschichtforschung*, Vieweg und Sohn, pp. 304–314.

Gosse, R., Kimmel, R. and Johnson, H.: 2010, Cfd study of the HIFiRE-5 flight experiment, *40th Fluid Dynamics Conference and Exhibit*, AIAA Pap. 2010-4854.

Gosse, R., Kimmel, R. and Johnson, H. B.: 2013, Study of boundary-layer transition on hypersonic international flight research experimentation 5, *Journal of Spacecraft and Rockets* **51**(1), 151–162.

Gottlieb, D., Hussaini, M. and Orszag, S.: 1984, Theory and applications of spectral methods, *Spectral Methods for Partial Differential Equations*, SIAM, Philadelphia, pp. 1–54.

Gregory, N., Stuart, J. T. and Walker, W.: 1955, On the stability of three-dimensional boundary layers with application to the flow due to a rotating disk, *Philosophical Transactions of the Royal Society of London. Series A, Mathematical and Physical Sciences* **248**(943), 155–199.

Gu, X.-J. and Emerson, D. R.: 2009, A high-order moment approach for capturing non-equilibrium phenomena in the transition regime, *J. Fluid Mech.* **636**, 177–216.

Gulyaev, A., Kozlov, V., Kuznetsov, V., Mineev, B. and Sekundov, A.: 1989, Interaction of a laminar boundary layer with external turbulence, *Fluid Dynamics* **24**(5), 700–710.

Hall, P.: 1983, The linear development of Görtler vortices in growing boundary layers, *Journal of Fluid Mechanics* **130**, 41–58.

Hall, P., Malik, M. and Poll, D.: 1984, On the stability of an infinitive swept attachment line boundary layer, *Proc. R. Soc. Lond. A* **395**, 229–245.

Hanifi, A., Schmid, P. J. and Henningson, D. S.: 1996, Transient growth in compressible boundary layer flow, *Physics of Fluids* **8**(3), 826–837.

Haynes, T. S. and Reed, H. L.: 2000, Simulation of swept-wing vortices using nonlinear parabolized stability equations, *Journal of Fluid Mechanics* **405**, 325–349.

He, W., Gioria, R., Pérez, J. and Theofilis, V.: 2017, Linear instability of low reynolds number massively separated flow around three naca airfoils, *Journal of Fluid Mechanics* **811**, 701–741.

Heeg, R. S. and Geurts, B. J.: 1997, Spatial instabilities of the incompressible attachment-line flow using sparse matrix jacobi–davidson techniques, *Applied scientific research* **59**(4), 315–329.

Helmholtz, H. v.: 1868, On discontinuous fluid motions, *Phil. Mag* **36**(4), 337–346.

Henningson, D. S., Lundbladh, A. and Johansson, A. V.: 1993, A mechanism for bypass transition from localized disturbances in wall-bounded shear flows, *Journal of Fluid Mechanics* **250**, 169–207.

Herbert, T.: 1984a, Analysis of the subharmonic route to transition in boundary layers, *22nd Aerospace Sciences Meeting*, AIAA paper 1984-0009.

Herbert, T.: 1984b, Secondary instability of shear flows, *AGARD–R–709 Special Course on Stability and Transition of Laminar Flow*, pp. 7.1–7.13.

Herbert, T.: 1988, Secondary instability of boundary layers, *Annual review of fluid mechanics* **20**, 487–526.

Herbert, T.: 1994, Parabolized stability equations, *AGARD Report No. 793. Special Course on Progress in Transition Modelling* pp. 4(1)–4(34).

Herbert, T.: 1997, Parabolized stability equations, *Annual Review Fluid Mechanics* **29**, 245–283.

Herbert, T. and Bertolotti, F.: 1987, Stability analysis of nonparallel boundary layers, *Bull. Am. Phys. Soc* **32**, 2079.

Hermanns, M. and Hernández, J.: 2008, Stable high-order finite-difference methods based on non-uniform grid point distributions, *International Journal for Numerical Methods in Fluids* **56**, 233–255.

Hida, K.: 1953, An approximate study on the detached shock wave in front of a circular cylinder and a sphere, *Journal of the Physical Society of Japan* **8**(6), 740–745.

Hill, D.: 1992, A theoretical approach for analyzing the restabilization of wakes, *30th Aerospace Sciences Meeting and Exhibit*, AIAA 92-0067.

Holden, M. S.: 1998, Experimental studies of laminar, transitional, and turbulent hypersonic flows over elliptic cones at angles of attack, *Technical report*, CALSPAN ub research center Buffalo NY.

Hollis, B.: 2010, Blunt-body entry vehicle aerothermodynamics: transition and turbulence on the cev and msl configurations, *40th Fluid dynamics conference and exhibit*, AIAA paper 2010-4984.

Horvath, T. J., Zalameda, J. N., Wood, W. A., Berry, S. A., Schwartz, R. J., Dantowitz, R. F., Spisz, T. S. and Taylor, J. C.: 2012, Global infrared observations of roughness induced transition on the space shuttle orbiter, *Technical report*, RTO-MP-AVT-200 (27). NATO.

Huerre, P. and Monkewitz, P.: 1985, Absolute and convective instabilities in free shear layers, *Journal of Fluid Mechanics* **159**, 151–168.

Huerre, P. and Monkewitz, P.: 1990, Local and global instabilities in spatially developing flows, *Annual Review Fluid Mechanics* **22**, 473–537.

Hultgren, L. and Gustavsson, H.: 1981, Algebraic growth of disturbances in a laminar boundary layer., *Physics of Fluids* **24**(1000).

Huntley, M. and Smits, A.: 2000, Transition studies on an elliptic cone in mach 8 flow using filtered rayleigh scattering, *European Journal of Mechanics-B/Fluids* **19**(5), 695–706.

Imai, I.: 1938, On the flow of a compressible fluid past a circular cylinder, *Proceedings of the Physico-Mathematical Society of Japan. 3rd Series* **20**, 636–645.

Iyer, P. S. and Mahesh, K.: 2013, High-speed boundary-layer transition induced by a discrete roughness element, *J. Fluid Mech* **729**, 524–562.

Jackson, C.: 1987, A finite-element study of the onset of vortex shedding in flow past variously shaped bodies, *Journal of Fluid Mechanics* **182**, 23–45.

Jiang, G. S. and Shu, C. W.: 1996, Efficient implementation of weighted eno schemes, *Journal of Computational Physics* **126**, 202–228.

Juliano, T. J., Adamczak, D. and Kimmel, R. L.: 2014, HIFiRE-5 flight test heating analysis, *52nd Aerospace Sciences Meeting*, AIAA paper 2014-0076.

Juliano, T. J., Adamczak, D. and Kimmel, R. L.: 2015, Hifire-5 flight test results, *Journal of Spacecraft and Rockets* **52**(3), 650–663.

Juliano, T. J., Borg, M. P. and Schneider, S. P.: 2015, Quiet tunnel measurements of HIFiRE-5 boundary-layer transition, *AIAA Journal* **53**(4), 832–846.

Juliano, T. and Schneider, S.: 2010, Instability and transition on the HIFiRE-5 in a mach 6 quiet tunnel, *40th Fluid Dynamics Conference and Exhibit*, AIAA paper 2010-5004.

Juniper, M. P., Hanifi, A. and Theofilis, V.: 2014, Modal stability theorylecture notes from the flow-nordita summer school on advanced instability methods for complex flows, stockholm, sweden, 2013, *Applied Mechanics Reviews* **66**(2), 024804.

Kachanov, Y. S.: 1994, Physical mechanisms of laminar-boundary-layer transition, *Annual review of fluid mechanics* **26**(1), 411–482.

Kachanov, Y. S. and Levchenko, V. Y.: 1984, The resonant interaction of disturbances at laminar-turbulent transition in a boundary layer, *Journal of Fluid Mechanics* **138**, 209–247.

Karniadakis, G. and Sherwin, S.: 2005, *Spectral/hp element methods for Computational Fluid Dynamics (2nd ed.)*, Oxford University Press.

Kendall, J.: 1975, Wind tunnel experiments relating to supersonic and hypersonic boundary-layer transition, *AIAA Journal* **13**(3), 290–299.

Kennard, E. H.: 1938, *Kinetic Theory Of Gases With An Introduction To Statistical Mechanics*, International Series In Pure And Applied Physics, McGraw-Hill Book Company, Inc.

Kimmel, R.: 2008, Aerothermal design for the HIFiRE flight vehicle, *38th Fluid Dynamics Conference and Exhibit*, AIAA paper 2008-4034.

Kimmel, R., Adamczak, D., Berger, K. and Choudhari, M.: 2010, HIFiRE-5 flight vehicle design, *40th Fluid Dynamics Conference and Exhibit*, AIAA paper 2010-4985.

Kimmel, R., Adamczak, D., Gaitonde, D., Rougeux, A. and Hayes, J.: 2007, HIFiRE-1 boundary layer transition experiment design, *45th AIAA Aerospace Sciences Meeting and Exhibit*, AIAA paper 2007-534.

Kimmel, R., Adamczak, D., Juliano, T. and Paull, A.: 2013, HIFiRE-5 flight test preliminary results, *51st AIAA Aerospace Sciences Meeting including the New Horizons Forum and Aerospace Exposition*, AIAA paper 2013-0377.

Kimmel, R., Adamczak, D., Paull, A., Paull, R., Shannon, J., Pietsch, R., Frost, M. and Alesi, H.: 2011, HIFiRE-1 preliminary aerothermodynamic measurements, *41st AIAA Fluid Dynamics Conference and Exhibit*, AIAA paper 2011-3413.

Kimmel, R. L., Poggie, J. and Schwoerke, S. N.: 1999, Laminar-turbulent transition in a Mach 8 elliptic cone flow, *AIAA Journal* **37**(9), 1080–1087.

Kitsios, V., Rodríguez, D., Theofilis, V., Ooi, A. and Soria, J.: 2009, BiGlobal stability analysis in curvilinear coordinates of massively separated lifting bodies, *Journal of Computational Physics* **228**, 7181–7196.

Klebanoff, P. S., Tidstrom, K. and Sargent, L.: 1962, The three-dimensional nature of boundary-layer instability, *Journal of Fluid Mechanics* **12**(1), 1–34.

Klebanoff, P. and Tidstrom, K.: 1972, Mechanism by which a two-dimensional roughness element induces boundary layer transition, *Physics of Fluids* **15**(7), 1173–1188.

Kleiser, L. and Schumann, U.: 1984, Spectral simulations of the laminar-turbulent transition process in plane poiseuille flow, *Spectral methods for partial differential equations* pp. 141–163.

Kleiser, L. and Zang, T. A.: 1991, Numerical simulation of transition in wall-bounded shear flows, *Annual review of fluid mechanics* **23**(1), 495–537.

Kligmann, B. B., Boiko, A., Westin, K. A., Kozlov, V. and Alfredsson, P.: 1993, Experiments on the stability of tollmien-schlichting waves, *European journal of mechanics. B, Fluids* **12**(4), 493–514.

Kloker, M.: 2008, *Lecture material*, PhD thesis, Universität Stuttgart.

Klothakis, A. G., Lygidakis, G. N. and Nikolos, I. K.: 2017, Rarefied gas flow analysis of a suborbital shuttle with the academic CFD code Galatea, *ASME 2017 International*

Mechanical Engineering Congress and Exposition, American Society of Mechanical Engineers Digital Collection.

Klothakis, A., Quintanilha Jr, H., Sawant, S., Protopapadakis, E., Theofilis, V. and Levin, D.: 2021, Linear stability analysis of hypersonic boundary layers computed by a kinetic approach: A semi-infinite flat plate at $4.5 \leq m_\infty \leq 9$, *Theoretical and Computational Fluid Dynamics* (under review).

Kosinov, A., Maslov, A. and Shevelkov, S.: 1990, Experiments on the stability of supersonic laminar boundary layers, *Journal of Fluid Mechanics* **219**, 621–633.

Kovasznay, L. S.: 1953, Turbulence in supersonic flow, *Journal of the Aeronautical Sciences* **20**(10), 657–674.

Krishnan, L. and Sandham, N.: 2006a, Effect of mach number on the structure of turbulent spots, *Journal of Fluid Mechanics* **566**, 225–234.

Krishnan, L. and Sandham, N. D.: 2006b, On the merging of turbulent spots in a supersonic boundary-layer flow, *International Journal of Heat and Fluid Flow* **27**(4), 542–550.

Kumar, A., Bushnell, D. M. and Hussaini, M. Y.: 1989, Mixing augmentation technique for hypervelocity scramjets, *Journal of Propulsion and Power* **5**(5), 514–522.

Kundu, P. K., Cohen, I. M. and Dowling, D. R.: 1990, *Fluid mechanics*, Academic press San Diego.

Landahl, M.: 1980, A note on an algebraic instability of inviscid parallel shear flows, *Journal of Fluid Mechanics* **98**(2), 243–251.

Landahl, M. T.: 1975, Wave breakdown and turbulence, *SIAM Journal on Applied Mathematics* **28**(4), 735–756.

Laufer, J. and Vrebalovich, T.: 1960, Stability and transition of a supersonic laminar boundary layer on an insulated flat plate, *Journal of Fluid Mechanics* **9**(2), 257–299.

Lees, L.: 1947, The stability of the laminar boundary layer in a compressible fluid, *Technical report*, No. 876, National Advistory Committee for Aeronautics (NACA).

Lees, L. and Lin, C.-C.: 1946, Investigation of the stability of the laminar boundary layer in a compressible fluid, *Technical Report 1115*, TN-1115, National Advisory Committee for Aeronautics (NACA).

Lele, S.: 1992, Compact finite difference schemes with spectral- like resolution, *Journal of Computational Physics* **103**, 16–42.

Leriche, E. and Labrosse, G.: 2007, Vector potential–vorticity relationship for the stokes flows: application to the stokes eigenmodes in 2d/3d closed domain, *Theoretical and Computational Fluid Dynamics* **21**(1), 1–13.

Li, F. and Choudhari, M.: 2008, Spatially developing secondary instabilities and attachment line instability in supersonic boundary layers, *46th AIAA Aerospace Sciences Meeting and Exhibit*, AIAA paper 2008-0590.

Li, F. and Choudhari, M.: 2011, Spatially developing secondary instabilities in compressible swept airfoil boundary layers, *Theoretical Computational Fluid Dynamics* **25**, 65–84.

Li, F., Choudhari, M., Chang, C.-L., Kimmel, R., Adamczak, D. and Smith, M.: 2011, Transition analysis for the HIFiRE-1 flight experiment, *41st AIAA Fluid Dynamics Conference and Exhibit*, AIAA paper 2011-3414.

Liepmann, H. W., Narasimha, R. and Chahine, M. T.: 1962, Structure of a plane shock layer, *Phys. Fluids* **5**(11), 1313–1324.

Lighthill, M. and Rosenhead, L.: 1963, Laminar boundary layers, *Clarendon Press, Oxford* .

Lin, C. C.: 1955, The theory of hydrodynamic stability, *Cambridge University Press* .

Lin, R. and Malik, M.: 1996, On the stability of attachment-line boundary layers. Part 1. the incompressible swept Hiemenz flow, *J. Fluid Mech.* **311**, 239–255.

Lin, R. S. and Malik, M. R.: 1995, Stability and transition in compressible attachment-line boundary-layer flow, *SAE Pap. 952041* .

Liu, W. W. and Fang, Y.: 2006, *Microfluid Mechanics - Principles and Modeling*, McGraw-Hill.

Lucas, J.: 2014, *Spatial optimal perturbations for transient growth analysis in three-dimensional boundary layers*, PhD thesis, Université de Toulouse.

Luchini, P.: 2000, Reynolds-number-independent instability of the boundary layer over a flat surface: optimal perturbations, *Journal of Fluid Mechanics* **404**, 289–309.

Luchini, P. and Bottaro, A.: 2014, Adjoint equations in stability analysis, *Annual Review of fluid mechanics* **46**.

Lysenko, V. I. and Maslov, A. A.: 1984, The effect of cooling on supersonic boundary-layer stability, *Journal of Fluid Mechanics* **147**, 39–52.

Lyttle, I. and Reed, H.: 1995, Use of transition correlations for three-dimensional boundary layers within hypersonic flows, AIAA Paper 1995-2293.

Macaraeg, M. and Streett, C.: 1988, A spectral multi-domain technique for viscous compressible reacting flows, *Int. J. Numer. Meth. Fluids* **8**, 1121–1134.

Mack, C. and Schmid, P.: 2010, A preconditioned Krylov technique for global hydrodynamic stability analysis of large-scale compressible flows, *Journal of Computational Physics* **229**(3), 541 – 560.

Mack, C., Schmid, P. and Sesterhenn, J. S.: 2008, Global stability of swept flow around a parabolic body: connecting attachment-line and crossflow modes, *Journal of Fluid Mechanics* **611**, 205 – 215.

Mack, L.: 1965, Computation of the stability of the laminar boundary layer, *Methods in Computational Physics* **4**, 247–299.

Mack, L.: 1969, Boundary layer stability theory. report 900-277 rev. a, *Jet Propulsion Laboratory, Pasadena, CA* **22**.

Mack, L.: 1976, A numerical study of the temporal eigenvalue spectrum of the blasius boundary layer, *Journal of Fluid Mechanics* **73**, 497–520.

Mack, L.: 1984, Boundary-layer stability theory, *AGARD Report No. 709. Special Course on Stability and Transition of Laminar Flow* pp. 3–1–3–81.

Mack, L. M.: 1987, Review of linear compressible stability theory, *Stability of time dependent and spatially varying flows*, (ed. D. L. Dwoyer & M. Y. Hussaini), Springer, pp. 164–187.

Malik, M.: 1989, e^{Malik}: a new spatial stability analysis program for transition prediction using the e^N method, *Rept. HTC-8902*, High Technology Corp., Hampton, VA.

Malik, M.: 1990, Numerical methods for hypersonic boundary layer stability, *Journal of Computational Physics* **86**, 376–413.

Malik, M. and Anderson, E.: 1991, Real gas effects on hypersonic boundary-layer stability, *Physics of Fluids A* **3**(5), 803–821.

Malik, M. R. and Orszag, S. A.: 1987, Linear stability analysis of three-dimensional compressible boundary layers, *Journal of Scientific Computing* **2**(1), 77–97.

Marquet, O., Sipp, D., Chomaz, J.-M. and Jacquin, L.: 2008, Amplifier and resonator dynamics of a low-reynolds-number recirculation bubble in a global framework, *Journal of Fluid Mechanics* **605**, 429–443.

Martin, P., Xu, S. and Wu, M.: 2003, Preliminary work on DNS and LES of STBLI, *33rd AIAA Fluid Dynamics Conference and Exhibit*, AIAA paper 2003-3464.

Masad, J. and Nayfeh, A.: 1990, Subharmonic instability of compressible boundary layers, *Physics of Fluids A: Fluid Dynamics* **2**(8), 1380–1392.

Masad, J. and Nayfeh, A.: 1991, Effect of heat transfer on the subharmonic instability of compressible boundary layers, *Physics of Fluids A: Fluid Dynamics* **3**(9), 2148–2163.

Matsubara, M. and Alfredsson, P. H.: 2001, Disturbance growth in boundary layers subjected to free-stream turbulence, *Journal of fluid mechanics* **430**, 149.

Maxwell, J. C.: 1879, On stresses in rarefied gases arising from inequalities of temperature, *Phi. Trans. R. Soc.* **170**, 231–256.

McKenzie, J. and Westphal, K.: 1968, Interaction of linear waves with oblique shock waves, *The Physics of Fluids* **11**(11), 2350–2362.

Meersman, J. A., Hader, C. and Fasel, H. F.: 2018, Hypersonic boundary-layer transition: comparison of the fundamental resonance breakdown for a flared and straight cone at mach 6, *2018 Fluid Dynamics Conference*, AIAA paper 2018-3851.

Meliga, P., Gallaire, F. and Chomaz, J.-M.: 2012, A weakly nonlinear mechanism for mode selection in swirling jets, *Journal of Fluid Mechanics* **699**, 216–262.

Meseguer-Garrido, F., De Vicente, J., Valero, E. and Theofilis, V.: 2014, On linear instability mechanisms in incompressible open cavity flow, *Journal of Fluid Mechanics* **752**, 219–236.

Miró Miró, F., Beyak, E. S., Pinna, F. and Reed, H. L.: 2019, High-enthalpy models for boundary-layer stability and transition, *Physics of Fluids* **31**(4), 044101.

Miró Miró, F. and Pinna, F.: 2020, Injection-gas-composition effects on hypersonic boundary-layer transition, *Journal of Fluid Mechanics* **890**, R4.

Moller, C. and van Loan, C.: 1978, Nineteen dubious ways to compute the exponential of a matrix, *SIAM Review* **20**, 801–836.

Moller, C. and van Loan, C.: 2003, Nineteen dubious ways to compute the exponential of a matrix, twenty-five years later, *SIAM Review* **45**, 3–000.

Monkewitz, P. A.: 1988, The absolute and convective nature of instability in two-dimensional wakes at low reynolds numbers, *The Physics of Fluids* **31**(5), 999–1006.

Montero, I. P. and Pinna, F.: 2020, Biglobal stability analysis of the wake behind an isolated roughness element in hypersonic flow, *Proceedings of the Institution of Mechanical Engineers, Part G: Journal of Aerospace Engineering* **234**(1), 5–19.

Morkovin, M.: 1994, Transition in open flow systems-a reassessment, *Bull. Am. Phys. Soc.* **39**, 1882.

Morzynski, M. and Thiele, F.: 1991, Numerical stability analysis of a flow about a cylinder, *Zeitschrift Angewandte Mathematik und Mechanik* **71**(5), T424–T428.

Morzyński, M. and Thiele, F.: 2008, Finite element method for global stability analysis of 3D flows, AIAA Paper 2008-3865.

Moyes, A. J., Kocian, T. S., Mullen, D. and Reed, H. L.: 2018, Boundary-layer stability analysis of HIFiRE-5b flight geometry, *Journal of Spacecraft and Rockets* **55**(6), 1341–1355.

Moyes, A. J. and Reed, H. L.: 2021, Preflight boundary-layer stability analysis of bolt geometry, *Journal of Spacecraft and Rockets* **58**(1), 78–89.

Murphy, J. and Rubesin, M.: 1966, Re-evaluation of heat-transfer data obtained in flight tests of heat-sink shielded re-entry vehicles., *Journal of Spacecraft and Rockets* **3**(1), 53–60.

Nagata, T., Noguchi, A., Kusama, K., Nonomura, T., Komuro, A., Ando, A. and Asai, K.: 2020, Experimental investigation on compressible flow over a circular cylinder at reynolds number of between 1000 and 5000, *Journal of Fluid Mechanics* **893**, A13.

Ng, L. L. and Erlebacher, G.: 1992, Secondary instabilities in compressible boundary layers, *Physics of Fluids A: Fluid Dynamics* **4**(4), 710–726.

Nichols, J. W., Larsson, J., Bernardini, M. and Pirozzoli, S.: 2017, Stability and modal analysis of shock/boundary layer interactions, *Theoretical and Computational Fluid Dynamics* **31**(1), 33–50.

Nompelis, I., Drayna, T. and Candler, G.: 2005, A parallel unstructured implicit solver for hypersonic reacting flow simulation, AIAA paper 2005-4867.

Orr, W. M.: 1907, The stability or instability of the steady motions of a perfect liquid and of a viscous liquid. part ii: A viscous liquid, *Proceedings of the Royal Irish Academy. Section A: Mathematical and Physical Sciences*, Vol. 27, pp. 69–138.

Orszag, S.: 1971, Accurate solution of the Orr-Sommerfeld stability equation, *Journal of Fluid Mechanics* **50**, 689–703.

Orszag, S. A. and Gottlieb, D.: 1980, High resolution spectral calculations of inviscid compressible flows, *Approximation Methods for Navier-Stokes Problems*, Springer, pp. 381–398.

Pagella, A., Babucke, A. and Rist, U.: 2004, Two-dimensional numerical investigations of small-amplitude disturbances in a boundary layer at Ma= 4.8: Compression corner versus impinging shock wave, *Physics of Fluids* **16**(7), 2272–2281.

Paredes, P.: 2014, *Advances in global instability computations: from incompressible to hypersonic flow*, PhD thesis, Technical University of Madrid.

Paredes, P., Choudhari, M. M. and Li, F.: 2017, Blunt-body paradox and transient growth on a hypersonic spherical forebody, *Physical Review Fluids* **2**(5), 053903.

Paredes, P., Choudhari, M. M. and Li, F.: 2018, Blunt-body paradox and improved application of transient-growth framework, *AIAA Journal* **56**(7), 2604–2614.

Paredes, P., De Tullio, N., Sandham, N. and Theofilis, V.: 2015, Instability study of the wake behind a discrete roughness element in a hypersonic boundary-layer, *Instability and control of massively separated flows*, (ed. V. Theofilis & J. Soria), Springer International Publishing, pp. 91–96.

Paredes, P., Gosse, R., Theofilis, V. and Kimmel, R.: 2016, Linear modal instabilities of hypersonic flow over an elliptic cone, *Journal of Fluid Mechanics* **804**, 442–466.

Paredes, P., Hermanns, M., Le Clainche, S. and Theofilis, V.: 2013, Order 10^4 speedup in global linear instability analysis using matrix formation, *Computer Methods in Applied Mechanics and Engineering* **253**, 287–304.

Paredes, P. and Theofilis, V.: 2015, Centerline instabilities on the hypersonic international flight research experimentation HIFiRE-5 elliptic cone model, *Journal of Fluids and Structures* **53**, 36–49.

Pérez, J. M., Aguilar, A. and Theofilis, V.: 2017, Lattice boltzmann methods for global linear instability analysis, *Theoretical and Computational Fluid Dynamics* **31**(5), 643–664.

Petrov, G.: 1985, Stability of thin viscous shock layer on a wedge in hypersonic flow of a perfect gas, *IUTAM Symposium on Laminar-Turbulent Transition, Novosibirsk, USSR*, (ed. V. V. Kozlov), Springer-Verlag, pp. 487–493.

Plimpton, S. J., Moore, S. G., Borner, A., Stagg, A. K., Koehler, T. P., Torczynski, J. R. and Gallis, M.: 2019, Direct simulation monte carlo on petaflop supercomputers and beyond, *Physics of Fluids* **31**(8), 086101.

Pralits, J., Byström, M., Hanifi, A., Henningson, D. and Luchini, P.: 2007, Optimal disturbances in three-dimensional boundary-layer flows, *Ercoftac Bulletin* **74**, 23–31.

Pralits, J. O., Airiau, C., Hanifi, A. and Henningson, D. S.: 2000, Sensitivity analysis using adjoint parabolized stability equations for compressible flows, *Flow, turbulence and combustion* **65**(3), 321–346.

Quintanilha Jr, D. A. H., Kataras, P., Theofilis, V. and Hanifi, A.: 2018, Nonmodal stability analysis of the HIFiRE-5 elliptic cone model flow in different flight altitudes, *58th Israel Annual Conference on Aerospace Sciences, IACAS 2018*, Israel Annual Conference on Aerospace Sciences, pp. 1543–1555.

Quintanilha Jr, H. R. D. A., Santos, R., Alves, L. S. and Theofilis, V.: 2017, Distributed solution of global eigenvalue problems on large clusters, *23rd AIAA Computational Fluid Dynamics Conference*.

Raghavendar, J. and Dharmaiah, V.: 2017, Geometrical interpretation of singular value decomposition (SVD) and applications of SVD, *International Journal of Scientific and Innovative Mathematical Research* **5**(4), 23–26.

Rayleigh, J. W. S. B.: 1896, *The theory of sound*, Vol. 2, Macmillan.

Rayleigh, L.: 1878, On the instability of jets, *Proceedings of the London mathematical society* **1**(1), 4–13.

Rayleigh, L.: 1880, On the stability, or instability, of certain fluid motions, *Proc. London Math. Soc.* **9**, 57–70.

Rayleigh, L.: 1917, On the dynamics of revolving fluids, *Proceedings of the Royal Society of London. Series A, Containing Papers of a Mathematical and Physical Character* **93**(648), 148–154.

Reddy, S. C. and Henningson, D. S.: 1993, Energy growth in viscous channel flows, *Journal of Fluid Mechanics* **252**, 209–238.

Reed, H. L. and Saric, W. S.: 1989, Stability of three-dimensional boundary layers, *Annu. Rev. Fluid Mech.* **21**, 235–284.

Reibert, M., Saric, W., Carrillo, Jr, R. and Chapman, K.: 1996, Experiments in nonlinear saturation of stationary crossflow vortices in a swept-wing boundary layer, *34th Aerospace Sciences Meeting and Exhibit*, p. 184.

Reshotko, E.: 2001, Transient growth: a factor in bypass transition, *Physics of Fluids* **13**(5), 1067–1075.

Reshotko, E., Leidy, A., Siddiqui, F. and Bowersox, R. D.: 2016, Characterizing the transient growth mechanism on a hypersonic blunt body at a high angle of attack, *46th AIAA Fluid Dynamics Conference*, AIAA Paper 2016-3951.

Reshotko, E. and Tumin, A.: 2004, Role of transient growth on roughness-induced transition, *AIAA Journal* **42**(4), 766–770.

Reynolds, O.: 1883, An experimental investigation of the circumstances which determine whether the motion of water shall be direct or sinuous, and of the law of resistance in parallel channels, *Philosophical Transactions of the Royal society of London* (174), 935–982.

Ribner, H. S.: 1954, Shock-turbulence interaction and the generation of noise, *Technical report*, TN-3255, National Advisory Committee for Aeronautics (NACA).

Robinet, J.: 2007, Bifurcations in shock-wave/laminar-boundary-layer interaction: global instability approach, *Journal of Fluid Mechanics* **579**, 85–112.

Rodríguez, D. and Theofilis, V.: 2009, Massively parallel numerical solution of the BiGlobal linear instability eigenvalue problem using dense linear algebra, *AIAA J.* **47**(10), 2449–2459.

Rodríguez, D. and Theofilis, V.: 2010, Structural changes of laminar separation bubbles induced by global linear instability, *Journal of Fluid Mechanics* **655**, 280–305.

Rodríguez, D. and Theofilis, V.: 2011, On the birth of stall cells on airfoils, *Theor. Comp. Fluid Dyn.* **25**(1-4), 105–118.

Rodríguez, D., Tumin, A. and Theofilis, V.: 2011, Towards the foundation of a global modes concept, AIAA Paper 2011-3603.

Rosenhead, V.: 1963, Laminar boundary layers, *Oxford University Press*.

Saad, Y.: 1980, Variations on arnoldi's method for computing eigenelements of large unsymmetric matrices, *Linear algebra and its applications* **34**, 269–295.

Salwen, H., Cotton, F. W. and Grosch, C. E.: 1980, Linear stability of poiseuille flow in a circular pipe, *Journal of Fluid Mechanics* **98**(2), 273–284.

Sandham, N. and Adams, N.: 1993, Numerical simulation of boundary-layer transition at mach two, *Applied Scientific Research* **51**(1-2), 371–375.

Sandham, N., Adams, N. A. and Kleiser, L.: 1995, Direct simulation of breakdown to turbulence following oblique instability waves in a supersonic boundary layer, *Applied scientific research* **54**(3), 223–234.

Santos, R.: 2020, *Um estudo sobre os metodos de Runge-Kutta com forte estabilidade linear e não linear*, PhD thesis, Universidade Federal Fluminense.

Saric, W. S.: 1994, Görtler vortices, *Annual Review of Fluid Mechanics* **26**(1), 379–409.

Saric, W. S., Reed, H. L. and White, E. B.: 2003, Stability and transition of three-dimensional boundary layers, *Annual review of fluid mechanics* **35**(1), 413–440.

Saric, W. S. and Thomas, A.: 1984, Experiments on the subharmonic route to turbulence in boundary layers, *Turbulence and chaotic phenomena in fluids*, (ed. T. Tatsumi), North-Holland, pp. 117–122.

Sawant, S. S., Theofilis, V. and Levin, D. A.: 2021, Kinetic modelling of three-dimensional shock/laminar separation bubble instabilities in hypersonic flows over a double wedge, *arXiv preprint arXiv:2101.08957* .

Sawant, S. S., Tumuklu, O., Theofilis, V. and Levin, D. A.: 2019, Linear instability of shock-dominated laminar hypersonic separated flows, *arXiv preprint arXiv:2101.03688* .

Schlichting, H.: 1932, Berechnung ebener periodischer grenzschichtstromungen, *Phys. z.* **33**, 327–335.

Schmid, P. and Henningson, D. S.: 2001, *Stability and transition in shear flows*, Springer.

Schmid, P. J.: 2007, Nonmodal stability theory, *Annu. Rev. Fluid Mech.* **39**, 129–162.

Schmid, P. J. and Brandt, L.: 2014, Analysis of fluid systems: Stability, receptivity, sensitivitylecture notes from the flow-nordita summer school on advanced instability methods for complex flows, stockholm, sweden, 2013, *Applied Mechanics Reviews* **66**(2), 024803.

Schmid, P. J. and Henningson, D. S.: 1994, Optimal energy density growth in hagen–poiseuille flow, *Journal of Fluid Mechanics* **277**, 197–225.

Schmidt, O. and Rist, U.: 2014, Viscid-inviscid pseudo-resonance in streamwise corner flow, *Journal of Fluid Mechanics* **743**, 327–357.

Schmidt, O. T. and Rist, U.: 2011, Linear stability of compressible flow in a streamwise corner, *Journal of Fluid Mechanics* **688**, 569–590.

Schmisseur, J., Schneider, S. and Collicott, S.: 1998, Receptivity of the Mach-4 boundary-layer on an elliptic cone to laser-generated localized free stream perturbations, AIAA Paper 1998-0532.

Schmisseur, J., Schneider, S. and Collicott, S.: 1999, Response of the Mach-4 boundary layer on an elliptic cone to laser-generated free stream perturbations, AIAA Paper 1999-0410.

Schneider, S.: 2008a, Effects of roughness on hypersonic boundary-layer transition, *Journal of Spacecraft Rockets* **45**(2), 193–209.

Schneider, S. P.: 2004, Hypersonic laminar–turbulent transition on circular cones and scramjet forebodies, *Progress in Aerospace Sciences* **40**(1-2), 1–50.

Schneider, S. P.: 2008b, Summary of hypersonic boundary-layer transition experiments on blunt bodies with roughness, *Journal of Spacecraft and Rockets* **45**(6), 1090–1105.

Schubauer, G. B. and Skramstad, H. K.: 1947, Laminar boundary-layer oscillations and transition on a flat plate, *Technical Report 909*, Rept. 909, National Advisory Committee for Aeronautics (NACA).

Sharma, A., Abdessemed, N., Sherwin, S. and Theofilis, V.: 2011, Transient growth mechanisms of low reynolds number flow over a low-pressure turbine blade, *Theoretical and Computational Fluid Dynamics* **25**(1-4), 19–30.

Shi, M., Zhu, W. and Lee, C.: 2020, Engineering model for transition prediction based on a hypersonic quiet wind tunnel, *AIAA Journal* **58**(8), 3476–3485.

Simen, M.: 1992, Local and non-local stability theory of spatially varying flows, *Instability, Transition, and Turbulence*, (ed. M. Y. Hussaini, A. Kumar & C. L. Streett), Springer-Verlag, pp. 181–201.

Sipp, D. and Lebedev, A.: 2007, Global stability of base and mean flows: a general approach and its applications to cylinder and open cavity flows, *Journal of Fluid Mechanics* **593**, 333–358.

Smith, A. and Gamberoni, N.: 1956, Transition, pressure gradient and stability theory., *Rept. ES-26388.*, Douglas Aircraft Co., El Segundo, California.

Sommerfeld, A.: 1908, Ein Beitrag zur hydrodynamischen Erklärung der turbulenten Fluessigkeitsbewegungen, *Proceedings 4th International Congress of Mathematicians, Rome*, Vol. 3, pp. 116–125.

Spalart, P. R. and Yang, K.-S.: 1987, Numerical study of ribbon-induced transition in blasius flow, *Journal of Fluid Mechanics* **178**, 345–365.

Squire, H. B.: 1933, On the stability for three-dimensional disturbances of viscous fluid flow between parallel walls, *Proceedings of the Royal Society of London. Series A, Containing Papers of a Mathematical and Physical Character* **142**(847), 621–628.

Stanfield, S., Kimmel, R. and Adamczak, D.: 2012, HIFiRE-1 flight data analysis: Turbulent shock-boundary-layer interaction experiment during ascent, *42nd AIAA Fluid Dynamics Conference and Exhibit*, AIAA paper 2012-2703.

Strykowski, P. J. and Sreenivasan, K. R.: 1990, On the formation and suppression of vortex 'shedding' at low reynolds numbers, *Journal of Fluid Mechanics* **218**, 71–107.

Stuckert, G. and Reed, H.: 1994, Linear disturbances in hypersonic, chemically reacting shock layers, *AIAA Journal* **32**, 1384–1393.

Taira, K., Brunton, S. L., Dawson, S. T. M., Rowley, C. W., Colonius, T., McKeon, B. J., Schmidt, O. T., Gordeyev, S., Theofilis, V. and Ukeiley, L. S.: 2017, Modal analysis of fluid flows: An overview, *AIAA Journal* **55**(12), 4013–4041.

Tam, C. and Webb, J.: 1993, Dispersion-relation-preserving finite difference schemes for computational acoustics, *Journal of Computational Physics* **107**, 262–281.

Tamada, K.: 1939, On the flow of a compressible fluid past a sphere, *Proceedings of the Physico-Mathematical Society of Japan. 3rd Series* **21**(12), 743–752.

Tamada, K. and Saito, Y.: 1939, Note on the flow of a compressible fluid past a circular cylinder, *Proceedings of the Physico-Mathematical Society of Japan. 3rd Series* **21**(7), 403–409.

Tatsumi, T. and Yoshimura, T.: 1990, Stability of the laminar flow in a rectangular duct, *Journal of Fluid Mechanics* **212**, 437–449.

Tempelmann, D., Hanifi, A. and Henningson, D. S.: 2010, Spatial optimal growth in three-dimensional boundary layers, *Journal of Fluid Mechanics* **646**, 5–37.

Tempelmann, D., Schrader, L.-U., Hanifi, A., Brandt, L. and Henningson, D. S.: 2012, Swept wing boundary-layer receptivity to localized surface roughness, *Journal of Fluid Mechanics* **711**, 516–544.

Tezuka, A. and Suzuki, K.: 2006, Three-dimensional global linear stability analysis of flow around a spheroid, *AIAA J.* **44**(8), 1697–1708.

Theofilis, V.: 1995, Spatial stability of incompressible attachment-line flow, *Theoretical and computational fluid dynamics* **7**(3), 159–171.

Theofilis, V.: 2000a, Globally unstable basic flows in open cavities, *6th Aeroacoustics Conference and Exhibit*, AIAA Paper 2000-1965.

Theofilis, V.: 2000b, On steady–state flow solutions and their nonparallel global linear instability, *in* C. Dopazo (ed.), 8^{th} *European Turbulence Conference, June 27–30, 2000*, Barcelona, Spain, pp. 35–38.

Theofilis, V.: 2000c, On steady laminar basic flows and their global eigenmodes: an elliptic cone in compressible flow, *Final Report F61775-99-WE049*, European Office of Aerospace Research and Development.

Theofilis, V.: 2002, Inviscid global linear instability of compressible flow on an elliptic cone: Algorithmic developments, *Final Report F61775-99-WE049*, European Office of Aerospace Research and Development.

Theofilis, V.: 2003, Advances in global linear instability analysis of nonparallel and three-dimensional flows, *Progress in Aerospace Sciences* **39**(4), 249–315.

Theofilis, V.: 2007, On instability properties of incompressible laminar separation bubbles on a at plate prior to shedding, *AIAA Paper 2007-0540* .

Theofilis, V.: 2011, Global linear instability, *Annual Review of Fluid Mechanics* **43**, 319–352.

Theofilis, V.: 2017, The linearized pressure Poisson equation for global instability analysis of incompressible flows, *Theoretical Computational Fluid Dynamics* **31**, 623–642.

Theofilis, V.: 2018, Global linear stability theory in aerospace applications, *61st Ludwig Prandtl Memorial Lecture - Extended*, Elsevier.

Theofilis, V.: 2020, Massively parallel solution of the global linear instability non-symmetric complex generalized eigenvalue problem, *60th Israel Annual Conference on Aerospace Sciences, IACAS 2020*.

Theofilis, V., Barkley, D. and Sherwin, S.: 2002, Spectral/hp element technology for global flow instability and control, *The Aeronautical Journal* **106**(1065), 619–625.

Theofilis, V. and Colonius, T.: 2004, Three-dimensional instabilities of compressible flow over open cavities: Direct solution of the BiGlobal eigenvalue problem, AIAA 2004-2544.

Theofilis, V., Duck, P. and Owen, J.: 2004, Viscous linear stability analysis of rectangular duct and cavity flows, *Journal of Fluid Mechanics* **505**, 249–286.

Theofilis, V., Fedorov, A. and Collis, S.: 2004, Leading-edge boundary layer flow - Prandtl's vision, current developments and future perspectives, (ed. GEA Meier & K. Sreenivasan), Springer-Berlin, pp. 73–82.

Theofilis, V., Fedorov, A. V., Obrist, D. and Dallmann, U. C.: 2003, The extended Görtler-Hämmerlin model for linear instability of three-dimensional incompressible swept attachment-line boundary layer flow, *J. Fluid Mech.* **487**, 271–313.

Theofilis, V., Hein, S. and Dallmann, U.: 2000, On the origins of unsteadiness and three-dimensionality in a laminar separation bubble, *Philosophical Transactions of the Royal Society of London A: Mathematical, Physical and Engineering Sciences* **358**(1777), 3229–3246.

Thome, J., Dwivedi, A., Nichols, J. W. and Candler, G. V.: 2018, Direct numerical simulation of bolt hypersonic flight vehicle, *2018 Fluid Dynamics Conference*, AIAA Paper 2018-2894.

Thomson, W.: 1871, Xlvi. hydrokinetic solutions and observations, *The London, Edinburgh, and Dublin Philosophical Magazine and Journal of Science* **42**(281), 362–377.

Thumm, A.: 1991, *Numerische Untersuchungen zum laminar-turbulenten Strömungsumschlag in transsonischen Grenzschichtströmungen*, PhD thesis, University of Stuttgart.

Timme, S.: 2020, Global instability of wing shock-buffet onset, *Journal of Fluid Mechanics* **885**(37), 01–32.

Tollmien, W.: 1929, Über die entstehung der turbulenz. 1. mitteilung, Nachr. Ges. Wiss. Göttingen, Math. Phys. Klasse, pp. 21–44.

Tomboulides, A. G. and Orszag, S. A.: 2000, Numerical investigation of transitional and weak turbulent flow past a sphere, *Journal of Fluid Mechanics* **416**, 45–73.

Touber, E. and Sandham, N. D.: 2009, Large-eddy simulation of low-frequency unsteadiness in a turbulent shock-induced separation bubble, *Theoretical and Computational Fluid Dynamics* **23**(2), 79–107.

Trefethen, L. N.: 1992, Pseudospectra of matrices, *in* D. F. Griffiths and G. A. Watson (eds), *Numerical Analysis 1991*, Longman Scientific & Technical, Harlow, Essex, UK, pp. 234–265.

Trefethen, L. N.: 1997, Pseudospectra of linear operators, *SIAM review* **39**(3), 383–406.

Trefethen, L. N. and Embree, M.: 2005, *Spectra and pseudospectra: the behavior of nonnormal matrices and operators*, Princeton University Press.

Trefethen, L. N., Trefethen, A. E., Reddy, S. C. and Driscoll, T. A.: 1993, Hydrodynamic stability without eigenvalues, *Science* **261**(5121), 578–584.

Tufts, M. W., Borg, M. P., Gosse, R. C. and Kimmel, R. L.: 2018, Collaboration between flight test, ground test, and computation on HIFiRE-5, *2018 Applied Aerodynamics Conference*, pp. AIAA paper 2018–3807.

Tufts, M. W., Gosse, R. C. and Kimmel, R. L.: 2017, PSE analysis of crossflow instability on HIFiRE 5b flight test, *47th AIAA Fluid Dynamics Conference*, pp. AIAA Paper 2017–3136.

Tumin, A. and Reshotko, E.: 2001, Spatial theory of optimal disturbances in boundary layers, *Physics of Fluids* **13**(7), 2097–2104.

Tumuklu, O., Levin, D. A. and Theofilis, V.: 2019, Modal analysis with proper orthogonal decomposition of hypersonic separated flows over a double wedge, *Physical Review Fluids* **4**(3), 033403.

Tumuklu, O., Levin, D. and Theofilis, V.: 2018, Investigation of unsteady, hypersonic, laminar separated flows over a double cone geometry using a kinetic approach (editor's choice), *Phys. Fluids* **30**, 046103.

Tumuklu, O., Theofilis, V. and Levin, D. A.: 2018, On the unsteadiness of shock–laminar boundary layer interactions of hypersonic flows over a double cone, *Physics of Fluids* **30**(10), 106111.

Van Ingen, J.: 1956, A suggested semi-empirical method for the calculation of boundary layer transition region., *Rept. UTH-74.*, Univ. of Techn., Dept. of Aero. Eng., Delft.

von Smoluchowski, M.: 1898, Über Wärmeleitung in verdünnten Gasen, *Annalen der Physik* **300**, 101–130.

Wang, X. and Zhong, X.: 2008, Receptivity of a hypersonic flat-plate boundary layer to three-dimensional surface roughness, *Journal of Spacecraft Rockets* **45**(6), 1165–1175.

Wheaton, B. M., Berridge, D. C., Wolf, T. D., Stevens, R. T. and McGrath, B. E.: 2018, Boundary layer transition (bolt) flight experiment overview, *2018 Fluid Dynamics Conference*, AIAA Paper 2018-2892.

White, E.: 2002, Transient growth of stationary disturbances in a flat plate boundary layer, *Physics of Fluids* **14**(12), 4429–4439.

White, E., Rice, J. and Ergin, F.: 2005, Receptivity of stationary transient disturbances to surface roughness, *Physics of Fluids* **17**(064109).

W.M. Zhang, G. M. and X.Wei: 2012, A review on slip models for gas microflows, *Microfluid Nanofluid* **13**, 845–882.

Zang, T. A., Hussaini, M. Y. and Bushnell, D. M.: 1984, Numerical computations of turbulence amplification in shock-wave interactions, *AIAA journal* **22**(1), 13–21.

Zebib, A.: 1984, A chebyshev method for the solution of boundary value problems, *Journal of Computational physics* **53**(3), 443–455.

Zuccher, S., Tumin, A. and Reshotko, E.: 2006, Parabolic approach to optimal perturbations in compressible boundary layers, *Journal of Fluid Mechanics* **556**, 189–216.